Dissertation

submitted to the
Combined Faculties for the Natural Sciences and for Mathematics
of the Ruperto-Carola University of Heidelberg, Germany
for the degree of
Doctor of Natural Sciences

presented by
Diplom-Physicist Frank Sprenger
born in Ravensburg

Oral examination: 12th November, 2003

Production of cold electron beams for collision experiments with stored ions

Referees: **Prof. Dr. Andreas Wolf**
Prof. Dr. H.-Jürgen Kluge

Kurzfassung

Erzeugung kalter Elektronenstrahlen für Stoßexperimente mit gespeicherten Ionen

Für den Speicherring TSR wurde eine neue Elektronentargetsektion (ETS) als reines Elektronentarget gebaut und getestet, mit dessen Hilfe sich Stoßexperimente und Phasenraumkühlung (Elektronenkühlung) eines gespeicherten Ionenstrahls unabhängig voneinander durchführen lassen. An dieser Apparatur wurden vorbereitende Messungen zur Untersuchung der adiabatischen magnetischen Expansion und adiabatischen Beschleunigung der Elektronen vorgenommen. Die longitudinale Energieverteilung der Elektronen konnte in Abhängigkeit von verschiedenen Parametern mittels des eingebauten Gegenfeldenergieanalysators bestimmt werden.
Beim Betrieb im Speicherring konnte die Funktion der ETS zusammen mit dem existierenden Elektronenkühler demonstriert werden. Die Beeinflussung des andauernd gekühlten gespeicherten Strahls durch das Elektronentarget konnte untersucht werden. Zur Diagnose der longitudinalen und transversalen Elektronentemperatur wurde eine Resonanz von dielektronischer Rekombination an lithiumähnlichem Fluor $^{19}F^{6+}$ benutzt. Eine Verbesserung der energetischen Auflösung gegenüber früheren Messungen mit dem TSR Elektronenkühler als Target konnte demonstriert werden.

Abstract

Production of cold electron beams for collision experiments with stored ions

A new electron target section (ETS) as a dedicated electron target for the storage ring TSR has been mounted and tested. With the help of this device electron collision experiments on a stored ion beam can be performed independently of the phase space cooling (electron cooling) of this beam. Preparatory measurements to study the adiabatic magnetic expansion and the adiabatic acceleration of the electrons have been performed on this device. Longitudinal energy spreads where studied in dependence of several parameters using the installed retarding field energy analyzer.
The operation of the ETS together with the existing electron cooler device could be demonstrated in a storage ring experiment. An interaction of the continuously cooled stored ion beam with the electron target beam could be studied. A dielectronic recombination resonance in lithium-like fluorine $^{19}F^{6+}$ was used to determine the longitudinal and transverse electron temperature. An improvement of the energy resolution compared to earlier measurements with the electron cooling device as target could be demonstrated.

Für Friedrich Deihle

Contents

1 Introduction **3**

2 Overview of the electron target project **7**
2.1 Basic design considerations 7
2.2 Experimental applications 9
2.3 Ultracold electron target history 10

3 Electron-ion collision experiments using cold electron beams **13**
3.1 Storage ring merged beams experiments 13
3.1.1 Electron beam as a target 13
3.1.2 Ion motion in the storage ring 17
3.2 Coulomb interactions in charged particle beams 17
3.2.1 Plasma physics quantities 17
3.2.2 Electron-ion collisions 19
3.3 Magnetized cold electron beams 23
3.3.1 Electron sources 23
3.3.2 Electron acceleration 24
3.3.3 Adiabatic magnetic transverse expansion (ATE) 25
3.3.4 Potential energy relaxation 27
3.3.5 Kinetic energy relaxation 28
3.4 Dielectronic recombination for temperature diagnostics 32
3.5 Cold electron targets - optimizing the energy resolution 35

4 The new TSR electron target section **39**
4.1 Electron beam formation 39
4.1.1 The electron gun for thermal cathodes 40
4.1.2 Cold electron source development 42
4.1.3 Magnetic expansion region 43
4.1.4 Gun section assembly and field measurements 45
4.1.5 Adiabatic acceleration section 51
4.2 TSR interaction section 53
4.2.1 Toroid sections 53
4.2.2 Interaction region 58
4.3 Collector section 65
4.4 Electronics 71

4.5 Control system . . . 74
4.6 Ion detector setup . . . 75
4.7 Alignment and bakeout . . . 76
4.8 TSR diagnostics . . . 77
4.8.1 Beam profile monitor (BPM) . . . 77
4.8.2 Schottky spectra . . . 78

5 Preparatory measurements **81**
5.1 Current density distributions at L-test setup . . . 81
5.1.1 Pierce voltage . . . 83
5.1.2 Expansion . . . 84
5.1.3 Deformation by clearing electrodes . . . 87
5.2 EDC measurements . . . 88
5.2.1 Experimental procedure . . . 88
5.2.2 Problems Analyzer version 1 . . . 90
5.2.3 Technical systematics . . . 93
5.2.4 Relaxation processes . . . 101
5.2.5 Discussion . . . 109
5.2.6 Conclusion . . . 116

6 First operation in the storage ring **117**
6.1 ETS in the TSR . . . 117
6.1.1 Procedure . . . 117
6.1.2 ETS as cooler . . . 118
6.1.3 Two electron coolers - Drag effect . . . 120
6.2 First DR measurements . . . 128
6.2.1 Procedure . . . 128
6.2.2 F^{6+} DR spectra . . . 129
6.2.3 Conclusion . . . 138

7 Summary and Outlook **139**

1. Introduction

Electron beams are widely used for atomic physics collision experiments with ions in various experimental arrangements, like single-pass configurations, ion storage rings (magnetic or electrostatic rings) or ion traps (e.g. EBITs, linear electrostatic traps). Especially in storage rings electron beams with low energy spreads ("cold electron beams") are required for electron cooling and as electron targets as we will see in the following. The production of a cold electron beam as an electron target for the storage ring TSR at the Max-Planck-Institut für Kernphysik in Heidelberg (MPIK), Germany will be discussed in this work.
In general storage rings have the advantage that a big number of charged particles can be accumulated and stored over long periods of time (typically minutes, in some cases up to days) being thus available for experiments. Moreover the ion beam momentum spread can be drastically reduced by electron cooling. For electron cooling the stored ion beam is overlapped with an electron beam at zero relative velocity in one of the straight sections of the storage ring (see Fig. 1.1 for the TSR). By Coulomb-interactions energy is transferred from the initially hot ion beam to the electron beam. In every circulation energy is taken away by the renewed cold electrons leading to a low longitudinal momentum spread of the ion beam on the order of $\Delta p/p = 1 \cdot 10^{-4}$. During the cooling process the ion beam diameter is strongly reduced within $\approx 1\,\mathrm{s}$ from typically 25 mm to $\approx 1\,\mathrm{mm}$. For efficient cooling the electron beam diameter has to be much bigger than the ion beam diameter. The cooling force acts as a friction force on the ions which changes the ion velocity towards the electron velocity.
In most existing heavy ion storage rings the electron cooler device is not only used for cooling but also for collision experiments with the stored ions. The electron velocity is detuned from the cooling velocity for some time which leads to a controlled collision energy in the CM-frame of the ion beam. Then the reaction products (charge-changed ions or fragmented molecules) are separated from the stored ion beam in the dipole magnet following the electron cooler and registered on a detector; after such measurement intervals the electron velocity is switched back to the cooling velocity.
The collisions between atomic and molecular ions with electrons studied at storage rings (in particular recombination) show a great variety of sharp resonant structures at CM energies in the range from meV to keV depending on the individual species. Natural widths of 0.1 meV are common, and measurements of absolute cross sections at the highest possible energy resolution and energy accuracy are of interest. The alternating operation of a single electron beam device as a cooler and as a target for collision experiments bears several disadvantages, that in particular limit the experimental precision and energy resolution. During the time where the electron beam is detuned to a relative velocity the ion beam is not cooled anymore and the *momentum spread increases* by intrabeam scattering.

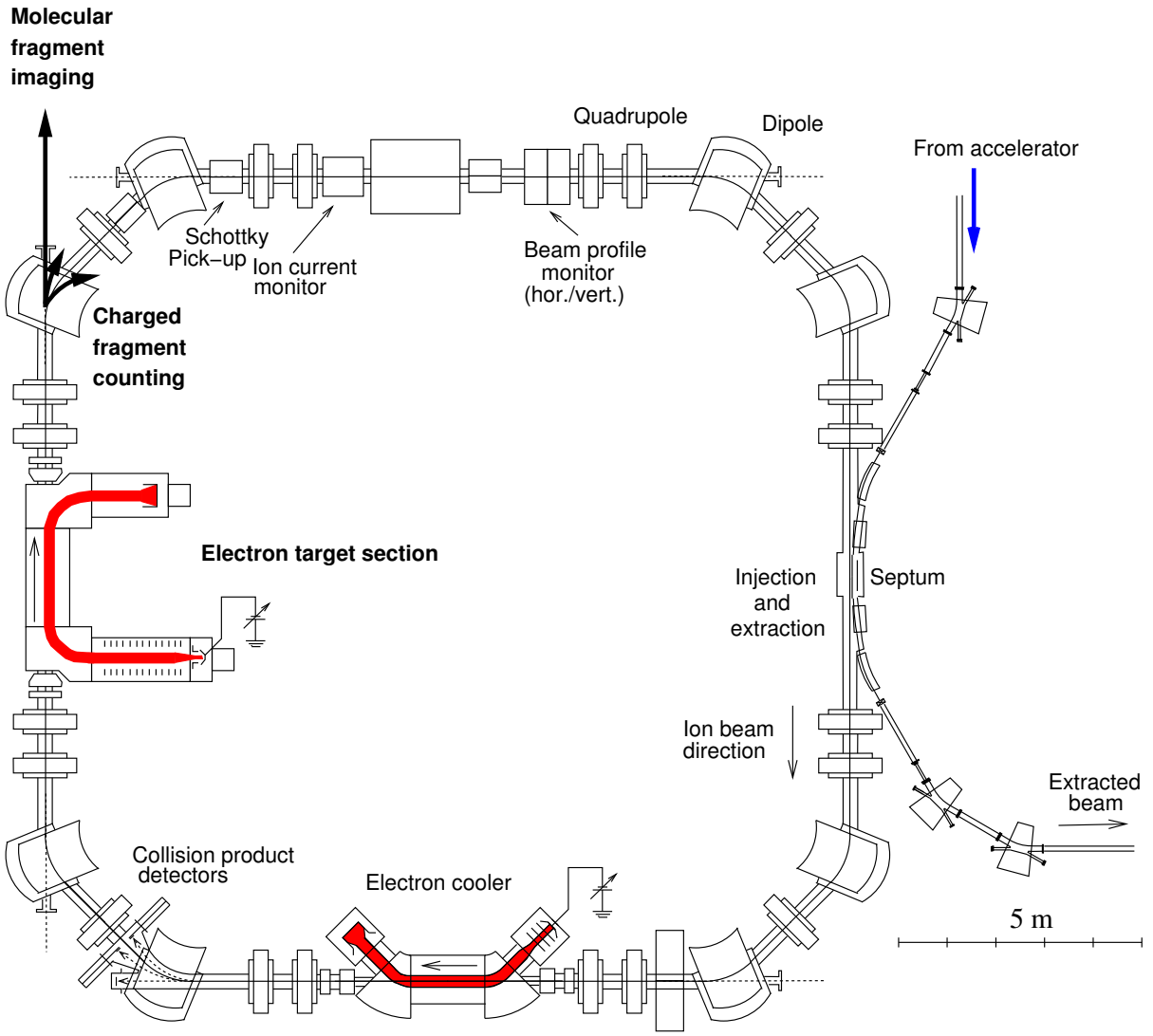

Figure 1.1: Overview of the storage ring TSR with the main components and diagnostic tools. The electron cooler device is installed in the first section following the injection section. In the following experimental section the new ETS with the detectors are installed.

Moreover at low detuning velocities the cooling force is very large which tends to *drag the ion beam* to another energy so that low collision energies cannot be kept up in a stable situation. This implies a trade off between the duty cycle of the measurement and the energy resolution. The required short switching times (few ms time scale) hinder a precise control of the CM collision energy and reduce the effective count rate of the measurement. On the other hand coolers need an electron beam of large transverse size to efficiently cool the large, hot injected ion beam. The main disadvantage is that in the region where the electron beam is bent and merged with the ion beam unavoidable angles between both beams occur. They lead to relative velocities that smear out the collision energy (*toroid effect*). This effect is reduced by a smaller electron beam. Moreover the total

beam current is higher in larger electron beams. This requires strong efforts to reduce the load on the vacuum system.
Because of the mentioned restrictions it is preferable to build an electron target dedicated to collision experiments. It can be operated at arbitrary energy while the ion beam is continuously cooled by the existing electron cooler device. The new high resolution electron-ion collision facility at the TSR is designed as an electron target and to implement consequently the techniques for the production of cold and ultracold electron beams. The quality of both, the ion beam and the electron beam, will be strongly improved to enhance the experimental resolution and to make new experiments possible. The facility installed in the experimental section of TSR (see Fig. 1.1) following the electron cooler device (EC) consists of the actual electron target section (ETS) and the detector system in the following TSR dipole magnet. The whole ETS is horizontally mounted on rails for easy installation and removal from the storage ring. Outside the storage ring, the ETS can be used for electron beam studies in a stand-alone operation.
The development of the new storage ring electron target required a number of complex tasks to be accomplished. Initial work and the basic design was performed by Schmitt [Sch00a]. In this work the detailed realization and preparation up to the completion and operation of the facility will be presented. The layout of the mechanical components, especially vacuum parts according to the UHV conditions of the storage ring, had to be performed and completed. Electrical parts for the electron beam transport (e.g. magnets) and the beam acceleration had to be designed and installed. For experiments with the electron beam, diagnostic methods were implemented and improved. It was necessary to perform electron beam experiments with different acceleration methods trying to suppress heating processes in the beam. Operational parameters suited for the later storage ring experiments had to be found. The completed electron target had to be implemented into the storage ring and the operation together with the existing electron cooler had to be understood. For recombination measurements new experimental schemes had to be explored.
We will start with an overview of the TSR electron target project in chapter 2. The design goals and the experimental applications will be discussed. In chapter 3 the properties of cold magnetized electron beams for collision experiments will be reviewed. The energy resolution for the collision processes is limited by the energy spreads of both the electron and the ion beam and by interactions of the electrons with the stored ions. For the production of cold electron beams an understanding of the relaxation processes in the magnetized electron beam is essential. Following this theoretical part, in chapter 4 the ETS will be presented as it is realized. All of the components from the production of the electron beam in the electron gun, the magnetic expansion (with field measurements), the acceleration and merging with the ion beam, up to the collector with the installed electron beam diagnostics will be presented. Preparatory measurements at the ETS outside the storage ring with the goal to produce a cold electron beam are discussed in chapter 5. Current density distributions of the electron beam have been measured. With the installed retarding field energy analyzer relaxation processes (potential energy and kinetic energy relaxation) in the electron beam have been studied by measuring longitudinal energy distribution curves (EDC). Very low thermal energies in the co-moving frame of 25–30 μeV (290–348 mK) at an electron density of $3 \cdot 10^{13}\,1/\mathrm{m}^3$ and a kinetic energy of 2 keV have

been obtained. Calculations of the TLR heating rates for the experimental conditions are presented which made the qualitative understanding of the processes possible. Finally in chapter 6, results from two beamtimes are presented. In the first C^{6+} beamtime the ETS has been used as electron cooler and it was possible to cool the ion beam without the TSR EC. The action of two electron coolers at different cooling energies on the same ion beam could be observed for the first time using Schottky analysis. The second lithium-like F^{6+} DR beamtime was used for temperature analysis of the electron beam and a very low transverse energy spread $\approx$2.9–3.4 meV (33–40 K) at expansion 60 was found. The measured value is about a factor of 1.7–1.9 bigger than the expected theoretical value. A summary of this work and an outlook will be given in chapter 7.

2. Overview of the electron target project

2.1 Basic design considerations

The storage ring TSR has four different sections of which three are already used for injection/extraction, electron cooling and for beam diagnostics (see Fig. 1.1). This leaves the experimental section following the EC for the installation of new experimental arrangements. The layout of the ETS was restricted by the available space between the TSR quadrupole magnets.
To keep the experimental section also available for other experiments the complete ETS has been installed horizontally on rails. The storage ring and the ETS have been equipped with valves which allows an easy removal of the ETS from the experimental section without putting the ETS or large parts of the TSR to air. An alignment of the beamline is also not necessary due to the rails. A second beamline parallel to the ETS is also mounted on the rails and can be exchanged with the ETS. This has the advantage that the beamline outside the storage ring can be prepared for experiments without blocking the TSR operation. The time for the exchange of the beamlines is only limited by the time needed for the bakeout of the parts that have been put to air. The bakeout is required to reach the UHV conditions of the storage ring.
The advantages of having a dedicated electron target for the ion beam quality, the stability and count rates of the experiments has already been discussed in the introduction. In the following we will discuss how the design of the electron beam was done to improve the experimental resolution. We will distinguish three parts in the ETS (see Fig. 2.1): the electron formation section, the interaction section and the electron collector section. The main parameters of the ETS are summarized in Tab. 2.1. In Fig. 2.2 a picture of the ETS installed in the TSR is shown.
A thermionic electron gun (small cathode diameter of 1.6 mm) or a photocathode gun can be installed into the ETS. The thermionic cathode is much hotter (1100–1300 K) than the photocathode which can be cooled to cryogenic temperatures (90 K). Thus the photocathode allows the production of an ultracold electron beam. Technically, photocathodes are a lot more complicated to handle because the cathodes have to be prepared and activated under very clean conditions for a high surface quality (pressure in the range of 10^{-12} mbar). Also the lifetime is limited to several hours which requires a system for a fast exchange of the cathodes inside the UHV chamber. The achievable currents are below the intensities from thermionic cathodes but nowadays sufficient for experiments.

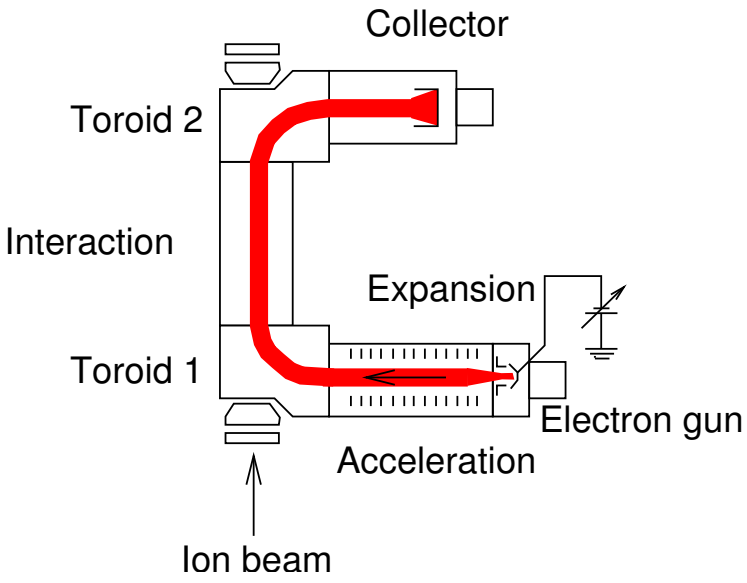

Figure 2.1: Main parts of the ETS: (i) Beam formation section: Electron production, beam expansion and acceleration. (ii) Interaction section: merging the electron beam with the ion beam and interaction region. (iii) Collector section: beam dump and diagnostics.

In the following we will distinguish two electron temperatures: the longitudinal temperature $T_{\parallel}$ along the beam direction and the transverse temperature $T_{\perp}$ perpendicular to it. By the magnetic guiding field of the electron beam both temperatures are decoupled. The initial electron temperature for both degrees of freedom at the electron gun is given by the cathode temperature.
$T_{\parallel}$ is strongly reduced by the electrostatic acceleration to the final energy by the kinematic transformation. But relaxation processes due to Coulomb-interactions in the beam (potential energy relaxation) limit the final temperature that can be obtained. In a long acceleration section with 77 independent electrodes (length 1490 mm) we therefore perform a slow (adiabatic) acceleration to suppress this relaxation. This also means that the extraction of the electrons from the electron gun is separated from the acceleration to the final energy (max. 20 keV).
The transverse temperature is lowered by putting the electron gun into a strong magnetic field (superconducting solenoid magnet, field up to 3.5 T) and extracting the electrons then to a region with lower magnetic field (magnetic expansion). Doing the expansion slowly (adiabatic transverse expansion) $T_{\perp}$ is reduced by the expansion ratio α (up to ≈ 90) between the initial and final magnetic field strength. The electron beam area is increased by the expansion ratio.
For the merging of the electron beam with the ion beam in the interaction section, the radius of the toroid magnets is kept small (only 600 mm) to reduce geometrically shifts in the relative energy. The smaller radius leaves more space for the interaction region following the toroid.
A split solenoid magnet in the interaction region (length 1490 mm) is installed which can be opened up to 40 mm for additional photon detectors for future experiments. With

Orientation	horizontal
Maximum acceleration voltage	20 kV
Magnetic field (gun)	0.04–3.5 T
Magnetic guiding field	0.04–0.1 T
Toroid radius	600 mm
Interaction solenoid length	1476 mm
Interaction mag. field angles (design)	$< 10^{-4}$
Adiabatic acceleration length	1490 mm
Electron gun (thermionic cathode):	
Cathode diameter	1.6 mm
Maximum emission current	180 mA
Gun perveance	1.8 μPerv

Table 2.1: Main parameters of the ETS with the thermionic cathode.

the closed interaction solenoid the magnetic field can be kept homogeneous (field angles $< 10^{-4}$) for high resolution experiments.
In the collector section tools for beam diagnostics are installed. A retarding field energy analyzer in the back of the collector cup allows us to measure longitudinal energy distribution curves for the determination of the longitudinal electron temperature. The small entering aperture of the energy analyzer (50 μm) can be moved over the electron beam two-dimensionally. We are thus able to obtain complete 2D current density distributions of the beam. In the analyzer mode the magnetic field in the collector section is kept homogeneous. For the operation in the storage ring at high current intensities the magnetic field can be expanded by reversing the polarity of two magnet coils which reduces the power density of the beam at the collector (collector mode).
Because of the modular concept of the ETS the electron formation section can be exchanged with the collector section. The electron beam direction is then opposite to the ion beam direction in the storage ring. This leads to high collision energies in the CM-frame of the ion beam (up to 40 keV for a 6 MeV/u ion beam).

2.2 Experimental applications

At the TSR different electron ion-collision processes are studied: dielectronic recombination (DR) of atomic ions, dissociative recombination (DiR) of molecular ions and electron cooling. In the past this has been done with the existing electron cooler.
DR can be used for precision spectroscopy of ionic resonances and for measuring recombination rate coefficients. Studied are e.g. lithium-like system like Scandium in the reaction $Sc^{18+}(1s^2 2s) + e^- \rightarrow Sc^{17+}(1s^2 2p\,nl)(n = 10)$ where then excitation energies $\Delta E(2s - 2p)$ of the beryllium-like ion are obtained. These systems are still simple enough to compare the experiment with theoretical calculations looking for relativistic and QED effects at high Z [Kie03].
Rate coefficients are interesting for astrophysical applications because DR is the domi-

nant recombination process in cosmic plasmas. For the modeling of these mechanisms accurate recombination rate coefficients are required. An example is the DR of Fe XIX: $Fe^{18+}(2s^22p^4) + e^- \rightarrow (Fe^{17+})^{**}$ [Sav02].
With DiR vibrational and rotational resonances of molecular ions can be studied. In the reaction

$$H_2^+(1s\sigma, v = 0, J) + e^- \rightarrow H_2(1s\sigma nl\lambda, v', J') \rightarrow H^* + H,$$

e.g. an initially vibrationally cold molecule recombines with an electron to a specific vibrational and rotational atomic state which afterwards dissociates. Electron cooling of vibrational states as a function of time can be observed in the reaction

$$H_2^+(v = 2, J) + e^- \rightarrow H_2^+(v = 1, J') + e^-.$$

Inelastic collisions are cooling the homonuclear molecule, which does not cool radiatively [Kro00]. The cooling is seen by observing the population of the vibrational states as a function of time.
Ideas for dedicated electron targets exist also for other projects, e.g. for the NESR storage ring which is part of the planned new international accelerator facility at GSI, Darmstadt, Germany, for beams of ions and antiprotons [GSI03].

2.3 Ultracold electron target history

With the installation of the ETS into the TSR in December 2002 and the first operation in the TSR in April 2003, together with the realization of a cryogenic photocathode electron source [Wei03], a long period of development comes to an end and opens many new experimental possibilities. The first ideas for an ultracold electron target with a photocathode came up already in 1988 with TSR becoming operational [Hab88, Hab89]. A first photocathode development was launched at the MPIK shortly after that [Zwi91, Zwi93]. In parallel the relaxation processes in magnetized electron beams have been studied with the goal to reduce the longitudinal energy spread by adiabatic acceleration [Kra92]. In the mid 90's the photocathode had been further developed with new experimental techniques to measure also the transverse energy spread of the electron beam [Pas97a, Pas97b]. At CRYRING in Stockholm, and shortly after that at the TSR electron cooler the magnetic expansion of the electron beam had been implemented to reduce the transverse energy spread [Dan94, Pas96]. In 1996 the detailed planning of the ETS was started and the first components were finished and tested in 1999 [Sch00a]. Much progress has been achieved with the photocathode improving the current intensity and the lifetime of the cathodes [Orl01, Hop01, Wei03]. In this work the final development phase of the ETS, together with the production of cold electron beams from a thermionic cathode and the first TSR measurements will be presented.

Figure 2.2: Photo of the installed ETS in the storage ring with the main components labeled. In the background the TSR electron cooler and the dipole magnets are visible.

3. Electron-ion collision experiments using cold electron beams

The development of cold and ultracold electron beams opens up new experimental possibilities in electron-ion collision experiments in storage rings. Much progress has been made over the years, in reducing the transverse energy spread by adiabatic magnetic expansion and the longitudinal one by adiabatic acceleration. Furthermore cold electron sources are becoming available for collision experiments now. But only improving the electron beam quality is not enough because the ion beam itself has a finite momentum spread that reduces the resolution. Moreover there are interactions of the electron beam with the ion beam that might become the limiting factor. In this chapter we will discuss the most important processes that are involved. We will start with an overview about the collision energy in the CM-frame of the beams (section 3.1) and the motion of the ions in the storage ring. In section 3.2 plasma physics quantities will be introduced to discuss the interaction of the electron beam and the ion beam. This is interesting from two points of view. The first is the force that is exerted on the ion beam by the electrons. In our application this will be a superposition of the two electron beams that are involved in the experiment. The second is the collision dynamics in the presence of a magnetic guiding field that is modified because of the constrained electron motion. The description of the process is similar to that used for describing heating processes in a magnetized electron beam (see section 3.3). Two relaxation processes will be distinguished in the electron beam: potential energy relaxation which is important for the acceleration process and transverse-longitudinal relaxation (TLR) which is partly suppressed by the magnetic field. Different models to describe the TLR process will be discussed. In section 3.4 we will discuss dielectronic recombination for temperature diagnostics of the electron beam. We will see how the electron temperatures contribute to the widths of the measured resonances. Finally we will estimate the experimental resolution one can expect for several electron temperatures and ion energy spreads as we are able to produce them in our experiment (section 3.5).

3.1 Storage ring merged beams experiments

3.1.1 Electron beam as a target

The typical situation of a storage ring electron-ion collision experiment is shown in Fig. 3.1. In one section of the storage ring an electron beam is merged with the ion beam at

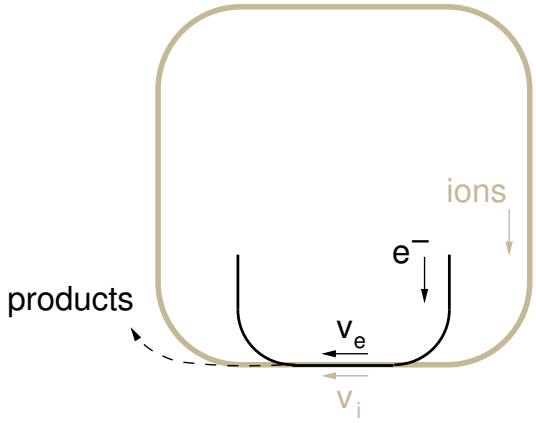

Figure 3.1: Typical storage ring electron-ion collision experiment. The stored ion beam is overlapped with an electron beam in one section of the ring at a certain relative velocity. The charge changed products are no longer stored.

a certain relative velocity. After the reaction the charge changed products are no longer stored in the ring and can be detected.
We will describe this in a more general form with intersecting electron-ion beams. The electrons are traveling at a mean velocity $\langle\vec{v}_e\rangle$ and the ions at a different mean velocity $\langle\vec{v}_i\rangle$ leading to a relative velocity

$$\begin{aligned} \vec{v} &= \langle\vec{v}_e\rangle - \langle\vec{v}_i\rangle && (3.1)\\ \Rightarrow v &= \sqrt{\langle v_e\rangle^2 + \langle v_i\rangle^2 - 2\langle v_e\rangle\langle v_i\rangle\cos\phi} && (3.2)\\ &= \sqrt{(\langle v_e\rangle - \langle v_i\rangle)^2 + 2\langle v_e\rangle\langle v_i\rangle(1-\cos\phi)}, && (3.3)\end{aligned}$$

where ϕ is the angle between the electron and the ion beam in the interaction section. In collinear beam experiments, the two beams are aligned to $\phi = 0$ to avoid shifts in the collision energy. Only for $\phi = 0$, a zero relative velocity between the particles is possible. Additionally the transverse electron temperature seen by the ion beam would be increased which results in a decreased experimental resolution. The collision energy in the CM frame for a given laboratory frame energy can be expressed by

$$E_{coll} = \left(\sqrt{E_e} - \sqrt{\frac{m_e}{m_i}E_i}\right)^2 + 2\sqrt{\frac{m_e}{m_i}E_eE_i}\,(1-\cos\phi), \tag{3.4}$$

using the non-relativistic expression $E = \frac{1}{2}mv^2$ and taking into account that the reduced mass $\mu = \frac{m_im_e}{m_i+m_e} \approx m_e$ because of $m_i \gg m_e$. The cooling energy for electron cooling is given by

$$E_c \equiv \frac{m_e}{m_i}E_i. \tag{3.5}$$

The smallest influence of an angular spread $d\phi$ on the collision energy appears for collinear beams with $\phi = 0$ and π because $dE_{coll}/d\phi \propto \sin\phi$. In this case eq. (3.4) is simplified to

$$E_{coll}(\phi = 0, \pi) = \left(\sqrt{E_e} \mp \sqrt{\frac{m_e}{m_i}E_i}\right)^2. \tag{3.6}$$

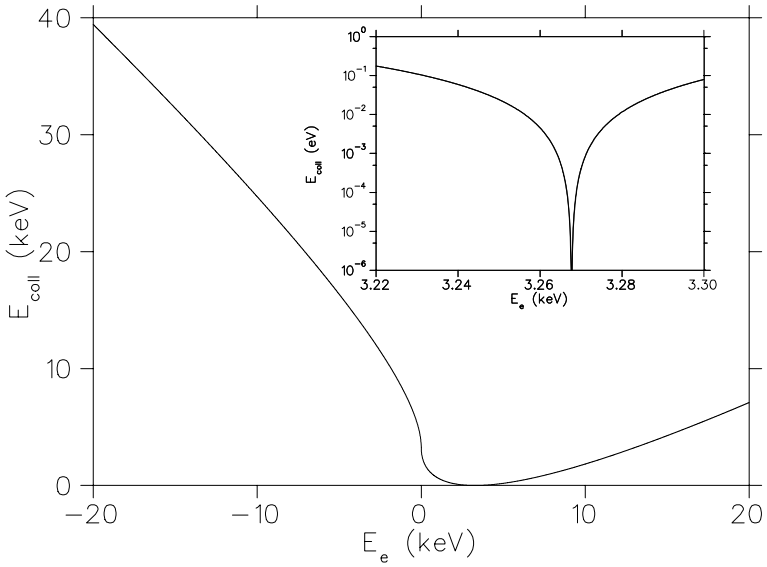

Figure 3.2: Collision energy in the CM frame as a function of the electron energy for collinear beams (ion beam energy 6 MeV/u). Negative electron energies correspond to opposite velocities. In the smaller window a magnified range of small relative velocities is shown (very small collision energies).

For a typical ion energy of 6 MeV/u the collision energy for collinear beams is shown in Fig. 3.2. Negative electron energies correspond to $\phi = \pi$, which leads to large collision energies. For electron energies close to E_c (smaller window) the collision energy becomes very small.
Eq. (3.6) can be used for approximative calculations at low energies but the relativistic correct collision energy is given approximately by [Kil90]

$$E_{coll} \simeq E_e \left(1 + \frac{E_i}{m_i c^2}\right) + m_r E_i - \sqrt{[(m_r E_i)^2 + 2 m_i c^2 m_r E_i] \left(\frac{E_e^2}{m_e^2 c^4} + 2\frac{E_e}{m_e c^2}\right)}, \quad (3.7)$$

with $m_r = m_e/m_i$.
Several effects can contribute to uncertainties in the collision energy of which we will discuss the most important ones in the following.

Electron space charge

The electron energy is not constant over the beam radius due to the space charge potential. Electrons in the beam center are screened by the surrounding electrons from the external potentials, which lowers the electron energy in the center by $e\Phi_{SC}(r, n_e)$, according to the electron density n_e. After an acceleration of the electrons by a voltage U_0, the electron energy is then

$$E_e(r) = eU_0 - e\Phi_{SC}(r, n_e). \quad (3.8)$$

The radial charge distribution of the electron beam with radius R can be described in a good approximation by a homogeneous charge density $\rho_0 = en_e$ by

$$\rho(r) = \begin{cases} \rho_0 & \text{for } r \leq R, \\ 0 & \text{for } r > R. \end{cases} \tag{3.9}$$

In the present work this could be verified experimentally (see section 5.1) showing that typical variations are below 10%. The space-charge potential in a vacuum tube of radius R_0 can now be calculated to

$$\Phi_{SC}(r) = \frac{en_eR^2}{4\epsilon_0} \begin{cases} 1 - \frac{r^2}{R^2} + 2\ln\frac{R_0}{R} & \text{for } r \leq R, \\ 2\ln\frac{R_0}{r} & \text{for } r > R. \end{cases} \tag{3.10}$$

Because of the dependence of the electron density on the electron energy, the space-charge potential can be obtained only in an iterative procedure. For an electron beam accelerated by $U_0 = 2000\,\mathrm{V}$ with total current $1\,\mathrm{mA}$ at expansion 32 one finds $\Phi_{SC} \approx 2\,\mathrm{V}$. However, this can increase quickly with higher currents because $\Phi_{SC} \propto I_{tot}$.
Calculating the radial part of the electric field inside the electron beam by $\mathcal{E}_r = -\frac{\partial\Phi(r)}{\partial r}$ gives $\mathcal{E}_r = \frac{en_er}{2\epsilon_0}$. This electric field would lead to a divergence of the beam if there was no magnetic guiding field. In the magnetic guiding field B_0 the beam starts to rotate collectively because of the Lorentz force with a frequency [Rub77]

$$\Omega_S = \frac{\omega_c}{2}\left(1 - \sqrt{1 - \frac{B_B^2}{B_0^2}}\right), \tag{3.11}$$

and the Brillouin field

$$B_B = \sqrt{\frac{2n_em_e}{\epsilon_0}}. \tag{3.12}$$

B_B is the minimal flux density necessary to prevent the beam from diverging. For a typical electron density of $n_e = 10^{14}\,\mathrm{m}^{-3}$ one calculates $B_B = 4.5\,\mathrm{mT}$.

Ion energy variations

The stored ion beam interacts with the electron beam of the electron cooler (see section 3.2.2 below) and of the electron target which changes the ion beam energy. In collision experiments performed only with the electron cooler one tries to suppress this beam dragging by switching the electron energy between the measurement energy E_{coll} and the cooling energy E_e on time scales where the drag effect is small (typically 100 ms). Another reason for the switching is, that the ion beam heats without effective electron cooling, which lowers the beam lifetime and the experimental resolution. In the first experiments with the ETS, ion beam dragging has been observed in the operation with two electron beams (see 6.1.3).
Starting with eq. (3.6), one can calculate the change of the collision energy by a change

in the ion energy

$$\frac{dE_{coll}}{dE_i} = -\frac{\sqrt{E_e} - \sqrt{m_r E_i}}{\sqrt{m_r E_i}} \cdot m_r \tag{3.13}$$

$$= -\sqrt{m_r \frac{E_{coll}}{E_i}}. \tag{3.14}$$

3.1.2 Ion motion in the storage ring

In the storage ring the particles move on a closed orbit. We will call the coordinate along the particle trajectory s, while x is the horizontal (storage ring plane) and y the vertical coordinate, respectively. The trajectory is manipulated by dipole, quadrupole and sextupole magnets. Taking only ideal vertical dipole and ideal quadrupole magnets into account, one gets the following solution of the equations of motion [Wil92]

$$x(s) = \sqrt{\epsilon_x \beta_x(s)}\, \cos(\Psi_x(s) + \Phi) \tag{3.15}$$

$$x'(s) = -\frac{\sqrt{\epsilon_x}}{\sqrt{\beta_x(s)}} \left(-\frac{\beta_x'(s)}{2} \cos(\Psi_x(s) + \Phi) + \sin(\Psi_x(s) + \Phi) \right), \tag{3.16}$$

and for $y(s)$ respectively. $\beta_x(s)$ is the *betatron function* that describes the amplitude, $\Psi(s)$ and Φ stand for the phase of the betatron oscillation of the particle as a function of the position s. ϵ_x is the *emittance* which is proportional to the phase space area (phase space ellipse), that is occupied by the stored particle. The square root of the product of the emittance and the betatron function $\sqrt{\epsilon_x \beta_x(s)}$ describes the envelope of all the betatron oscillations of the particle which is the maximum deviation from the reference orbit trajectory. For the interaction of a single ion with the electron beam, this implies that the ion orbit is changing from passage to passage because the phase varies.
Taking the momentum spread $\Delta p/p$ into account leads to a total deviation from the reference orbit

$$\tilde{x}(s) = x(s) + \frac{\Delta p}{p} \cdot D(s), \tag{3.17}$$

where $D(s)$ is the dispersion that describes the additional deviation from the reference orbit trajectory. By the dispersion the orbit length and the revolution frequency is changed as a function of the momentum.

3.2 Coulomb interactions in charged particle beams

3.2.1 Plasma physics quantities

Charged particle beams can be considered as a one component plasma, seen from their co-moving reference frame. The collective motion in such systems is characterized by the *plasma frequency*

$$\omega_p = \sqrt{\frac{q^2 n}{m \epsilon_0}}, \tag{3.18}$$

which depends on the particle density n, the charge q and the particle mass m (electron m_e, ion m_i). ω_p defines the time scale of relaxation processes in the plasma. In our context the plasma frequency is particularly important for electron beams because relaxation processes depend on it. If the electron motion is influenced by a magnetic field $\vec{B}$, they will form a magnetized plasma, where they move on spiral trajectories around the magnetic field lines. The frequency of the rotation is given by the *cyclotron frequency*

$$\omega_c = \frac{q}{m}B, \tag{3.19}$$

and the radius of the spiral is given by the *Larmor radius*

$$r_c = \frac{v_\perp}{\omega_c} = \frac{mv_\perp}{qB}, \tag{3.20}$$

where $v_\perp$ is the velocity perpendicular to the magnetic field lines. The *cyclotron length*

$$\lambda_c = \frac{2\pi v_\parallel}{\omega_c} = \frac{2\pi m v_\parallel}{qB} \tag{3.21}$$

is the distance that the particle travels along the magnetic field lines during one cyclotron period. Typical values for r_c are in the range of several μm and for λ_c in the range of cm. Inside the plasma every particle is surrounded by many other charged particles. This leads to a modified electric potential. For distances smaller than the *Debye length*

$$\lambda_D = \sqrt{\frac{kT}{m}}\omega_p^{-1} \tag{3.22}$$

the deviation from the Coulomb potential is small.
Important for the description of collision processes is the *thermal distance of closest approach*

$$b = \frac{q^2}{4\pi\epsilon_0}(kT)^{-1}, \tag{3.23}$$

that depends on the particle motion due to the plasma temperature. In the following we will use subscripts $\parallel$ and $\perp$ in the plasma quantities to distinguish between the longitudinal direction ($\parallel$) and the direction perpendicular ($\perp$) to the magnetic field. Associated with the magnetic field are longitudinal and transverse temperatures $T_\parallel$ and $T_\perp$ that can be rather different in an electron beam, as we will see in the next sections.
For ions the cyclotron frequency is much smaller than for electrons and the cyclotron length is much longer because of their higher mass. The ion trajectories are therefore much less influenced by the magnetic field than for the electrons. This is important for the electron-ion collision dynamics in the presence of a magnetic field, as we will discuss it below.

Beam ordering

Ordering in plasmas can be described by the coupling constant Γ which gives a measure for the correlation of the particles. It is defined as the ratio of the average potential

energy due to the inter-particle Coulomb forces to the thermal energy (as represented by the plasma temperature kT). For one-component plasmas the potential energy is given by the Coulomb potential with a mean particle distance estimated by the Wigner-Seitz radius

$$d = \left(\frac{4\pi}{3}n\right)^{-1/3}, \tag{3.24}$$

where n is the plasma density. One obtains [Ich82]

$$\Gamma = \left(\frac{4\pi}{3}n\right)^{1/3} \frac{(Ze)^2}{4\pi\epsilon_0 kT} = \frac{b}{d}. \tag{3.25}$$

Different states of aggregation can now be classified by

$$\Gamma \begin{cases} < 1 & \text{ideal gas} \\ \geq 1 & \text{beginning liquid behavior} \\ \gg 1 & \text{transition to crystal} \end{cases} \tag{3.26}$$

For homogeneous one component plasmas, the transition to the crystalline state is predicted by calculations to appear at $\Gamma \gtrapprox 170$ [Ich82]. Ordering in stored ion beams has been observed recently [Ste01, Sch02].

Electron temperatures

The longitudinal magnetic guiding field leads to a decoupling of the transverse and the longitudinal degrees of freedom of the electron motion. We can now define a transverse and a longitudinal temperature from the energy spreads in the CM-frame of the beam. The energy spread is defined by the variance $\sigma^2(\vec{v}) = \langle(\Delta\vec{v})^2\rangle$. For an electron ensemble at the mean velocity $\langle\vec{v}\rangle$ we write [Jan90]

$$\frac{1}{2}kT_\parallel = \frac{1}{2}m_e\left(\langle v_\parallel^2\rangle - \langle v_\parallel\rangle^2\right) \tag{3.27}$$

$$2\cdot\frac{1}{2}kT_\perp = \frac{1}{2}m_e\left(\langle v_\perp^2\rangle - \langle v_\perp\rangle^2\right). \tag{3.28}$$

The factor 2 in eq. (3.28) considers that there are two degrees of freedom for the transverse direction.

3.2.2 Electron-ion collisions

In the next sections the physics of a binary Coulomb collision between ions and electrons at a certain relative velocity will be discussed. The calculation of the resulting friction forces under realistic conditions has been considered in detail within the theory of electron cooling [Pot90]. In the ETS we have the new situation that two electron beams are acting on the same ion beam which will both exert forces on the stored ion beam, especially at low collision energies.
A related interesting aspect is the collision dynamics in the presence of a magnetic field.

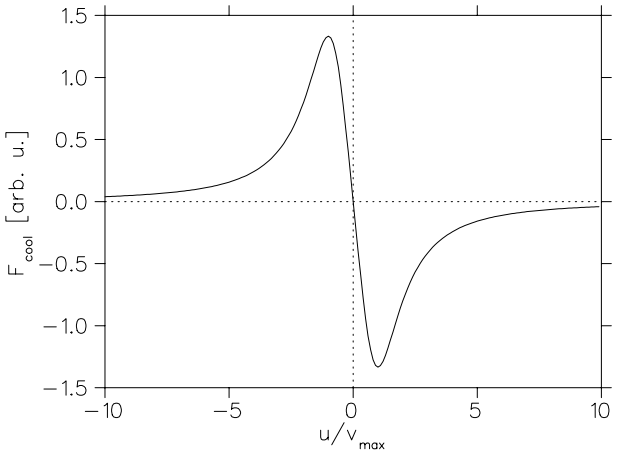

Figure 3.3: Cooling force as a function of the relative velocity u between electron and ion beam (in units of the velocity v_{max}, where the cooling force has its maximum).

The dynamics is strongly changed because the magnetic guiding field along the electron beam axis forces the electrons on a narrow cyclotron orbit. The similarity between the electron cooling theory and the physics of magnetized electron beams (see section 3.3) is a motivation to summarize the description of electron cooling in some detail here.
The basic idea of electron cooling [Bud78] is to overlap a hot ion beam with a cold electron beam. The interaction between them leads to an energy loss of the ions, which increases the achievable phase space density in the stored ion beam. Besides electron cooling there are other methods available to cool stored ion beams, such as stochastic cooling and laser cooling.

Binary collision model without magnetic field

A simple model to calculate the ion energy change due to Coulomb collisions in electron cooling is the binary collision model [Pot90]. In the simplest case, the magnetic guiding field of the electrons will be neglected. An ion with charge Z and velocity u collides with an electron at rest. The transferred momentum to the electron is then

$$\Delta p = \frac{2Ze^2}{4\pi\epsilon_0 ub}, \tag{3.29}$$

with the impact parameter b. The energy loss of the ion in the reference frame, where the electron was initially at rest, is

$$\Delta E_i(b) = -\frac{(\Delta p)^2}{2m_e}. \tag{3.30}$$

Assuming homogeneously distributed electrons with a density n_e and a length dx traveled by the ions leads to

$$\frac{dE_i}{dx} = 2\pi \int_{b_{min}}^{b_{max}} n_e b \Delta E_i(b) db = \frac{4\pi Z^2 e^4 n_e}{(4\pi\epsilon_0)^2 m_e u^2} L_C, \tag{3.31}$$

with minimum and maximum impact parameters b_{min} and b_{max} and the Coulomb logarithm $L_c := \int_{b_{min}}^{b_{max}} db/b = \ln(b_{max}/b_{min})$. The friction force on the ion is thus given by $F = dE_i/dx$. This is a good approximation if $b_{max} \gg b_{min}$ and leads to Coulomb logarithms $L_c \gtrsim 5$. We will discuss the problem of choosing appropriate impact parameters below.
The binary collisions do not only lead to an energy loss but also to a scattering of the ions described by a diffusion coefficient

$$D_{mn} = \frac{\langle \Delta u_m \Delta u_n \rangle}{\Delta t}. \tag{3.32}$$

In the binary collision model one can now calculate the well known expressions for the cooling force and the diffusion tensor. For an electron distribution $f(\vec{v}_e)$ in the center of mass frame of electrons with mean velocity $\langle v_e \rangle$ one gets

$$\vec{F}(\vec{u}) = -\frac{4\pi Z^2 e^4}{(4\pi\epsilon_0)^2 m_e} n_e \int L_c(\vec{u}) f(\vec{v}_e) \frac{\vec{u}}{|\vec{u}|^3} d^3 v_e \tag{3.33}$$

$$D_{mn} = \frac{4\pi Z^2 e^4}{(4\pi\epsilon_0)^2} n_e \int L_c(\vec{u}) f(\vec{v}_e) \frac{u^2 \delta_{mn} - u_m u_n}{|\vec{u}|^3} d^3 v_e, \tag{3.34}$$

where $\vec{u} = \vec{v}_i - \vec{v}_e$.
For simple estimates the following approximation is useful [Pot90]

$$\vec{F}(\vec{u}) = -\frac{3}{2} \frac{4\pi Z^2 e^4}{(4\pi\epsilon_0)^2 m_e} n_e L_c \frac{u}{|u|^3 + 2(kT/m_e)^{3/2}} \frac{\vec{u}}{u}. \tag{3.35}$$

This function is shown in Fig. 3.3. The slope $\partial F(\vec{u})/\partial u_{\parallel,\perp}|_{u_{\parallel,\perp}=0}$ determines the cooling rate of the electron beam.
A second method to calculate the cooling force and the diffusion coefficient is a dielectric description where the cooling force is calculated by the electric field induced by the ion to the plasma. This induced field is then acting back on the ion. In the non magnetic case this leads to the same results. A detailed description can be found in the review article of Poth [Pot90].

Magnetized collision dynamics

In the previous calculation of the cooling force the collisions are all treated as binary collisions between an ion and an electron with the Rutherford cross section for Coulomb interactions. Up to now nothing has been said about how the surrounding particles in the plasma are influencing the collision process. We will discuss this part in more detail because the physical picture will be very useful in the following section about magnetized electron beams (section 3.3).
Previously only maximum and minimum impact parameters b_{max} and b_{min}, respectively, have been introduced to avoid the divergence of the integral over the energy change. This can be explained by a modified short range effective potential where the surrounding

interaction	distance	$u > \sqrt{kT/m_e}$	$u < \sqrt{kT/m_e}$
screened	b_{max}	$\omega_p^{-1} u$	$\omega_p^{-1}\sqrt{kT/m_e}$
weak	b_{min}	$\frac{Ze^2}{4\pi\epsilon_0}(m_e u^2)^{-1}$	$\frac{Ze^2}{4\pi\epsilon_0}(kT)^{-1}$
strong			

Table 3.1: Collision dynamics parameters without magnetic field. Different interaction regimes are distinguished which depend on the particle distance (see text).

electrons are screening the long range Coulomb potential which leads to a *screening length*

$$\lambda = \frac{\langle u \rangle}{\omega_p}. \tag{3.36}$$

The *maximum impact parameter* is then given by $b_{max} = \lambda$. For distances smaller than λ, the effective potential can be well approximated by the Coulomb potential. For distances larger than b_{max} the interaction is screened and the energy of the ion is not changed. At shorter distances ($b_{min} \leq b \leq b_{max}$) the potential is not screened and the interaction becomes stronger. The *minimum impact parameter* $b_{min} = d$, corresponds to the collision distance where the momentum transfer reaches its kinematical maximum (collision at an angle of 180°).
In the case of an isotropic electron plasma without magnetic field we get the expressions summarized in Tab. 3.1 for the impact parameters in different velocity regimes.
For an anisotropic plasma where $T_\perp \gg T_\parallel$ the temperature in Tab. 3.1 will be replaced by $T_\perp$.
Taking now the magnetic field into account leads to a cyclotron motion of the electrons around the magnetic field lines. The ion motion is only weakly disturbed. This will modify the collision dynamics in a regime where the relative velocity is slow, compared to the transverse velocity. At large distances the ions will not "see" the electrons as point particles anymore, but rather as charged disks with the Larmor radius. The impact parameters are thus divided into a non-magnetic regime (NM) and an adiabatic regime. The limit between the two regimes is given by the cyclotron length $\lambda_c = \frac{u_A}{\omega_c}$, which is the distance that the electron travels within one cyclotron rotation at the adiabatic relative velocity $\vec{u}_A$ given by

$$\vec{u}_A = \vec{v}_i - \vec{v}_{e,\parallel}. \tag{3.37}$$

The transverse electron velocity is suppressed for the adiabatic collisions. The impact parameters for an anisotropic plasma in the presence of a magnetic field are given in Tab. 3.2.
The magnetized dynamics in electron-electron collisions uses similar criteria. We will discuss this further in the context of electron beam heating (see section 3.3.5).

interaction	distance	$u > \sqrt{kT_\perp/m_e}$	$\sqrt{kT_\parallel/m_e} < u < \sqrt{kT_\perp/m_e}$	$u < \sqrt{kT_\parallel/m_e}$
screened	b_{max}	$\omega_p^{-1} u$	$\omega_p^{-1} u_A$	$\omega_p^{-1}\sqrt{kT_\parallel/m_e}$
magn. weak	λ_c	$\omega_c^{-1} u$	$\omega_c^{-1} u_A$	$\omega_c^{-1}\sqrt{kT_\parallel/m_e}$
NM weak	b_{min}	$\frac{Ze^2}{4\pi\epsilon_0}(m_e u^2)^{-1}$	$\frac{Ze^2}{4\pi\epsilon_0}(m_e u_A^2)^{-1}$	$\frac{Ze^2}{4\pi\epsilon_0}(kT_\parallel)^{-1}$
strong				

Table 3.2: Collision dynamics parameters with magnetic field. By the magnetic field the interaction is divided into a magnetized and a non magnetized (NM) regime, the limit is given by λ_c (see text).

3.3 Magnetized cold electron beams

Before we want to discuss the heating processes in the electron beam, the production and acceleration of the electrons will be discussed. Another important aspect is the magnetic expansion of the beam, in order to reduce the transverse temperature.

3.3.1 Electron sources

The free electrons for the electron beam can be created by different emission processes. The most common process is the thermionic emission where the cathode material is heated to a high temperature, which allows bound electrons to overcome the potential barrier of the solid to the surface [Ash76]. But also the photoemission or field emission (see below) can be used to create free electrons. It is also possible to store electrons in a trap (e.g. penning trap) and extract electrons from there [Kur98]. The velocity distribution at the cathode surface is given by a Maxwell-distribution and depends only on the cathode temperature. In front of the cathode surface a space charge cloud is formed by the free electrons, which leads to a potential minimum. An electric field is used to extract electrons from the space charge cloud. One distinguishes between space charge limited extraction where not all electrons are extracted, maintaining the space charge cloud, and current limited extraction where all electrons are extracted. For our application the space charged limited mode is preferable, because the electron beam is then independent of inhomogeneities and temperature fluctuations on the cathode surface.
To avoid transverse heating of the electron beam by the extraction, the electric field lines of the extraction voltage U_{ext} have to be parallel to the cathode surface. However the extraction potential is disturbed by the space charge cloud. One can compensate this by using a Pierce geometry configuration which consists of an additional electrode around the cathode under an angle of 67.5° to the cathode surface [Pie54].
In space charge limited extraction the current density perpendicular to the cathode surface

at distance z is described by the Child-Langmuir-relation [Kir67]:

$$j_e = \frac{4}{9}\epsilon_0\sqrt{2\frac{e}{m_e}}\frac{U_{ext}^{3/2}}{z^2}. \tag{3.38}$$

For practical use the perveance P (unit Perv=A/V$^{3/2}$) of an electron gun is defined containing the geometrical aspects of the cathode. The emission current from an electron gun can then be written as [Pie40]

$$I_e = PU_{ext}^{3/2}. \tag{3.39}$$

As mentioned above, the initial electron velocity distribution and thus the initial electron temperature depends only on the cathode temperature. To create free electrons at high intensities from thermionic cathodes they have to be heated to temperatures of 1200–1500 K (103–129 meV) typically. This situation can be much improved by creating free electrons by photoemission from a semiconductor that can be cooled to cryogenic temperatures with liquid nitrogen, e.g. down to ≈ 90 K (8 meV) which is a factor of over 10 smaller.
Technically photocathodes are produced by covering a heavily p-doped semiconductor (e.g. GaAs) with cesium and oxygen or fluorine [Pas00]. The coating leads to a band bending region close to the surface with the vacuum level below the conduction band minimum (negative electron affinity). Between the solid and the vacuum a potential barrier is present. By illuminating the semiconductor with a laser beam, an electron from the valence band is excited to the conductance band. The electron thermalizes to the conductance band minimum and can then diffuse to the surface and then tunnel to the vacuum. Eventually scattering processes in the surface region take place which heat the electrons. The temperature can also be increased by the power of the illuminating laser. It is therefore preferable to keep the laser power low. The photocathodes developed for the ETS deliver currents of ≈ 1 mA for a laser power below 1 W. Quantum yields for activated cathodes are about 31% [Orl01]. Using a laser beam, free electrons with very low energy spreads can also be created from photoionization of neutral atoms [Böm01].
An alternative process to create free electrons is the field emission. A high electric field is changing the potential barrier for the electrons in the metal to the vacuum, increasing the tunnel probability. In carbon nanotubes relatively large emission currents up to 4 A/cm^2 have been produced recently [Tho01].

3.3.2 Electron acceleration

Because of the quadratic relation between the velocity and the energy, the longitudinal temperature is strongly reduced by an acceleration to a higher kinetic energy. This can be understood by considering an electron with a kinetic energy in the laboratory frame given by $E_L = \frac{1}{2}m_e v_e^2$. Accelerating the electron to a velocity v_0 leads to a total energy $E_{tot} = E_L + \frac{1}{2}m_e v_0^2$. In the rest-frame of the electron the energy is given by $E_0 = \frac{1}{2}m_e(v_e')^2$. By a transformation of this energy to the laboratory frame we find for the total energy

$E_{tot} = \frac{1}{2} m_e (v_e' + v_0)^2$. We therefore write

$$\begin{aligned} v_e' + v_0 &= \sqrt{v_e^2 + v_0^2} && (3.40)\\ &\approx v_0 \left(1 + \frac{1}{2}\frac{v_e^2}{v_0^2}\right) && (3.41)\\ \Rightarrow v_e' &\approx \frac{v_e}{2v_0}, && (3.42) \end{aligned}$$

where the square root has been developed because of $v_e \ll v_0$. Thus, the initial velocity is reduced in the rest-frame of the accelerated electron.
Generalizing this to an electron ensemble with an initial energy distribution given by the cathode temperature T_C and with the kinetic energy $E_{kin} = eU_0$, given by the accelerating voltage U_0, one finds for the final temperature of the electrons in the CM-frame after acceleration [Jan90]

$$kT_{\parallel}^{f} = \frac{(kT_C)^2}{2E_{kin}}. \tag{3.43}$$

In our application $E_{kin} \gg kT_C$, therefore the temperature $kT_{\parallel}^{f}$ can be reduced to very low values. But eq. (3.43) is only valid if Coulomb interactions between the particles are neglected. We will discuss the influence of interactions below.

3.3.3 Adiabatic magnetic transverse expansion (ATE)

Like the initial longitudinal temperature, the initial transverse temperature is given by the cathode temperature [Jan90]

$$kT_{\perp i} = kT_C. \tag{3.44}$$

But in the transverse direction the electron beam cannot be accelerated to decrease the transverse temperature. The thermionic dispenser cathode is typically operated at temperatures of $T_C \approx 1100\,\mathrm{K}$ ($kT_C = 94\,\mathrm{meV}$) whereas the photocathode is cooled with liquid nitrogen to $T_C \approx 90\,\mathrm{K}$ ($8\,\mathrm{meV}$). With the magnetic expansion [Dan94, Pas96, Dan00] which will be explained below it is possible to reduce these temperatures to $1.24\,\mathrm{meV}$ for the thermionic and $0.09\,\mathrm{meV}$ for the photocathode, respectively, corresponding to field ratios of ≈ 90. Comparing this to the longitudinal temperature, $T_{\parallel}$ is always much smaller than $T_{\perp}$.
In the magnetic guiding field the electrons are spiraling around the magnetic field lines because of the Lorentz force that acts on the particles moving in the transverse direction because of $T_{\perp} > 0$. In a spatially varying longitudinal magnetic field, the single electrons are accelerated due to a resulting longitudinal component of the Lorentz force. These accelerations change the temperatures of the particle ensemble. To characterize this we will look at adiabatic changes of the magnetic field.
As a measure for the adiabaticity of the magnetic field variation we use

$$\xi = \frac{\lambda_c}{B}\left|\frac{dB}{dz}\right|, \tag{3.45}$$

comparing the cyclotron length λ_c of the spiraling electrons to the magnetic field change along the electron beam axis. For $\xi \ll 1$ the magnetic expansion is adiabatic [Pas96]. Measurements at the TSR electron cooler showed a limit of $\xi < 0.1$, where no increase in the transverse temperature was seen anymore [Sch00a]. In the case of an adiabatic transverse expansion (ATE), one can find an adiabatic invariant in the product of the squared beam diameter and the flux density $R^2B = \text{const.}$ [Spi62]. The beam diameter after expansion is given by

$$R_f = \sqrt{\frac{B_i}{B_f}} R_i, \tag{3.46}$$

and the electron density is reduced by

$$n_e^f = \frac{B_f}{B_i} n_e^i, \tag{3.47}$$

where i denotes the initial state and f the final state respectively. We can now define the expansion factor α (which must not be confounded with the DR rate coefficient, see below) given by the field ratio

$$\alpha := \frac{B_i}{B_f}. \tag{3.48}$$

A second adiabatic invariant $E_\perp/B = \text{const.}$ leads to the mean transverse energy (MTE) of a particle ensemble [O'N85]

$$\frac{\langle E_\perp \rangle}{B} = \text{const.} \tag{3.49}$$

and in a changing magnetic field one calculates

$$\langle E_{\perp f} \rangle = \frac{B_f}{B_i} \langle E_{\perp i} \rangle \Leftrightarrow kT_{\perp f} = \frac{B_f}{B_i} kT_{\perp i}. \tag{3.50}$$

Because of energy conservation $\langle E_\perp \rangle + \langle E_\parallel \rangle = \text{const.}$ the mean longitudinal energy (MLE) is increased. This can be used to determine $T_\perp$ by measuring the longitudinal energy spread using different field ratios [Pas97a]. This can be expressed as

$$\langle E_{\parallel f} \rangle - \langle E_{\parallel i} \rangle = \langle E_{\perp i} \rangle \left(1 - \frac{B_f}{B_i} \right). \tag{3.51}$$

With $\langle E_{\parallel i} \rangle = 0$ one can calculate the increase in temperature in the CM-frame with (3.43) to

$$kT_{\parallel f} = kT_{\parallel i} + \frac{(1 - \alpha^{-1})^2 (kT_{\perp i})^2}{2E_{kin}}. \tag{3.52}$$

3.3.4 Potential energy relaxation

Inside the beam the electrons have a certain potential energy because of the Coulomb interaction, depending on their position in the beam. In thermal equilibrium the electrons are distributed on positions where the potential energy is in equilibrium with the kinetic energy. The repulsive Coulomb force is compensated by the longitudinal magnetic field (see 3.1.1).
Accelerating the electron beam disturbs now the equilibrium state. The acceleration leads to a longitudinal expansion of the beam which results in an anisotropy in the density distribution. Related to this anisotropy is an increased potential energy that relaxes into kinetic energy. Due to the magnetic field, the transverse temperature is decoupled (assuming strong magnetization) from the longitudinal one and only the longitudinal temperature is increased. This potential energy relaxation in the presence of a magnetic field is also called longitudinal-longitudinal relaxation (LLR).
The time scale of relaxation processes in the beam is given by the plasma frequency ω_p. The relaxation can now be reduced by doing an *adiabatic acceleration* where the electron plasma is always kept close to the equilibrium state [Dik88]. An estimate for the adiabaticity of the acceleration is given by [Kud82]

$$\lambda = -\frac{1}{\omega_p(z)} \cdot \frac{1}{T_\parallel} \frac{dT_\parallel}{dt}, \tag{3.53}$$

with $T_\parallel \cdot E_{kin} = \text{const.}$ follows

$$\lambda = \frac{v_e}{\omega_p(z)} \cdot \frac{1}{E_{kin}} \frac{dE_{kin}}{dz}, \tag{3.54}$$

where v_e is the electron velocity. The relative change of the kinetic energy has to be small compared to the plasma frequency. For $\lambda < 1$ the acceleration is adiabatic and for $\lambda > 1$ fast. In section 5.2.5 λ will be calculated for parameters as used in the experiments.
An upper limit for the heating in a fast acceleration can be calculated from the total potential energy contained in an electron plasma with an anisotropic density distribution. One finds [Dik88]

$$kT_\parallel^{LLR} \simeq 1.9 \frac{e^2}{4\pi\epsilon_0} n_e^{1/3}. \tag{3.55}$$

This is the potential energy of electrons with a mean distance $n_e^{-1/3}$ given by the electron density multiplied with a constant factor of $C_{max} = 1.9$. For smaller λ one can replace C_{max} by a factor $C \leq C_{max}$ that describes the "quality" of the acceleration. The final longitudinal electron temperature can then be expressed together with eq. (3.43) by [Dik88]

$$kT_\parallel^f = \frac{(kT_C)^2}{2E_{kin}} + C \frac{e^2}{4\pi\epsilon_0} n_e^{1/3}. \tag{3.56}$$

Numerical simulations using molecular dynamics calculations showed also the reduction of the final temperature by adiabatic acceleration [Sch00b].

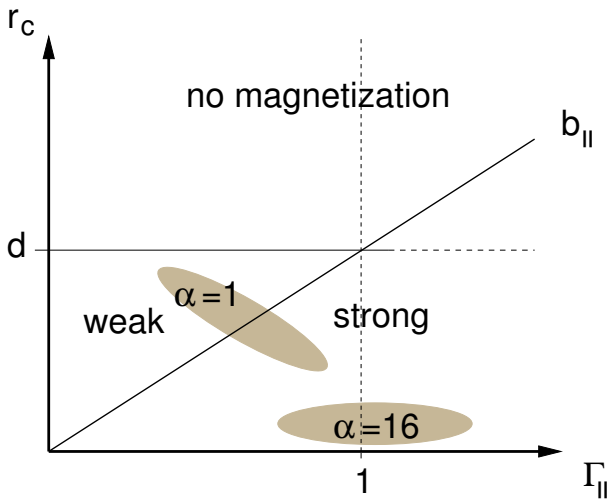

Figure 3.4: Criteria for magnetization of the electron beam: on the x-axis the longitudinal plasma parameter is drawn which indicates the regimes for weak correlation ($\Gamma_\parallel < 1$) and strong correlation ($\Gamma_\parallel > 1$). On the y-axis the Larmor radius is drawn. The regime between weak magnetization and no magnetization is limited by the mean particle distance $r_c = d$. $b_\parallel = \Gamma_\parallel d$ indicates the criterion for strong magnetization. The grey areas indicate regions that have been studied in the experiments (see section 5.2.5).

3.3.5 Kinetic energy relaxation

The strong anisotropy of the longitudinal and the transverse electron temperature leads to a relaxation of thermal energy through binary collisions similar to the intrabeam scattering observed in ion beams (transverse-longitudinal relaxation, TLR). The much smaller longitudinal temperature will be increased while the transverse temperature is not much affected because the relaxation time is long compared to the time of flight of the electrons. The relaxation time and thus the amount of energy that is transferred depends also on the magnetic guiding field which is always present to avoid the electron beam divergence. Especially in the region of the ATE of the electron beam, TLR is playing an important role.
In the literature different theories can be found for the TLR heating rate. We will discuss in this section two different approaches. One is an empirical formula from TLR measurements where arguments from the electron cooling theory are used as discussed in section 3.2.2 [Dik88]. A second theory calculates binary electron collisions in a magnetic field by classical mechanics for a weakly correlated one-component plasma [O'N85, Gli92]. The physical picture in both cases is similar to the electron cooling theory in the presence of a magnetic field where adiabatic collisions of the magnetized electrons appear. The difference in the case of the electron beam is that both collision partners are magnetized and cannot move freely.

	Aleksandrov [Ale90]	Dikansky [Dik88]	Krause [Kra92]
C_1	$6.43^{+2.26}_{-1.48}$	0.87 L_c ($L_c \approx 6$)	6.75 ± 1.75
C_2	$1.3^{+0.4}_{-0.35}$	2.8	1.85 ± 0.15
C_3	$0.4^{+0.21}_{-0.14}$	1	0.3 ± 0.1

Table 3.3: Numerical constants for eq. (3.57) according to different authors. [Ale90] is unpublished, values contained in [Kra92].

Empirical theory

As a result of TLR measurements, Parkhomchuk proposed an empirical formula where the relaxation rate for the unmagnetized case $(dT_\parallel/dz)^0$ is exponentially suppressed in the case of magnetization. Dikansky formulates two criteria where the electron kinetics is influenced by the magnetic field and TLR suppression appears [Dik88]:

(i): $r_c \ll d$: the Larmor radius is much smaller than the mean particle distance. The electrons rotate around the magnetic field and "see" each other as charged disks. These arguments are similar to the ones in sec. 3.2.2 for the electron cooling in the presence of a magnetic field.

(ii): $r_c \ll b_\parallel$: the Larmor radius has to be much smaller than the distance of closest approach due to the longitudinal temperature.

The first criterion is not sufficient for a complete suppression of the transverse to longitudinal energy exchange (strong magnetization) but one could understand it as a regime where the magnetization starts to influence the kinetics (weak magnetization). Based on the relation $b_\parallel = \Gamma_\parallel d$ (see eq. (3.25)) the ranges of r_c and $\Gamma_\parallel$ where TLR suppression is expected is illustrated in Fig. 3.4. As one can see for $\Gamma_\parallel < 1$, $b_\parallel$ is always smaller than d. Hence, the two cases of weak and strong magnetization exist. For $\Gamma_\parallel > 1$ this is reversed and only a range of strong magnetization exists. The exponential function proposed by Parkhomchuk is a combination of factors representing both criteria. The general form of the heating rate by adiabatic collisions is given by

$$\left(\frac{dT_\parallel}{dz}\right)^{ad} = \left(\frac{dT_\parallel}{dz}\right)^0 C_1 \exp\left(-\frac{C_2}{r_c\left(n_e^{1/3} + \frac{C_3}{b_\parallel}\right)}\right), \tag{3.57}$$

with

$$\left(\frac{dT_\parallel}{dz}\right)^0 = \frac{\pi e^4 n_e}{(4\pi\epsilon_0)^2 k\sqrt{E_{kin} k T_\perp}}. \tag{3.58}$$

In several publications different constants are given that are summarized in Tab. 3.3. As one can see the given errors are considerably high, especially the factors C_2 and C_3 will strongly influence the calculated heating rate. C_1 can be interpreted as Coulomb

logarithm.
For an anisotropic Maxwellian velocity distribution the longitudinal heating rate without a magnetic guiding field can be derived from the electron cooling theory with eq. (3.34) and one obtains [Sør87]

$$\left(\frac{dT_\parallel}{dz}\right)^{fast} = \frac{4\pi e^4 n_e L_c}{(4\pi\epsilon_0)^2 k\sqrt{E_{kin} k T_\perp}}, \tag{3.59}$$

which differs in a factor of 4 and the Coulomb logarithm L_c from eq. (3.58).

Adiabatic collisions

Within the previous empirical theory nothing has been said about the nature of the adiabatic collisions. Another approach is given by a classical theory where the electron equations of motion in the presence of a magnetic field are solved numerically [O'N83, O'N85, Gli92] for an isotropic plasma. We will shortly outline this approach.
The theory is based on the existence of adiabatic invariants of the collision process that are preserved on the time scale of a few collisions. The adiabatic invariant is given by the total kinetic energy related to the transverse velocity components

$$E_{kin\perp} = \sum_{j=1,2} \frac{m_e v_{j\perp}^2}{2}. \tag{3.60}$$

Significant for the heating process are the time scales where the adiabatic invariant is not conserved. This time scale is estimated by the velocity $v_\parallel$ along the field lines and the distance of closest approach ρ to

$$\tau = \frac{\pi}{2}\frac{\rho}{v_\parallel}. \tag{3.61}$$

The energy exchange per collision is calculated by

$$-\Delta E_\perp = \Delta E_\parallel \propto e^{-\omega_c \tau}. \tag{3.62}$$

A weakly correlated pure electron plasma is assumed with a magnetic field in the parallel direction of the electrons with $T_\perp \approx T_\parallel$. This is a condition that is not given in the electron beam. Formally the temperature change with heating rate ν can be written as

$$\frac{dT_\parallel}{dt} = \nu(T_\perp - T_\parallel). \tag{3.63}$$

The heating rate without the adiabatic suppression effect is calculated to [Ich70]

$$\nu_0 = n_e\sqrt{\frac{2kT}{m}} \cdot 4b^2 \ln\left(\frac{r_c}{2b}\right), \tag{3.64}$$

with the Coulomb logarithm changed from $\ln(\lambda_D/(2b))$ to $\ln(r_c/(2b))$.

For strong magnetization ($r_c \ll b$) the adiabatic heating rate is found as

$$\nu^{ad} = n_e \sqrt{\frac{2kT}{m}} \cdot 4b^2 \ln\left(\frac{\lambda_D}{2b}\right) I\left(\frac{1}{\sqrt{2}}\frac{b}{r_c}\right), \tag{3.65}$$

where I is the summation over many adiabatic collisions and contains all magnetic field dependence. Analytically this is calculated to

$$I\left(\frac{1}{\sqrt{2}}\frac{b}{r_c}\right) \sim \exp\left[-\frac{5}{6}\left(3\pi\frac{1}{\sqrt{2}}\frac{b}{r_c}\right)^{2/5}\right] \approx \exp\left[-2.3\left(\frac{b}{r_c}\right)^{2/5}\right]. \tag{3.66}$$

The application to our case of a strongly anisotropic electron plasma in the electron beam has to be done carefully and it is not clear if the model is still applicable. In our case the transverse temperature is always much higher than the longitudinal one ($T_\perp \gg T_\parallel$). From this it follows that the distances of closest approach fulfill $b_\perp \ll b_\parallel$. The temperature change can then be written as

$$\frac{dT_\parallel}{dt} \approx \nu T_\perp, \tag{3.67}$$

which can also be expressed as a function of the position with $dz = v_\parallel \cdot dt$, where $v_\parallel$ is the electron velocity in the laboratory frame:

$$\frac{dT_\parallel}{dz} \approx \frac{\nu}{v} T_\perp. \tag{3.68}$$

For calculating ν_0 in eq. (3.64) we choose $b = b_\perp$ because this quantity represents the unmagnetized collision dynamics. The temperature is given by $T \approx T_\perp$. One then obtains from eq. (3.64) an expression similar to eq. (3.59)

$$\left(\frac{dT_\parallel}{dz}\right)^0 = \frac{4e^4 n_e}{(4\pi\epsilon_0)^2 k\sqrt{E_{kin} k T_\perp}} \ln\frac{r_c}{2b_\perp}, \tag{3.69}$$

which differs only in a factor π and the Coulomb logarithm. In eq. (3.66) we are setting $b = b_\parallel$ because of the definition of a strongly magnetized plasma in the case of weak correlation, which gives us the TLR heating rate in the presence of a magnetic field

$$\left(\frac{dT_\parallel}{dz}\right) = \frac{4e^4 n_e}{(4\pi\epsilon_0)^2 k\sqrt{E_{kin} k T_\perp}} \ln\frac{r_c}{2b_\perp} \exp\left[-2.3\left(\frac{b_\parallel}{r_c}\right)^{2/5}\right]. \tag{3.70}$$

Important to notice is that the exponential behavior of eq. (3.70) (exponent 2/5) is different from eq. (3.57). For $b_\parallel/r_c > 1$ the energy exchange for the exponent 2/5 is larger than for the other case. In [Gli92] numerical values from Monte-Carlo simulations are given for eq. (3.66) for the intermediate regime $b/r_c \sim 1$. The significant range is shown in Fig. 3.5. In section 5.2.5 the magnetization is estimated for the conditions used in our experiments. It is found that the magnetization for small expansion ratios can be in the regime of weak but not strong magnetization.

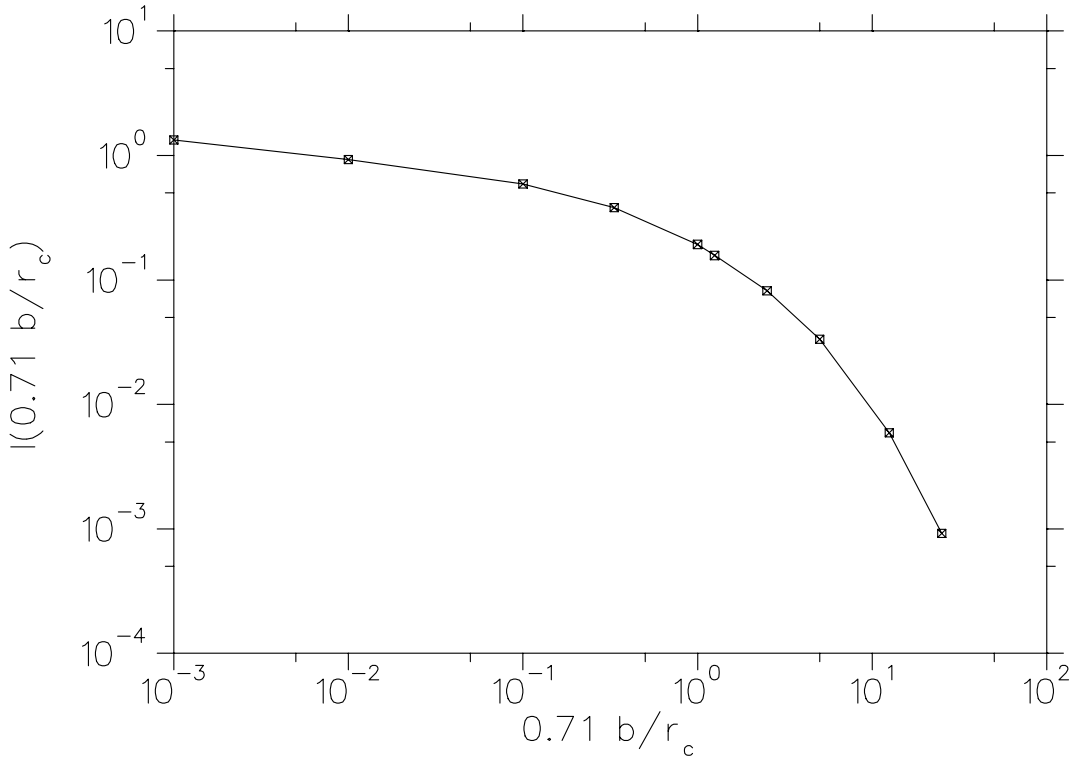

Figure 3.5: Suppression of the energy transfer between the transverse and the longitudinal degree of freedom in a magnetic field. Results from Monte-Carlo simulations taken from [Gli92] are shown in the graph. The x-axis is proportional to the magnetic guiding field and the y-axis shows the summation over adiabatic binary collisions (details see text).

3.4 Dielectronic recombination for temperature diagnostics

In electron-ion collisions an important process is the recombination of free electrons with ions. At electron densities as they are reached in the EC or the ETS the most dominant recombination processes are radiative recombination and dielectronic recombination (DR). This has been studied extensively at several storage rings in merged beam experiments over the years [Sch99].
Radiative recombination is the inverse photoionization process: a free electron is captured into a bound atomic state n_f, accompanied by the simultaneous emission of a photon that carries away the binding energy:

$$A^{q+} + e^- \rightarrow A^{(q-1)+}(n_f) + h\nu. \tag{3.71}$$

This is a non-resonant one-step process.
The dielectronic recombination on the other hand is a resonant two-step process: the free electron is captured into a bound state, exciting a bound electron which leads to a doubly

excited ionic state. The state is then stabilized by emission of a photon:

$$A^{q+} + e^- \rightarrow \left(A^{(q-1)+}\right)^{**} \rightarrow \left(A^{(q-1)+}\right)^{*}(n_f) + h\nu. \tag{3.72}$$

This can also be called an inverse Auger process.
In the experiment the rate R as a function of the detuning energy $E_d = \frac{1}{2}m_e v_d^2$, given by a mean relative velocity v_d from eq. (3.2) in the center of mass of the electron beam, is measured at the detector. Formally this can be expressed as a convolution of the phase space overlap between electrons and ions in the volume V [Mül97]

$$R(v_d) = \int_V \int_0^\infty n_e(\vec{r}) n_i(\vec{r}) \sigma(v) v f(v_d, \vec{v}) d^3v \, d^3r, \tag{3.73}$$

where n_e and n_i are the electron and ion density, σ is the recombination cross section and $f(v_d, \vec{v})$ is the distribution function of the electron velocities, which is centered at the relative velocity v_d. Neglecting the toroid effect both integrals can be separated and one can define the rate coefficient α by

$$\alpha(v_d) := \int_0^\infty \sigma(v) v f(v_d, \vec{v}) d^3v = \langle \sigma v_d \rangle. \tag{3.74}$$

The spatial integral can be evaluated assuming parallel merged beams with an interaction length L on the circumference of the storage ring C defined by the interaction section of the electron target:

$$\int_V n_e(\vec{r}) n_i(\vec{r}) d^3r = \frac{L}{C} \gamma^2 N_i n_e, \tag{3.75}$$

where γ is the relativistic Lorentz factor and N_i the number of stored ions. The rate coefficient can thus be calculated from the experimental background-corrected detector count rate by [Kil92]

$$\alpha(E_d) = \frac{R(E_d)}{\eta} \gamma^2 N_i n_e. \tag{3.76}$$

The lineshape of the resonances depends on the electron velocity distribution function which is given by a flattened Maxwell distribution due to the strong difference in the longitudinal and transverse temperatures $T_\parallel \ll T_\perp$ [Kil92]:

$$f(v_d, \vec{v}) = \sqrt{\frac{m_e}{2\pi k T_\parallel}} \exp\left(-\frac{m_e (v_\parallel - v_d)^2}{2kT_\parallel}\right) \frac{m_e}{2\pi k T_\perp} \exp\left(-\frac{m_e v_\perp^2}{2kT_\perp}\right). \tag{3.77}$$

One can now distinguish the two limits $T_\parallel \rightarrow 0$ and $T_\perp \rightarrow 0$ which lead to different lineshapes in the rate coefficient for sharp resonances $\sigma(v_d) = \delta(v_d - v_{res})$. For $T_\parallel \rightarrow 0$ one calculates [Kil90]

$$\alpha(E_d) \propto \begin{cases} \exp\left(-\frac{E_{res} - E_d}{kT_\perp}\right) & \text{for } E_d \leq E_{res} \\ 0 & \text{for } E_d > E_{res}, \end{cases} \tag{3.78}$$

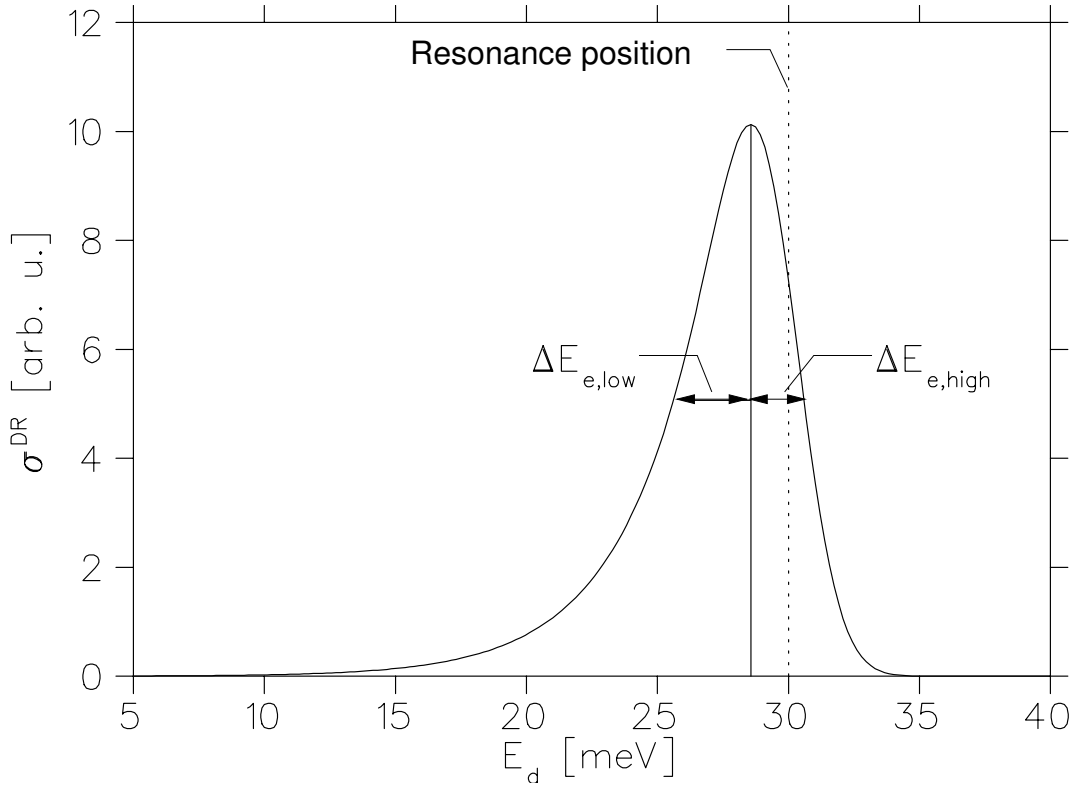

Figure 3.6: Broadening and shift of a δ-like resonance at $E_{res} = 30\,\text{meV}$. The electron temperatures have been chosen to $kT_{\parallel} = 30\,\mu\text{eV}$ (symmetric broadening) and $kT_{\perp} = 3\,\text{meV}$ (asymmetric broadening on the low energy side). Two contributions are shown: the broadening on the low energy side $\Delta E_{e,low}$ and at the high energy side $\Delta E_{e,high}$.

where E_{res} is the energy of the resonance. This is strongly asymmetric and the lineshape on the low energy side depends only on the transverse temperature with a width (FWHM) of [Tok02]

$$\Delta E_{\perp} = \ln(2) kT_{\perp}. \tag{3.79}$$

For $T_{\perp} \to 0$ on the other hand one gets a symmetric Gaussian lineshape

$$\alpha(E_d) \propto \exp\left(-\frac{(E_d - E_{res})^2}{4E_{res}kT_{\parallel}}\right), \tag{3.80}$$

where E_{res} is the resonance energy. The width (FWHM) of the measured resonance is then

$$\Delta E_{\parallel} = 4\sqrt{\ln(2) E_{res} kT_{\parallel}}. \tag{3.81}$$

The finite electron temperatures lead not only to a broadening of the resonances, but shifts the resonance position to lower energies, too. In Fig. 3.6 a calculation of the broadening and shift of a δ-like resonance at $E_{res} = 30\,\text{meV}$ is shown. In section 6.2 we will determine the electron temperatures from DR spectra by fitting $\alpha(v_d)$ to the measured data. Two

cathode temp.	E_i [MeV/u]	$\Delta E_i/E_i$	$kT_\parallel$ [μeV]	α ($kT_\perp$)
$kT_C = 108\,\mathrm{meV}$	0.5,2,10,30	$1\cdot10^{-4}, 5\cdot10^{-4}, 1\cdot10^{-3}$	30, 60	16, 90
$kT_C = 7.7\,\mathrm{meV}$	0.5,2,10,30	$5\cdot10^{-5}, 1\cdot10^{-5}, 5\cdot10^{-4}$	3, 10	16, 90

Table 3.4: Beam parameters used for the calculations in Fig. 3.7 and 3.8

contributions to the broadening, on the low energy side $\Delta E_{e,low}$ and on the high energy side $\Delta E_{e,high}$, can be distinguished. From eq. (3.79) and (3.81) we get

$$\Delta E_{e,low} = \sqrt{(\ln(2)kT_\perp)^2 + 4\ln(2)E_{res}kT_\parallel} \tag{3.82}$$

$$\Delta E_{e,high} = 2\sqrt{\ln(2)E_{res}kT_\parallel}, \tag{3.83}$$

$$\tag{3.84}$$

which lead to the total width of

$$\Delta E_e = \Delta E_{e,low} + \Delta E_{e,high}. \tag{3.85}$$

Important for the determination of the electron temperatures using DR measurements is the resonance energy $\tilde{E}$ where the contribution of the broadening due to the transverse temperature is equal to that of the longitudinal one which amounts to [Tok02]

$$\tilde{E} = \frac{\ln(2)(kT_\perp)^2}{4kT_\parallel}. \tag{3.86}$$

With a longitudinal energy spread of $kT_\parallel = 60\,\mu$eV and a transverse energy spread of $kT_\perp = 4\,$meV this yields $\tilde{E} = 44\,$meV. In the experiment one should determine the temperatures at an isolated sharp resonance with an energy not far away of $\tilde{E}$. In our case this can be satisfied by lithium-like F^{6+} which has a low lying resonance at 11.4 meV.

3.5 Cold electron targets - optimizing the energy resolution

Several parameters are limiting the experimental resolution in electron-ion collision experiments. We will focus in this section on the beam parameters itself like the electron temperatures and the ion beam energy spread. Technical aspects like the energy calibration and the beam alignment are neglected here. Another effect that has to be investigated in the future is the beam dragging at low relative energies. A first study has been performed with the ETS and the electron cooler (see section 6.1.3).
The influence of the electron temperatures has already been discussed above. A further broadening occurs through the ion beam energy spread which amounts non-relativistically to [Kil90]:

$$\Delta E_{i,r} = \sqrt{E_d E_i \frac{m_e}{m_i}}\frac{\Delta E_i}{E_i}. \tag{3.87}$$

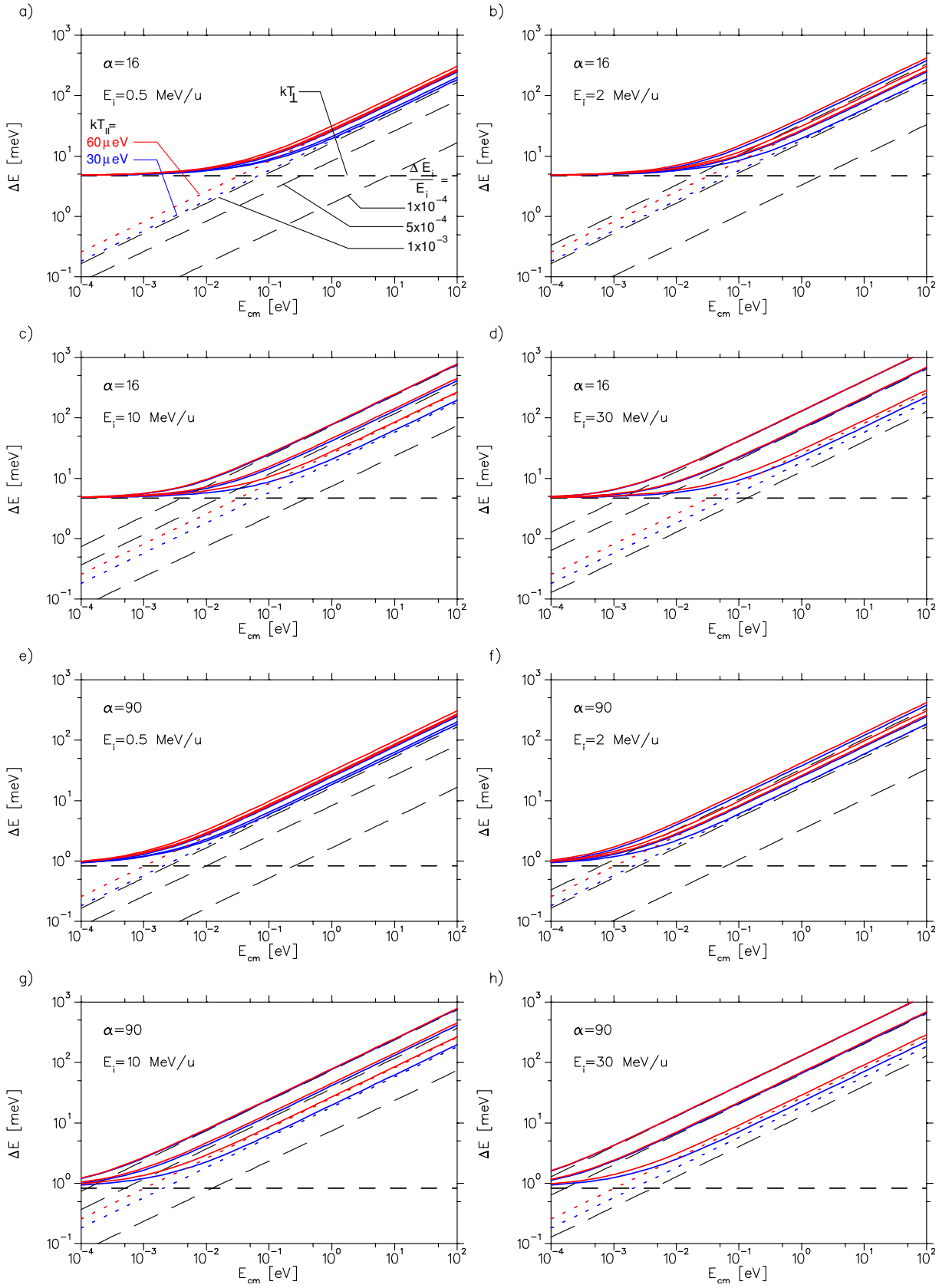

Figure 3.7: Resolution of collision experiments using the thermal cathode as a function of the relative energy in the center of mass of the ion beam for different ion energies E_i. Contribution from $kT_\perp$ (108.5 meV/α, horizontal dashed line), form $kT_\parallel$ (30 and 60 μeV, blue and red dotted lines) and from the ion energy spread (long dashed lines, values as indicated). The sum of all contributions is drawn as solid line (blue and red).

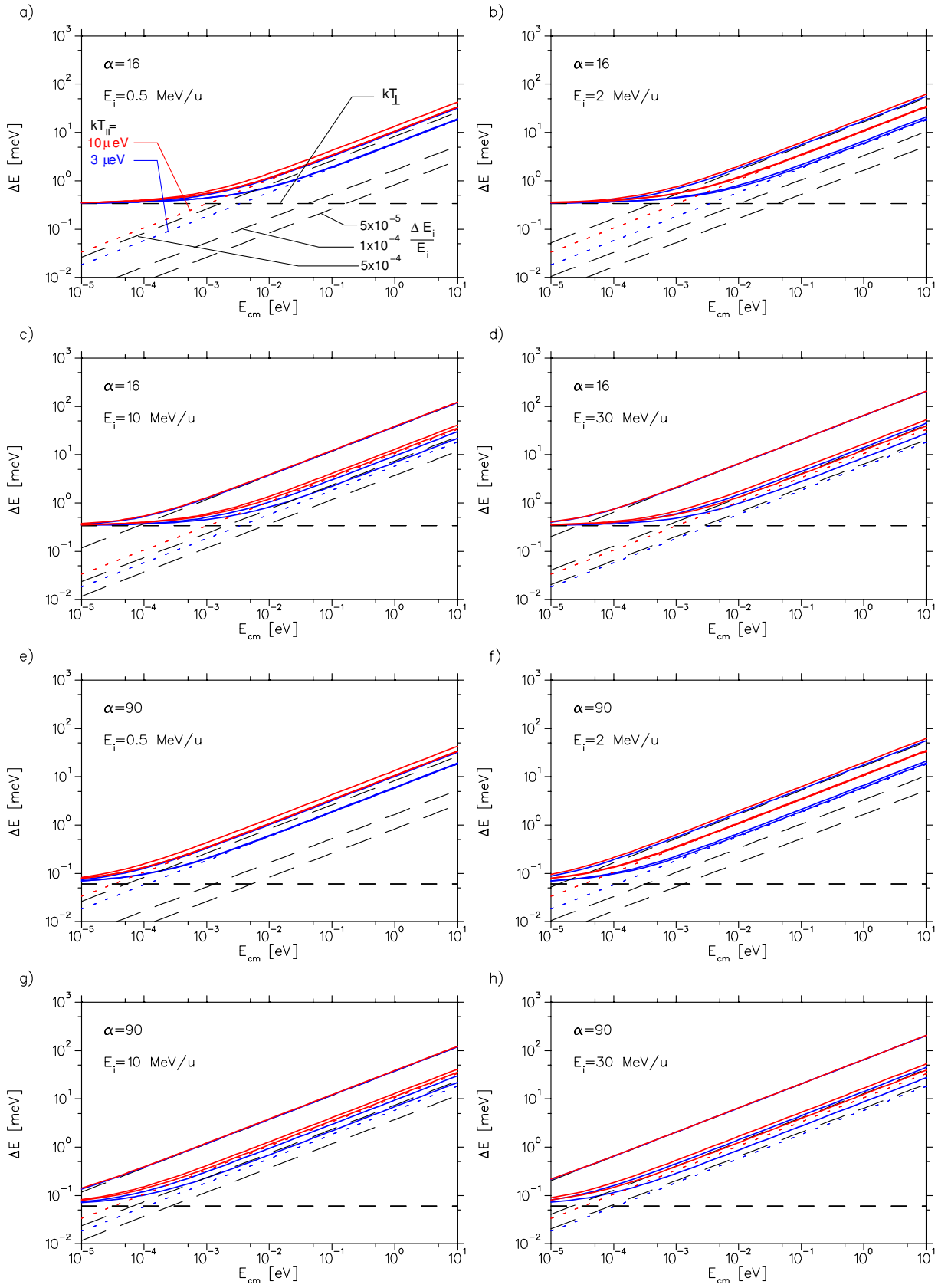

Figure 3.8: Resolution of collision experiments using the photocathode as a function of the relative energy in the center of mass of the ion beam for different ion energies E_i. Contribution from $kT_\perp$ (7.7 meV/α, horizontal dashed line), form $kT_\parallel$ (3 and 10 μeV, blue and red dotted lines) and from the ion energy spread (long dashed lines, values as indicated). The sum of all contributions is drawn as solid line (blue and red).

With eq. (3.85) we can write the total uncertainty as the squared sum of the single errors

$$\Delta E_{tot}(E_d) = \sqrt{\left(\sqrt{E_d E_i \frac{m_e}{m_i}} \frac{\Delta E_i}{E_i}\right)^2 + (\Delta E_e)^2}. \tag{3.88}$$

Thus, the resolution depends on the relative energy E_d, the ion energy E_i, the ion energy spread $\Delta E_i/E_i$ and the longitudinal and transverse electron temperatures. From eq. (3.88) we will now calculate the resolution as a function of the relative energy for the thermal and the photocathode for the parameters given in Tab. 3.4.
The results of the calculation are shown in Fig. 3.7 (thermal cathode) and in Fig. 3.8 (photocathode). The blue and red solid lines represent ΔE_{tot} for the small longitudinal temperature (blue) and the higher longitudinal temperature (red). We will start with the thermal cathode. The longitudinal and the transverse temperature are approximately a factor of 10 higher than for the photocathode. For $\alpha = 16$ (a-d) the transverse temperature (horizontal dashed line) is the limiting value for all ion energies at low relative energies. The longitudinal temperature (blue and red dotted lines) is responsible for the resolution at low ion energies and high relative energies. But with increasing ion energy the contribution from the ion energy spread (dashed lines of positive slope) becomes more and more important especially for ion beams that are not well cooled ($\Delta E_i/E_i = 1 \cdot 10^{-3}$). For $E_i = 2\,\mathrm{MeV/u}$ this happens already at $E_{cm} \approx 10\,\mathrm{meV}$. This is a situation where the separation of the cooling from the target operation becomes important to maintain a good ion beam quality. For $E_i = 30\,\mathrm{MeV/u}$ the longitudinal temperatures are only dominating for the lowest ion energy spread $\Delta E_i/E_i = 1 \cdot 10^{-4}$.
For the small transverse temperature at $\alpha = 90$ (e-g) even at low relative energies the longitudinal temperature and the ion energy spread become important. For $E_i = 0.5\,\mathrm{MeV/u}$ the longitudinal temperatures are dominating and at $E_i = 30\,\mathrm{MeV/u}$ it is mostly the ion energy spread.
In Fig. 3.8 the results for the photocathode are shown. The scale for the relative energy starts now at values one order of magnitude smaller and the lowest assumed ion energy spread is smaller (see Tab. 3.4), supposing a better cooled ion beam. At $\alpha = 16$ (a-d) again the transverse temperature is the limiting value at ion energies below $30\,\mathrm{MeV/u}$ and low relative energies. At $E_i = 30\,\mathrm{MeV/u}$ the contribution from the longitudinal temperature and from the lower ion energy spreads ($5 \cdot 10^{-5}, 1 \cdot 10^{-5}$) is almost equal. For the lower transverse temperature ($\alpha = 90$) the contribution from $kT_\perp$ is only important at very low relative energies up to $E_{cm} \approx 3 \cdot 10^{-5}\,\mathrm{eV}$ (for small ion energy spreads). This underlines again that an excellent ion beam quality is essential for high resolution experiments with ultracold beams.

4. The new TSR electron target section

In chapter 2 the basic design ideas for the new electron target section have been already discussed. We will now go through all of the installed components in detail. Starting with the three different main sections: beam formation (see section 4.1), interaction (4.2) and collector (4.3), we will then come to the electric circuit of the device (4.4). Further components are the control system (see section 4.5) and the detector arrangement (see section 4.6). Finally the alignment to the TSR (see section 4.7) and the TSR diagnostic tools (see section 4.8) that are needed for the operation in the storage ring will be discussed. In Fig. 4.1, a horizontal cut through the ETS in the plane of the beam axis is shown. The vacuum system and the different magnet coils are visible.
In the following we will denote the direction of the electron beam with the coordinate z, the horizontal coordinate in the plane of the ETS component perpendicular to the electron beam motion by x and the vertical component by y.

4.1 Electron beam formation

A completely new concept compared to the existing electron cooler in the TSR, and to other electron cooling devices, is the separation of the electron production from the electron acceleration (overview see Fig. 4.2). In the TSR electron cooler gun the first electrode (extraction electrode) is put already to ground potential accelerating the electrons directly to their final energy in a fast acceleration [Sch00a]. Furthermore the electron current can not be controlled. It depends completely on the cathode potential which has to be taken into account in the DR measurements (see section 6.2). In the ETS the situation is different. The electron current depends only on the extraction voltage and is then accelerated to the desired final energy.
Another new feature is the Pierce electrode that is insulated from the cathode and the extraction electrode. The Pierce electrode is necessary to form a homogeneous electric field in front of the cathode with parallel field lines (see section 3.3.1). Normally the Pierce electrode is kept on cathode potential but due to different work functions of the cathode and the electrode materials and possible surface layers there will always be an electric field disturbing the electron optics. Therefore the current density will be influenced at the edges of the beam leading to a non homogeneous density distribution. This can be corrected by a certain potential applied to the Pierce electrode. Moreover the shape of the electron beam can be manipulated (cf. section 5.1 for more details).

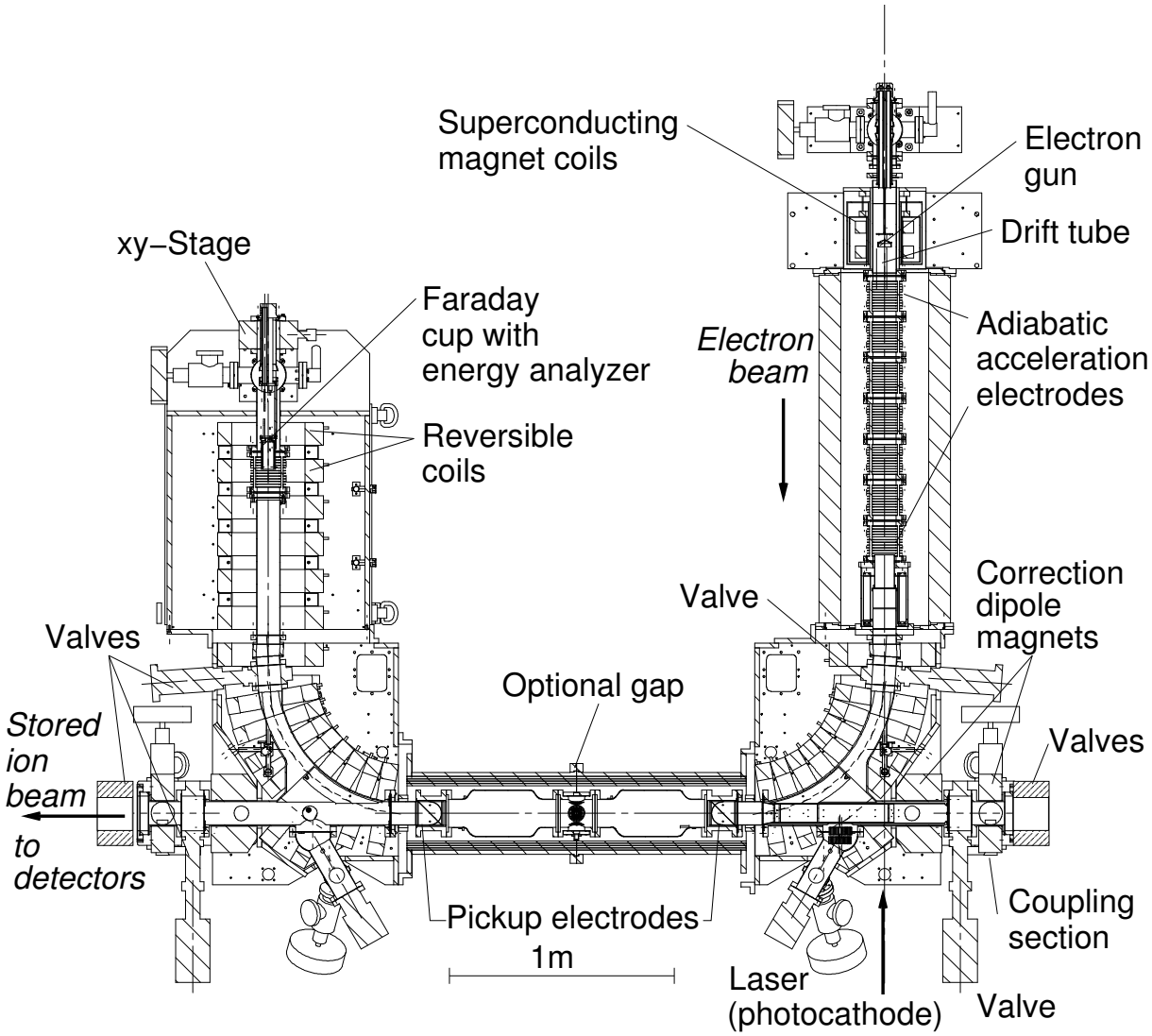

Figure 4.1: Overview of the ETS: shown is a horizontal cut through the whole section in the plane of the beam axis making the magnet and the vacuum system visible.

4.1.1 The electron gun for thermal cathodes

An electron gun for IrCe-cathodes has been developed and tested by [Sch00a]. It was also used in a test setup for the ETS which is described in [Spr00, Lan01]. Fig. 4.3 shows the main parts of the electron gun: cathode support, cathode, Pierce electrode, extraction electrode. The electron gun is designed for a 1.6 mm diameter cathode and was optimized for small transverse energies in the beam edge. With a calculated perveance of 1.8 μPerv and a maximal extraction voltage of 2000 V one can achieve a maximum emission current of 170 mA. The cathode is positioned to the center of the Pierce electrode which has an opening of 2 mm leaving a space of 0.2 mm from the cathode to the electrode. Following the Pierce electrode, the extraction electrode comes at a distance of 1 mm.

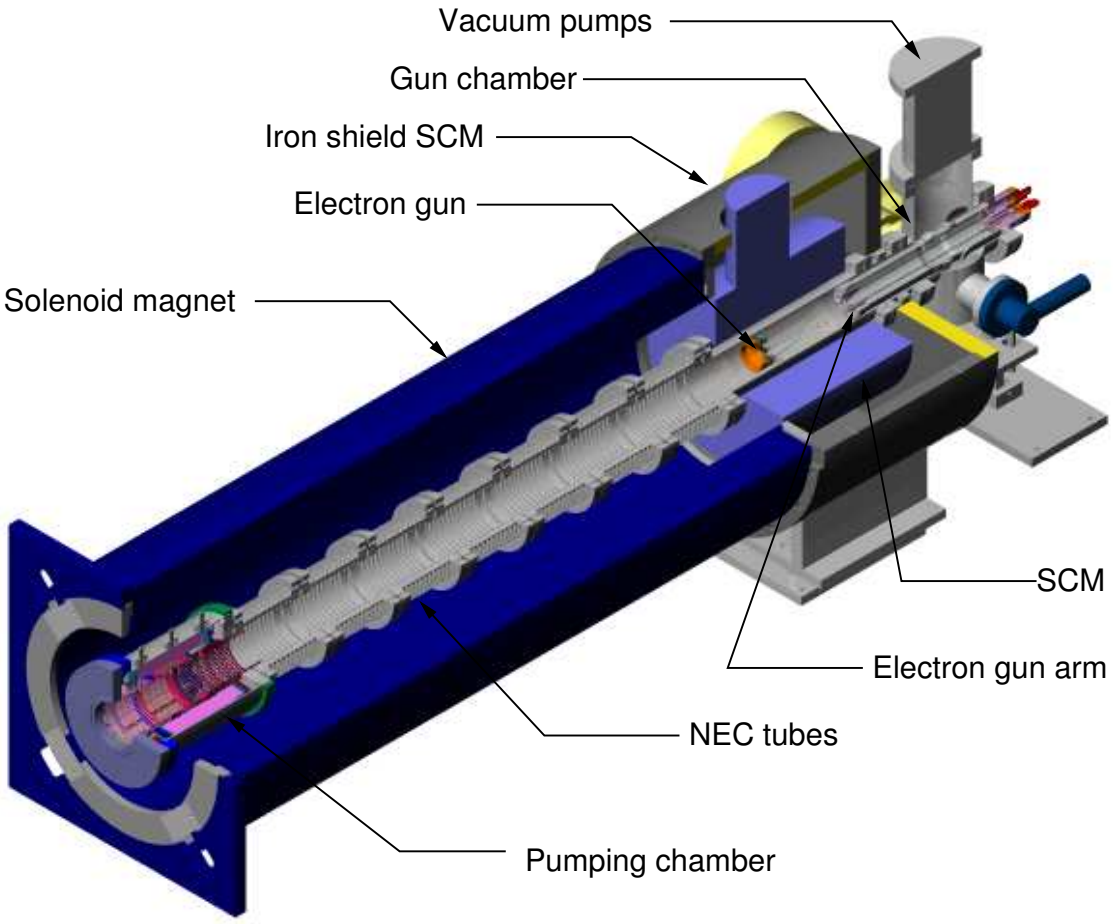

Figure 4.2: Electron beam formation section: Electron gun in the field of the superconducting solenoid magnet (SCM) and adiabatic acceleration section inside the normal conducting solenoid magnet.

A number of problems connected to the IrCe-cathodes were observed. Two-dimensional electron density distributions that were measured in the test setup at small extraction voltages $U_{ext} \approx 1\,\mathrm{V}$ and low electron energies $U_0 = 60\,\mathrm{V}$ showed four positions with a significantly higher electron density for high cathode temperatures corresponding to a high DC heating power [Spr00]. These peaks were explained as a result of the cathode structure with two pairs of heating wires holding the IrCe-disk $\approx 2\,\mathrm{mm}$ above the carrier (see Fig. 4.4 (b). The current through the wires was thought to modify the extracting electric field resulting in a locally disturbed electron density distribution. Heating the cathode with an AC power supply removed the peaks; however, the heating scheme still leaves a further uncertainty regarding in particular the starting energy of the electrons. After many hours of operation the adjustment of the cathode surface to the Pierce electrode was found to be no longer parallel.
To avoid the ensemble of these problems the IrCe-cathode has been replaced by a BaO-

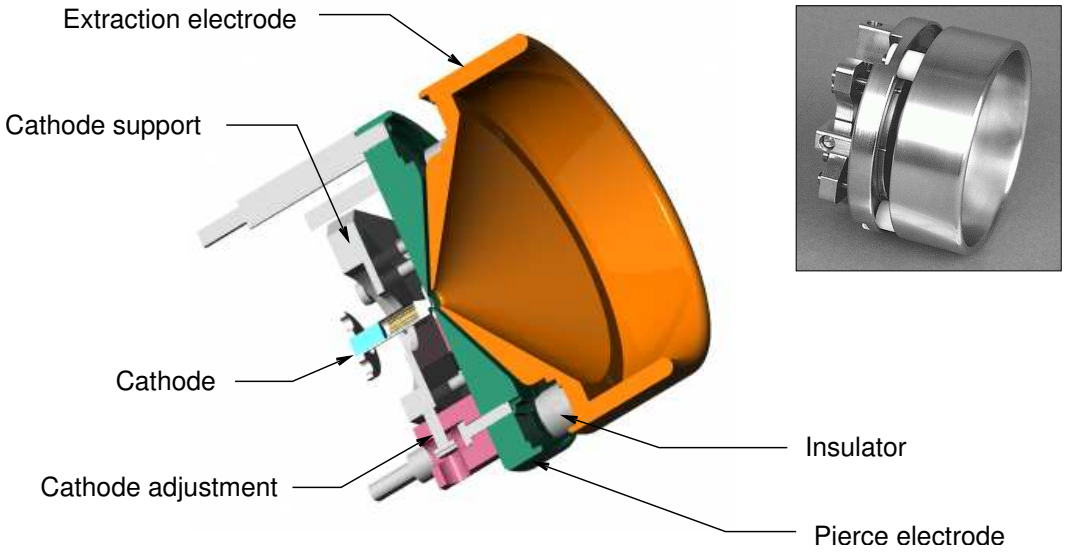

Figure 4.3: Electron gun for thermal cathodes: Cut in a plane parallel to the beam axis with the thermionic cathode, the Pierce electrode and the extraction electrode. In the upper right corner a picture of the electron gun is shown.

dispenser cathode[1] with a well established, different heating concept. Fig. 4.4 (a) shows a cut through the cathode where one can see the coiled heating wires to avoid any disturbing electric and magnetic fields and the emissive tip. The rigid structure of the cathode also avoids problems with the alignment of the cathode to the Pierce electrode. The cathode support at the electron gun was modified to hold the new cathode type. In sec. 5.2.3 temperature measurements of the cathode will be discussed.
The electron gun is mounted at the end of the electron gun arm as shown in Fig. 4.5. This construction with the long arm has several functions. By adjusting the length of the rods at the end of the arm the gun could be placed to the maximum of the magnetic field in the expansion region (see below). A ceramic insulator which is soldered to the stainless steel tube insulates the cathode potential from ground. Vacuum feedthroughs are installed for the cathode heating, the Pierce and extraction voltages. The electron gun arm is connected to the gun chamber (see Fig. 4.2) where the adjustment and pumping (one ion getter pump[2] and one Ti-sublimation pump) is done. Additionally a vacuum valve and a vacuum gauge are installed there.

4.1.2 Cold electron source development

Since the total beam current required for the ETS is much smaller than that required for electron cooling, it is attractive to consider the use of cold electron sources. Depending on the experiment the ETS can be operated either with a thermal cathode for high emission

[1] cathode material: porous tungsten impregnated with Ba0, 612 M-type cathode, Heatwave Watsonville, CA, USA

[2] Varian StarCell VacIon 75 plus, pumping speed ≈ 120 l/s (nitrogen)

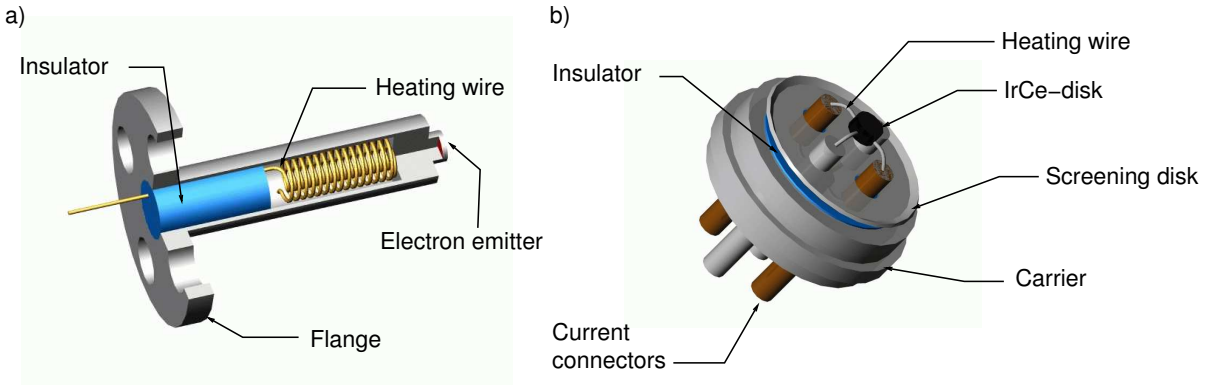

Figure 4.4: Two types of thermionic cathodes (schematic view): a) BaO-cathode with the internal heating wire visible. b) IrCe-cathode used in initial tests.

currents or with a photocathode for ultracold electron beams. A big advantage of the photocathode is the very small initial electron energy distribution due to the low cathode temperature (about liquid nitrogen temperature) [Pas97b]. Important for a long operation of the cathode is a very low pressure in the range of 10^{-12} mbar because the electron beam creates rest gas ions. Due to the negative cathode potential these particles bombard and destroy the cathode surface. This limits the lifetime to several hours. For an operation in storage ring experiments one desires a continuous operation in the order of one week. Therefore it is necessary to have several cathodes in the vacuum chamber which can then be exchanged, cleaned and activated over this period of time. For a detailed description of the TSR photocathode setup and operation see [Pas00, Orl01, Wei03]. Presently emission currents in the order of 1 mA with a cathode temperature of ≈ 8 meV (90 K) are achieved. Altogether the operation of a photocathode electron gun is quite challenging.
Thermal cathodes, on the other hand, are easy to use and are able to produce emission currents in the order of hundreds of mA over long periods of time. A big variety of cathode types is commercially available. In this work we will focus on the use of thermal cathodes.

4.1.3 Magnetic expansion region

The free electrons are produced in a region with a magnetic field up to 3.5 T. In the transfer to the adiabatic acceleration section (see section 4.1.5) the magnetic guiding field is then reduced to $\approx$0.1–0.04 T (expansion factor $\alpha \approx$35–90). As described in section 3.3.3, the electron beam is transversely expanded resulting in a bigger beam diameter (up to $\approx$ 15 mm) and a lower density ($n_e \propto 1/\alpha$). In this process energy is transferred from the transverse to the longitudinal degree of freedom, lowering the transverse temperature by a factor $1/\alpha$.
The high initial magnetic field is produced by a superconducting solenoid magnet[3] (SCM). A schematic drawing is shown in Fig. 4.6. The magnet consists of a pair of independent coils in a Helmholtz configuration with the cathode positioned in the center of the two

[3]Everson Electric Company, now Everson Tesla Inc., Nazareth, PA 18064, USA.

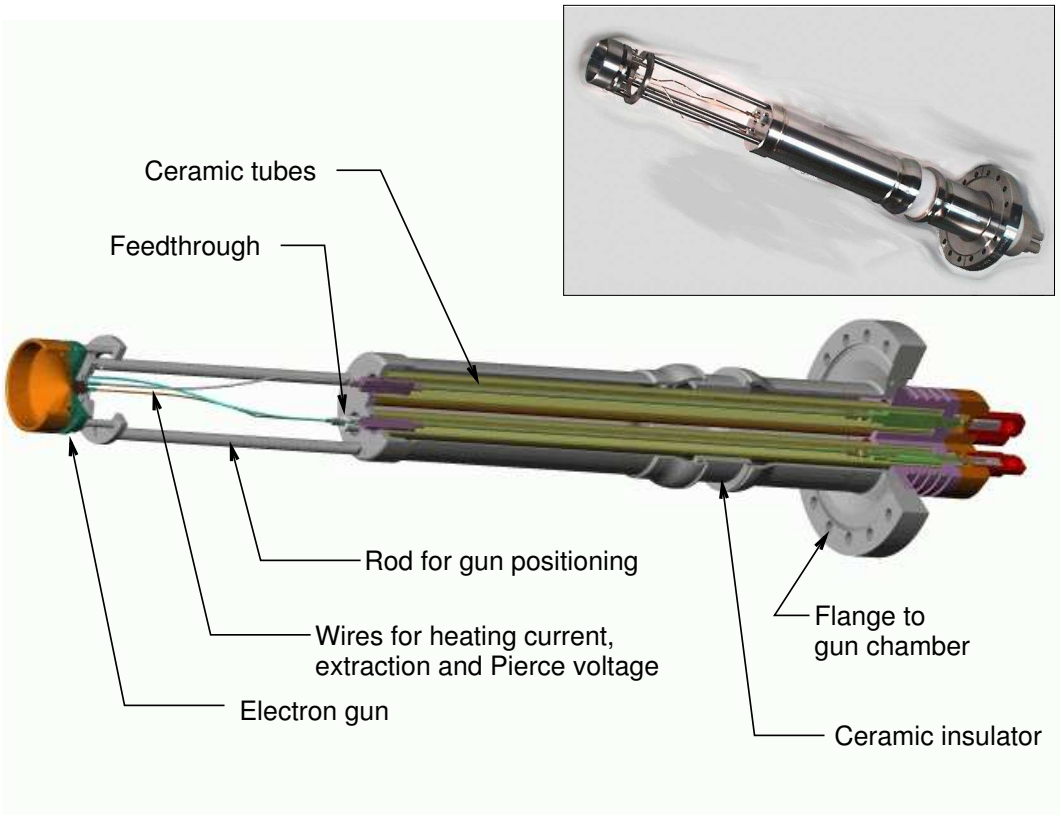

Figure 4.5: Electron gun arm for cathode positioning inside the magnetic field. The electron gun is mounted at the end of the arm. A picture of the gun arm is shown in the upper right corner.

coils. Because of the varying expansion ratios in the experiment that require a change in the magnet current the SCM is operated in a non-persistent mode with a dedicated power supply. The technical data is summarized in Tab. 4.1. The current-field relation is given by the manufacturer as

$$B[\mathrm{T}] = 0.08 \cdot I[\mathrm{A}].$$

The iron shielding (see Fig. 4.2) around the SCM serves a physical and a technical purpose. First, stray fields are reduced by closing the magnetic field lines and redirecting the magnetic flux. The second purpose is to compensate mechanical forces on the coils. This is achieved by putting the iron plate opposite to the normal conducting solenoid at a position where the force on the coils becomes minimal. This construction makes it possible to use only a relatively small fiber glass tube to hold the coils inside the cryostat. In addition this reduces the heat transfer into the cryostat which reduces the helium loss. The connection from the current connectors outside the cryostat to the superconducting coils is made by high temperature superconducting (HTS) connectors in the upper part of the helium reservoir.

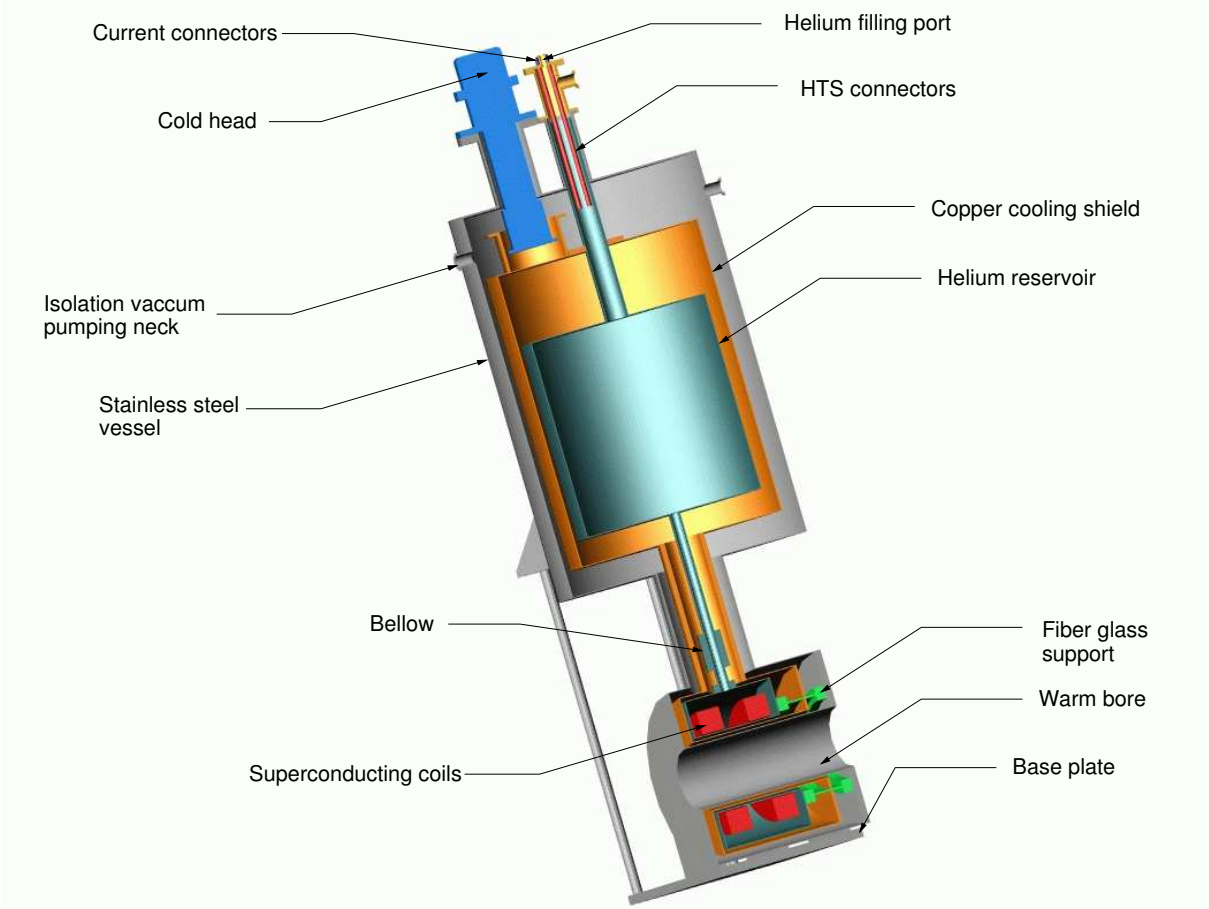

Figure 4.6: Superconducting solenoid magnet for high initial magnetic field (schematic view): the magnet system is shown in a cut in a plane parallel to the electron beam axis. The liquid helium reservoir and the coil arrangement is visible.

4.1.4 Gun section assembly and field measurements

For assembly of the gun section, the acceleration solenoid was installed first on its support structure and aligned to the precision rails and the storage ring reference height. The alignment of the SCM magnet coil to the beam axis defined by the acceleration solenoid is complicated by the surrounding liquid helium reservoir. The base plate of the SCM (see Fig. 4.6) is assigned as the mechanical reference, while the outer shell of the reservoir was not manufactured with enough mechanical precision. To verify the alignment, magnetic field measurements have been performed.
The iron shielding of the acceleration solenoid will be attracted by the SCM magnetic field resulting in rather high forces which are able to destroy the fiber glass support. To reduce the forces on the coil the backplate of the SCM iron shielding is used to transfer as much force as possible into the radial parts between the backplate and the acceleration solenoid [Sch00a]. Therefore it is not possible to operate the SCM without the iron shielding.

Coil inner diameter	80 mm
Coil outer diameter	120 mm
Coil width	51 mm
Total turns	19171
Total inductance	56.2 H
Coil material	NbTi
HTS connectors material	Bi2223
Warm bore diameter	129 mm
Length system	343 mm
Cooling type	single stage
Cooling medium	liquid helium
Cold head	Leybold COOLPOWER 120T
Radiation shield material	copper

Table 4.1: Summary of some of the SCM technical data.

Operating the SCM close to the acceleration solenoid, which is the normal operation mode for the ETS, results in a shift of the SCM magnetic field maximum and a field asymmetry because of the summation of the two fields. It is important to quantify this shift with magnetic field measurements because the electron gun has to be put into the magnetic field maximum. Deviations from the maximum position would lead to wrong expansion factors in particular at small expansion ratios. This effect was taken into account in the SCM design, using two independent coils that can be powered separately. With a bias current to one of the coils, one can move the maximum to the desired position and compensate the field asymmetry. Presently, however, both coils are operated in series with both the same current.
A large angle φ between the electron gun axis and the magnetic field lines will also lead to an increase of the transverse electron temperature. One can estimate the temperature increase by calculating the mean transverse velocity of a single particle moving in a magnetic field under an angle φ with [Orl02]

$$\Delta E_\perp = \frac{m}{2}\frac{\mathcal{E}^2\varphi^2}{e^2B^2}.$$

With an angle $\varphi = 10°$ (174 mrad), an electric field $\mathcal{E} = 1000\,\mathrm{V/cm}$ and $B = 1\,\mathrm{T}$ one calculates $\Delta E_\perp = 1.7\,\mathrm{meV}$. This value is very small for a rather large angle. From measurements at the TSR electron cooler ($B = 1.2\,\mathrm{T}$) an increase in the transverse temperature of 0.25 meV was measured for angles in the range of 1–3 mrad [Sch00a].

Longitudinal field

The longitudinal magnetic flux density was measured, using a longitudinal hall probe fixed on a carriage. The carriage was moved in a long aluminum tube that was aligned to the beam axis. Using a tube has two advantages: the radial position is defined very well inside the tube and the bending of the guiding device is very well suppressed due to

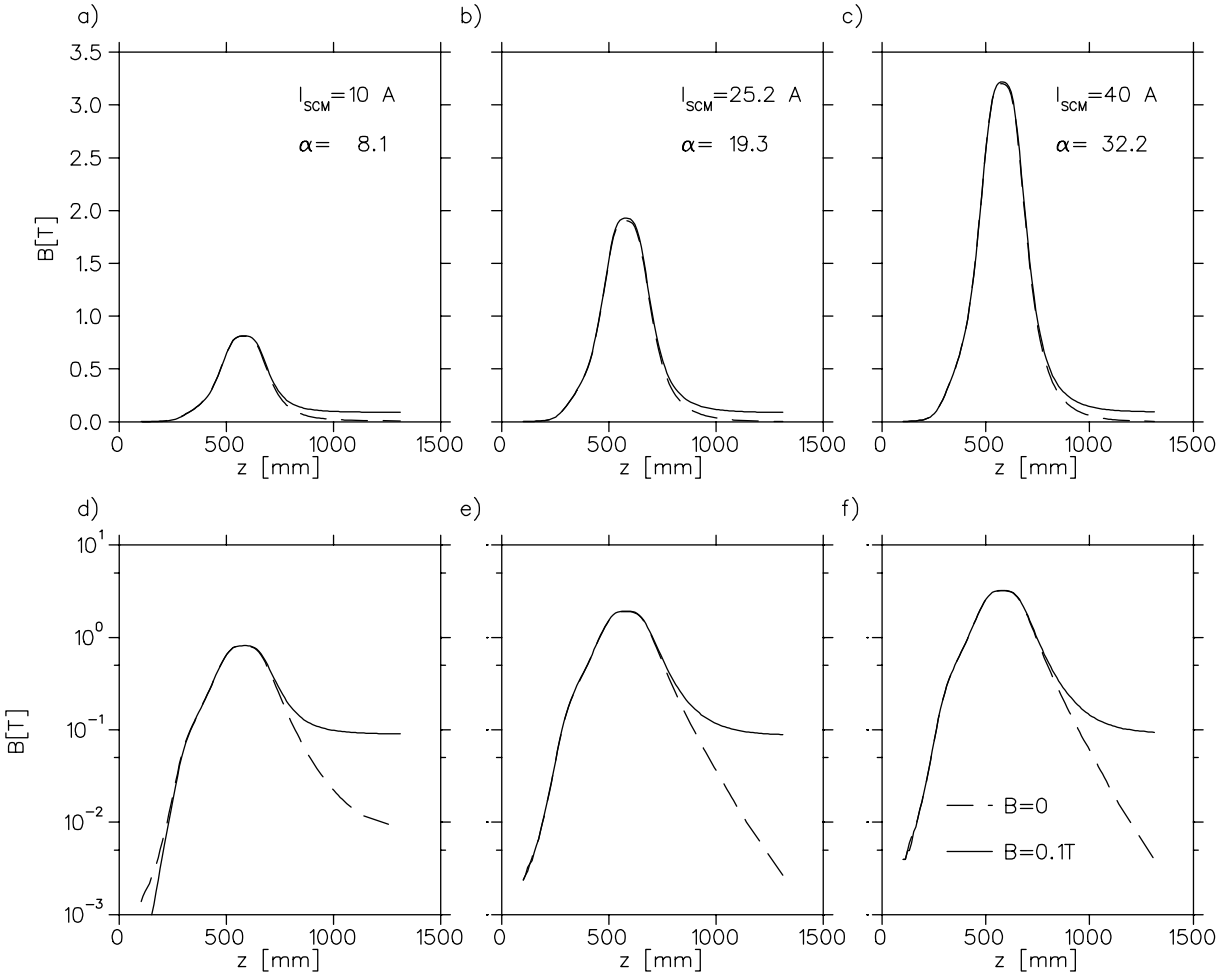

Figure 4.7: Magnetic flux density of the expansion region for three different expansion ratios in a linear plot (a-c) and a logarithmic plot (d-f) (definition of z see text). Acceleration solenoid $B = 0$ (dashed line) and $B = 0.1\,\mathrm{T}$ (solid line). Details near maximum see Fig. 4.8.

the high rigidity.
Fig. 4.7 shows the result for three different expansions ratios $\alpha = 8.1, 19.3$ and 32.2. The distance z is measured from the flange of the gun chamber where the gun arm is mounted (see Fig. 4.2). Each expansion ratio was measured with $B = 0.1\,\mathrm{T}$ and $B = 0\,\mathrm{T}$ in the acceleration solenoid, to see the change of the flux density due to the superposition of the fields. In Fig. 4.7 (d) at $z \approx 200\,\mathrm{mm}$ there is a small deviation of the order of $1 \cdot 10^{-3}\,\mathrm{T}$ between the two curves that are visible. With the acceleration solenoid on, the magnetic flux is slightly smaller which could be an artifact related to the turning on of the magnets because the dashed curve was measured first.
The region of the maximum has been measured with better resolution and the result is shown in Fig. 4.8 (a-c). The curves for $B = 0.1\,\mathrm{T}$ have been shifted on the y-axis about 0.3–1% of the maximum value to agree for $z = 552$. Reasons for this deviation could be a drift in the hall probe or some magnetization effect of the surrounding iron.

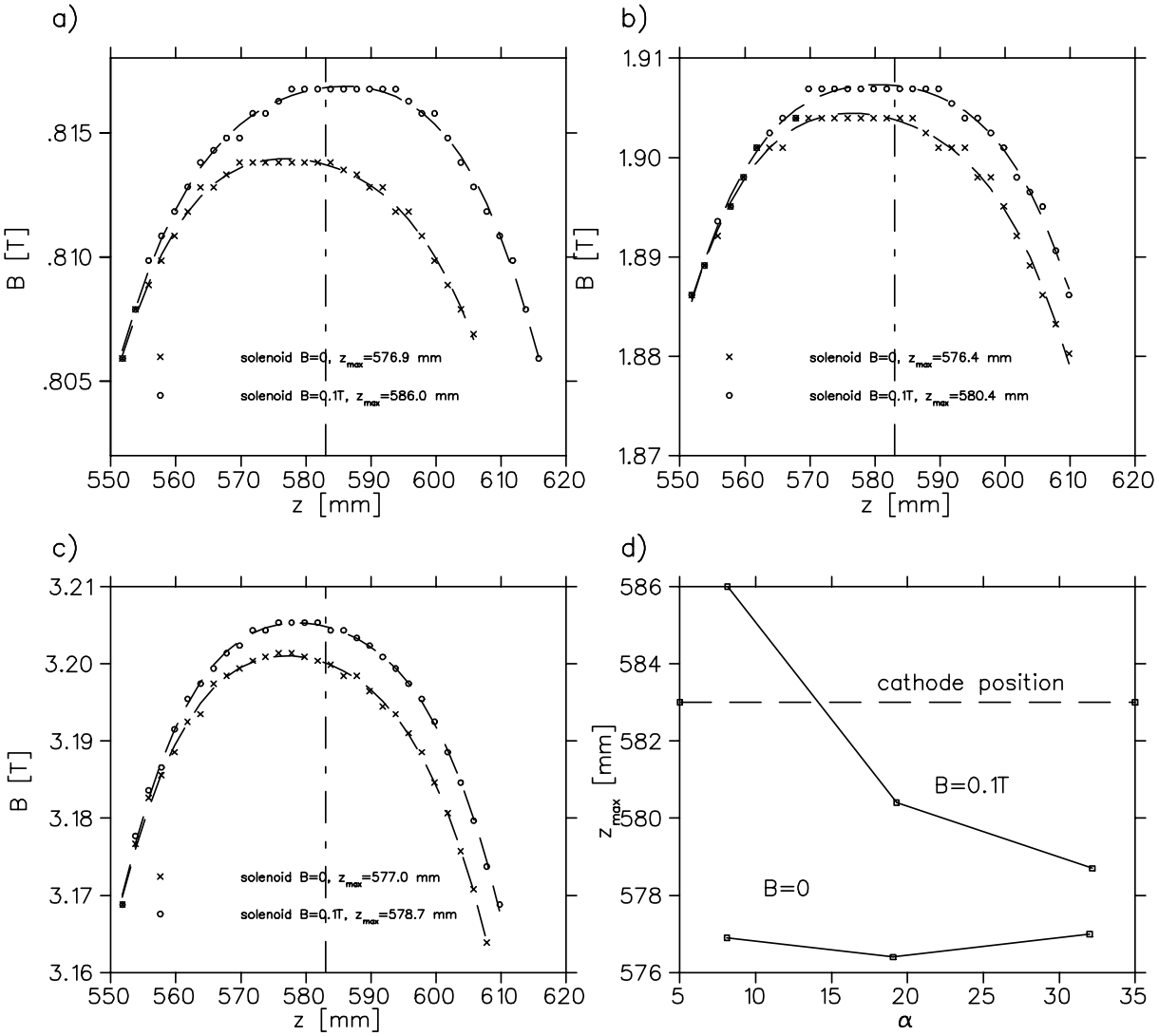

Figure 4.8: (a-c) Magnetic flux density at the maximum measured with better spatial resolution. Two measurements are shown in each window: one with the acceleration solenoid switched off ($B = 0$, crosses) and with the acceleration solenoid switched on ($B = 0.1\,\mathrm{T}$, circles). The dashed line is calculated from an analytical formula (see text) and fitted to the data points. The dash-dotted vertical line shows the position of the cathode. The z-position is indicated for each curve in the graphs. d) Positions of the magnetic field maxima for (a-c).

A theoretical curve describing the SCM coils (formula can be found in [Sch73]) has been fitted to the data points to find the maximum (result see Fig. 4.8 (d)). The agreement of the fitted curve with the measurement is good. As one can see the shift of the maxima is strong for $\alpha = 8.1$ with 8.9 mm and only 1.7 mm for $\alpha = 32.2$. Also the contribution of the absolute value decreases with increasing SCM current as expected. From these measurements the desired cathode position has been deduced to $z_{cathode} = 583\,\mathrm{mm}$, trying to find a compromise between the low and the high expansion ratios.

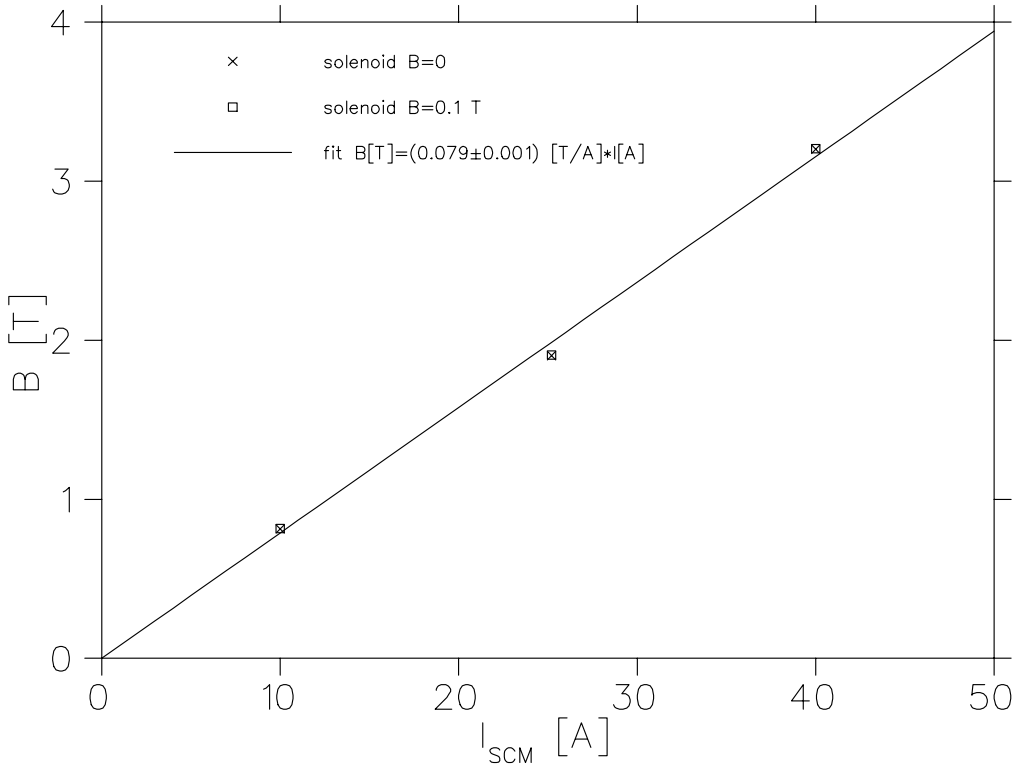

Figure 4.9: Magnetic flux density in the SCM at the maximum as a function of the coil current.

The magnetic flux density (maximum for $B = 0$ and $B = 0.1\,\mathrm{T}$) as a function of the coil current is shown in Fig. 4.9 and one calculates a flux increase of $0.079 \pm 0.001\,\mathrm{T/A}$ which agrees within the error with the value given by the manufacturer of $0.08\,\mathrm{T/A}$.

Transverse field

The transverse part of the magnetic flux density $B_\perp$ has been measured at $\alpha = 32.2$ with a transverse hall probe mounted on a similar carriage as the longitudinal probe. The carriage was moved in the same aluminum tube as described above. The measurement of the transverse part of magnetic field is more complicated because the longitudinal component is much stronger. If the probe is not perfectly aligned to the longitudinal direction, this will always lead to an offset in the measurement. By rotating the probe in the magnetic field, one can separate the offset from the transverse component. Fig. 4.10 shows the rotation of the probe along the "theoretical" (geometrical center of the magnet) electron beam axis. At several z-position of the electron beam axis such rotations have been performed and the relative transverse component $\rho = B_\perp / B_\parallel$ as a function of the rotation angle φ is shown in Fig. 4.11 (a). A cosine function

$$\rho(\varphi) = \rho_1 \cos(\omega\varphi + \varphi_0) + \rho_0 \tag{4.1}$$

with the amplitude ρ_1, the frequency ω, the phase φ_0 and an offset ρ_0 has been fitted to the data points and reproduces the expected sinusoidal behavior very well. The horizon-

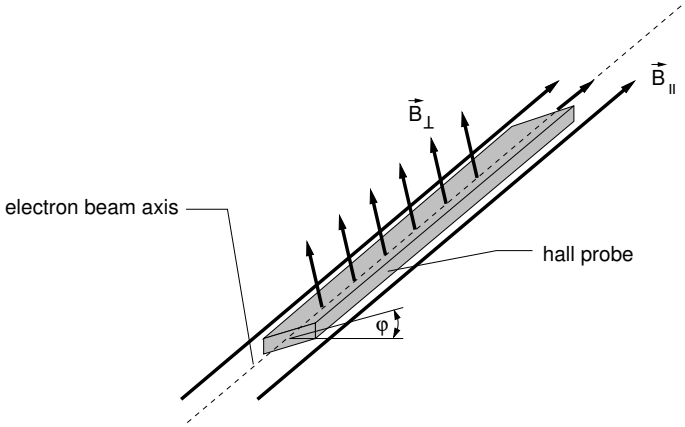

Figure 4.10: Geometry of the measurement of the transverse field components with a transverse Hall probe. The probe is rotated around the beam axis about angles φ.

tal dashed line indicates the mean offset $\overline{\rho_0} = 12.0 \pm 0.2\,\mathrm{mrad}$ at all z-positions which represents the part of the longitudinal magnetic field that is measured because of the misalignment. The amplitude ρ_1 of the fitted cosine function is shown in Fig. 4.11 (b) as a function of the position. One can see that the amplitude is changing with the position which represents higher order distortions of the magnetic field. We will not discuss this further in this context. The cathode is located at $z = 583\,\mathrm{mm}$ where a deviation of $\approx 7\,\mathrm{mrad}$ was found. From the measurements at the EC one could therefore expect an increase of the transverse temperature of 0.6–1.7 meV. This could be already a limiting factor at high expansion ratios especially with the photocathode. A further alignment of the SCM could become necessary to improve the situation.

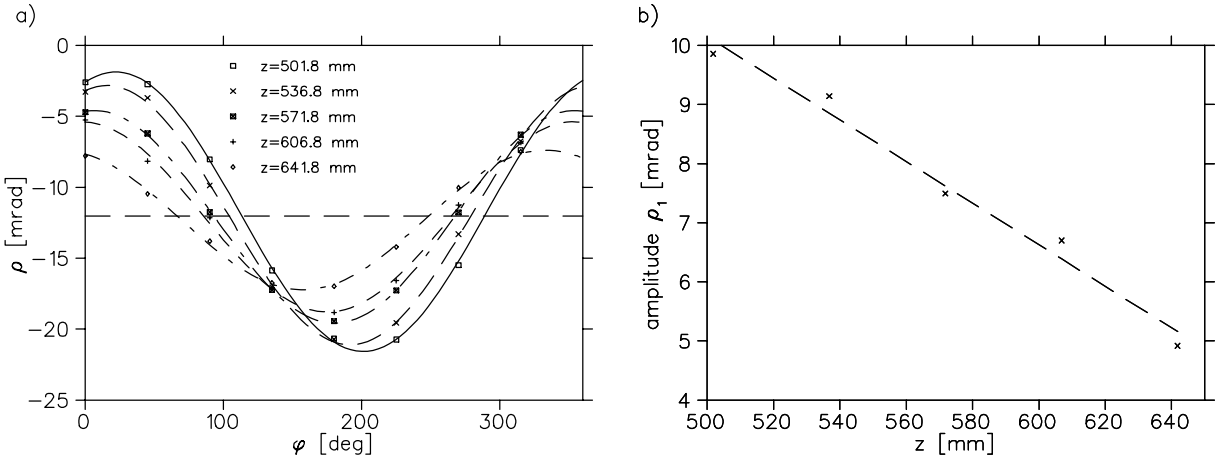

Figure 4.11: a) Relative transverse component $\rho = B_\perp / B_\parallel$ as a function of the rotation angle φ for different z positions (as indicated in the graph) on the beam axis. The different lines are sinusoidal fits to the data points (see text). The horizontal dashed line indicates the mean offset for all z positions. b) Amplitude of the fitted curves as a function of the z position. The dashed line is drawn to guide the eye.

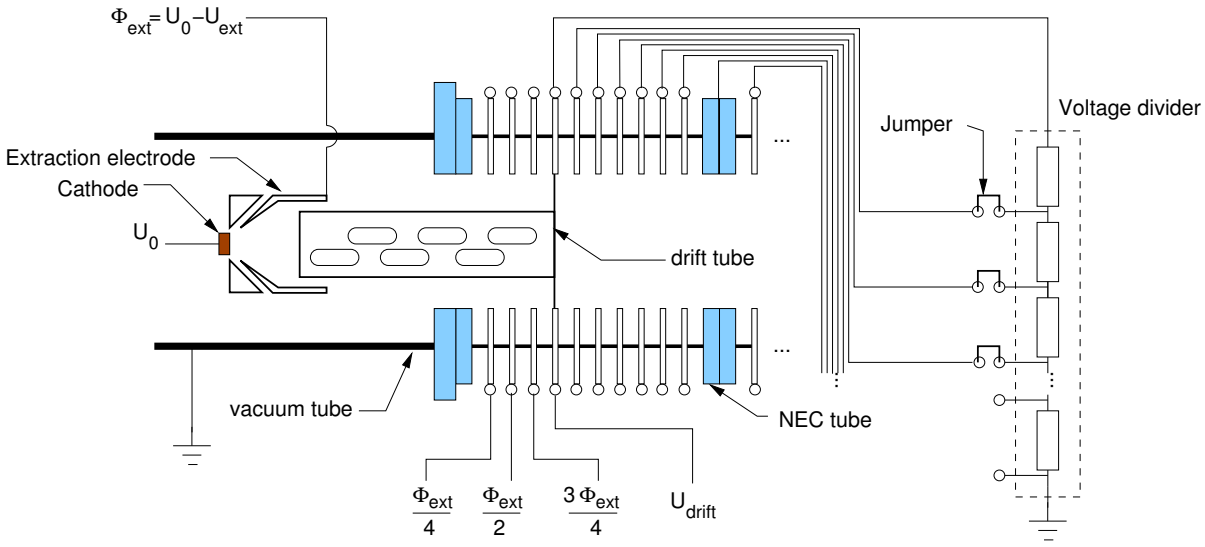

Figure 4.12: Detail of the electrical connections in the expansion region: the drift tube is insulated from the extraction electrode. The first three electrodes are used to build up the potential from ground potential. The drift tube voltage U_{drift} defines the kinetic energy of the electrons in the expansion region. The accelerating potential in the acceleration section can be adjusted with jumper wires.

4.1.5 Adiabatic acceleration section

The acceleration section is situated within a solenoid magnet of length $l = 1512\,\mathrm{mm}$, inner diameter $d = 381\,\mathrm{mm}$ and inductance $L = 1.47\,\mathrm{mH}$ (see Fig. 4.2). The field-current relation is given by [Blu87]:

$$B[\mathrm{T}] = 3.435 \cdot 10^{-4}\, I[\mathrm{A}].$$

After the adiabatic magnetic expansion, where energy from the transverse degree of freedom has been transferred to the longitudinal degree of freedom, the electrons still have a very low kinetic energy. The kinetic energy is at least the extraction potential but can also be increased by applying a preaccelerating potential U_{drift} to the drift tube (length 202 mm) which begins directly at the extraction electrode and shields the potential from the surrounding vacuum tube which is on ground potential (see Fig. 4.12). For high extraction voltages the extraction process is non-adiabatic.
The electrons are then accelerated further to the desired final energy. The final energy is controlled by the cathode potential U_0. As shown in section 3.3.4 Coulomb interactions due to non-equilibrium conditions of the electron ensemble lead to a longitudinal heating of the electron beam during a fast acceleration; this can be suppressed by using a slow (adiabatic) acceleration. A general measure for the adiabaticity of the acceleration can be calculated from eq. (3.54) by the average adiabaticity parameter ($\lambda < 1$ adiabatic)

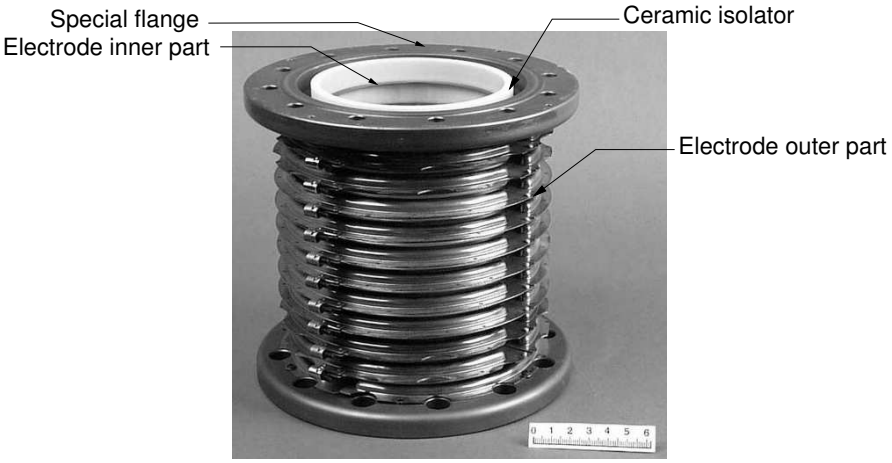

Figure 4.13: Acceleration tube with 11 insulated titanium electrodes for the long adiabatic acceleration section.

[Sch00a]:

$$\overline{\lambda}(U_0) = \frac{1}{U_0} \int_0^{U_0} \lambda(U) dU, \tag{4.2}$$

which for a linear potential drop $U = Az$ becomes

$$\overline{\lambda} = \frac{4}{3} \left(\frac{8e\epsilon_0^2}{m_e} \right)^{1/4} \frac{U_0^{3/4}}{j_e^{1/4} z}. \tag{4.3}$$

$\overline{\lambda}$ is mainly determined by the final energy U_0 and the length z. For $U_0 = 20\,\mathrm{kV}$, $j = 100\,\mathrm{mA/cm^2}$ and $z = 1\,\mathrm{m}$ one obtains $\overline{\lambda} = 1.7$.
The maximum length of the accelerating section is limited by the acceleration solenoid magnet to 1.5 m. To have larger experimental flexibility, we use elements of 11 electrodes each (see Fig. 4.13). In total, seven elements with a single length of 173.5 mm are used. The titanium electrodes with an inner diameter of 101.6 mm (4 inch) are soldered to ceramic insulators of length 12.7 mm (1/2 inch). This gives a total length of the elements of $L_{acc} = 1226.5\,\mathrm{mm}$ (including gaskets).
The last acceleration element is connected to a pumping chamber (see Fig. 4.14) with NEG[4]-stripes that have a pumping speed of $\approx 900\,\mathrm{l/s}$ H_2. Three drift tubes are installed in this chamber which can be powered separately by electric feedthroughs, thus extending the acceleration section. Altogether, this gives a total accelerating length of $L_{tot} = 1490\,\mathrm{mm}$. An aperture (inner diameter 30 mm) is installed in the last drift tube to block ions flowing from the toroid section to the cathode.
All electrodes are connected via HV cables to a voltage divider with 80 taps and a total resistivity of $32\,\mathrm{M\Omega}$ (see Fig. 4.12). Using jumper wires each electrode can be connected to a separate potential which allows the shape of the accelerating potential to be

[4]Non Evaporative Getter, SAES Getters (Deutschland), Köln, Germany

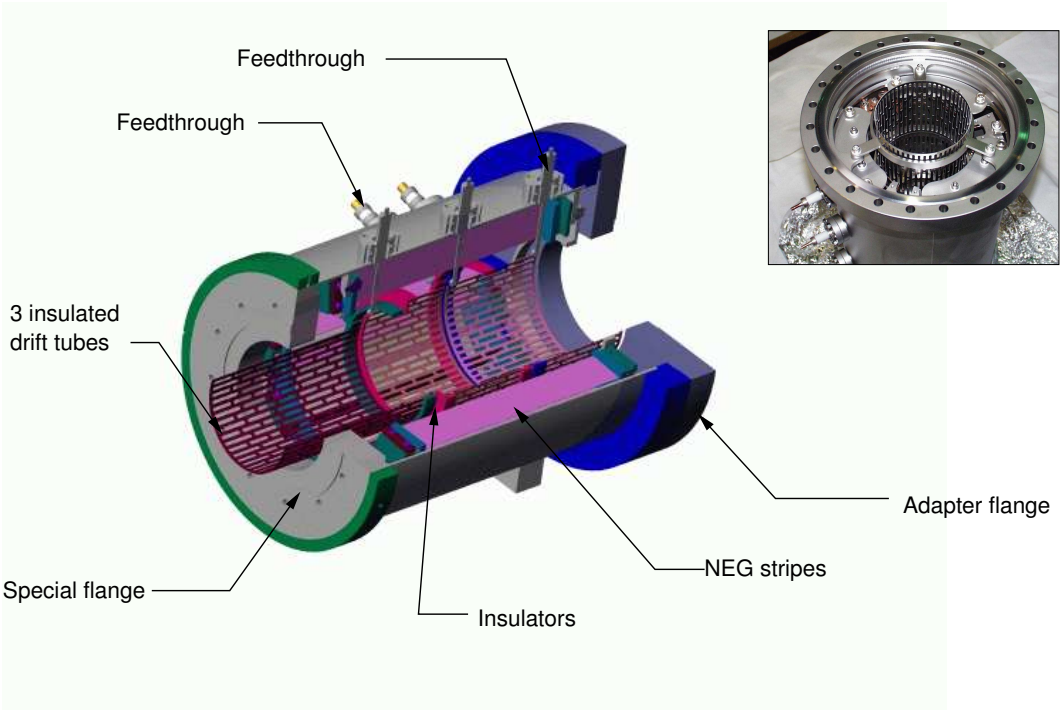

Figure 4.14: NEG-pumping chamber at the end of the acceleration section with three insulated drift tubes. In the upper right corner a picture of the chamber is shown where the adapter flange is removed.

changed easily. The first four electrodes are used to build up the extraction potential $\Phi_{ext} = U_0 - U_{ext}$ from ground potential avoiding electrical breakdowns.

4.2 TSR interaction section

Technically challenging was the construction of the interaction section in the limited space of the experimental section of the storage ring, together with the goal to obtain the highest possible straight section and to minimize the relative influence of the toroid regions. The interaction section consists of three parts: two toroid sections and the interaction region between them (see the overview in Fig. 4.1). The accelerated electron beam is merged with the ion beam in the first toroid section and then moves collinear with the stored ion beam. After the interaction, the electrons are separated from the ions in a second toroid section. Because of the magnetic field in the toroid section, the ion orbit is disturbed. This has to be corrected with a pair of dipole magnets at each toroid section.

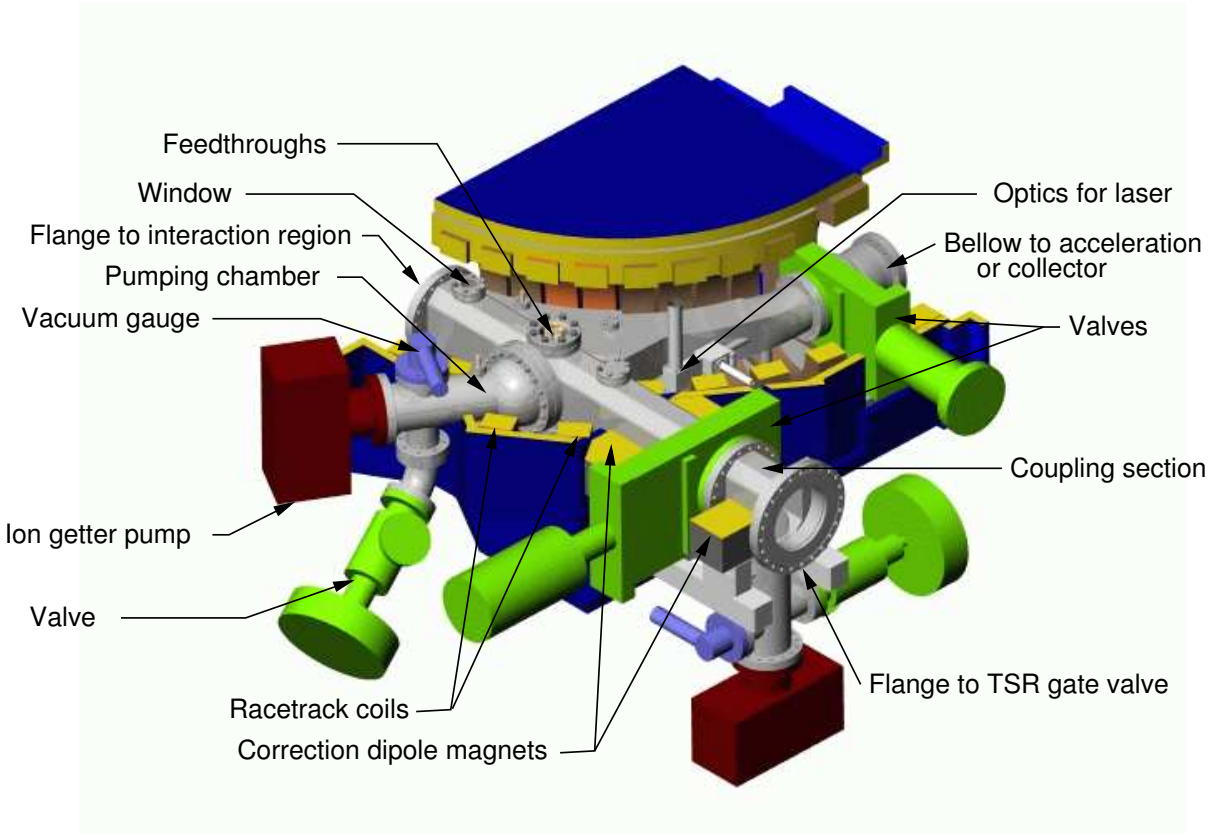

Figure 4.15: Model of the toroid section with the magnet system cut open and the most important parts.

4.2.1 Toroid sections

Vacuum and magnetic system

After the acceleration, the electrons are bent onto the ion beam trajectory in a 90° toroid with a radius of 600 mm (see Fig. 4.15). While the electrons are merged with the stored ions, there is a certain distance where the electron beam is not parallel to the ion beam. This angle leads to a shift in the collision energy between the two particle species and is seen as a broadening in the measured recombination spectra [Ken95]. In the data analysis of the recombination experiments this can be taken into account performing a deconvolution of the spectra (toroid deconvolution) with the known perturbation.
Geometrically this effect can be minimized by keeping the electron beam diameter low and by shortening the distance where angles between the two particle beams appear. This has lead to the smaller toroid radius and the bigger bending angle in the ETS compared to the TSR EC (bending radius 800 mm, angle 45°).
The magnetic field is created by single coils (see Tab. 4.2), eight smaller ones (coil type A), of which two have racetrack geometry (coil type B), allowing the passage of the ion beam, and one bigger coil (coil type C, the same as used for the collector magnetic field) which makes the magnetic connection to the acceleration solenoid and the collector

coil type	A	B	C
inner diameter [mm]	280	280	320
outer diameter [mm]	380	380	440
coil width [mm]	70	70	100
straight part [mm]	-	160	-
turns	55	65	36

Table 4.2: Toroid coils technical data. Coil type B has racetrack geometry: between the round edges of the coil a straight part of the given length is inserted.

coils respectively. This bigger coil is connected in series with the collector coils. Three-dimensional calculations are available to determine the magnetic field strength created by the applied current. For the operation of the toroid coils the following relation is used [Sch97]

$$B[\mathrm{T}] = 5.92 \cdot 10^{-4}\, I[\mathrm{A}].$$

This refers to the magnetic field along the electron trajectory in the toroid region. In Fig. 4.16 the calculated magnetic field along the ion beam axis is shown. In the smaller inset the angle between the B_x and B_z-component is shown that is needed for the toroid deconvolution. Moreover, the precise magnetic field characteristics is needed for the precise interaction length L that is used to calculate the absolute rate coefficient (eq. (3.76)). Magnetic field measurements are planned for the future.

An advantage of the single coils, compared to one closed coil, is the additional space between the coils (angle of 10°) that can be used for electrical connections, pumps and windows. One window is installed in the axis of the accelerated electron beam with subsequent laser optics for the front-side illumination of the photocathode. If the thermionic cathode is used, it can be observed through this window making, e.g. a pyrometer temperature measurement during the operation possible. On the top side of the vacuum chamber there is a window installed on both toroids for observing fluorescence light of the ion beam. Two different pumps are installed, one ion getter pump (Varian StarCell) and a pump module with NEG-stripes (pumping speed $\approx 750\,\mathrm{l/s}$ H_2).

Inner parts of the toroid vacuum chamber are shown in Fig. 4.17. For the operation of the ETS in the storage ring most important are the clearing electrodes which suppress the backstream of ions to the electron gun, making the electron beam more stable. On each toroid there is a pair of these electrodes creating an electric field in the vertical direction of the storage ring perpendicular to the electron beam. Normally only the clearing electrodes at the toroid 2 following the interaction region are used because they are also deflecting the electron beam slightly. In current density distribution measurements it has also been seen that the beam was deformed by the clearing electrodes (see section 5.1.3). Behind the toroid, the shift by the clearing electrodes can be corrected by the collector steering coils; the electron beam properties in the interaction region are not influenced.

Additional electrodes are installed in the straight section for the ion beam which can be used to locally accelerate or decelerate the ion beam. These electrodes have been installed for laser cooling experiments [Eis00]. Currently these electrodes are grounded.

The complete toroid sections are mounted on rails which allow a displacement along the ion beam axis for installation purposes (see section 4.7 for details). Gate valves at the connection to the acceleration and the collector section make a separation of the vacuum

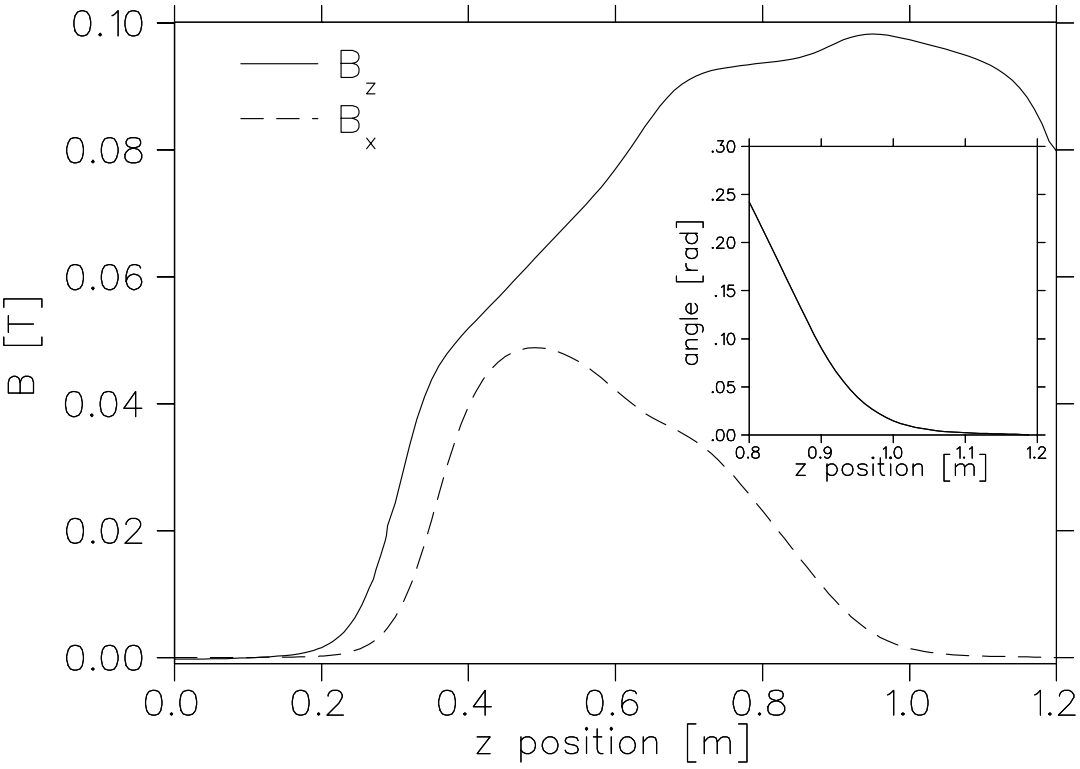

Figure 4.16: Calculated magnetic field components (B_x dashed line, B_z-component solid line) of the toroid section along the TSR ion trajectory (z-axis). The smaller inset shows the angle between B_x and B_z for the interesting region where the electron beam is merged with the ion beam. The center of the interaction region is located at $z \approx 1670\,\text{mm}$.

systems possible. This becomes especially important if one wants to exchange the acceleration section with the collector section for higher collision energies. The complete interaction section inside the TSR can then be kept under vacuum. During the bakeout of the acceleration and the collector section, the TSR can be used for beamtimes where the electron target is not needed.

	KDY1	KDY2
length [mm]	100	190
turns	24	24
yoke gap [mm]	110	110
yoke material	XC06	XC06
power supply	1000 A/24 V	1000 A/30 V

Table 4.3: Technical data and dimensions of the correction dipoles. XC06 is a high permeability steel [Sig02].

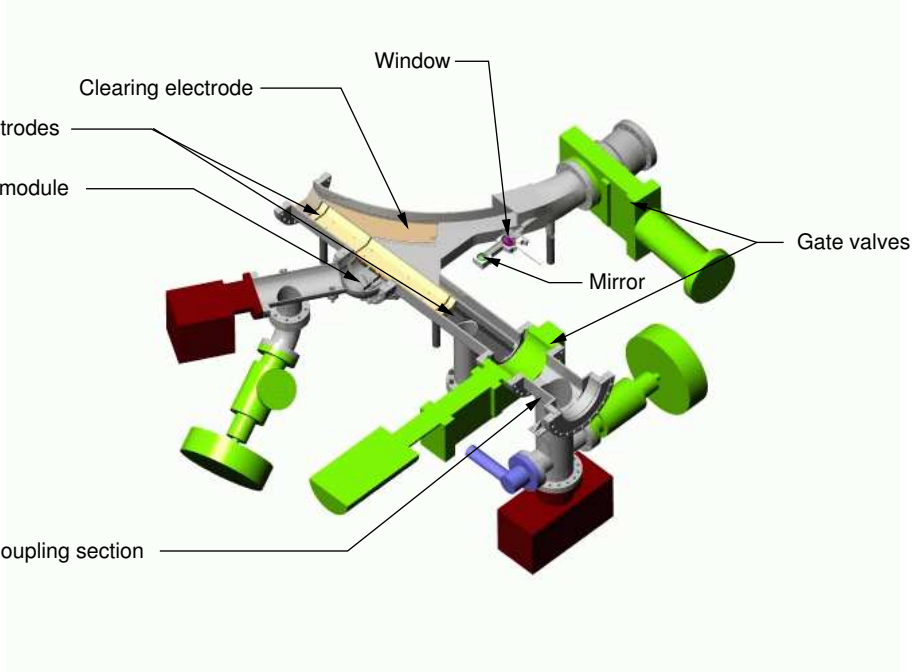

Figure 4.17: Cut through toroid vacuum chambers with the position of the installed clearing electrodes visible.

Correction dipole magnets

Because the electron target is mounted in the horizontal plane, the ion orbit perturbation by the toroid magnets is in the vertical direction. The magnetic guiding field in the toroid sections has a non zero component in the x-direction of the TSR reference frame, which leads to a deflection of the stored ions in the storage ring in the y-direction. In Fig. 4.16 the calculated x component of the magnetic flux of the first toroid section along the TSR beam axis is shown for a guiding toroid field $B_{guide} = 0.1\,\mathrm{T}$. This disturbance of the ion beam which occurs twice, at the entrance to the ETS and at the exit, can be completely compensated by two pairs of dipole magnets (position see Fig 4.1). KDY1 makes a deflection in the same direction as Toroid 1. KDY2, which is longer and creates a stronger magnetic field in the opposite direction, overcompensates the first deflection in the opposite direction. By adjusting the currents in KDY1 and KDY2, one can control the ion beam position in the y direction and the angle of the ion beam momentum to the reference orbit trajectory after the toroid sections.
Complete three dimensional simulations with the MAFIA-package[5] and one dimensional trajectory calculations for $^{12}C^{6+}$ at 73.3 MeV had to be carried out to find an optimal yoke shape for the magnets. As a basic design a C-shape was chosen. The limited space between the gate valves of the TSR, the gate valves of the ETS and the toroid sections did not allow any freedom in the choice of the yoke length. KDY1 is 100 mm long and KDY2 is 190 mm long with a cut in the y-direction to fit to the iron shielding of the toroid

[5]MAFIA 3.02, CST, Darmstadt, Germany

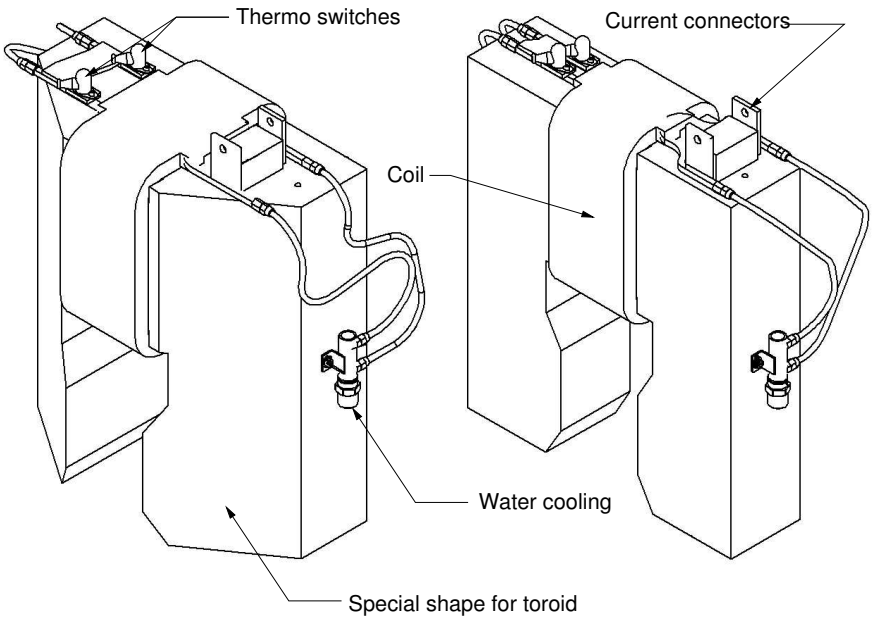

Figure 4.18: Model of the short correction dipole KDY1 (right hand side) and the long KDY2 (left hand side). The special shape of KDY 2 to fit into the toroid section can be seen.

section (see Fig. 4.18). The yoke gap is defined by the width of the vacuum chamber of 110 mm which is a compromise between a small gap needed for the reduction of magnetic stray fields and a large diameter of the beam tube. Because of the missing space between the yoke and the vacuum chamber we have to remove the correction dipole magnets for the bakeout procedure.
A critical point in the design was the distance between KDY2 and the toroid iron shielding. If the gap is too short, a big amount of the magnetic flux will go to the toroid iron and the obtained magnetic field for the ion deflection will be only small. In addition space is needed for the magnet coils. A distance of 20 mm has been found sufficiently in the trajectory calculations to compensate the deflection by the toroid section with 24000 A×turns. Tab. 4.3 summarizes the technical data and the dimensions.

Coupling sections

The connection of the ETS to the storage ring is done by two coupling sections at the toroid sections (see Fig. 4.15). On both sides gate valves are installed. This construction allows the ETS to be installed and removed from the storage ring putting to air only the short coupling sections. After installation only short sections have to be baked. An ion getter pump (Varian StarCell) and a vacuum gauge are installed. A CF 63 valve is used for the evacuation by a turbo pump. The length of the vacuum chamber exactly corresponds to the short correction dipole magnet which is put over the chamber.

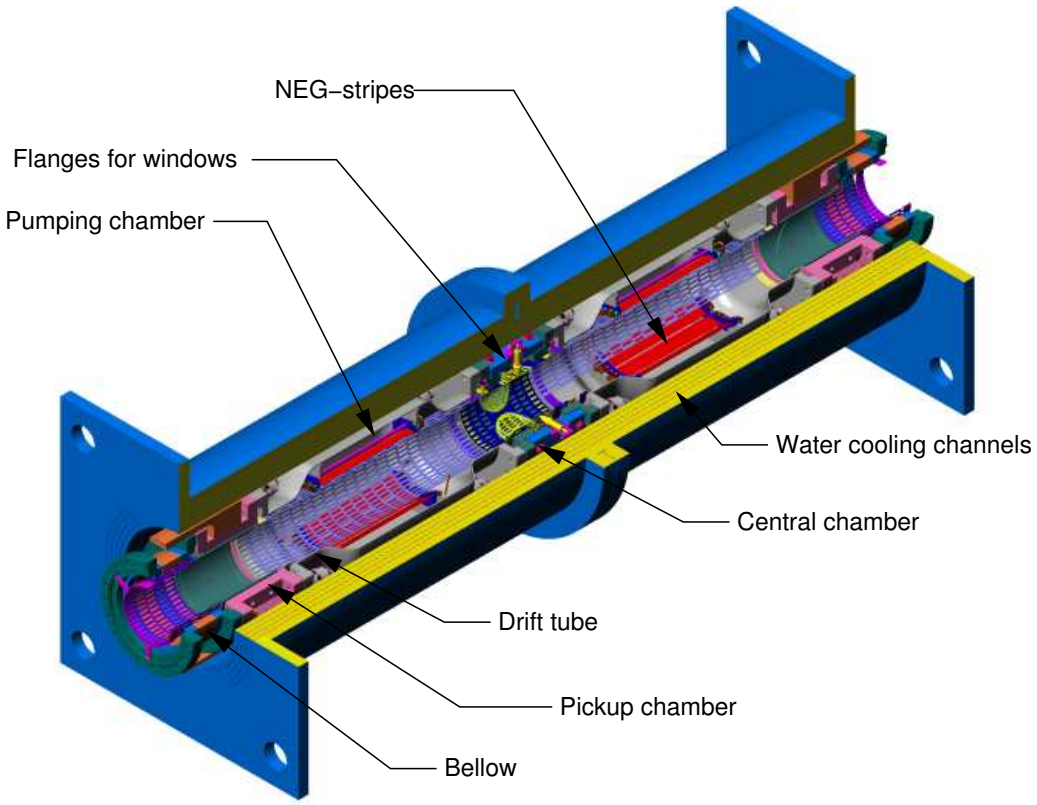

Figure 4.19: Cut through the split solenoid magnet along the ion beam axis with the vacuum chambers of the interaction region.

4.2.2 Interaction region

Requirements and design goals

The interaction region where the stored ion beam is overlapped with the electron beam is located between the two toroid sections. In the interaction region a good magnetic field homogeneity is essential for high resolution in the recombination experiments. An angle between the ion and the electron beam (as defined by the guiding field $\vec{B}$) leads to a variation of the relative energies and broadens the measured spectra. To avoid this broadening a magnetic field angular spread of $\Delta B_{\perp}/B \leq 10^{-4}$ is necessary. The specially designed solenoid magnet consists of two parts, mounted on rails which allow the magnet to be opened in the center by up to 40 mm. Detectors can then be installed into this gap in the future to detect photons from recombination events. The following section will discuss how this is achieved technically.

Split solenoid magnet

Fig. 4.19 shows the interaction region with the the split solenoid magnet. Each side has a length of 738 mm with 4 coil layers and a total number of 984 turns. The magnet

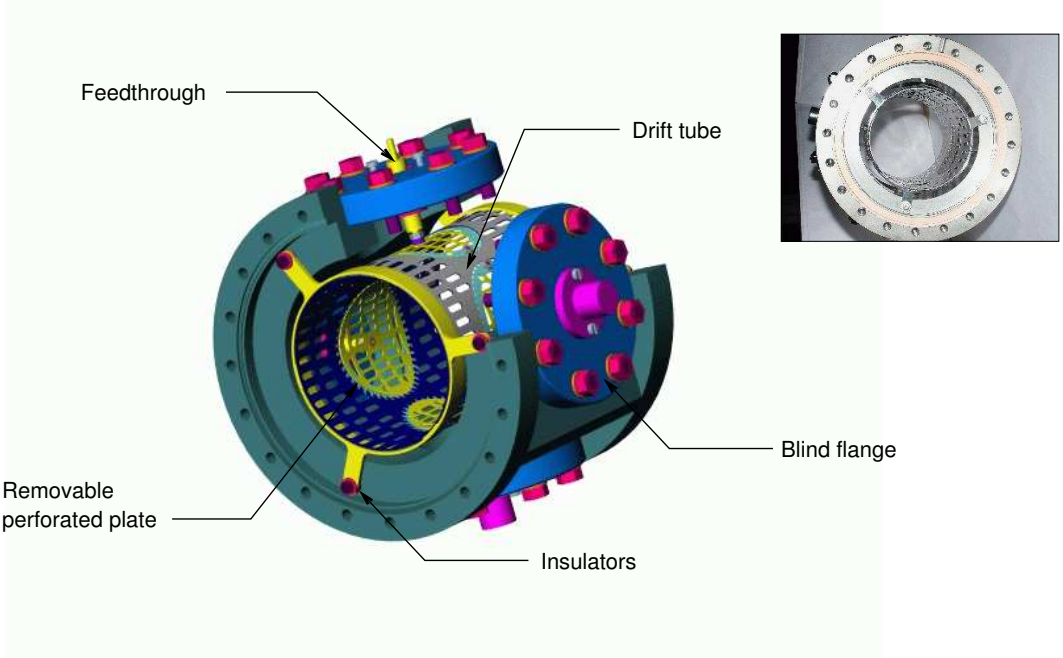

Figure 4.20: Cut through the central section of the interaction region. Four openings are available that are currently closed with blind flanges but can be replaced by windows in the future. In the upper right corner a picture of the vacuum chamber is shown.

was manufactured at our institute with special emphasis on the mechanical precision of the coil. Around the outermost layer an iron tube for the magnetic flux redirection is installed. At one end there is a flange where both magnets can be connected with screws. This is necessary because only one of the two magnets is fixed rigidly to the carriages on the rails. The other one is mounted on springs which only support the magnet and allow it to define the position by the rigidly fixed magnet without tensions between the magnets. If the two magnets are used with a gap in between, iron blocks have to be installed to hold the magnets in the desired distance.
As the winding density $N/L = 984/0.738 = 1333\,1/\mathrm{m}$ is known with high accuracy the field strength in the solenoid can be calculated relative precisely form the formula for a long solenoid $B = \mu_0 \frac{N}{L} I$ to

$$B[\mathrm{T}] = 1.68 \cdot 10^{-3}\, I[\mathrm{A}].$$

Vacuum chambers

As shown in Fig. 4.19 the vacuum system consists of two pickup chambers, two pumping sections and a central section. The central section (see Fig. 4.20) has four CF63 flanges perpendicular to the beam axis which can be equipped with windows for photon detectors as discussed above. Presently the chamber is closed with flanges that hold perforated plates connected to electrical feedthroughs; these plates close the drift tube installed in the vacuum chamber allow it to set the drift tube on a desired potential.
The two pumping sections (see Fig. 4.21) hold NEG-stripes with a pumping speed of

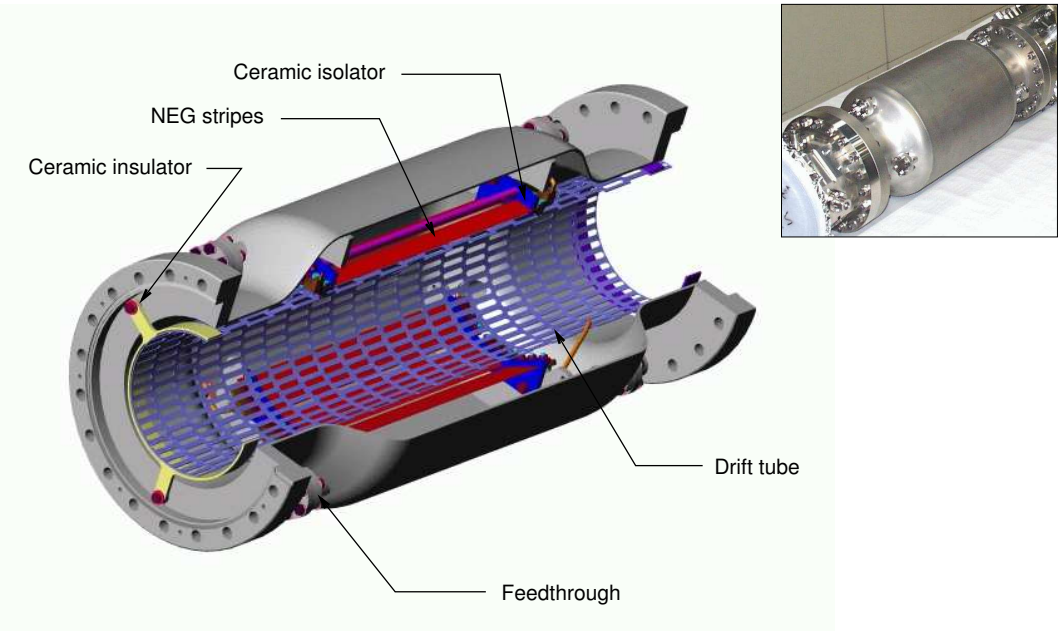

Figure 4.21: Cut through the pumping chamber in the interaction region. Two NEG-pumping modules are installed. In the upper right corner a picture of the vacuum chamber is shown.

approx. 300 l/s H_2 in each chamber. Drift tubes are installed in these chambers, too, which can be put onto potential to locally change the electron energy.
Important for the operation in the storage ring are the Pickup chambers (Fig. 4.22) which monitor the beam position (electron beam and ion beam) in x- and y-direction by electrostatic pickup signals.

Position pickup electrodes

The electrostatic pickup consists basically of two electrically insulated electrodes. If an charge Q is placed between the electrodes it will create charges Q_1 and Q_2 by electrostatic induction on the surfaces where the relation between them depends on the position of the charge. This relation can be used to determine the position of the stored ion beam.
By choosing a hollow tube with a radius R_0 in the x-y-plane and the axis along the z-axis which is cut along the diagonal of the projection of the tube to the x-z-plane into two electrodes one can achieve the following linearity equations [Sik99] :

$$Q_1 + Q_2 \qquad = Q \tag{4.4}$$

$$Q_1 - Q_2 \qquad \propto x\text{-position of } Q \tag{4.5}$$

$$Q_1 - Q_2 \quad \text{independent on } y\text{-position of } Q \tag{4.6}$$

Using a second set of electrodes which is rotated by 90° one gets the y-position of the charge. Calculating the relation of the difference $\Delta Q_k = Q_1 - Q_2$ and the sum of the charges $\sum Q_k = Q_1 + Q_2$ where $k = x, y$, one gets equations which are independent on

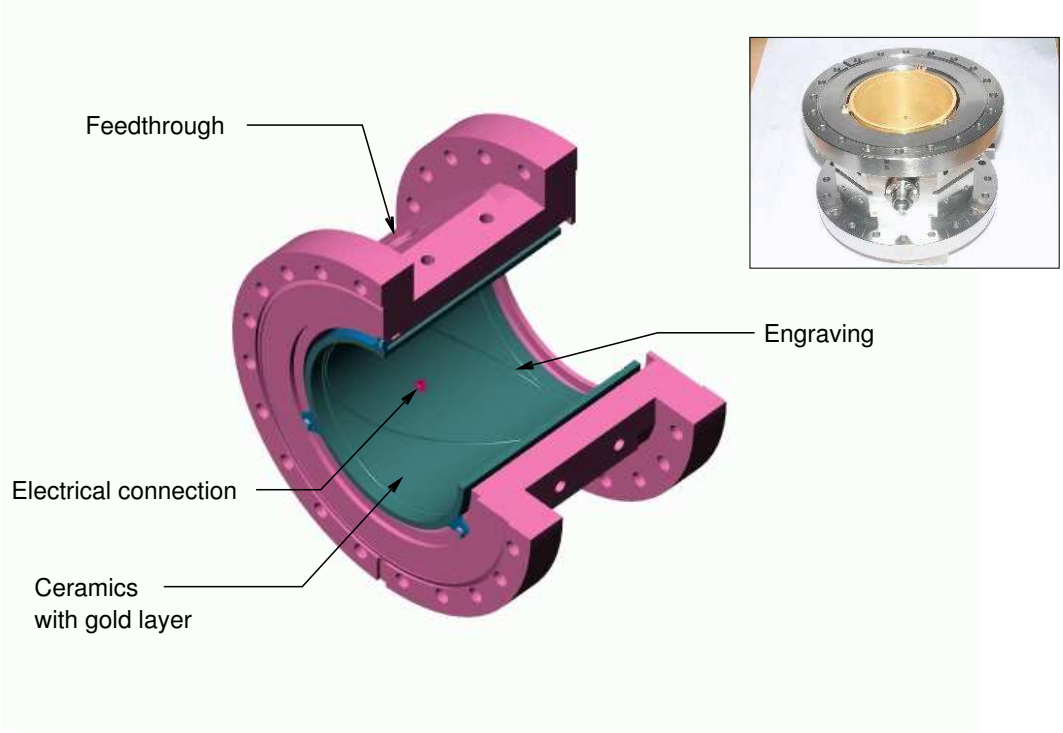

Figure 4.22: Cut through the pickup chamber in the interaction region. The segmented electrode engraved into the gold layer is visible. In the upper right corner a picture of the vacuum chamber is shown.

the charge in the pickup tube which then are also independent on the beam intensity:

$$\frac{\Delta Q_k}{\sum Q_k} = \frac{k_0}{R_0}. \tag{4.7}$$

Fig. 4.23 shows the equivalent circuit diagram of one electrode pair. R is the input resistance of the amplifier, C_e the capacity to ground and C_d the coupling capacity between the two electrodes. Technically one measures the voltages U_1 and U_2 and not the charges which is possible if the impedances of the electrodes to ground are all the same. C_e causes an additional voltage drop which changes the linearity in 4.7 to

$$k_0 = s_k \frac{\Delta U_k}{\sum U_k}, \tag{4.8}$$

where s_i is a calibration constant which has to be determined experimentally (see below). The pickup electrodes installed in the ETS [Sik99] are a further development of the basic principle described above which is realized and used in the TSR. One pair of electrodes for one direction (e.g. the $x-$direction) is partitioned by a second diagonal cut which is rotated about 90° around the beam axis into 6 electrodes. Fig. 4.24 shows the unwind pickup electrode with the two cuts. Combining the areas that are needed for one coordinate, allows us to measure the x and $y-$coordinate simultaneously on the half of

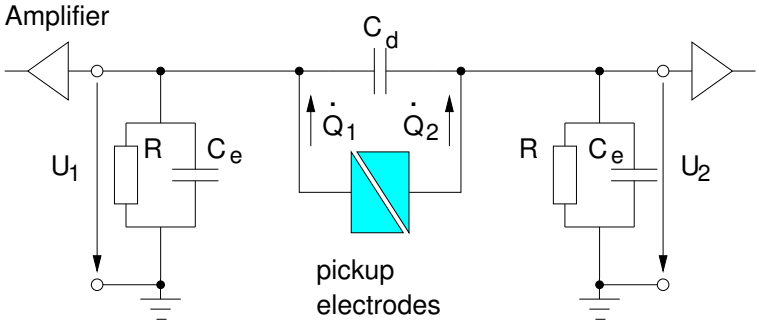

Figure 4.23: Principle electric circuit of the pickup electrodes with the current measurement and the amplifiers.

the distance which saves space in the TSR that is used for pumping sections. The small areas no. 5 and 6 belong to the electrodes no. 3 and 1, respectively, which is realized by keeping a small edge to directly connect them. Applying eq. (4.8) to the given electrode numbering gives:

$$x_0 = s_x \frac{(U_2 + U_3) - (U_1 + U_4)}{U_1 + U_2 + U_3 + U_4} = s_x \frac{\Delta U_x}{\sum U} \tag{4.9}$$

$$y_0 = s_y \frac{(U_1 + U_2) - (U_3 + U_4)}{U_1 + U_2 + U_3 + U_4} = s_y \frac{\Delta U_y}{\sum U} \tag{4.10}$$

A readout electronics does the necessary summations and subtractions of the pickup voltages. The output signals are amplified by 60 dB (factor 1000). The signals can then be displayed with an oscilloscope or processed by the existing TSR pickup electronic [Alb93]. Mechanically the electrodes are realized on a ceramic tube (Al_2O_3, length 120 mm, inner diameter 100 mm, outer diameter 108 mm) that is covered on its inside with a thin layer of molybdenum by engraving the electrode shape into the surface. Four symmetric holes, that are insulated from the outside surface by removed molybdenum around the holes, are used to connect the feedthroughs to the inner electrodes. A titanium ring is soldered to the outside surface. It is used to attach the pickup construction to the vacuum chamber and make the electrical connection of the outside to ground potential. Finally everything was coated with a thin layer (some μm) of gold to improve the electrical conductivity.

Pickup electrodes calibration

Before the installation of the pickup electrodes they have been calibrated using a wire to simulate the electron or the ion beam (for details about the method see [Sik99]). With a frequency generator a sinusoidal voltage has been induced in the wire with two different frequencies $f = 10$ kHz and 3 MHz. The wire was moved parallel along the x and y-axis inside the electrode and the sum and difference signals were monitored on an oscilloscope or a vector voltmeter (VM). The calculated calibration factors are summarized in Tab. 4.4.

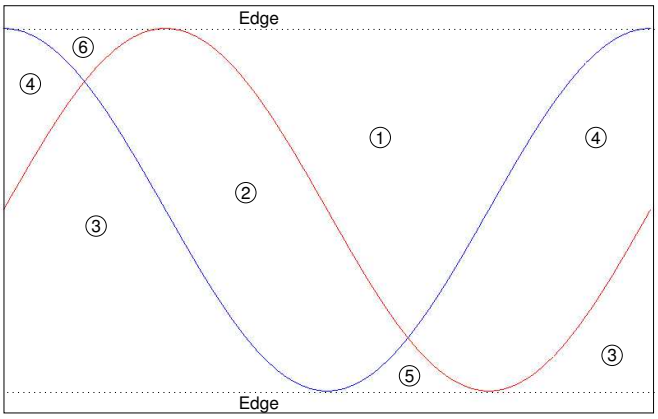

Figure 4.24: Pickup electrode surface with the six areas created by the engraving.

		oscilloscope		VM	
Pickup	f	s_x [mm]	s_y [mm]	s_x [mm]	s_y [mm]
1	10 kHz	50.9	50.0	-	-
1	3 MHz	53.6	-	54.4	53.9
2	10 kHz	50.4	49.0	-	-
2	3 MHz	50.4	49.0	54.5	53.9

Table 4.4: Calibration factors for the position pickup electrodes.

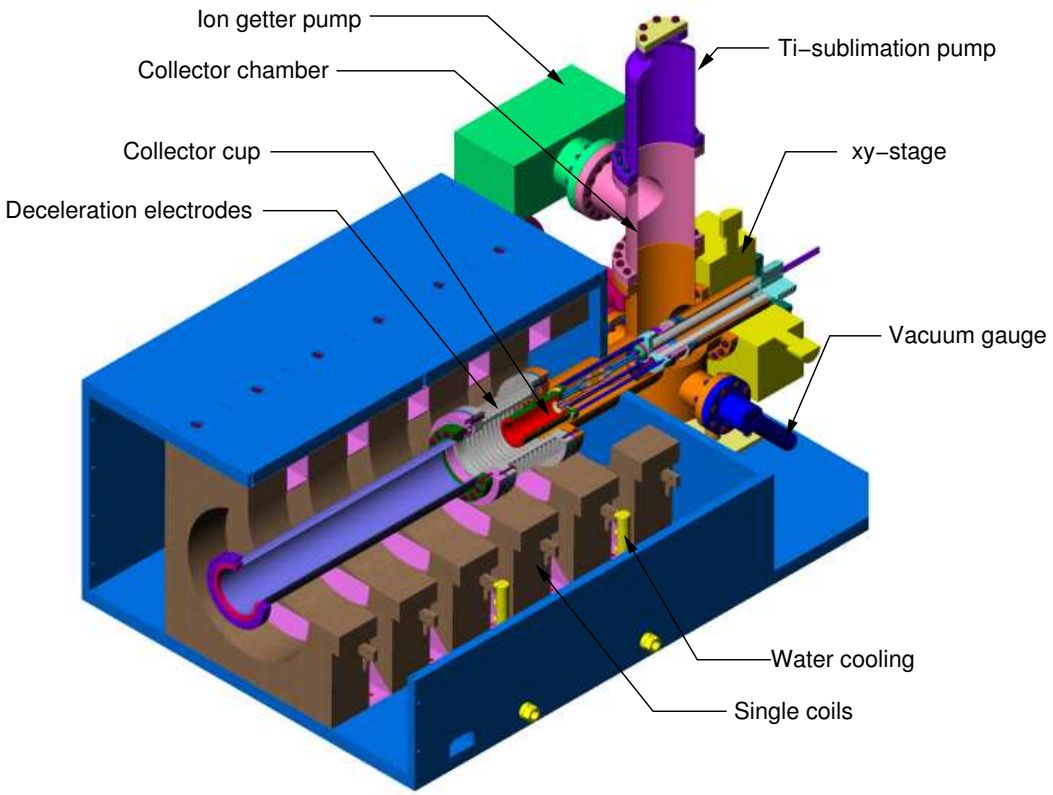

Figure 4.25: Model of the collector section with a cut along the electron beam axis.

4.3 Collector section

The electron collector is the anode for the electron beam where the free electrons are transferred back to the metal. A good efficiency of the collector is necessary to minimize loss currents, and in the design care has to be taken to reduce secondary electron or ion emission processes. The electron energy results mainly in a heating of the collector material, only a small amount of energy is converted into bremsstrahlung. The electron power that has to be dissipated depends on the electron current and on the potential difference between the cathode and the anode. Thus, the electron power can be reduced by decelerating the electron beam in front of the collector. In the ETS the maximal electron current is 170 mA and the maximum potential difference is 3.5 keV which gives a maximum power of 595 W that has to be taken away by water cooling. Another problem with the electron power is related to the small size of the electron beam which leads to a rather high power density. The power density can be decreased by expanding the electron beam and distributing the power over a larger surface.
Fig. 4.25 shows the main components of the collector section. The collector cup is installed at the end of a long collector arm (see Fig. 4.26) and positioned into the magnetic field created by six single coils (coil type C, see Tab. 4.2). The collector arm is connected to a xy-stage that can be two-dimensionally positioned by two stepping motors. The xy-stage

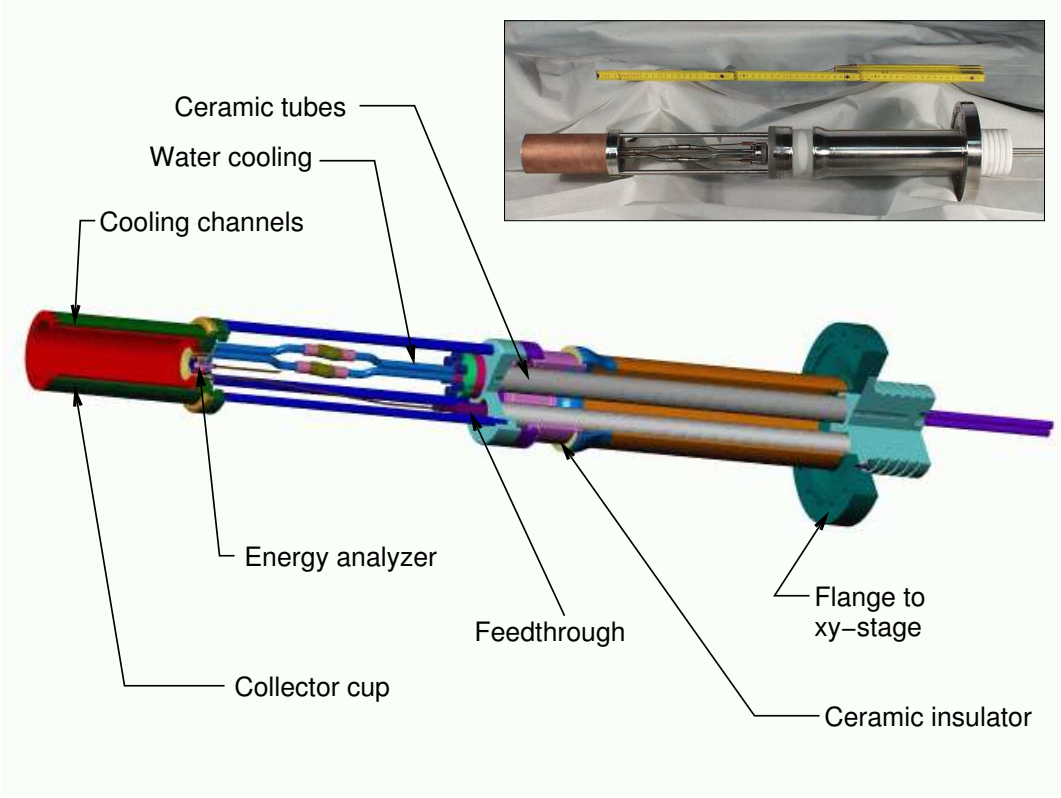

Figure 4.26: Electron collector arm with a cut along the electron beam axis. In the upper right corner a picture of the collector arm is shown.

is connected to the collector chamber where an ion getter pump and a Ti-sublimation pump similar to the gun chamber (see section 4.1.1), together with a valve and a vacuum gauge are installed. In front of the collector cup eleven electrodes are available for the electron beam deceleration. Fig. 4.27 (b) shows the electrical connections of the electrodes to a voltage divider. The electrodes are symmetrically connected where the inner two electrodes are on the same potential as the collector cup.
In the *collector mode* the electron beam is expanded in front of the collector cup (shown in a magnified drawing of the collector cup region in Fig. 4.27 (a)). The polarity of the last two coils is reversed which leads to a magnetic cusp field distributing the electrons over a large area of the cup. In Fig. 4.26 the collector cup is shown with a cut along the z-axis where the water cooling channels are visible. The water circulating in the cooling channels is provided by a dedicated closed cooling circuit. The water is circulating in a heat exchanger with installed ion filters to reduce the conductivity of the water avoiding a strong potential drop over the cooling water.

Energy analyzer

An retarding field energy analyzer, installed at the back of the collector cup in the collector arm (see Fig. 4.27 (a) and 4.26), allows us to measure electron energy distributions

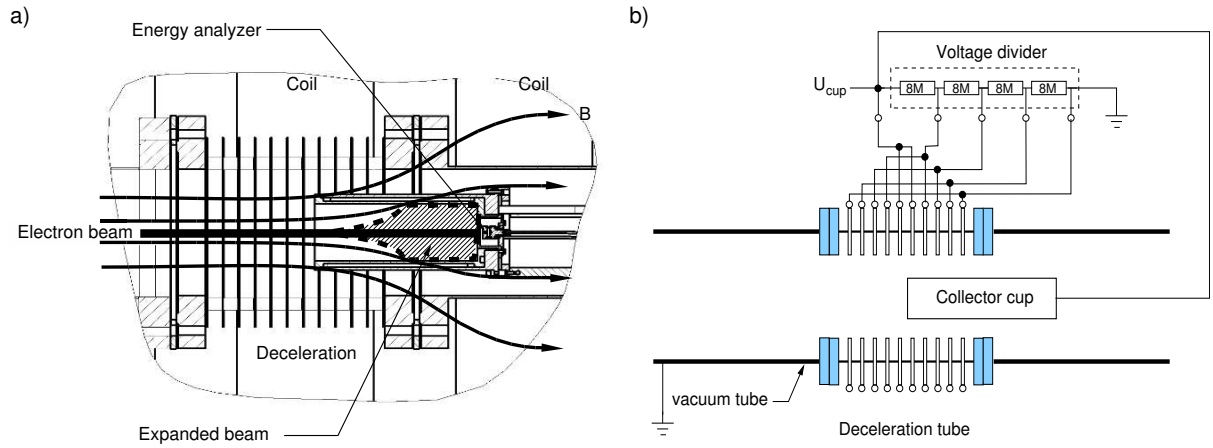

Figure 4.27: a) Expansion of the electron beam in the collector cup by reversal of the polarity of the last two coils. b) Connection of the voltage divider to the deceleration electrodes.

(*analyzer mode*). The retarding field energy analyzer principle is shown in Fig. 4.28. Most of the incoming beam is blocked by the entering aperture and only a small portion reaches the blocking electrode. By changing the potential at the blocking electrode and measuring the current which reaches the collector one gets an integral energy distribution (see section 5.2.1). The entering diaphragm consists of a thin gold foil (0.5 μm) on a molybdenum carrier (diameter 3.02 mm, thickness 0.2 mm) with an opening diameter of 50 μm.

Two different designs for the energy analyzer have been realized and used in measurements. Fig. 4.29 and 4.30 show the two different versions. Version 1 has a short blocking electrode (length $l = 1.1$ mm) with a big opening (diameter $d = 3$ mm). The ceramics used for insulation and mounting are relatively close to the beam without any electric shielding. Blocking electrode and collector are made of titanium. This version has been used for most of the measurements presented in chapter 5. Version 2 has a longer blocking electrode (length $l = 3.5$ mm) with a smaller opening (diameter $d = 1.5$ mm). Here the ceramic balls between the blocking electrode and the collector have been moved backwards and shielded by the surrounding metal surfaces. Additionally the ceramics plate between the entering diaphragm and the blocking electrode has been replaced by an insulator behind the base plate. The material has been changed to molybdenum because of the better thermal properties. All edges have been rounded and a minimum distance

Version	material	l [mm]	d [mm]	a
1	titanium	1.1	3	2.9
2	molybdenum	3.5	1.5	2

Table 4.5: Analyzer dimensions l blocking electrode length, d blocking electrode opening, a distance between entering aperture and blocking electrode.

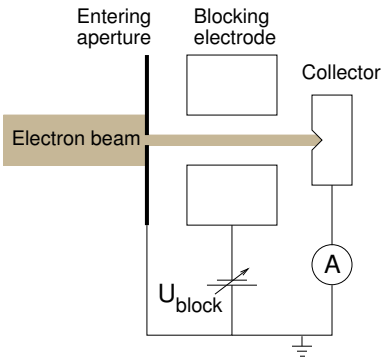

Figure 4.28: Retarding field energy analyzer: most of the incoming beam is block at the entering aperture. Depending on the potential at the blocking electrode, a certain current is reaching the analyzer electrode that is measured.

of 2 mm is assured between all parts on different potentials. Table 4.5 summarizes the dimensions.
The design of the second version has become necessary because of some problems with version 1 during the preparatory measurements. Because of the large value for d and the small value for l the potential that the electrons in the center see is always smaller than the applied value. This has several disadvantages as we will show in the following. Normally the blocking electrode is connected to the cathode potential U_0 which would then block all the electrons if the electron energy distribution was very small and the work functions of the used materials were all the same. In reality this is not the case and one also wants to vary the blocking potential to scan the electron energy distribution. This is accomplished by a voltage U_{block} on the HV platform. The electrostatic potential in the analyzer has been calculated with the MAFIA software package for the old and the new analyzer design. Fig. 4.31 shows two-dimensional potential distributions for $U_0 = 2\,\mathrm{kV}$ and $U_{cup} = 0\,\mathrm{V}$ for the two analyzer versions. In Fig. 4.32 the potential on the electron beam axis is shown for different cup potentials. U_{cup} changes the potential ratio between the blocking electrode which was kept on the cathode potential and the entering aperture in the back of the collector cup. This modifies the depth of the potential minimum U_{min} and the shape of the potential. The new analyzer shows only a very small dependence on U_{min} from U_{cup}; U_{min} is always close to U_0.
As one can see from Fig. 4.32 (a) the potential difference $\Delta U_{block} = U_0 - U_{min}$ can become several hundreds of volts for $U_0 = 2\,\mathrm{kV}$, whereas the energy spread of the EDC which has to be scanned is in the range of only one volt. It is difficult to produce this voltages with a high stability. For a power supply with a maximal voltage of 1000 V and a stability of $1 \cdot 10^{-4}$ the noise is 100 mV while for a maximum voltage of 100 V and the same stability the noise is only 10 mV.
The width of the measured EDCs has to be scaled because of a relation

$$\Delta U_{EDC} = c \cdot \Delta U_{block}$$

with $c \leq 1$, where U_{EDC} is the voltage that the electrons "see". c has to be calculated which increases the uncertainty of the results. For details about the determination of c see section 5.2.2.
Furthermore there were indications that the ceramics tend to charge up and disturb the electron beam. A strong shift of the mean longitudinal energy was observed during the

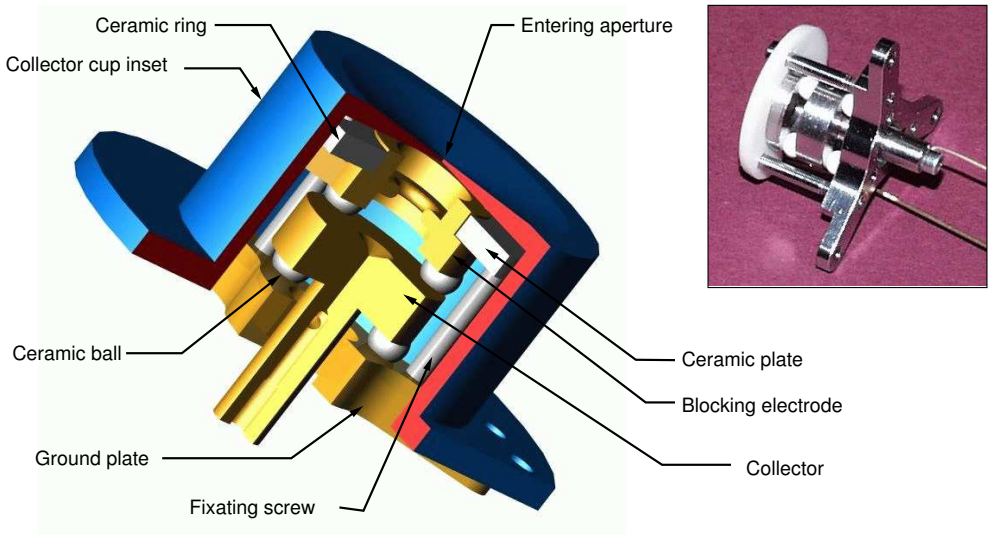

Figure 4.29: Energy analyzer version 1: cut along the electron beam axis. In the upper right corner a picture of the analyzer without the collector cup inset is shown.

measurements (see section 5.2.2). This effects should be reduced by shielding the ceramics with the surrounding electrodes. With the new analyzer version 2 (see Fig. 4.30) the problems could be solved. Another problem was an electrical breakdown in version 1 at a voltage $U_0 \approx 3.5\,\mathrm{keV}$.

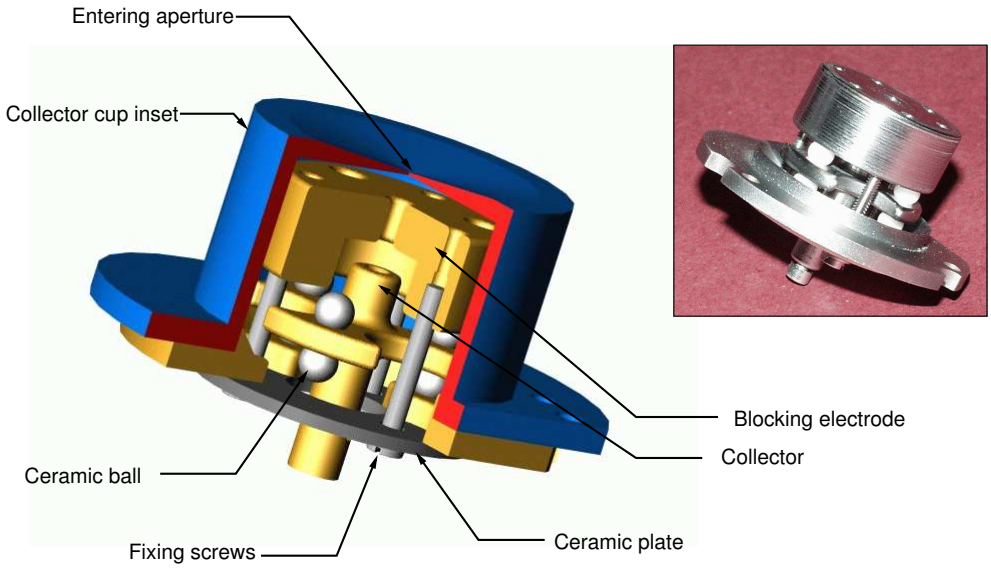

Figure 4.30: Energy analyzer version 2: cut along the electron beam axis. In the upper right corner a picture of the analyzer without the collector cup inset is shown.

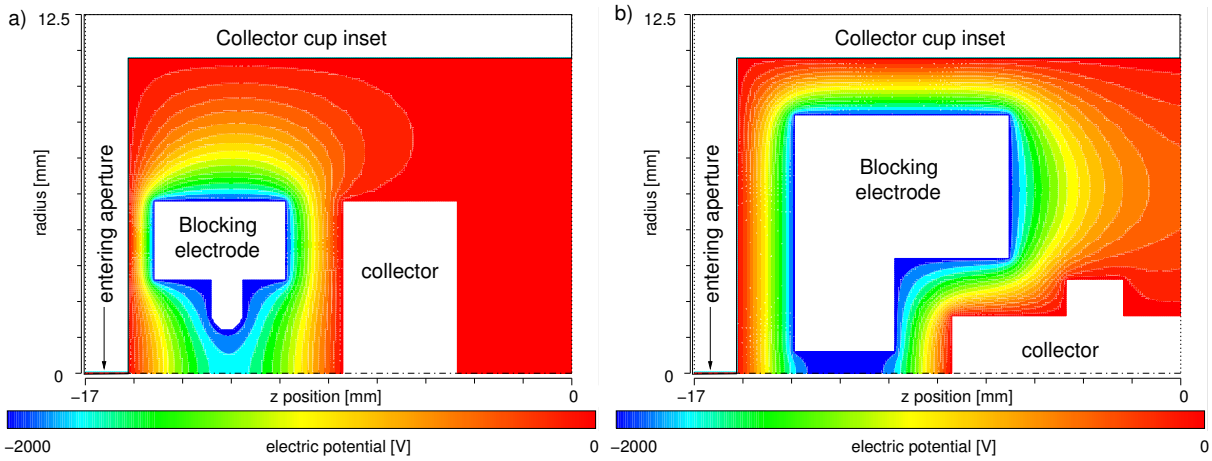

Figure 4.31: Calculated electric potential distribution for the two versions of the energy analyzer in a plane parallel to the electron beam: a) analyzer version 1 and b) analyzer version 2. The potential of the blocking electrode was set to $U_{Block} = 2000\,\mathrm{V}$ and the collector cup was on $U_{cup} = 0\,\mathrm{V}$.

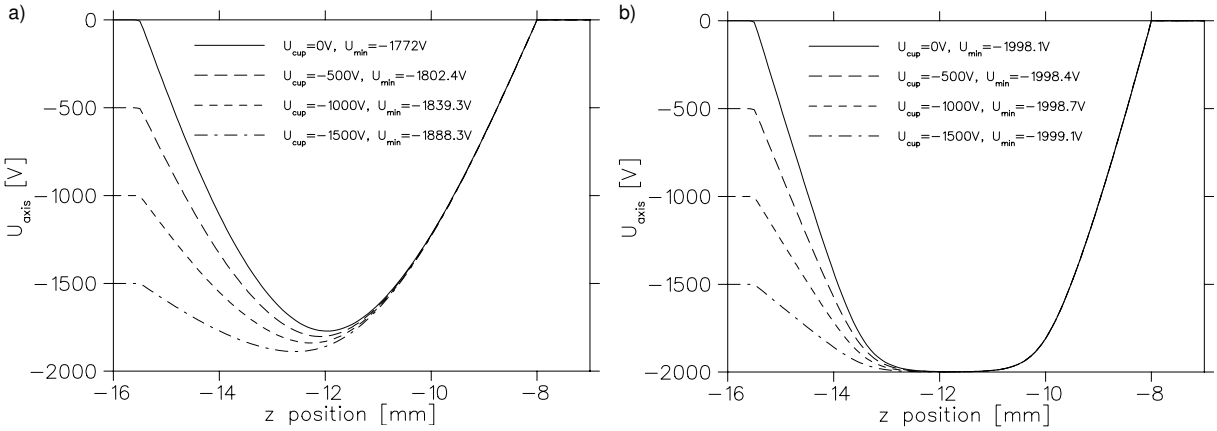

Figure 4.32: Calculated electric potential on the electron beam axis for the two versions of the energy analyzer: a) analyzer version 1 and b) analyzer version 2. The blocking electrode was set to $U_{Block} = 2000\,\mathrm{V}$ and the collector cup was set on different potentials as indicated in the graphs. The minima of the calculated potentials are also plotted in the graphs.

4.4 Electronics

An overview of the main electric circuit of the ETS is given in Fig. 4.33. All power supplies for manipulating the electron beam are placed on a HV-platform and are powered by an insulation transformer (insulation voltage 35 kV). The potential of the platform is defined by the main power supply which produces the cathode voltage U_0; an offset of ΔU for collision experiments is is performed by an additional power supply (1000 V/40 mA). Exceptionally a capacitor (up to 2 μF have been used) has been installed between ground and platform potential to stabilize U_0. This became necessary for initial experiments with the pulsed electron beam because the voltage of the main power supply did not stay stable. It is not used normally. An operation of the ETS with such big capacities is rather dangerous. A big amount of energy is stored in the system which discharges relative slowly; electric devices can be destroyed and it is dangerous for the experimentalist.
Signals to the HV-platform are transmitted via the digital control system (see section 4.5) and in some cases with optical fibers. A voltage to frequency converter (V/F) translates the voltage signals into frequencies which then are transmitted to the platform and converted back (F/V) to a voltage signal. Important for the operation is the fast extraction switch which can switch the electron beam on and off. For switching the beam off, the extraction potential is put to cathode potential, allowing no electrons to leave the electron gun. For the pulsing of the electron beam there is a pulser, where the pulse length and the repetition rate can be set.
The electron current is driven by the collector power supply (3.5 kV/200 mA) which reduces the required power because the electron current stays on the platform. Although the electrons see ground potential after their acceleration, the power that has to be provided is only the potential difference between cathode and anode. This allows the usage of a relatively small main power supply for the platform potential (10 kV, 2 mA). The main power supply has to provide only the loss current which is normally small (below 1%) and the current for the voltage dividers ($\approx 30\,\mu$A at 2 kV). The loss current is measured by the voltage drop at a resistor (470 Ω) and is a sensitive device for optimizing the electron current.
In Fig. 4.34 the circuit for the HV-switch is shown. The HV switch is designed for switching high voltages on the ns time scale. Switching high voltages at high frequencies requires a careful adjustment of the RC-components of the electric circuit avoiding oscillations and long raise times. We want to switch up to 2 kV on the ms time scale which requires raise times in the μs range. Results of the switching behavior are shown in Fig. 4.35 measured with a HV-probe. As one can see the raise time of the switch is sufficiently small for our demands and there is no oscillation visible.
Important for the safety of the electrical circuit is the interlock system which shuts down the dangerous voltages if HV-devices are opened accidentally or in case of emergency. Interlock switches are installed at the access to the HV-platform, the back of the electron gun and the collector arm where the cathode and the collector cup potentials, resp., are applied, at the voltage divider for the acceleration section and the heat exchanger for the collector cooling. If one of the switches is open then the main power supply for U_0 is switched off, together with the drift, extraction and cup voltage. The collector water cooling can be bypassed for electron beams with low current and energy.

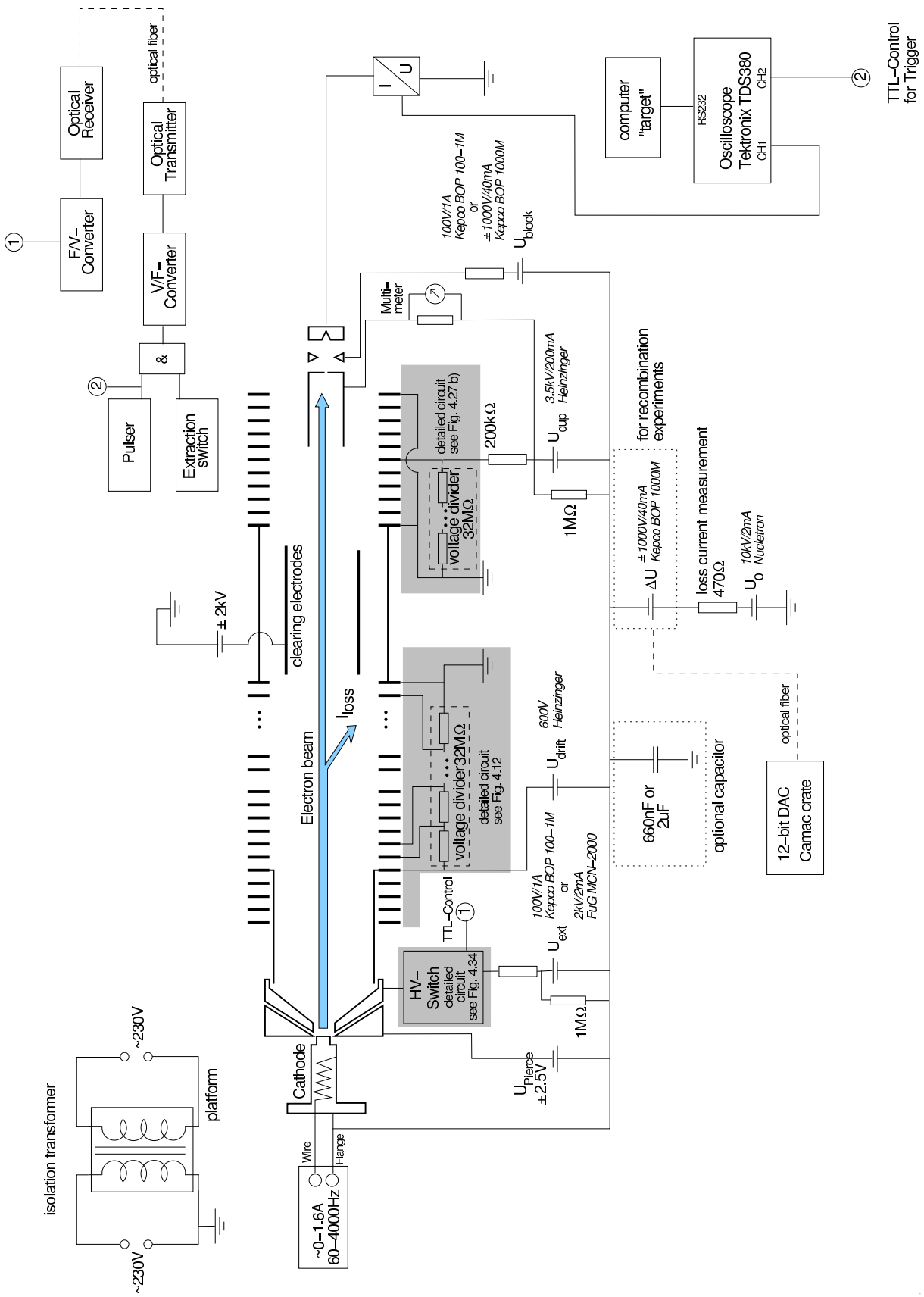

Figure 4.33: ETS electronics: schematic overview.

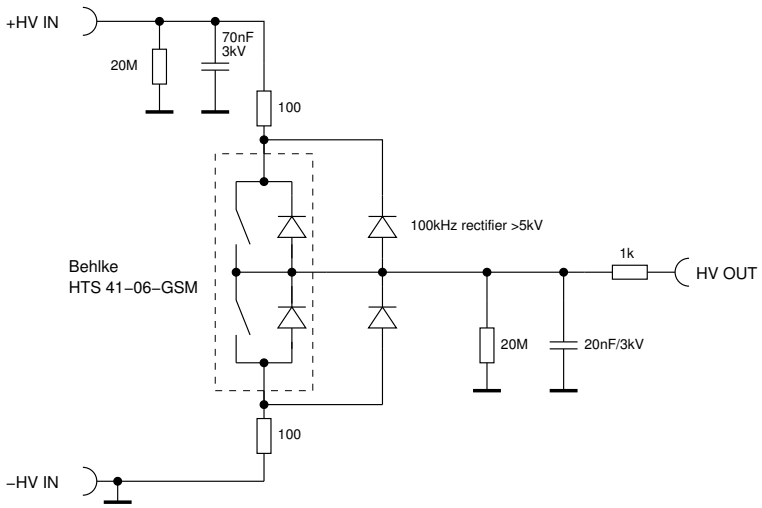

Figure 4.34: Circuit for the fast HV-switch used for switching the extraction voltage on and off.

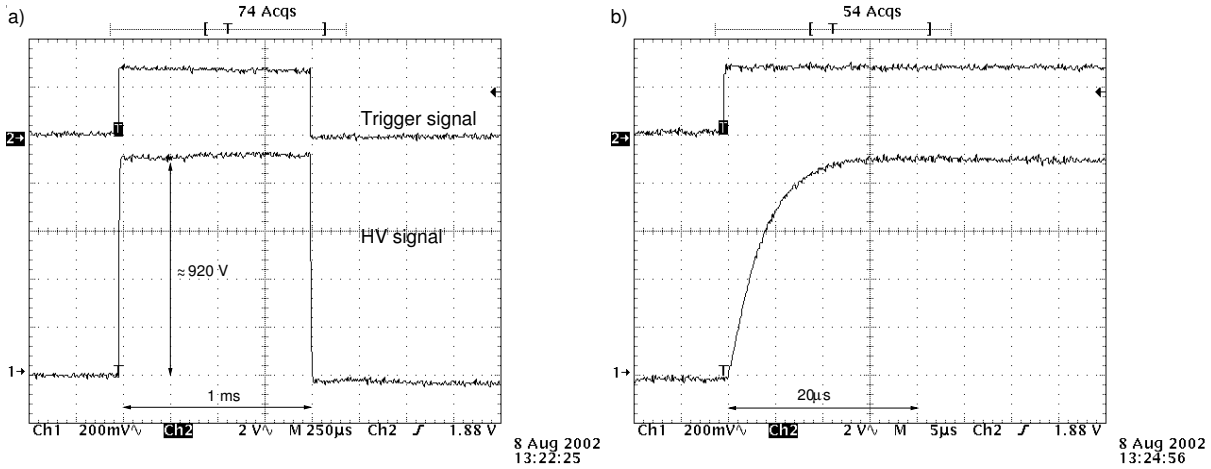

Figure 4.35: Oscilloscope pictures of the switching behavior of the HV-Switch obtained with a HV probe. a) total pulse of 1 ms length. b) magnified region of the raising signal.

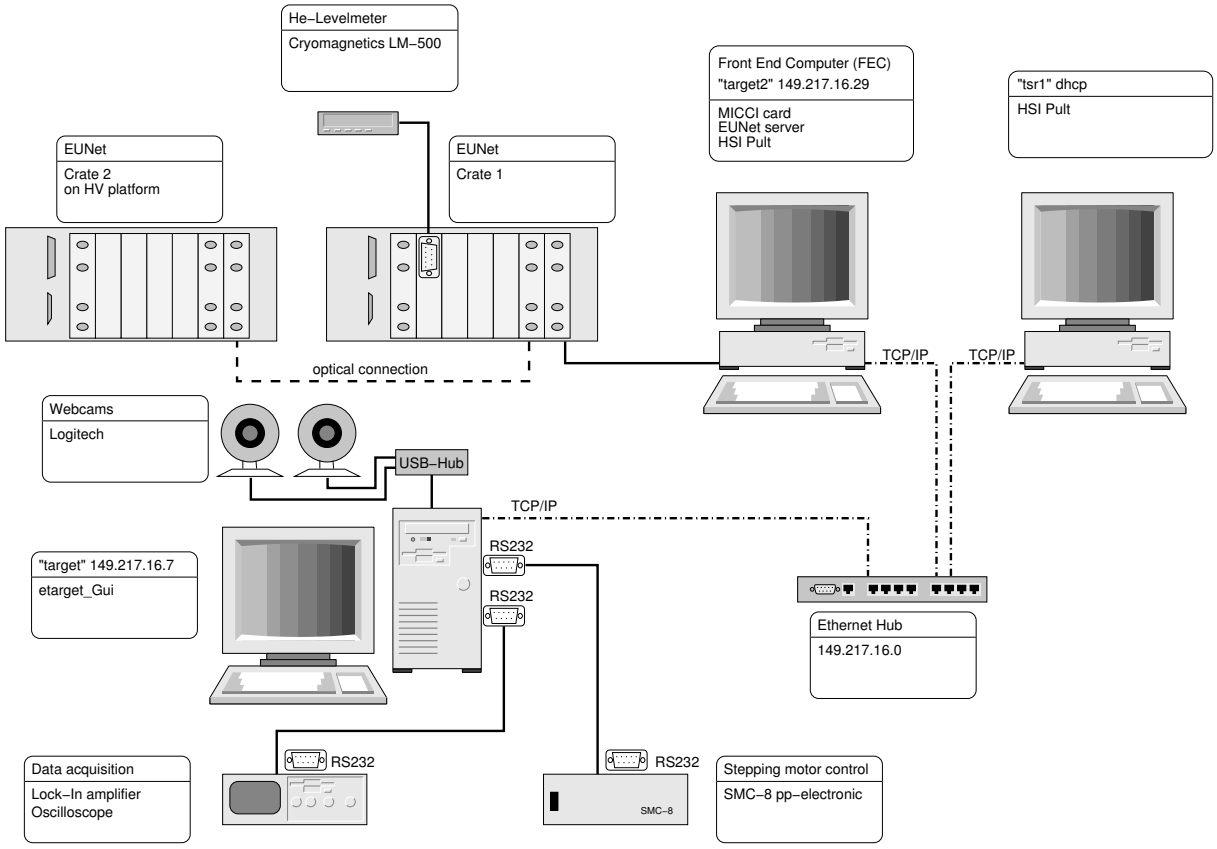

Figure 4.36: ETS control system: Data acquisition for electron beam diagnostics and EUNet control system.

4.5 Control system

Most of the used devices are connected to the EUNet control system which has been developed at our institute for controlling the accelerator and storage ring facilities. EUNet consists of a front end computer (FEC) with a dedicated PCI card which is connected to an electronics crate with an EUNet CPU and a data bus inside. Different I/O-cards are available for the system. EUNet can be easily expanded because several crates can be connected in series.
A server software ("EUNet server") is running on the FEC (operating system Microsoft Windows NT4.0) which can be reached via network by a TCP/IP connection. The EUNet server is the interface between the network and the electronics. The commands sent to the EUNet server are translated into commands for the EUNet CPU which controls the I/O cards. Results of the I/O operations are distributed by the EUNet server over the network. This makes it possible that the system can be controlled by any computer in the intranet or in the Internet (access restricted by the server). Several computers can be connected to the EUNet server at the same time.
The control system of the ETS is shown schematically in Fig. 4.36. We are using two

crates, one on ground potential and one on the HV-platform (see Fig. 4.33 for details). The crates are interconnected over an optical transceiver. Installed in the crates are several I/O cards: 12 and 16 bit DACs and ADCs (unipolar and bipolar), digital I/O-cards and a RS232 card (for the Helium-Levelmeter of the SCM).
The FEC (hostname "*target2.mpi-hd.mpg.de*") with the EUNet server is connected to the institute network. A control software ("HSI Pult"[6]) running on this computer with a graphical user interface and four control buttons. The control buttons can be linked to the connected devices to manually set and adjust the device parameters. This forms the "basic" control system located close to the ETS.
A second computer (hostname "*tsr1.mpi-hd.mpg*", Microsoft Windows 2000) also equipped with the HSI-Pult-program and eight control buttons is situated at the control desk of the TSR. Over the TCP/IP institute network this computer is connected to the the FEC and the EUNet server software. This is the control system used during beam times.
An additional computer (hostname "*target.mpi-hd.mpg.de*", running under Linux) is connected to the FEC via network. This computer is mainly used for measurements without the storage ring and for flexible tasks which can be easily realized with Open Source programming tools. A C++ class has been developed for the communication with the EUNet server, allowing an easy data transfer to the connected devices. A graphical user interface ("etarget_Gui"[7]) has been developed for EDC and current density distribution measurements. Over the RS232 serial ports an oscilloscope or Lock-In amplifier and the stepping motor control for the xy-stage (see section 4.3) are connected. Thus, the software combines data acquisition, data visualization and online data analysis.
At the USB port of *target* a USB-Hub is available for the connection of several CCD-cameras ("Webcams"). These cameras can be used to survey devices that have no read out possibility. Especially the cameras are used to monitor the position of the collector cup which is visible at micrometer screws at the xy-stage.

4.6 Ion detector setup

For the installation of the required detectors for the charge-changed and fragmented particles a new vacuum chamber has been installed in the first TSR dipole magnet behind the ETS interaction section and new detectors have been developed [Wis03]. The goal of the new design was to make as many as possible charge-to-mass states accessible by the detectors. Especially the light and weakly charged fragments or charge-changed products of molecular ions are strongly deflected in the dipole magnet leading to trajectories that are difficult to access. In the EC detector setup there are no detectors available for them. In Fig. 4.37 the vacuum chamber with the position of the dipole magnet together with several ion trajectories and the possible detector positions are shown. There are three different detection schemes present: (i) detector for charge-changed atomic ions (periscope detector), (ii) detector for molecular fragments (for positive and negative molecules) and (iii) neutral fragments extended beamline for imaging experiments. The detectors are

[6]Developed for the HochStromInjektor (HSI, High Current Injector) part of the accelerator facilities at our institute
[7]Developed under the CERN ROOT library [ROO]

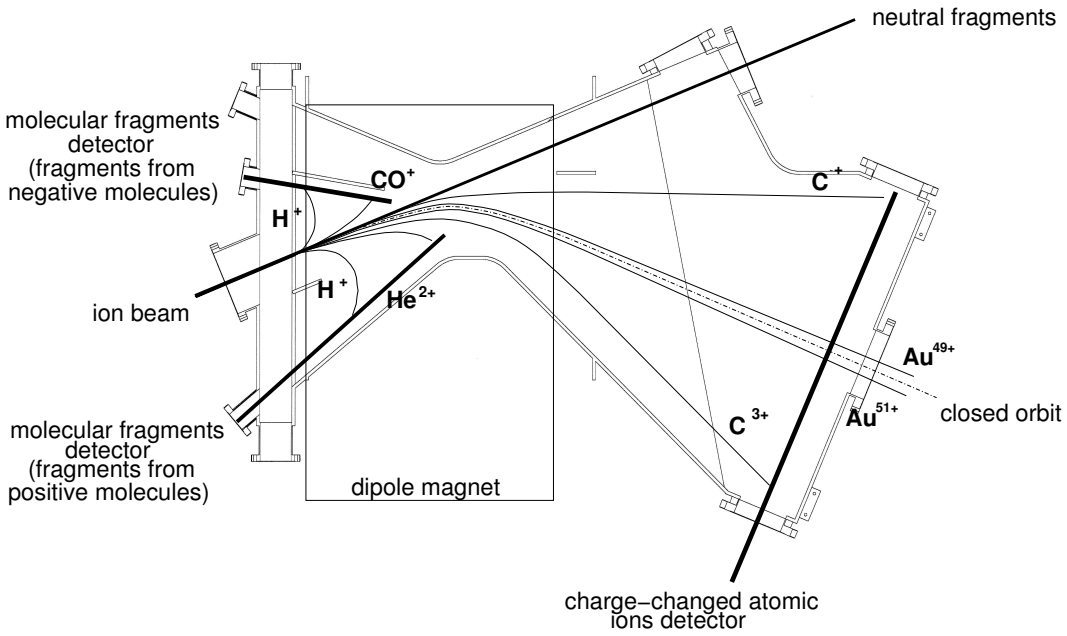

Figure 4.37: Vacuum chamber installed in the dipole following the ETS. The possible positions of the detectors are indicated by bold lines. Some typical ion trajectories are shown.

realized by a YAP:Ce-scintillator crystal with a photomultiplier. The YAP:Ce material is characterized by a good detection efficiency (40% NaI:Tl), a short fade-out time (25–35 ns) and good UHV properties [Wis03].
By using a detector which is hold into position by a mechanics that passes below the stored ion beam trajectory it was possible to realize the charge-changed atomic ions detector by only one detector that can detect the recombined and the ionized particles. The molecular fragments have to be detected in the strong magnetic field of the dipole, however, it is not possible to operate a photomultiplier in such an environment. The scintillation light is therefore guided to the outside of the magnet by a long lightpipe.
For the neutral fragments of DiR experiments an extended beamline is currently set up with detectors at a distance of ≈ 12 m from the center of the interaction section in the ETS. There will be a 3D detector [Str00] for recombination fragment imaging (RFI) [Kro02] and a surface barrier detector. The advantage of the extended beamline is a higher energy resolution for measuring the kinetic energy release of the dissociation process. The longer time of flight leads to a larger separation of the fragments. Compared to the 2D detector at the EC measurements with the 3D detector require less statistics for the reconstruction of the molecular geometry.

4.7 Alignment and bakeout

In December 2002 the ETS could be completed with the interaction section, and the alignment to the TSR beam axis was done. The old experimental section which was

already installed on the rails previously was moved out. A big part of the storage ring had been put to air because all the valves in the experimental section had to be open for the telescope. Windows for the alignment and for the laser experiments are installed in the TSR dipole vacuum chambers of the experimental section. First the toroid sections where aligned without the interaction region. The toroid chambers are equipped each with three removable telescope targets, two for the ion beam axis (at the entrance and at the exit) and one perpendicular to the ion beam axis for the alignment of the electron beam axis. With the aligned toroids the ion beam axis was transferred parallel, by moving the ETS on the rails, to the inner part of the storage ring. Two telescope targets have then been aligned to this axis which allows it to reproduce the ion beam axis for the ETS without putting the storage ring to air. Then the interaction section has been aligned and connected with bellows to the toroid sections.
Finally the toroid sections have been aligned to the electron beam axis of the acceleration and the collector section. The toroid sections are mounted on rails which allowed a more compact construction of the system but gives an additional degree of freedom for the alignment. With the toroids in their final position it was then possible to close the vacuum system to the acceleration and the collector section.
After completion the ETS has been baked to reach the UHV conditions required for the operation in the storage ring ($p_{TSR} = 5 \cdot 10^{-11}$ mbar typically). Different maximum temperatures have been used according to the installed components. The acceleration section with the SCM and the acceleration tubes and the collector section also with an acceleration tube was baked at 150°C. The toroid sections and the interaction section was baked at 200°C with a temperature gradient to the coupling sections with the valves. The temperature was kept 48 h and then slowly decreased with typically 5°C/h to 100°C. The vacuum reached after the first bakeout was $\approx 1 \cdot 10^{-10}$ mbar which still has to be improved for the photocathode operation.

4.8 TSR diagnostics

4.8.1 Beam profile monitor (BPM)

Information on the transverse spatial distribution of the ion beam is obtained with the beam profile monitor (BPM) installed in the diagnostic section of TSR (see Fig. 1.1). The principle is shown in Fig. 4.38. The circulating ion beam creates ions by collisions with the restgas. A high voltage is applied to a pair of electrodes perpendicular to the ion beam trajectory with a position sensitive detector on the negative side of the electrodes. If the pressure is constant in the vacuum tube then the number of created restgas ions is proportional to the ion beam density and one sees the projection of the ion beam on the detector. There are two pairs of electrodes one for the horizontal and one for the vertical direction.
The spatial resolution is limited by the thermal energy of the restgas ions and the transferred recoil momentum which leads to an displacement of the ion position on the detector.

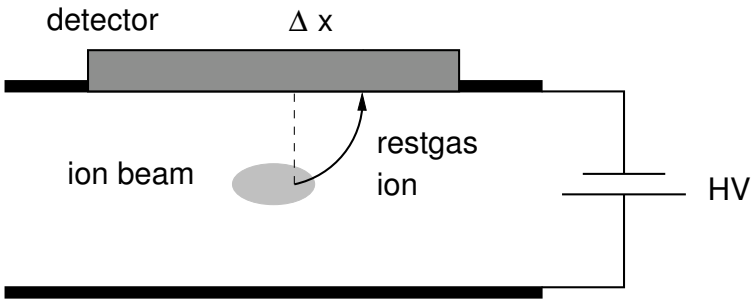

Figure 4.38: Beam profile monitor (principle): Restgas ions created by the ion beam are accelerated on a position sensitive detector. Velocity components transverse to the electric field result in a displacement Δx which limits the resolution.

Experimentally the resolution σ was measured to [Beu00]

$$\sigma_x \simeq 200\,\mu\text{m}$$
$$\sigma_y \simeq 300\,\mu\text{m}$$

4.8.2 Schottky spectra

If the ion beam is cooled with the electron beam, the energy of the ions is changed to the cooling energy. A device to monitor the ion energy via the revolution frequency f_0 is the so called Schottky pickup where the Schottky noise spectrum of the coasting beam is detected. This is not the classical continuous shot noise like in a continuous current but has separated bands that can also overlap at higher frequencies. A single particle that circulates with the revolution time T leads to a current signal

$$i(t) = e\delta(t - t_0 - hT) \text{ with } h = 0, 1, 2, \ldots, \tag{4.11}$$

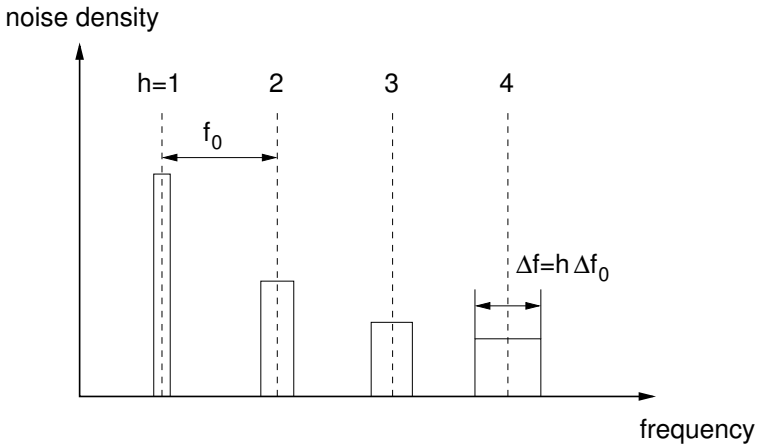

Figure 4.39: Schottky frequency spectrum: band structure at the harmonics h of the revolution frequency. The width and height of the bands is changing with h but the area stays constant.

(t_0 is an offset) with current peaks at every harmonic h of the revolution frequency

$$f_h = h \cdot f_0 \tag{4.12}$$

(see Fig. 4.39). Generalizing this to a particle beam leads to the Schottky band spectrum [Möh93]. The width of the h^{th} band is $\Delta f = h\Delta f_0$ but the spectral density decreases with $1/h$ keeping the area of the Schottky noise band constant. The total noise per band is proportional to the number of particles and to the squares of the ion charge and the revolution frequency. The big advantage of this method is that it is non-destructive because only a small amount of the ion energy is required for the measurement. From the frequency spectrum the longitudinal momentum spread can be obtained.
For high ion currents ($\gtrsim 10\,\mu$A for $^{12}C^{6+}$ at 73.3 MeV) the Schottky spectra show a double peak structure because of the coupling impedances (caused by wake fields from image charges created in the vacuum walls) [Beu00]. Thus it is not possible to deduce the momentum spread from this signals.

5. Preparatory measurements

During the setting up of the different components of the ETS, a variety of different measurements to characterize and to understand the new apparatus has been performed over the last four years. In 1999 first parts consisting of the acceleration section (without magnetic expansion) and the collector section were put together to a linear setup. Magnetic field measurements of the collector magnet (along the field axis and three-dimensionally at the collector cup position) have been performed [Spr00]. At this linear setup first studies of EDC and current density distributions at low energies (up to 200 eV) with a non-magnetically expanded electron beam and produced from an IrCe-cathode have been accomplished [Spr00, Lan01].
Having the SCM for the magnetic expansion and the toroid sections available, a second, L-shaped test setup was mounted, where the collector section was directly connected to the first toroid section and the acceleration section (see Fig. 5.1). Most of the parts could already be mounted to their final position on the base frame on the precision rails. This arrangement allowed us also to install most of the electrical connections and the control system. The acceleration section with the SCM could already be aligned. Magnetic field measurements in the expansion region were performed (section 4.1.4) to define the position of the electron gun. First measurements were then performed with the aim to implement the experimental procedures and to test the new components. For example current density distributions directly after the 90° bending of the first toroid could be recorded looking for deformations of the electron beam due to the transport (see section 5.1)
We were able to study EDCs under similar conditions like in the final setup at the L-shaped setup before the completion and the operation in the storage ring (see section 5.2). At the completed setup EDC measurements were performed that could be directly compared to the temperatures measured by DR in the storage ring (see chapter 6). Much effort has been spend on the understanding of the new combined expansion/acceleration region where the electron beam is expanded and simultaneously accelerated. We were able to find parameters suppressing the longitudinal heating by TLR, and by calculations these observations could be qualitatively reproduced.

5.1 Current density distributions at L-test setup

Using the energy analyzer at the collector, diagnostic measurements at relatively small electron beam powers (up to 4 W, corresponding to a beam current of 2 mA and an energy of 2 keV) can be performed. The retarding-field energy analyzer with its 50 μm entering

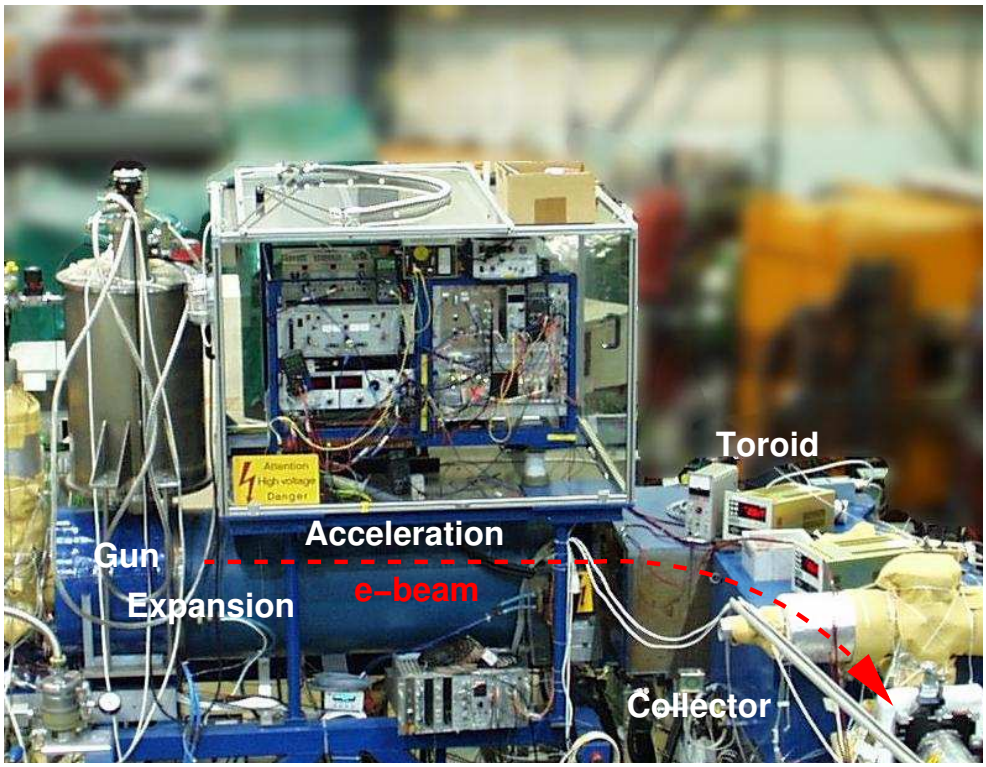

Figure 5.1: L-shaped testsetup for EDC and current density distribution measurements before completion of the setup.

aperture is used while the blocking electrode, as all the collector, is kept on ground. The magnetic field in the collector is kept homogeneous to measure two-dimensional spatial current density distributions (beam profiles) by scanning the entering aperture over the electron beam with two stepping motors. Normally only one-dimensional cuts along the x and y-axis are measured because they require much shorter time and almost all information about the beam is obtained. Complete two-dimensional scans are necessary to check for localized anomalies like small peaks that have been seen in earlier measurements with the previously used IrCe cathode [Spr00, Lan01].
The maximal scan length along the main axes is limited by the xy-stage and amounts to 25.4 mm (1 inch). This gives a theoretical maximum expansion ratio $\alpha \approx 250$ that can be scanned, which is much higher than the practically used values ($\alpha \lesssim 90$). For two-dimensional scans care has to be taken that the radius of the scan stays below 15.5 mm (collector cup outer diameter 69 mm) to not hit the vacuum wall.
If one wants to perform measurements at higher beam energy and higher electron currents the beam power has to be reduced which can be obtained by pulsing the beam, switching the extraction voltage on and off. A typical pulse length is 1 ms with an off time of 100 ms which reduces the beam power at the collector by a factor of 100.

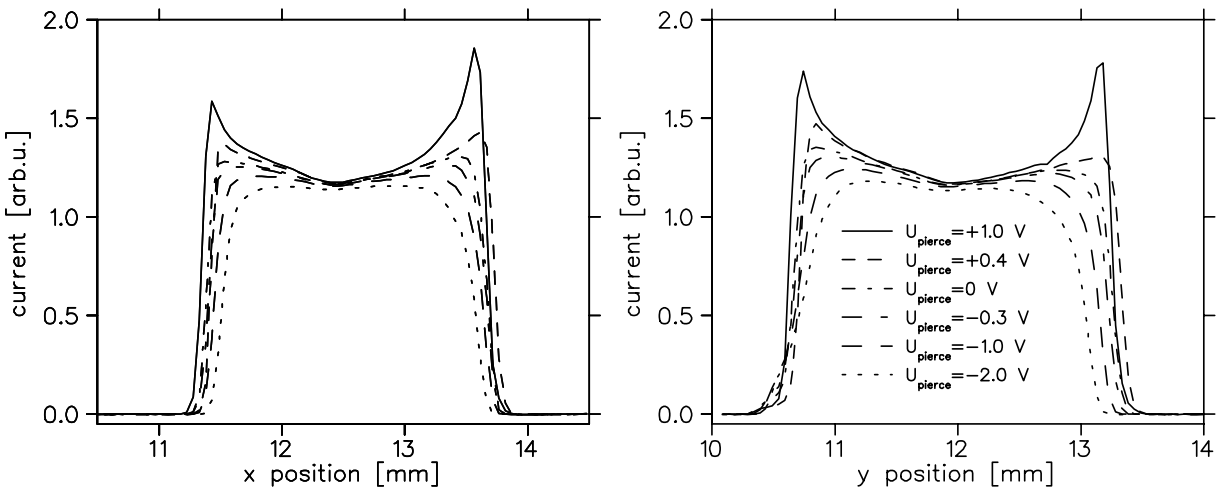

Figure 5.2: One dimensional current density distributions (cuts along the x (left hand side) and y-axis (right hand side)) for $\alpha = 2$, $I_{tot} = 0.3\,\mathrm{mA}$ and $E_{kin} = 200$. The voltage between the cathode and the Pierce shield has been changed in small steps (as indicated in the graph).

5.1.1 Pierce voltage

The shape of the electron beam can be manipulated by applying a bias voltage between the Pierce electrode and the cathode. Slightly hollow or constricted profiles can be obtained for positive or negative Pierce voltages, respectively. In recombination measurements it is important to have a homogeneous electron density distribution (n_e =const. inside the beam, $n_e = 0$ outside) for the absolute rate normalization and for the space charge correction [Kil92]. A homogeneous electron density distribution leads to a current density distribution $j_e = en_e v_e$ that is slightly higher at the beam edge because of the space charge that changes the electron velocity v_e.
For a low energy beam of $E_{kin} = 200\,\mathrm{eV}$, a small current of $0.3\,\mathrm{mA}$, an expansion ratio of $\alpha = 2$ and a guiding field of $B_0 = 0.097\,\mathrm{T}$ a series of measurements has been performed, where the Pierce voltage has been changed in small steps from $U_{Pierce} = 1$ to $-2\,\mathrm{V}$. For negative Pierce voltages we expect a constricted electron beam smaller than the cathode area because a potential barrier is created at the cathode edges. A positive voltage should increase the extracted current at the edges by the lowered barrier.
The result of cuts along the x and y-axis is shown in Fig. 5.2 and the derived beam diameters $d_{x,y}$ (FWHM), the position of the center x_0 and y_0 and the measured relative deviation from the cathode diameter d_{cath}

$$\gamma_{x,y} = \frac{d_{x,y}}{d_{cath}\sqrt{\alpha}} - 1,$$

are summarized in Tab. 5.1.
The measurement for $U_{Pierce} = 1\,\mathrm{V}$ (solid line) shows the biggest diameter of all measurements with very pronounced current peaks at the edge, forming a slightly hollow beam. In the y-direction, the beam is about 12% bigger in diameter than in the x-direction (discussion see below). With the Pierce voltage becoming more negative the beam size

U_{Pierce} [V]	d_x [mm]	d_y [mm]	x_0 [mm]	y_0 [mm]	γ_x [%]	γ_y [%]
1.00	2.3	2.6	12.5	11.9	1.6	14.9
0.40	2.3	2.5	12.6	12.0	1.6	10.5
0.00	2.2	2.5	12.5	12.0	-2.8	10.5
-0.30	2.2	2.5	12.5	11.9	-2.8	10.5
-1.00	2.1	2.4	12.5	11.9	-7.2	6.1
-2.00	2.0	2.2	12.5	11.9	-11.6	-2.8

Table 5.1: Results from current density distributions for different Pierce voltages extracted from Fig. 5.2. $d_{x,y}$ denotes the diameter (FWHM), x_0 resp. y_0 are the positions of the center and $\gamma_{x,y}$ the deviation from the cathode diameter (see text).

is reduced and the peaks at the edge become progressively smaller. In the center of the beam a local minimum is formed. For $U_{Pierce} \lesssim -1\,\mathrm{V}$ there are no peaks visible any more and the beam edge becomes rounder. The beam starts to become smaller than defined by the cathode diameter for $U_{Pierce} = 0\,\mathrm{V}$ in the x-direction and for $U_{Pierce} = -2\,\mathrm{V}$ in the y-direction. The local minimum in the center is disappering. The current density distribution which comes closest to the desired distribution for n_e =const. inside the beam is given for a value between $U_{Pierce} = -0.3$ and $-1\,\mathrm{V}$. The center of the distributions is not moving within the precision of the position determination ($\pm 0.05\,\mathrm{mm}$), for the different Pierce voltages.
Looking at the general form, the curves show a certain asymmetry (current density left and right from the center deviate) for almost all Pierce voltages. This can probably be explained by a slight misalignment of the cathode to the center of the Pierce electrode. Sitting closer to the cathode at one side leads to an increase of the electrical field, extracting more electrons then. Yet unclear is why the beam is slightly elliptical with a bigger diameter in the y-direction. Possible explanations are deformations of the magnetic field along the electron trajectory or a deviation of the cylindrical symmetry of the electron optics.

5.1.2 Expansion

High expansion ratios are necessary for low transverse electron beam temperatures. For the same parameters ($U_{Pierce} = -2\,\mathrm{V}$, $I_{tot} = 0.4\,\mathrm{mA}$, $E_{kin} = 1349\,\mathrm{eV}$, $B_0 = 0.04\,\mathrm{T}$) as

α	d_x [mm]	d_y [mm]	x_0 [mm]	y_0 [mm]	γ_x [%]	γ_y [%]
16	6.5	6.3	12.8	12.8	1.6	-1.6
32	9.3	8.9	12.0	13.4	2.8	-1.7

Table 5.2: Results from current density distribution for different expansions α extracted from Fig. 5.3. $d_{x,y}$ denotes the diameter (FWHM), x_0 resp. y_0 are the positions of the center and $\gamma_{x,y}$ the deviation from the cathode diameter (see text).

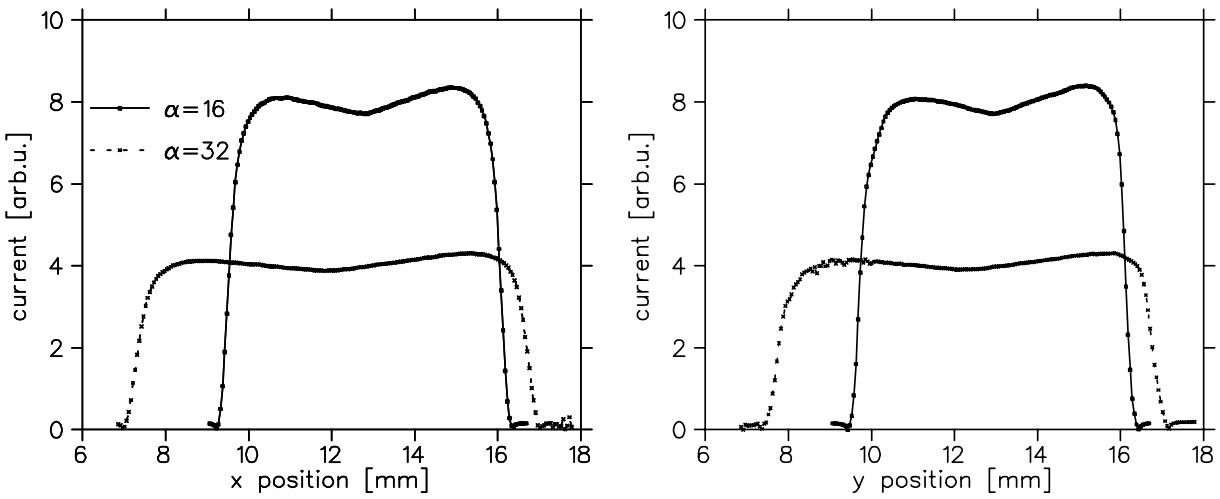

Figure 5.3: Comparison of beam profiles with $E_{kin} = 1349\,\text{eV}$ and $I_{tot} = 0.4\,\text{mA}$ for expansion $\alpha = 16$ and 32.

used in the first DR beamtime (see section 6.2) in the TSR two beam profiles with large α have been measured. The result is shown in Fig. 5.3 and the extracted beam values are summarized in Tab. 5.2.
As one can see the deviation $\gamma_{x,y}$ of the cathode diameter in both directions is small. The diameter in the x-direction is slightly bigger than in the y-direction ($\approx$3–4%) for both expansion ratios. The centers of the measured distributions do not agree because the beam was shifted with the steering coils between the measurements.
The shape of both profiles is only slightly asymmetric and the current distribution comes close to the desired one for a constant electron density. For $\alpha = 16$ a small minimum in the center can be seen. This can be corrected by changing the Pierce voltage. The plateau of the current density distribution is mainly flat with no localized perturbations. In Fig. 5.4 a complete two dimensional beam profile is shown in the lower left corner for $\alpha = 32$. In the upper right corner a contour plot of the profile is shown with cuts along the x and the y-axis. The spatial resolution of the scan was $\Delta x = \Delta y = 0.254\,\text{mm}$ (0.01 inch). In the contour plot a dashed circle is drawn where one can see the small deviation from the ideal round shape. By fitting an ellipse to the beam profile, the major axis of the ellipse has been found to $2a = 9.4\,\text{mm}$, the minor axis $2b = 8.7$ which is a deviation of about 8% from a circle. This value gives an approximate upper limit for what one has to expect for the deviation by measuring one-dimensional beam profiles only. The ellipse was found to be rotated about 28° which is indicated by the dashed line along the minor axis. One has to take the slightly elliptical form and the rotation into account when interpreting one dimensional cuts along the x and y-axis. Because of the rotation of the beam (see eq. (3.11)) the angle of the ellipse changes with the energy and the magnetic field. This explains why in some cases a bigger diameter in the y-direction and in other in the x-direction was found.

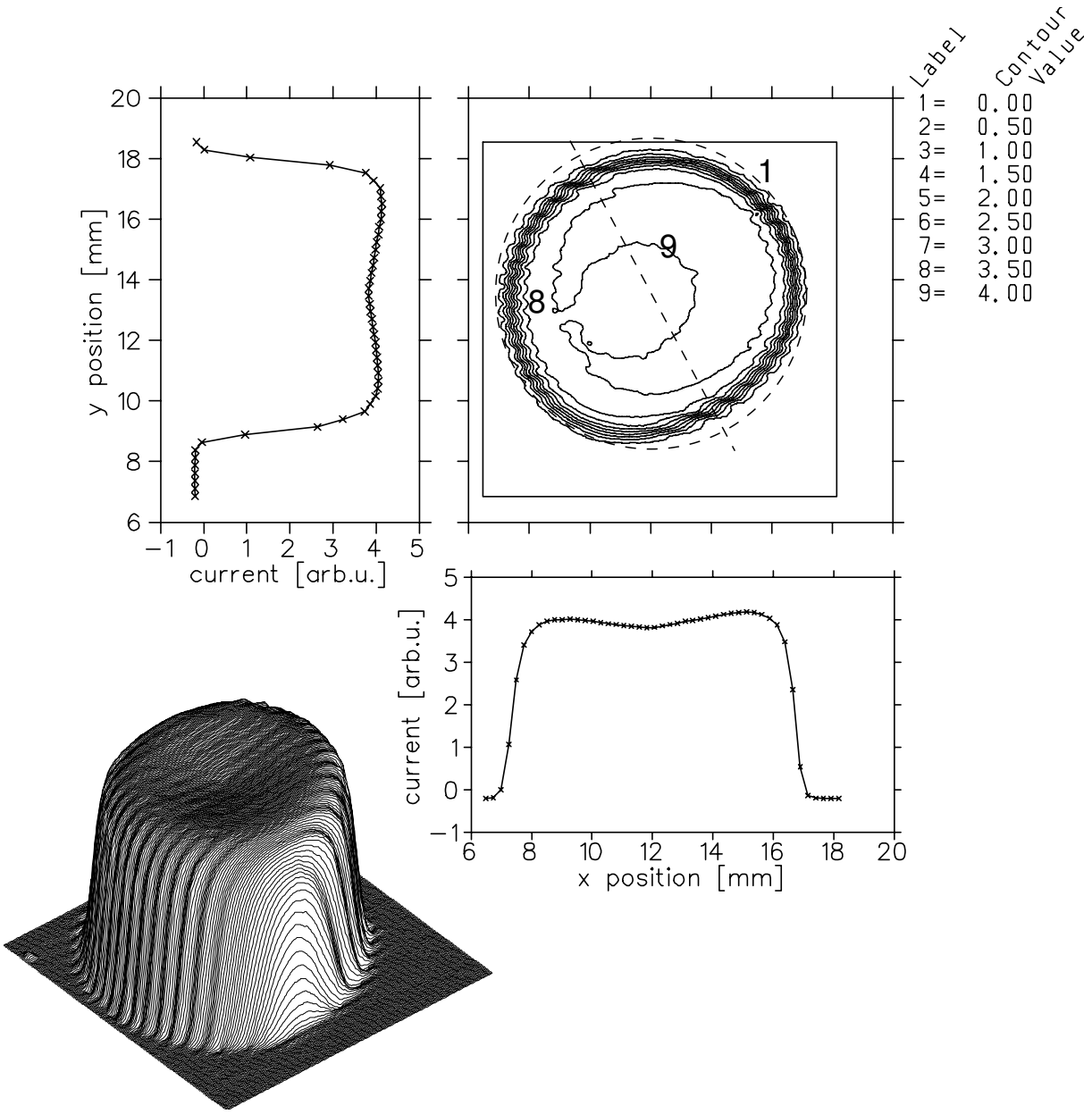

Figure 5.4: Two-dimensional beam profile (lower left corner) and a contour plot of the profile (upper right corner) with cuts along the x and y-axis for $\alpha = 32$, $I_{tot} = 0.4\,\text{mA}$ and $E_{kin} = 1349\,\text{eV}$. In the contour plot a dashed circle is shown indicating the ideal round shape of the profile. The dashed line indicates the minor axis of the elliptical beam profile and the rotation angle of $\approx 28°$.

Clearing electrodes	d_x [mm]	d_y [mm]	x_0 [mm]	y_0 [mm]	γ_x [%]	γ_y [%]
$U_{CE} = 0\,\mathrm{V}$	6.6	6.5	11.9	12.4	3.1	1.6
$U_{CE} = +754/-764\,\mathrm{V}$	5.9	7.1	12.7	12.7	-7.8	10.9

Table 5.3: Deformation of the beam profile due to the clearing electrode voltage extracted from Fig. 5.5. $d_{x,y}$ denotes the diameter (FWHM), x_0 resp. y_0 are the positions of the center and $\gamma_{x,y}$ the deviation from the cathode diameter (see text).

5.1.3 Deformation by clearing electrodes

For the operation of the ETS inside the storage ring the clearing electrodes at toroid 2 (see section 4.2.1) are used to suppress the backstream of ions from the collector to the cathode. A voltage of typically several hundred volts is applied (positive voltage at upper electrode and negative at lower) creating an electric field in the y-direction. The center between the electrodes should be almost on ground potential and the electron beam which is additionally bound to the magnetic field lines should not be much influenced.
In Fig. 5.5 two beam profiles for $\alpha = 16$ and $E_{kin} = 1349\,\mathrm{eV}$ are shown. One with the clearing electrodes kept on ground and one with $U_{CE} = +754/-764\,\mathrm{V}$. The derived beam values are given in Tab. 5.3.
There is a strong deformation and a displacement of the beam center visible for the measurement with the clearing electrodes on potential. The deviation of d_x from d_y is about 16% and is much higher than the upper limit estimated from the two-dimenisional beam profile. Therefore this can not be explained as an artefact because of the selection of the scanning axes. For the recombination measurements this creates no problem because

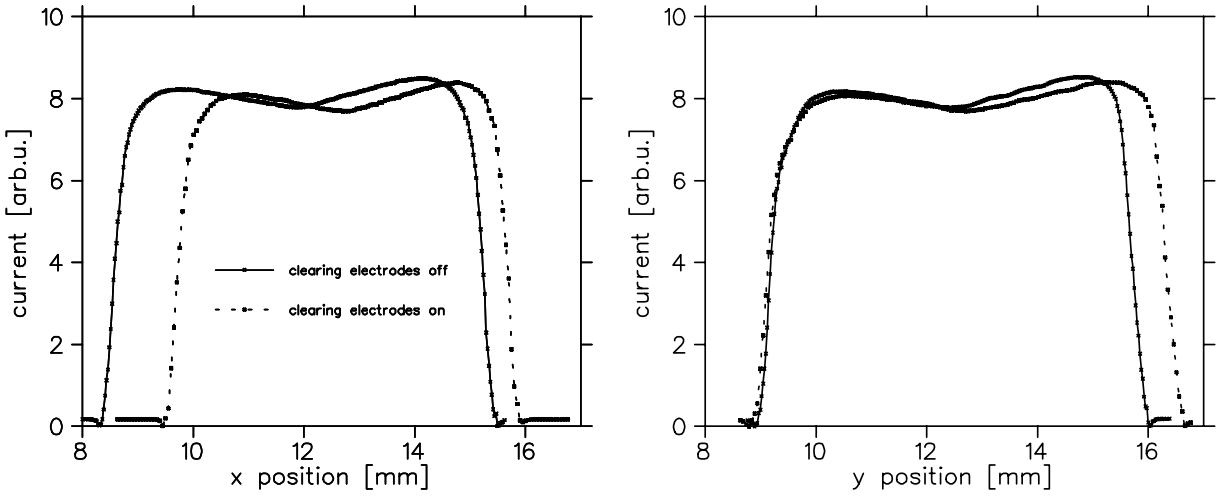

Figure 5.5: Deformation of the beam profile due to the clearing electrode voltage. Beam parameters $\alpha = 16$ and $E_{kin} = 1349\,\mathrm{eV}$ with clearing electrode voltages of $U_{CE} = 0\,\mathrm{V}$ and $U_{CE} \approx \pm 750\,\mathrm{V}$. The widths and center positions are given in Tab. 5.3.

the clearing electrodes are located behind the interaction region and are not disturbing the beam properties for the experiment. A two-dimensional measurement would be interesting to see the complete beam profile.

5.2 EDC measurements

With the energy analyzer installed in the collector cup we are able to measure the longitudinal energy distribution curves of the electron beam. This feature allows us to perform measurements outside the storage ring without an ion beam, giving a great flexibility and independence of the storage ring beam times. Interesting measurements are e.g. the study of the adiabatic acceleration procedure and heating due to transverse-longitudinal relaxation. In the present configuration we are not able to measure transverse electron temperatures. Nevertheless it is possible to measure the transverse temperature with a longitudinal energy analyzer by measuring at different magnetic expansion/compression ratios at the energy analyzer. From that one can determine the transverse temperature because of the changing energy transfer from the transverse to the longitudinal degree of freedom (see section 3.3.3). This method is used extensively at the photocathode setup [Pas97a, Orl01].
Most of the results presented in this section were obtained at the L-shaped setup. The retarding field energy analyzer could be tested and improved and the magnetic expansion could be studied for the first time together with the adiabatic acceleration. After the first DR beamtime some EDC measurements were performed to compare the longitudinal temperatures from both methods. We will start to discuss the experimental procedure of the EDC measurements together with some technical problems and the investigation of technical systematics.

5.2.1 Experimental procedure

In Fig. 4.28 the principle of the EDC measurements and in Fig. 4.33 the detailed circuit are shown. The electrons arrive at the collector cup and are decelerated to the potential of the cup and most of the beam is then blocked by the entering aperture in the back of the cup in front of the energy analyzer. The voltage at the blocking electrode U_{Block} in the analyzer is now ramped over a certain voltage region of 1–2 V with a step size of typical 20 mV and the current is measured at the collector electrode during the scan. Normally the time for measuring one data point is about one second. A current signal is measured and amplified by a current to voltage converter (I/U) and then transmitted to a digital oscilloscope. We have been using two different I/U-devices: one with a very short and one with a longer integration time (≈ 1 ms), where the output signal is averaged and the high frequency noise is suppressed. For detailed understanding and improvement of the measured signals it is very useful to have the noisy "raw" signal without any averaging. The fast device has also the advantage that the preamplifier is in a separate box that can be put very close to where the signal is detected, which improves the signal. One also has the possibility to average the voltage signal at the oscilloscope. We also measured pulsed EDCs which is only possible with the fast I/U-device because of the short pulse length of

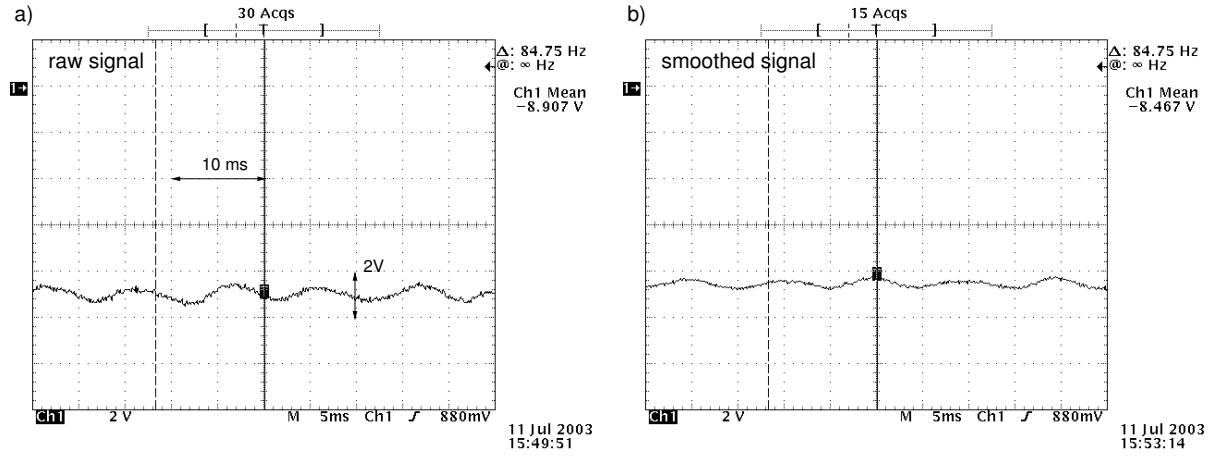

Figure 5.6: Amplified current signals from the energy analyzer (version 2) with the fast current to voltage converter: a) raw signal, b) signal smoothed at the oscilloscope.

1 ms. Typical signals seen on the oscilloscope from the I/U-device (short integration time) are shown in Fig. 5.6. On the left side the raw signal is shown and on the right side the averaged signal (≈ 4) at the oscilloscope. From the oscilloscope the mean value is readout with the computer. As one can see there is a modulation on the current signal with a frequency in the order of 100 Hz (probably ripple on the line voltage). The frequency used for the cathode heating was chosen to $f_{heat} = 284\,\mathrm{Hz}$ to distinguish it from the line voltage.
The measured curve is the integral current signal from the electron energy distribution $f(U)$

$$I(U_{Block}) = \int_{U_{Block}}^{\infty} f(U)dU. \tag{5.1}$$

For electron energies $E_{kin} \gtrsim 200\,\mathrm{eV}$ the distribution function can be very well described by a Gaussian [Kra92]

$$f(U) = \frac{1}{\sqrt{2\pi}\sigma} e^{-\frac{(U-U_{MLE})^2}{2\sigma^2}}, \tag{5.2}$$

where U_{MLE} is the mean longitudinal energy which leads to a shift of the curve (see 3.3.3). Using (5.2) with (5.1) gives a function similar to the Error function $\mathrm{erf}(x)$. To obtain the energy spread σ this function is then fitted to the measured integral current signal. From σ we calculate the electron temperature using eq. (3.43) by

$$kT_{\parallel}^{f} = \frac{\sigma^2}{2E_{kin}}. \tag{5.3}$$

Calculating the derivative of the $I(U)$ leads to the same results but is technically more complicated because the derivative has to be calculated numerically which requires often a smoothing of the data. In earlier measurements [Kra92, Spr00, Lan01] and in the photocathode setup [Pas97a, Hop01] a Lock-In-amplifier was and is used to create the

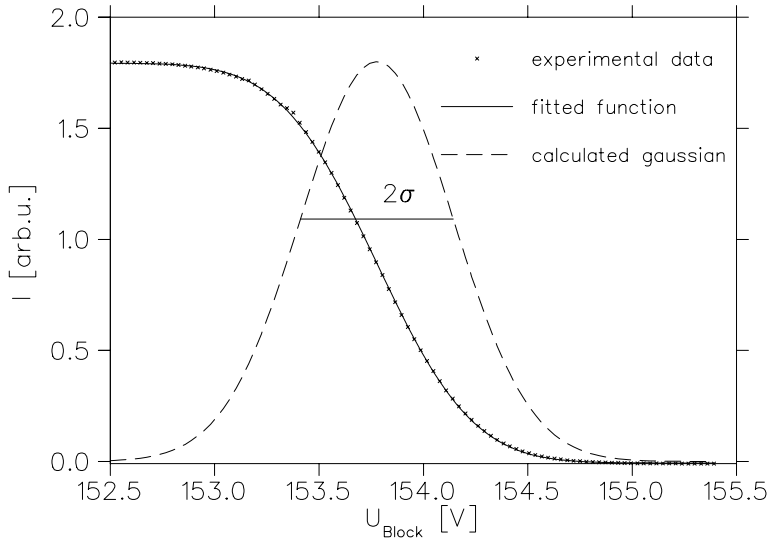

Figure 5.7: Typical energy distribution curve (analyzer version 1): the current reaching the collector electrode as a function of the blocking voltage (small crosses). A theoretical function (see text) is fitted to the data points (solid line) and a Gaussian distribution (dashed line) is calculated from that which yields σ.

voltage ramp and to measure the current signal. The advantage of this method is that one directly gets the derivative of the current signal from the Lock-In measurement and the method is very sensitive also at very small currents. On the other hand it is more complicated because one has to transmit the voltage ramp and the small modulation voltage on the HV platform which is normally done optically. This requires several analog-analog conversions where the linearity might be an issue. In our procedure the voltage ramp is transferred digitally to the HV platform over the control system and no modulation is needed. But the main reason is that the Lock-In method can not be used for pulsed electron beams. A typical result of a measured current signal with the fitted Gaussian is shown in Fig. 5.7. The scan starts always at the low energy side allowing the complete current to reach the analyzer in the beginning.
Before we want to discuss the results of the systematic EDC measurements some technical aspects of the experimental procedure will be discussed and it will be shown how they influence the results. In the following the given electron energies and final densities are not space-charged corrected and represent the cathode voltage only. This is well justified because we are not interested in accurate energies and the effect from the space charge is small for our conditions. For a beam with cathode potential $U_0 = 2000\,\mathrm{V}$, a total current $I_{tot} = 2\,\mathrm{mA}$ and expansion $\alpha = 32$ one calculates $\Phi_{SC} \approx 4\,\mathrm{V}$ and the deviation of the density is about 1%.

5.2.2 Problems Analyzer version 1

When we started the first measurements at the L-testsetup we discovered a couple of problems related to the installed energy analyzer. These problems could only be solved

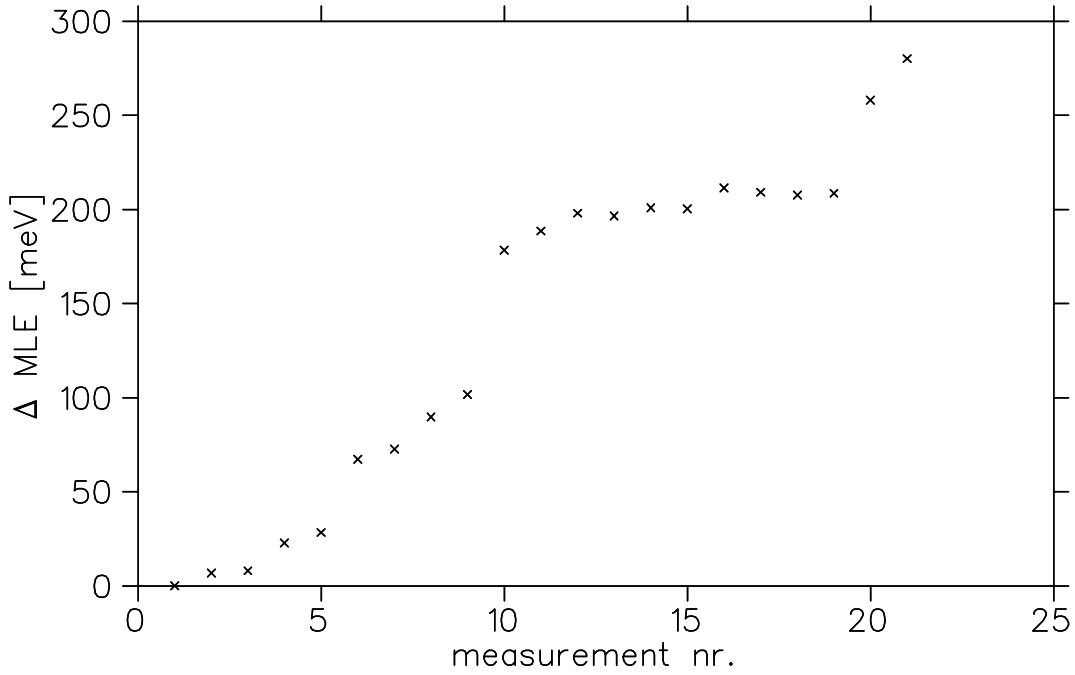

Figure 5.8: Observation of the shift in the mean longitudinal energy (MLE) for a series of measurements under the same experimental conditions: $E_{kin} = 200\,\text{eV}$, $\alpha = 8$, $n_e = 1.13 \cdot 10^{13}\,1/\text{m}^3$, $I_{tot} = 0.32\text{mA}$ ($U_{ext} = 30\,\text{V}$), $E_{drift} = e \cdot U_{ext}$. The total measurement time was $t \approx 5\,\text{h}$.

by a new design of the analyzer which then was installed into the completed ETS (see section 4.3). We will now discuss the main problems and the workarounds for the data analysis.

MLE shift

During the EDC measurements we observed a systematic MLE movement to higher energies with time. In Fig. 5.8, a series of measurements over a long period of time ($\approx 5\,\text{h}$) is shown. All the data points have been measured under the same conditions at a relatively low energy ($E_{kin} = 200\,\text{eV}$). But the effect has been observed also at higher energies.
Different explanations are possible which have been examined. Trapping of ions in the analyzer: the magnetic field has been switched off for a certain time but the MLE was not shifted back to a lower energy. Charging of the blocking electrode: the electrode was put to ground with no effect on the MLE. The most probable explanation is the charging of the ceramic balls installed for isolation of the different electrodes in the analyzer. After switching of the setup over night the MLE was shifted back to a lower energy the next morning.

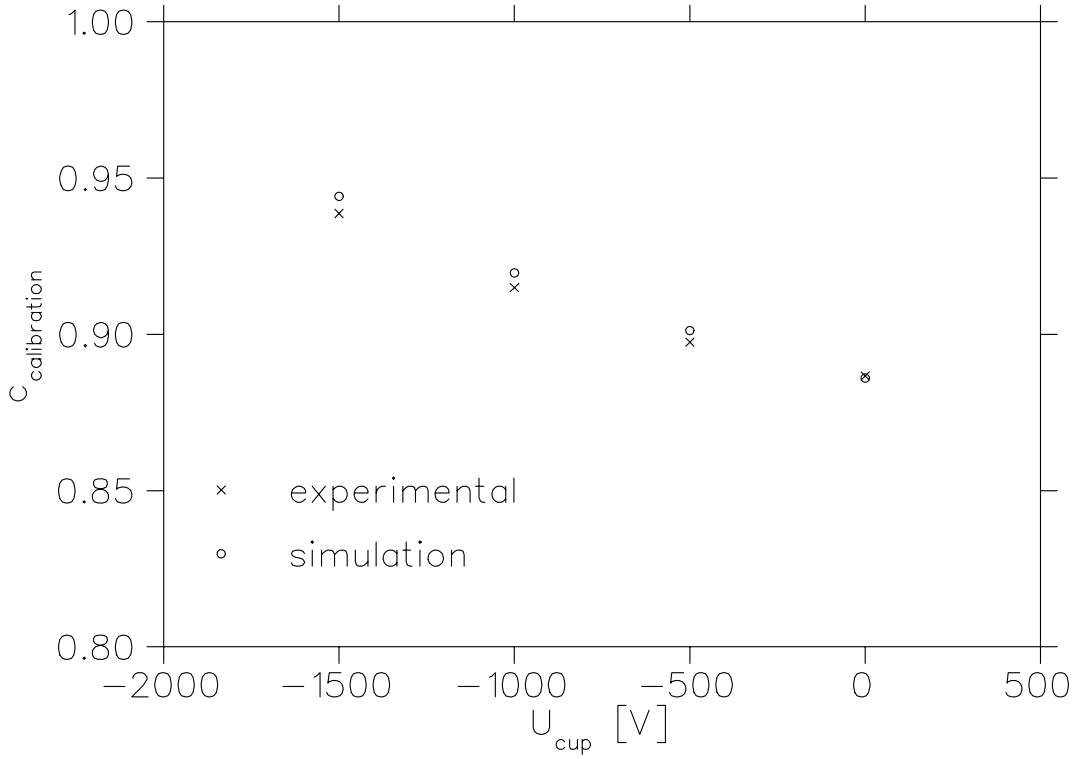

Figure 5.9: Comparison of the measured (crosses) and calculated (open circles) calibration factor c as a function of the blocking potential. The error bars for the measured values (3 EDC for each point) are very small and therefore not visible in the plot.

Barrier calibration

As previously discussed (see section 4.3) the blocking potential seen by the electrons at the blocking electrode was smaller than the applied voltage because of the big opening and the shortness of the electrode. Thus, the measured widths σ from the EDCs have to be scaled by a factor c to deduce the correct electron temperatures. Numerical calculations of the potential distribution in the analyzer have been performed, which allow us to compare the experimentally found calibration factor c_{exp} with the calculated one (c_{sim}) (see Fig. 4.32).
The calibration factor has been calculated by the following formula

$$c = 1 - \frac{U_{MLE}}{U_{block}}, \tag{5.4}$$

where the blocking voltage for the experiment is given by $U_{block} = U_0 + U_{MLE}$, and for the simulation by $U_{block} = U_0$; U_0 is the cathode potential. U_{MLE} is found with the Gaussian distribution function fitted to the experimental data as described above and in the simulation it is the minimum value of the calculated potential U_{min}. The calibration factors depend on the relation between the cathode potential and the blocking potential. In Fig. 5.9 the calculated calibration factors for different cup potentials are compared. The cup voltage is always given relative to ground potential. For $U_{cup} = 0\,\mathrm{V}$ both values

agree very well and for higher cup potentials the experimental values lie systematically below the calculated ones. Reasons could be differences in the geometry of the analyzer in the calculation and the experiment.
All energy spreads presented in the following that were obtained with the analyzer version 1 are corrected by the experimental calibration factor c_{exp}. With the new energy analyzer version 2 no MLE shift over time was observed anymore. Because of the longer blocking electrode it is also not necessary to correct the energy spreads with an calibration factor.

One series with smaller energy spreads

During the first measurements we observed that the MLE shift (see above) was very small on one day. Also the measured EDCs where significantly smaller than in the previous days and we were able to perform many measurements from very low to high densities at a constant kinetic energy without observing a strong MLE shift. After several hours, the energy spreads became broader and were in the same range as during the days before. We think that relatively small charging effects were present on this day. This might be related to temperature shifts in the environment or other parameters that can not be controlled. We measured at an electron energy of $E_{kin} = 2\,\mathrm{keV}$ with expansion $\alpha = 8$. For an extraction voltage $U_{ext} = 2.2\,\mathrm{V}$ with total current $I_{tot} = 0.2\,\mu\mathrm{A}$ we measured a small value $\sigma = 246.5 \pm 2.5\,\mathrm{meV}$ and this changed then to $\sigma = 309.8 \pm 5.9\,\mathrm{meV}$ which is an increase of $\approx 25\%$. The data points in Fig. 5.22 were taken from this measurement series.

5.2.3 Technical systematics

Cathode temperature

The initial electron temperatures depend only on the cathode temperature T_c. In the center of mass frame of the accelerated electron beam the longitudinal temperature depends mainly on potential energy relaxation. The initial distribution is strongly narrowed because of the kinematic reduction. The cathode temperature contributes only a small fraction to the final longitudinal temperature. However, the transverse temperature is only reduced by the expansion factor α. It is therefore important to know the cathode temperature precisely.
Before completion of the ETS a window has been installed at the end of the acceleration section. This makes a pyrometer measurement of the cathode temperature as a function of the heating power possible. The cathode is heated by an electronically generated AC current, allowing us to change the frequency of the heating current in the range of 60–2000 Hz with a maximum current of 1.5 A. By the manufacturer it is recommended to use an AC heating instead of a DC because the DC current leads to a physico-chemical process that reduces the cathode lifetime [Cro79]. The temperature which is measured with the pyrometer is not the true temperature but rather the brightness temperature. This is the temperature at which a black body is as bright as the heated material. The brightness temperature $\tilde{T}$ is always lower than the true temperature T and was converted with the spectral emissivity $\epsilon_\lambda = 0.57$ at the wavelength $\lambda = 650\,\mathrm{nm}$ (given by the

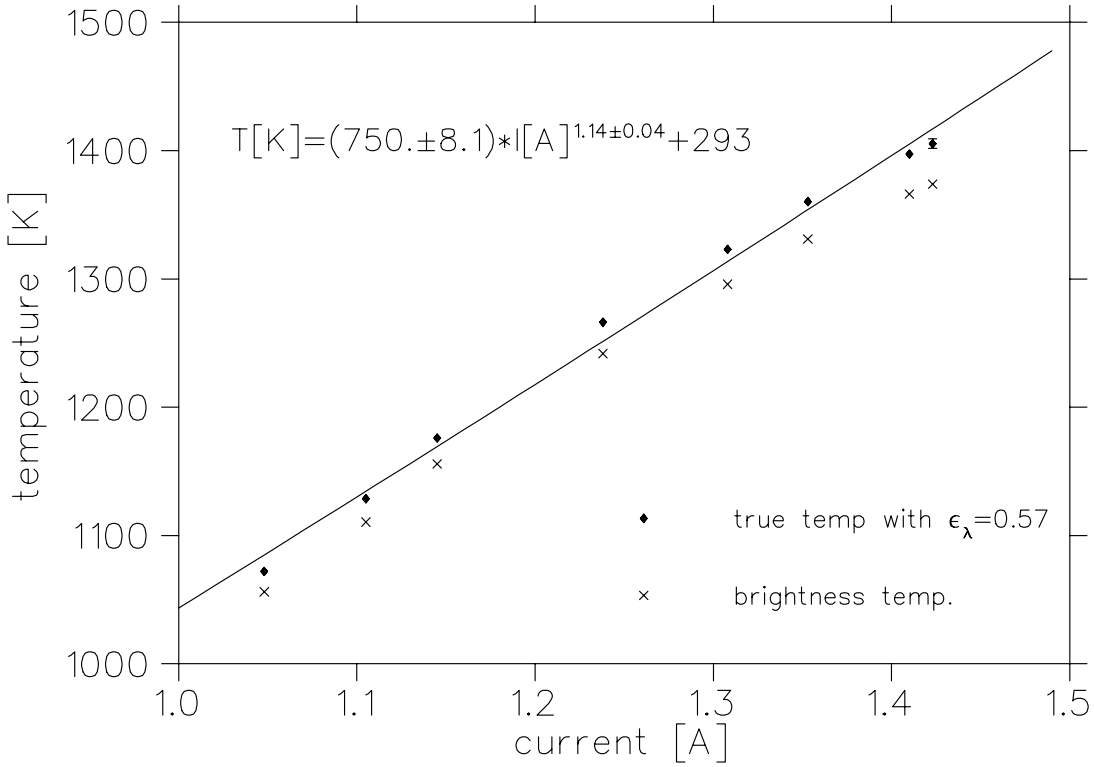

Figure 5.10: Determination of the cathode temperature: brightness temperature (crosses) and converted true temperature (diamonds) with the spectral emissivity $\epsilon_\lambda = 0.57$ as a function of the cathode heating current. Below 1000 mA the brightness is two weak for a pyrometer reading.

manufacturer [Spe02]) by [Ger99]

$$\frac{1}{T} = \frac{hc}{k\lambda}\ln(\epsilon_\lambda) + \frac{1}{\tilde{T}}.$$

In figure 5.10 the brightness and the calculated true temperature is shown as a function of the heating current. T was fitted to the heating current with the following result:

$$T[\mathrm{K}] = (750 \pm 8.1)\frac{\mathrm{K}}{\mathrm{A}} \cdot I[\mathrm{A}]^{1.14\pm0.04} + 293\mathrm{K}. \tag{5.5}$$

The heating power as a function of the heating current is shown in Fig. 5.11 with a dependence $P[\mathrm{W}] = R \cdot I^2 = 3.91 \cdot I[\mathrm{A}]^{0.94} \cdot I[\mathrm{A}]^2$. This dependence is related to a temperature resp. current dependence on the cathode resistance.
A second method to determine the cathode temperature is a relation between the MLE and the total emitted current I_{tot} that can be found calculating I_{tot} from the initial longitudinal electron distribution at the cathode (Maxwellian velocity distribution). In the regime of space charge limited emission a potential minimum is formed in front of the cathode which leads to a minimum kinetic energy E_{min} of the electrons. One finds the following relation [Kra92]

$$\langle E\rangle \propto E_{min} = kT_C \cdot \ln(I_{tot}) + \mathrm{const.} \tag{5.6}$$

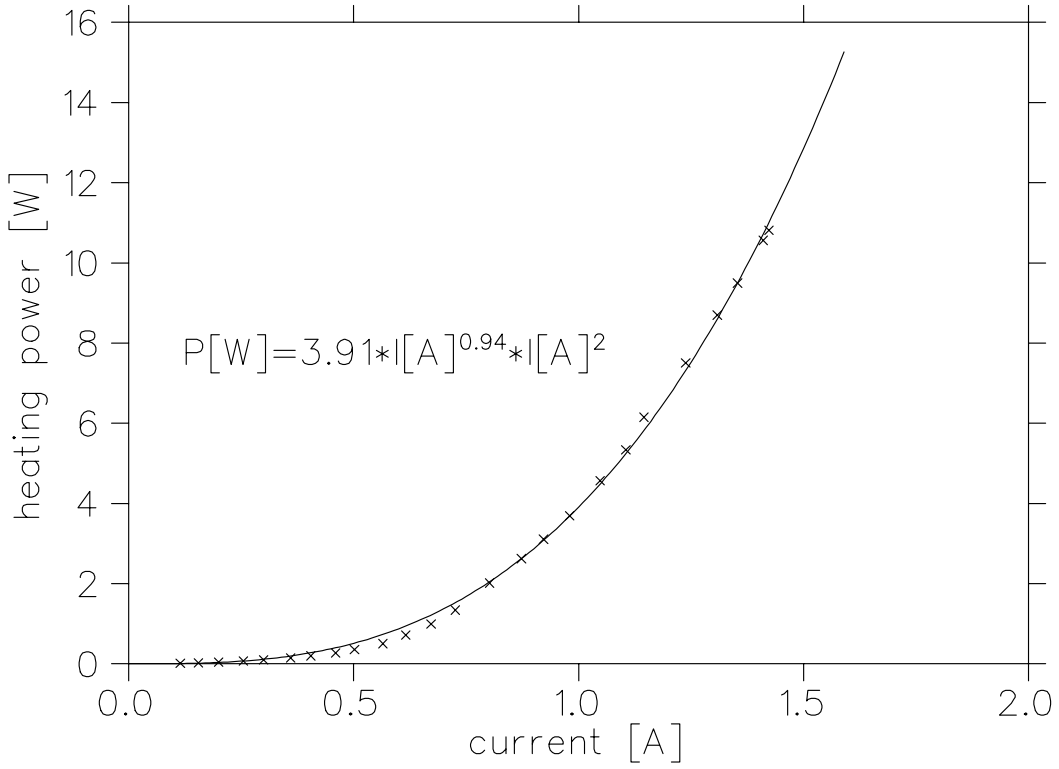

Figure 5.11: Heating power as a function of the cathode heating current. The resistance of the cathode is changing with the current (temperature) as $R(I) = 3.91 \cdot I^{0.94}$. In the range of $I = 0.5\,A$ there is a stronger deviation from the fitted curve.

Measuring the MLE shift as a function of I_{tot} is then a method to determine T_C. This has been done for three different heating currents $I_{heat} = 800, 1000$ and $1200\,\mathrm{mA}$. The result is shown in Fig. 5.12 where eq. (5.6) has been fitted to the data. In Tab. 5.4 the results of both methods are compared, with the values from the pyrometer measurements calculated from eq. (5.5).
There is a rather big discrepancy between the two results. This is probably explained by the fact that the MLE results were obtained "parasitic". They have been extracted from measurement series where no special attention has been paid to the heating current. Normally the heating current was adjusted to the desired value and the EDC measurements were performed. It was seen that the heating current dropped up to $50\,\mathrm{mA}$ with time and had then to be readjusted after some time. Therefore the given values for the heating current are only approximate values.
For the longitudinal EDC measurements this heating current change is negligible as one can see in Fig. 5.13 where measurements at two heating currents are compared. The σ values for $I_{heat} = 800\,\mathrm{mA}$ lie about 10% below the values for $I_{heat} = 1000\,\mathrm{mA}$. For a change in the current $\Delta I = 50\,\mathrm{mA}$ one can then estimate a change in σ about 2.5%. This fluctuation is automatically included in the error bars on the data points. At the highest density for $I_{heat} = 800\,\mathrm{mA}$ the energy spread drops significantly which might be related to the high current that is extracted from the relatively cold cathode.

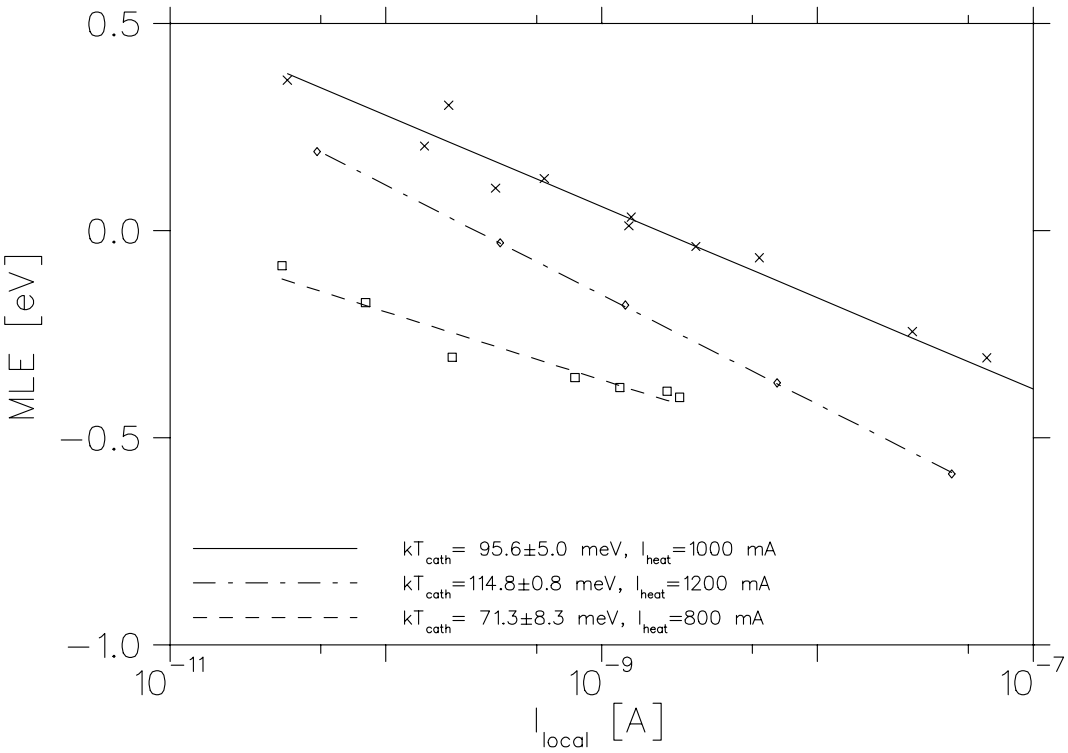

Figure 5.12: Cathode temperature calculated from MLE shift (see text): The position of the mean longitudinal energy (MLE) is plotted against the current (local current at the energy analyzer) for three different heating currents with the fitted curves: 800 mA (dashed line), 1000 mA (solid line) and 1200 mA (dash-dotted line). The curves have been slightly shifted on the y-axis for better distinction.

current [mA]	pyrometer T[K] (meV)	MLE shift T[K] (meV)
800	$875. \pm 6.2$ (75.3 ± 0.5)	$828. \pm 96.4$ (71.3 ± 8.3)
1000	$1043. \pm 8.1$ (89.8 ± 0.7)	$1110. \pm 58.1$ (95.6 ± 5.0)
1200	$1216. \pm 10.0$ (104.7 ± 0.9)	$1334. \pm 9.3$ (114.8 ± 0.8)

Table 5.4: Comparison between two temperature determination methods: pyrometer method and MLE shift (see text).

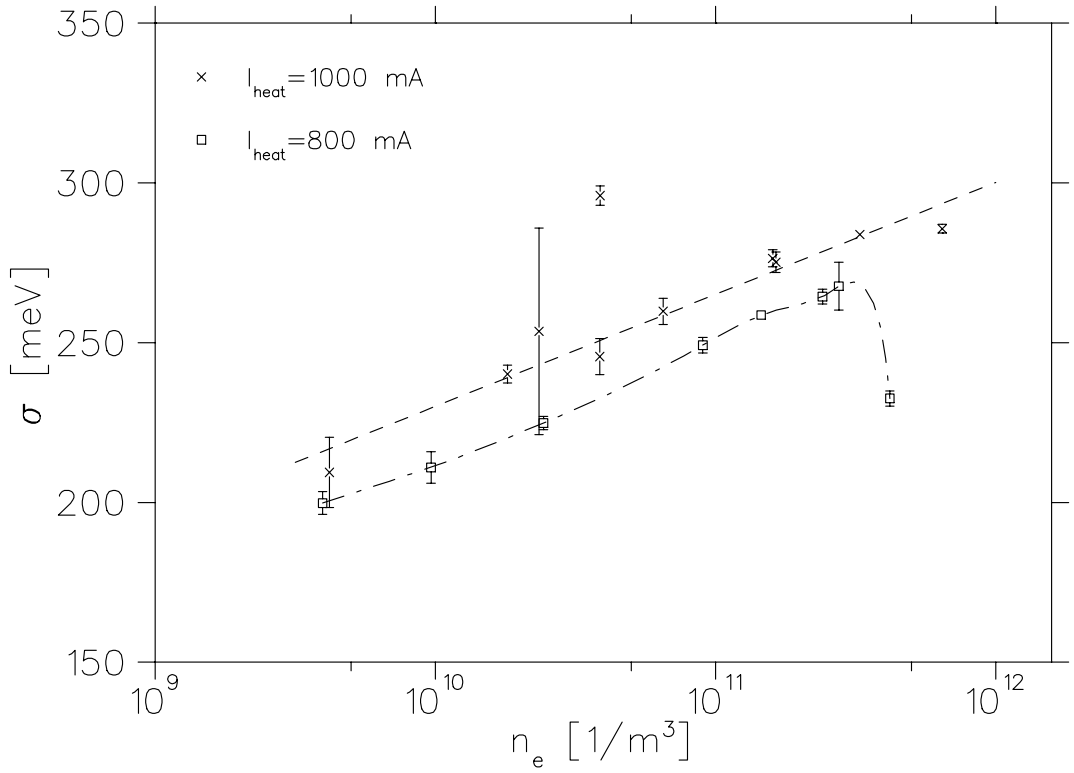

Figure 5.13: The widths of the energy distribution curves σ as a function of the final electron density for two heating currents $I_{heat} = 800$ and $I_{heat} = 1000$ mA are plotted. The dashed lines are drawn to guide the eye. Beam parameters $E_{kin} = 2000$ eV, $\alpha = 8$ and $E_{drift} = 200$ eV.

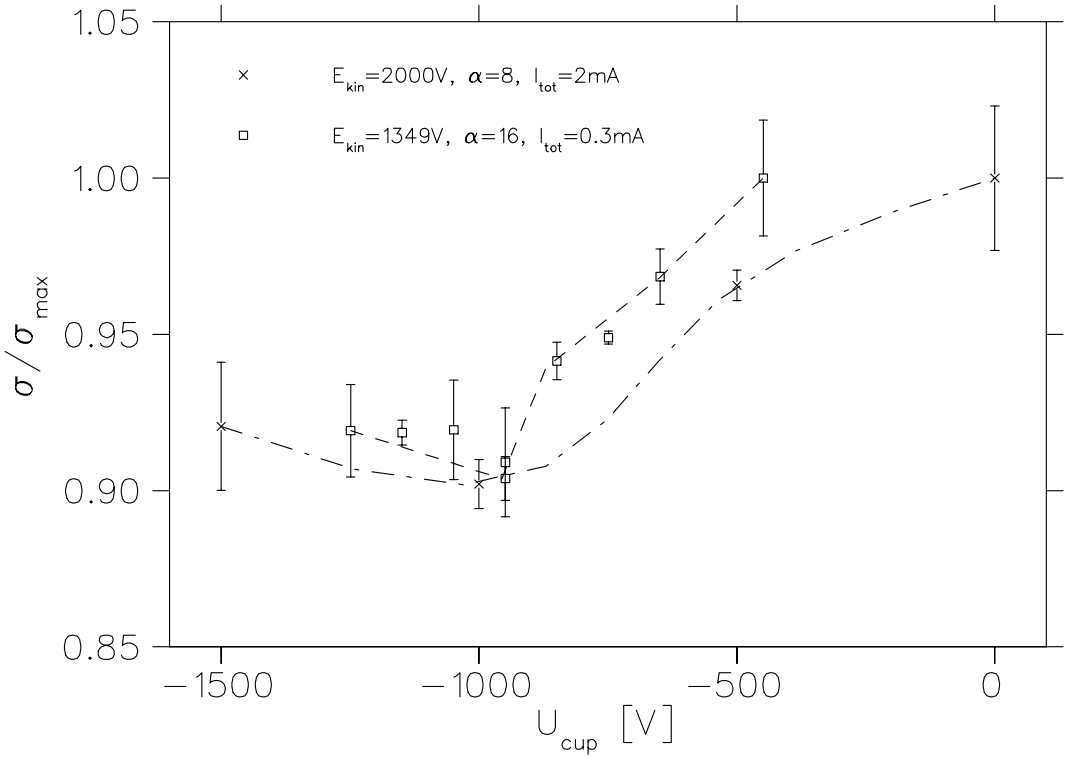

Figure 5.14: Dependence on σ from the cup potential: on the y-axis the relative energy spread σ_{max} is plotted. U_{cup} is defined versus ground potential. The upper curve (squares) has been measured at $E_{kin} = 1349\,\text{eV}$, $\alpha = 16$, $n_e = 3.7 \cdot 10^{12}\,1/\text{m}^3$, $I_{tot} = 0.3\,\text{mA}$ ($U_{ext} = 38\,\text{V}$), $E_{drift} = 400\,\text{eV}$, the lower curve (crosses) at $E_{kin} = 2000\,\text{eV}$, $\alpha = 8$, $n_e = 2.1 \cdot 10^{13}\,1/\text{m}^3$, $I_{tot} = 2\,\text{mA}$ ($U_{ext} = 100\,\text{V}$), $E_{drift} = 200\,\text{eV}$. The lines are plotted to guide the eye.

Cup potential

The influence of the potential at the collector cup on the measured energy spreads has been measured for different energies. Putting the cup to a positive voltage compared to the cathode potential (but still negative versus ground) results in a deceleration of the electrons before they can reach the energy analyzer. Additionally there are deceleration electrodes installed at the cup position (see section 4.3) which softens the deceleration. The central electrode is kept on the same potential applied to the cup.
Fig. 5.14 shows the result for two different energies $E_{kin} = 2000\,\text{eV}$ and $E_{kin} = 1349\,\text{eV}$ and two different total emission currents $I_{tot} = 2\,\text{mA}$ and $0.3\,\text{mA}$, respectively. The densities were $n_e = 2.93 \cdot 10^{13}\,1/\text{m}^3$ and $n_e = 2.67 \cdot 10^{12}\,1/\text{m}^3$. The cup potential is defined versus ground potential. The data for $E_{kin} = 2000\,\text{eV}$ has been measured with the analyzer version 1 and for $E_{kin} = 1349\,\text{eV}$ with the analyzer version 2. For both measurements we observed a reduction in the measured energy spread of about 10% for $U_{cup} \approx -900$ to -1000 V independent of the used analyzer. For EDC measurements it thus seems desireable to decelerate the electron beam to avoid a broadening because of a too fast deceleration at the analyzer. This could destroy the effect from the adiabatic

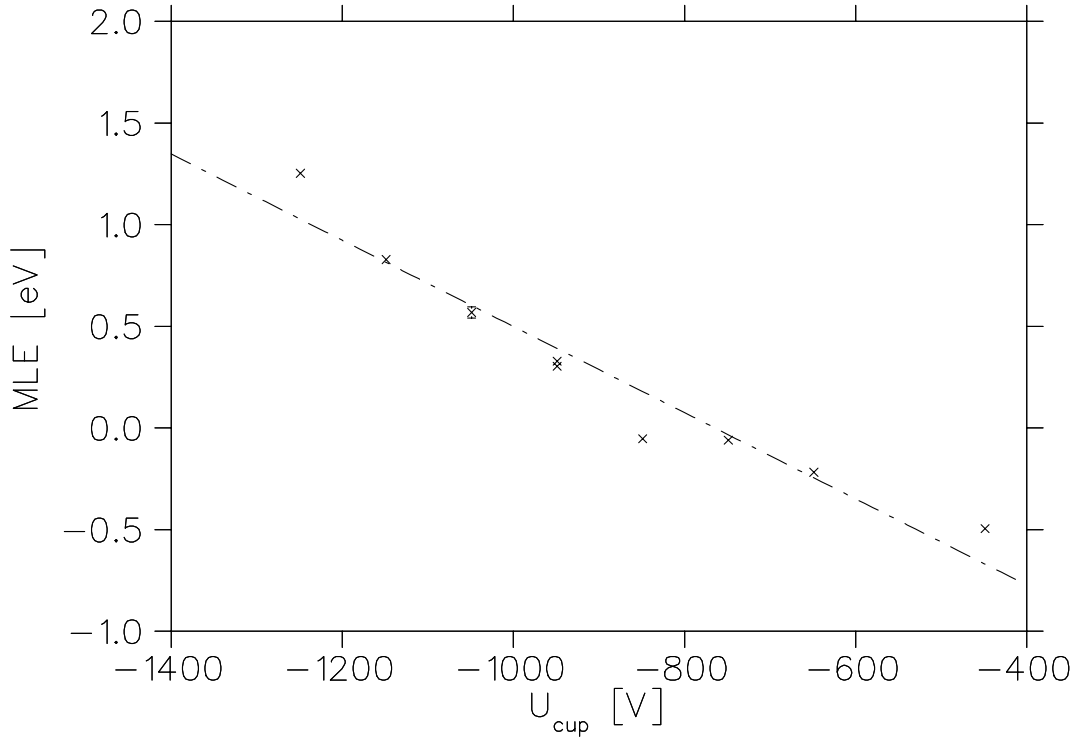

Figure 5.15: Position of the mean longitudinal energy (MLE) (relative to the cathode potential) as a function of the collector cup potential for $E_{kin} = 1349\,\text{eV}$, $\alpha = 16$, $n_e = 3.7 \cdot 10^{12}\,1/\text{m}^3$, $I_{tot} = 0.3\,\text{mA}$ ($U_{ext} = 38\,\text{V}$), $E_{drift} = 400\,\text{eV}$.

acceleration resulting in a broadening. This should also be studied for higher kinetic energies. In any case the EDC measurements should be compared to the temperatures obtained from dielectronic recombination measurements to rule out systematic effects.
In Fig. 5.15 the position of the mean longitudinal energy as a function of the cup potential obtained with analyzer 2 is shown. The zero of the MLE position around $U_{cup} = -800$ coincidences well with the minimum of the energy spread as found above. This is a second sign of good conditions at the analyzer.

Pulsed vs. non pulsed

EDC measurements are very useful to study and to optimize the electron beam outside the storage ring. However, the power density $p = \frac{U_0 I_{tot}}{A_{cath}\alpha}$ (A_{cath} denotes the cathode area) becomes very high at high current densities and energies and an expansion at the collector cup is not possible. Therefore care has to be taken to not destroy the entering aperture of the energy analyzer (thin gold foil). But the power density can be reduced by pulsing the electron beam. The highest power density with a DC beam used in the EDC measurements presented in this work was $p \approx 5\,\text{W/mm}^2$. To look for differences between both methods EDC measurements of a pulsed (pulse length 1 ms, 100 ms off) and a DC beam at a relatively low energy of $E_{kin} = 400\,\text{eV}$ at expansion $\alpha = 8$ have been compared for different densities (Fig. 5.16). As one can see there is no significant difference between

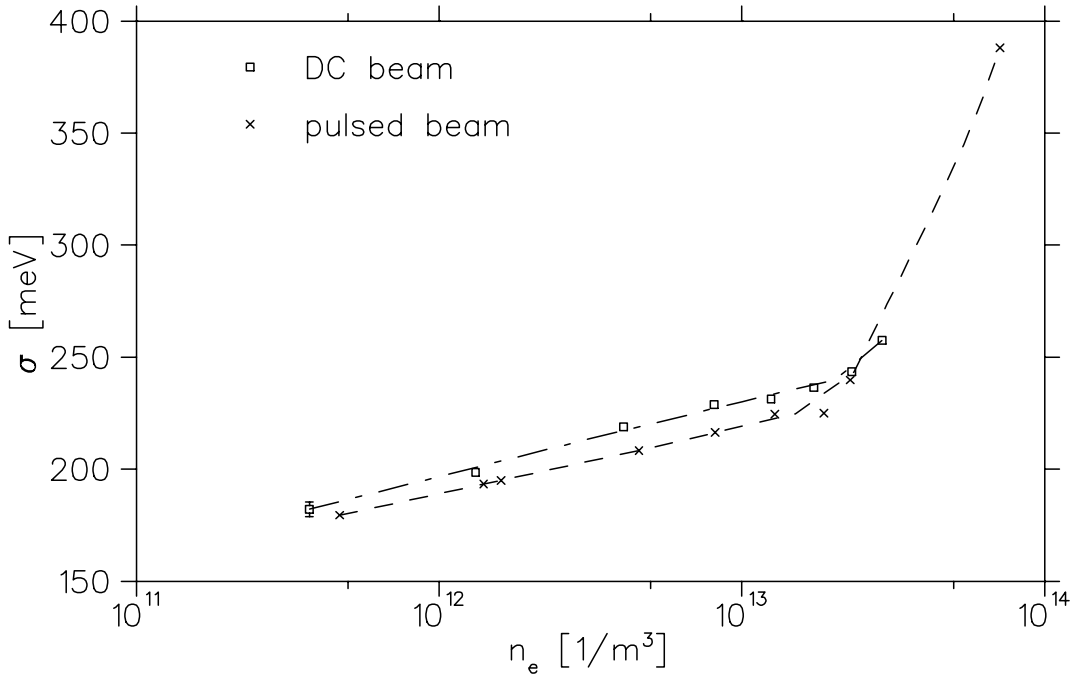

Figure 5.16: Comparison of the energy spreads a pulsed and a DC electron beam as a function of the density. The beam parameters for both experiments were $E_{kin} = 400\,\text{eV}$, $\alpha = 8$, $E_{drift} = e \cdot U_{ext}$. The lines are plotted to guide the eye.

the two methods. But the pulsed data points lie slightly below the DC ones. In future experiments this has to be studied also at higher energies.

Electron density

For a precise determination of contributions of the acceleration to the LLR process it is important to know the electron density with sufficient accuracy. From the experiment two different values are accessible to calculate the density. The first is the total electron current I_{tot}, which is measured at the collector cup. From this value we calculate $n_{e,total}$ which is the average density in the beam. The second is the local density $n_{e,local}$ from the local current I_{local} that reaches the collector electrode in the analyzer for blocking potential zero. This value comes directly from the EDC measurement via the I/U-device. For a homogeneous electron density distribution the two values should agree. Fig. 5.17 shows the densities calculated from the local and the total current for the same data points as in Fig. 5.22. In the graph a dashed line is drawn which indicates the equality of both densities. For high densities ($> 10^{12}\,\text{m}^{-3}$) both values agree very well, for lower densities $n_{e,local}$ is higher than $n_{e,total}$. This is probably an effect of the electron density distribution which changes with the extraction voltage and which has not been adjusted by the Pierce voltage before every measurement. The space charge should not play a role because the density changes only about 1% from the beam center to the edge for the given kinetic energy and expansion. The densities given in the following represent always the

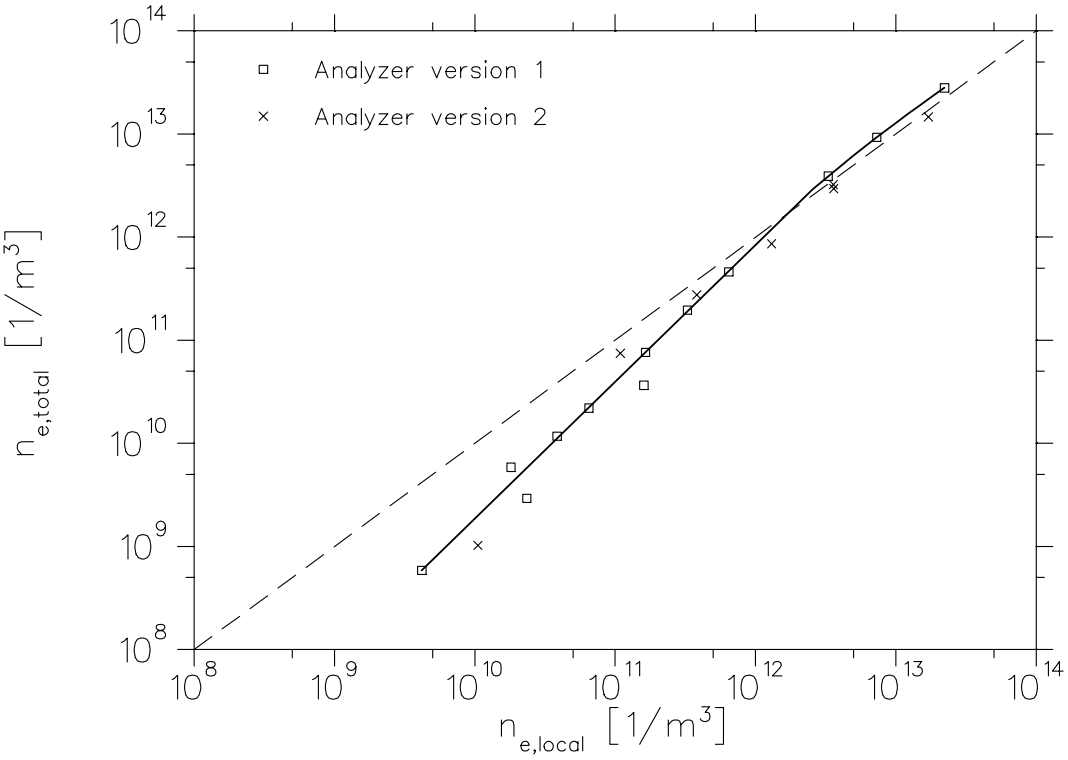

Figure 5.17: The density $n_{e,local}$ derived from the current measured at the energy analyzer versus the density $n_{e,total}$ derived from the total electron current is shown. Analyzer version 1 is compared to analyzer version 2 for $E_{kin} = 2000\,\text{eV}$ and $\alpha = 8$. The dashed line indicates the equality of the densities and the solid line through the data points is to guide the eye.

local density $n_{e,local}$.

5.2.4 Relaxation processes

In section 3.3 two relaxation processes in the magnetized electron beam have been presented: potential energy relaxation (LLR) and kinetic energy relaxation (TLR). With first EDC measurements at the ETS we tried to understand contributions to the final longitudinal temperature by these processes. In the following we show the influence of several beam parameters on the measured energy spreads.

Magnetic guiding field

The influence of the magnetic guiding field under conditions where the TLR should be strong has been measured for three field values. A slow electron beam with $E_{kin} = 200\,\text{eV}$ and an energy of $E_{drift} = 30\,\text{eV}$ in the expansion region has been used. Tab. 5.5 summarizes the measurement.
A small magnetic guiding field of $B_0 = 0.05\,\text{T}$ with no expansion gives a very broad

B_0 [T]	α	n_e [1/m^3]	σ [meV]
0.05	1	$4.32 \cdot 10^{12}$	916
0.05	4	$2.31 \cdot 10^{12}$	525
0.075	4	$2.39 \cdot 10^{12}$	325
0.097	8	$1.16 \cdot 10^{13}$	209

Table 5.5: Dependence on the measured energy spreads of the magnetic guiding field.

energy spread. By increasing the expansion to $\alpha = 4$ reduces σ by about 40%. Keeping the expansion and the density constant and increasing B_0 to 0.075 T, yet leads to a further reduction of σ. A lower limit for σ under the given conditions can probably be given by the last measurement in the above table with $B_0 = 0.097$ T and $\alpha = 8$. In the following measurements a magnetic guiding field $B \approx 0.09$ T has been used, we therefore do not expect a broadening of the measured EDCs because of a too low guiding field. The dependence on the expansion ratio will be shown in the following paragraph.

Magnetic Expansion

A series of measurements has been performed as a function of the expansion ratio α. We have chosen two different densities and the density was kept constant to be independent of LLR while α has been changed. Keeping the density constant implies that the emission current has to be increased which is done by increasing the extraction voltage. In this measurement the energy in the expansion region is given by the extraction voltage because U_{drift} has been kept on U_{ext}. This leads to a mixing of two effects: (i) suppression of TLR by the increasing initial magnetic field for higher α and (ii) dependence on the TLR of the kinetic energy in the expansion region (see next paragraphs). This relationship was not totally clear when the measurements have been performed and will be discussed in section 5.2.5.
In Fig. 5.18 the energy spread is shown for two final densities $n_e = 1.1 \cdot 10^{13}$ 1/m^3 and $n_e = 3.8 \cdot 10^{12}$ 1/m^3 at a final energy of $E_{kin} = 2$ keV as a function of α. For the lower density the dependence on α is much weaker. For $\alpha \gtrsim 8$ both densities show only a weak dependence on α.

Electron energy in the expansion region

Initially the electron energy is given by the extraction voltage which is necessary to extract the desired electron current from the cathode ($I_{tot} \propto U_{ext}^{3/2}$). The electron beam energy can now be further increased by applying an additional positive voltage U_{drift} to the drift tube following the extraction electrode before the electrons reach the long acceleration section (see section 4.1.5). In Fig. 5.19 the energy spread σ is shown as a function of the kinetic energy in the expansion region. For the final energy $E_{kin} = 2$ keV with no expansion ($\alpha = 1$) there is a strong reduction of σ of almost 25% by increasing E_{drift}. For $E_{kin} = 1349$ eV and $\alpha = 60$, σ does not depend on E_{drift}. This is a clear hint for a TLR process in the expansion region which can be suppressed either by increasing the magnetic field or by going to higher electron energies in the expansion region (200–300 eV). This

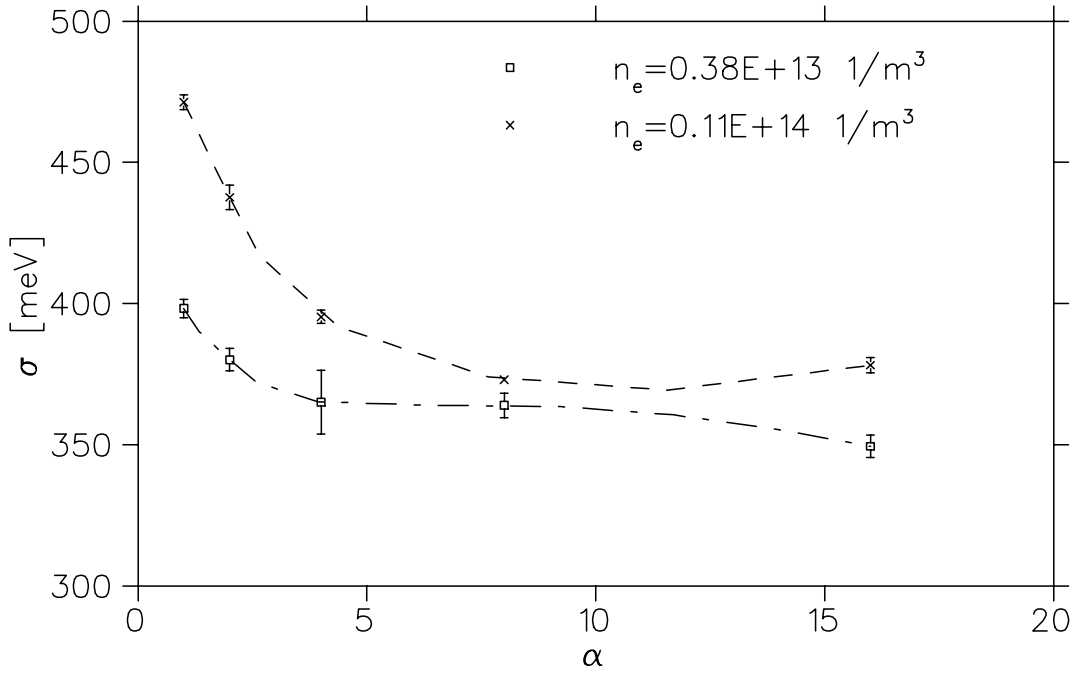

Figure 5.18: Energy spread σ as a function of the expansion ratio α with a constant final density (dashed lines are shown to guide the eye). For $n_e = 1.1 \cdot 10^{13}\,1/\mathrm{m}^3$ the extraction voltages were $U_{ext} = 17, 26, 41, 64, 100\,\mathrm{V}$ and for $n_e = 3.8 \cdot 10^{12}\,1/\mathrm{m}^3$ $U_{ext} = 9.4, 13.2, 20, 30, 50\,\mathrm{V}$. The other beam parameters were $E_{kin} = 2000\,\mathrm{eV}$, $E_{drift} = e \cdot U_{ext}$, $B_0 = 0.09\,\mathrm{T}$ and $l_a = 462\,\mathrm{mm}$ (30 electrodes, 11 steps).

will be discussed in detail in section 5.2.5. In the case of $\alpha = 60$ even a slight broadening for $E_{drift} > 300\,\mathrm{eV}$ is visible. This could be a small effect of the acceleration processes leading to a contribution by LLR.

Dependence on the kinetic energy

In Fig. 5.20 the measured energy spreads as a function of the kinetic energy are shown and in Fig. 5.21 the calculated temperatures are plotted with an expected contribution from the LLR theory. Two different currents $I_{tot} \approx 0.3\,\mathrm{mA}$ and $2.028\,\mathrm{mA}$ at expansion $\alpha = 8$ have been studied.
At first glance on Fig. 5.20 one can see that there is a minimum in the energy spread close to $E_{kin} = 300\,\mathrm{eV}$. Between the σ values for the smaller currents (open squares and crossed squares) there is no big difference visible. For lower kinetic energies, σ is strongly increasing and for higher energies it increases also, but more slowly. The curve for $I_{tot} = 2.028\,\mathrm{mA}$ (circles) lies $\approx 40\,\mathrm{meV}$ above the values for the lower current. This behavior can be explained looking at the CM-temperatures in Fig. 5.21. We see that the temperatures are strongly increasing for low kinetic energies because the kinematic reduction does not work anymore. For high energies the temperature is almost constant. The contribution from LLR has been estimated by eq. (3.56) with $C = 1$. Here we assume an acceleration that is slower than a fast acceleration ($C = 1.9$). The contribution

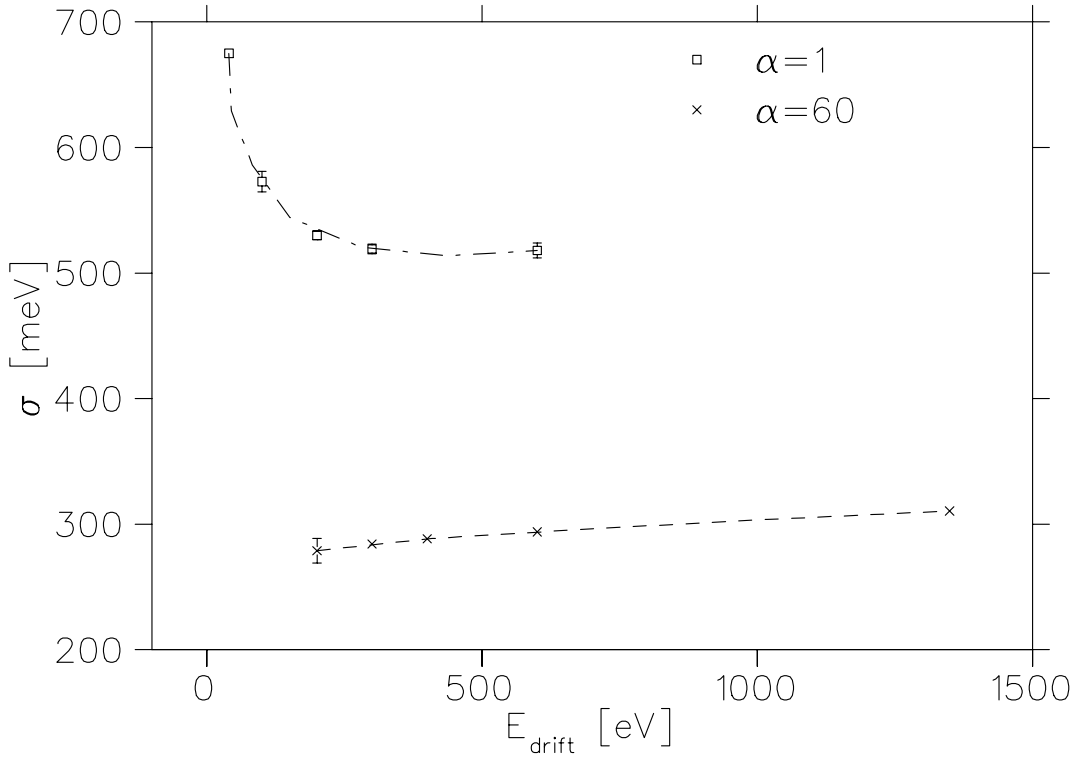

Figure 5.19: Dependence of the energy spread σ as a function of the kinetic energy in the expansion region E_{drift}. The kinetic energy is given by the voltage U_{drift} applied to the drift tube following the extraction electrode. For both curves the acceleration length was $l_a = 462\,\text{mm}$ (30 electrodes, 11 steps). The series for $\alpha = 1$ has been measured with $E_{kin} = 2000\,\text{eV}$, $I_{tot} = 0.46\,\text{mA}$ ($U_{ext} = 39.9\,\text{V}$) and $B_0 = 0.09\,\text{T}$. For $\alpha = 60$ $E_{kin} = 1349\,\text{eV}$, $I_{tot} = 1.86\,\text{mA}$ ($U_{ext} = 137.2\,\text{V}$) and $B_0 = 0.04\,\text{T}$. The plotted lines are to guide the eye.

from the cathode temperature (1050 K, dash-dotted line) and the contribution from the relaxation (density, dotted line) are drawn separately. As one can see at higher kinetic energies the temperature is only dominated by the relaxation process which is $\propto E_{kin}^{1/6}$ and therefore slowly decreasing towards this value. The line that shows the expected contribution of LLR ($C = 1$) lies slightly below the lowest measured curve. This shows that the acceleration is adiabatic. For low energies $\lesssim 500\,\text{eV}$ the deviation of the measured temperatures from the calculated LLR contribution increases strongly. The temperature is now limited by TLR (indicated area between the solid lines) which is difficult to calculate quantitatively. We will try to give some estimates in section 5.2.5. At very low kinetic energies the cathode temperature is the dominant contribution to LLR.
Additionally in Fig. 5.21 two series from Krause measured at a linear setup without expansion ($\alpha = 1$) are shown [Kra92]. The magnetic guiding field for these measurements was $B_0 = 0.07\,\text{T}$ and the total currents were $I_{tot} = 0.266\,\text{mA}$ (open diamonds) and $I_{tot} = 0.666\,\text{mA}$ (solid diamonds). The cathode used by Krause had a diameter of $d_{cathode} = 2\,\text{mm}$ which leads to a factor of $2^2/(1.6^2 \cdot \alpha) = 1.56/\alpha$ in the densities calculated by the given total currents. As one can see the ETS curves lie below these measurements which is

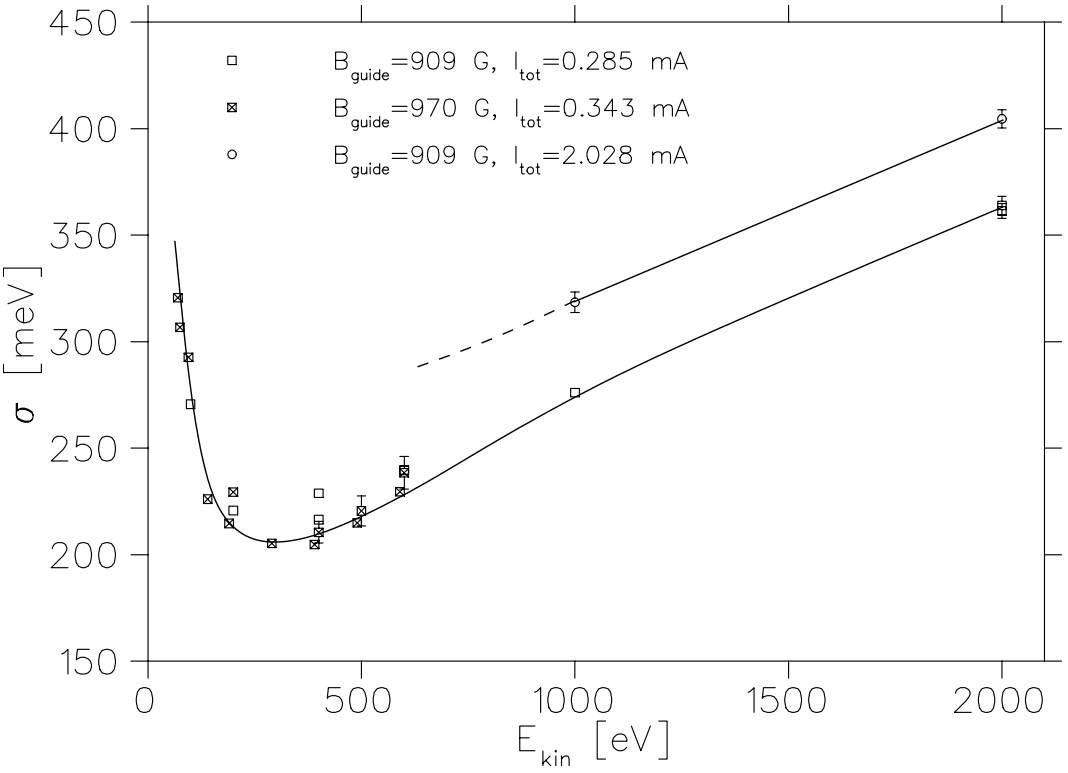

Figure 5.20: Dependence on the energy spread σ from the final kinetic energy. Two series for different currents $I_{tot} = 0.285\,(0.343)$ mA ($U_{ext} = 30$ V) and $I_{tot} = 2.028$ mA ($U_{ext} = 100$ V) are plotted. The following beam parameters have been used: $\alpha = 8$, $B_0 = 0.091\,(0.097)$ T, $U_{cup} = 0$ V, $E_{drift} = e \cdot U_{ext}$ (the lines are shown to guide the eye).

probably a manifestation of TLR suppression by the higher initial magnetic field ($\alpha = 8$).

Dependence on the density

In the LLR theory the mean particle distance for the Coulomb interaction is calculated from the electron density. In Fig. 5.22 the dependence of the longitudinal temperature on the final electron density is shown. We compared the analyzer version 1 with the new analyzer version 2 at $E_{kin} = 2000$ eV and one measurement series with the new analyzer was performed under the conditions used in the first F^{6+} beamtime (see section 6.2). For $n_e > 10^{12}\,1/\mathrm{m}^3$ the analyzer version 1 (squares, dash-dotted line) gives the same results as the new analyzer (crosses, solid line). But for smaller densities there is a significant discrepancy in the temperature in the order of 3–4 μeV. This is a clear sign of problems related to the design of analyzer version 1 like the supposed charging that lead to a broadening of the EDC (see section 5.2.2). Actually the data shown here are from a series of measurements where the charging was weak.
The temperatures determined for $E_{kin} = 1349$ eV (circles, dashed line) are 3–10 μeV higher than the values for $E_{kin} = 2000$ eV. This is probably a manifestation of TLR because the magnetic guiding field was a factor of 2 smaller. But the values are interesting because

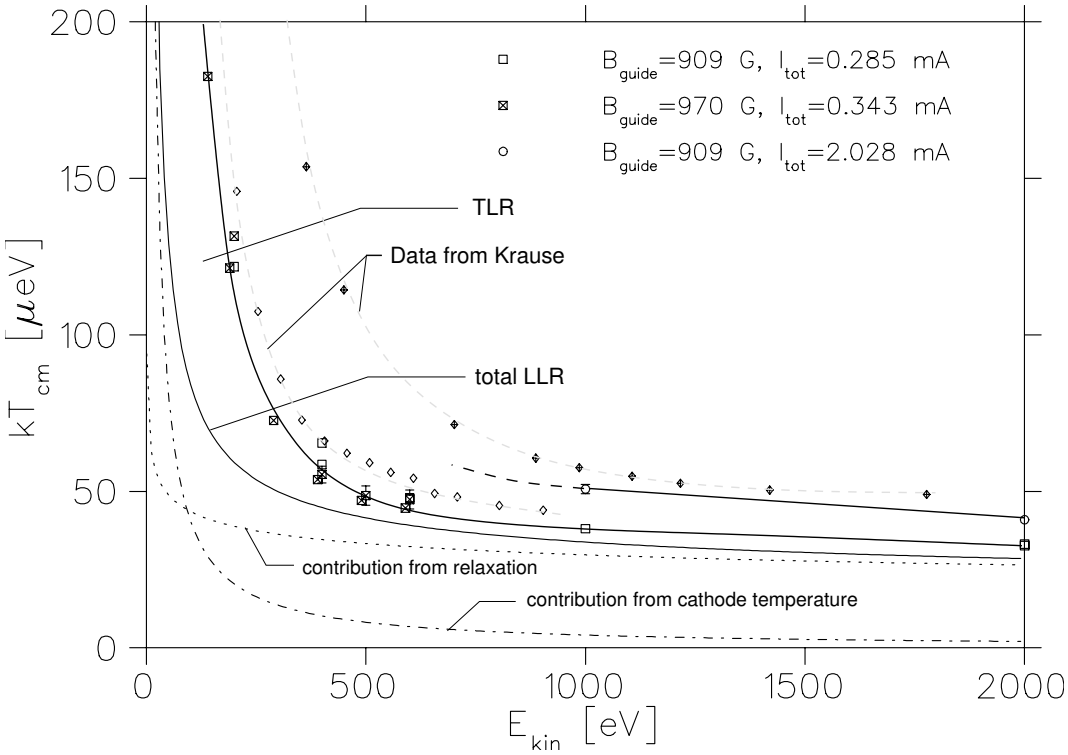

Figure 5.21: Longitudinal CM electron temperature calculated from the data points of Fig. 5.20. Two series from [Kra92] have been added for comparison and the theoretical contributions of the cathode temperature (1050 K) (dash-dotted line) and the relaxation (dotted line) from the LLR theory (see eq. (3.56)) have been calculated. The lines through the data points are plotted to guide the eye.

they can be compared to the longitudinal temperatures from the DR temperature analysis.
The resolution limit of the analyzer seems not be reached at the low temperatures of $10\,\mu$eV for densities smaller than $10^{10}\,1/\mathrm{m}^3$. We therefore estimate the analyzer resolution to $\Delta E_{res} < 10\,\mu$eV. Because of technical reasons it was not possible to extend the measurements to lower densities. For a more precise determination of the analyzer resolution this would be desirable.

Acceleration structure

The long adiabatic acceleration section of the ETS in combination with the magnetic expansion is a completely new feature in electron cooling devices which could be studied for the first time. The ideas of the adiabatic acceleration have been discussed in section 3.3.4 and go back to Parkhomchuk et al. Promising results from Krause [Kra92] and the ideas to install a photocathode for ultracold beams [Hab88] where a strong motivation to install a long acceleration section in the new ETS.
In the first measurements three different acceleration schemes have been studied. A short

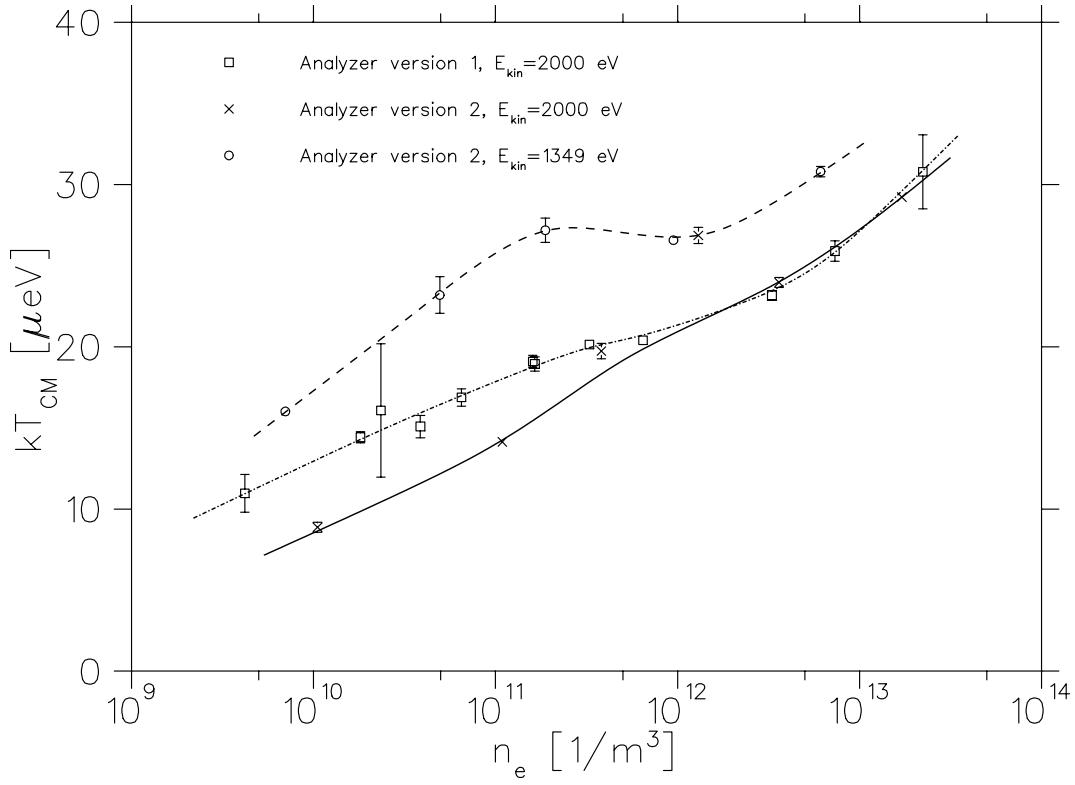

Figure 5.22: The graph shows the dependence on the longitudinal temperature in the CM frame of the electron beam as a function of the final electron density. Three different curves with an acceleration length $l_a = 462\,\text{mm}$ (30 electrodes, 11 steps) are plotted. Analyzer version 1 (squares) compared to analyzer version 2 (crosses) at $E_{kin} = 2000\,\text{eV}$, $\alpha = 8$, $E_{drift} = 200\,\text{eV}$, $B_0 = 0.091\,\text{T}$, $U_{cup} = -1500\,\text{V}$. Another measurement with analyzer version 2 (circles) under conditions that where used in the first F^{6+} beamtime was performed: $E_{kin} = 1349\,\text{eV}$, $\alpha = 60$, $E_{drift} = 400\,\text{eV}$, $B_0 = 0.04\,\text{T}$, $U_{cup} = -949\,\text{V}$. The plotted lines are only to guide the eye.

acceleration length of only $l_a = 12.7\,\text{mm}$ where the first electrode behind the drift tube was put to ground (one voltage step). An intermediate acceleration length of $l_a = 462\,\text{mm}$ (11 voltage steps, 33 electrodes with three electrodes on the same potential). Finally the longest possible length of $l_a = 1490\,\text{mm}$ with all electrodes has been used. For an electron energy of $E_{kin} = 2\,\text{keV}$ and a relatively high density of $n_e = 2.18 \cdot 10^{13}\,1/\text{m}^3$ the result is shown in Fig. 5.23. Within the error bars there is no significant change visible only a slight tendency to lower σ for the longest acceleration length if one looks at the mean values (indicated by the dashed line). This observation is in agreement with results from Krause where the dependence on the final temperature was studied as a function of the acceleration length at different energies. The result is also clear from geometrical considerations of the acceleration electrodes. The inner diameter of the electrodes is rather large ($\approx 100\,\text{mm}$) which smooths the potential distribution in the center. Moreover even for the shortest acceleration length the acceleration is performed in three steps: acceleration to extraction voltage, to drift voltage and then to the final

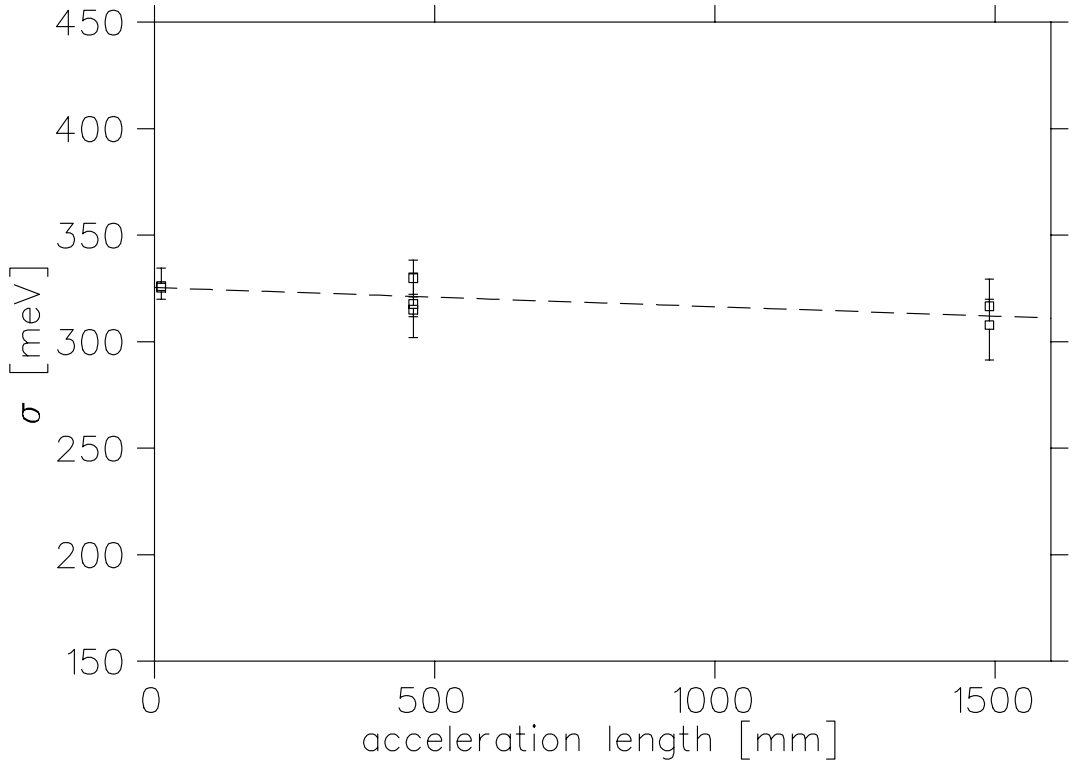

Figure 5.23: Longitudinal energy spread σ as a function of the acceleration length l_a with $E_{kin} = 2000\,\text{eV}$, $\alpha = 8$, $E_{drift} = 200\,\text{eV}$, $I_{tot} = 2\,\text{mA}$ ($U_{ext} = 100\,\text{V}$), $n_e = 2.2 \cdot 10^{13}\,1/\text{m}^3$, $B_0 = 0.091\,\text{T}$. The dashed line is a fit to the mean values.

voltage. For low kinetic energies in the range up to 2 keV this seems to be already sufficient for an adiabatic acceleration. In section 5.2.5 more detailed calculations of the adiabaticity parameter λ will be shown for $E_{kin} = 2\,\text{keV}$ and 10 keV which show that the longer acceleration will become important at higher energies.

data set	α	E_{drift} [eV]	I_{tot} [mA]	B_0 [T]	σ [meV]	$kT_\parallel$ [μeV]	Fig.
1	16	100	2	0.09	378	35	5.18
2	1	17	0.15	0.09	471	55	5.18
3	1	100	0.46	0.09	573	82	5.19
4	1	600	0.46	0.09	518	67	5.19

Table 5.6: Parameters used for the comparison of the measurements with calculations of the TLR heating.

5.2.5 Discussion

Approach to TLR

In this section we will try to explain some of the observations from the measurements by analyzing quantities that are used in the different TLR theories that have been presented in section 3.3.5. This explanation will be a qualitative one, trying to understand the processes that are going on, mainly in the magnetic expansion region of the experimental setup. Because of the exponential dependence of the TLR theories in the presence of a magnetic field it is difficult to give quantitative values calculated from the heating rates. Even in the prefactor $(dT_\parallel/dz)_0$ describing the heating rate without magnetic field there are differences (numerical factors and in the Coulomb logarithm) depending on the applied theory.
The measurements of the energy spread as a function of kinetic the energy in the expansion region (drift tube voltage, see Fig. 5.19) and as a function of the expansion ratio (Fig. 5.18) showed a behavior that can probably be explained by TLR. The influence of LLR effects are expected to be small because the acceleration is slow in the considered cases and will be discussed in the following section.
With the software package MAFIA the electric potential $\Phi(z)$ has been calculated for the experimental geometry giving the kinetic energy $E_{kin}(z)$ of the electrons along the beam axis. With the emission current, the density $n_e(z)$ has been calculated taking the expansion ratio into account. The magnetic field has been calculated by analytical formulas and this yields the transverse temperature by ATE with eq. (3.50). The longitudinal temperature is calculated by eq. (3.56) with $C = 1$ (which represents the adiabatic acceleration) without taking an increase of the temperature by TLR into account. But the transfer of energy from the transverse degree of freedom to the longitudinal temperature due to the expansion has been considered by eq. (3.52). We have chosen according to the performed measurements the data sets given in Tab. 5.6 (except the value for $\alpha = 32$ with $U_0 = 2000\,\mathrm{V}$ which was 60 with $U_0 = 1349\,\mathrm{eV}$ in the experiment) to compare them to the experiment. The measured energy spreads σ and the derived temperatures are also given in the table. In Fig. 5.24 the calculated beam properties as a function of the distance from the cathode are shown. In part (a) the kinetic energy for the different accelerations is shown, in (b) the magnetic field, in (c) the electron density, in (e) the longitudinal temperature and in (f) the transverse temperature.
One sees that in the expansion region ($z \lesssim 220\,\mathrm{mm}$) $kT_\parallel$ and $kT_\perp$ are strongly changing.

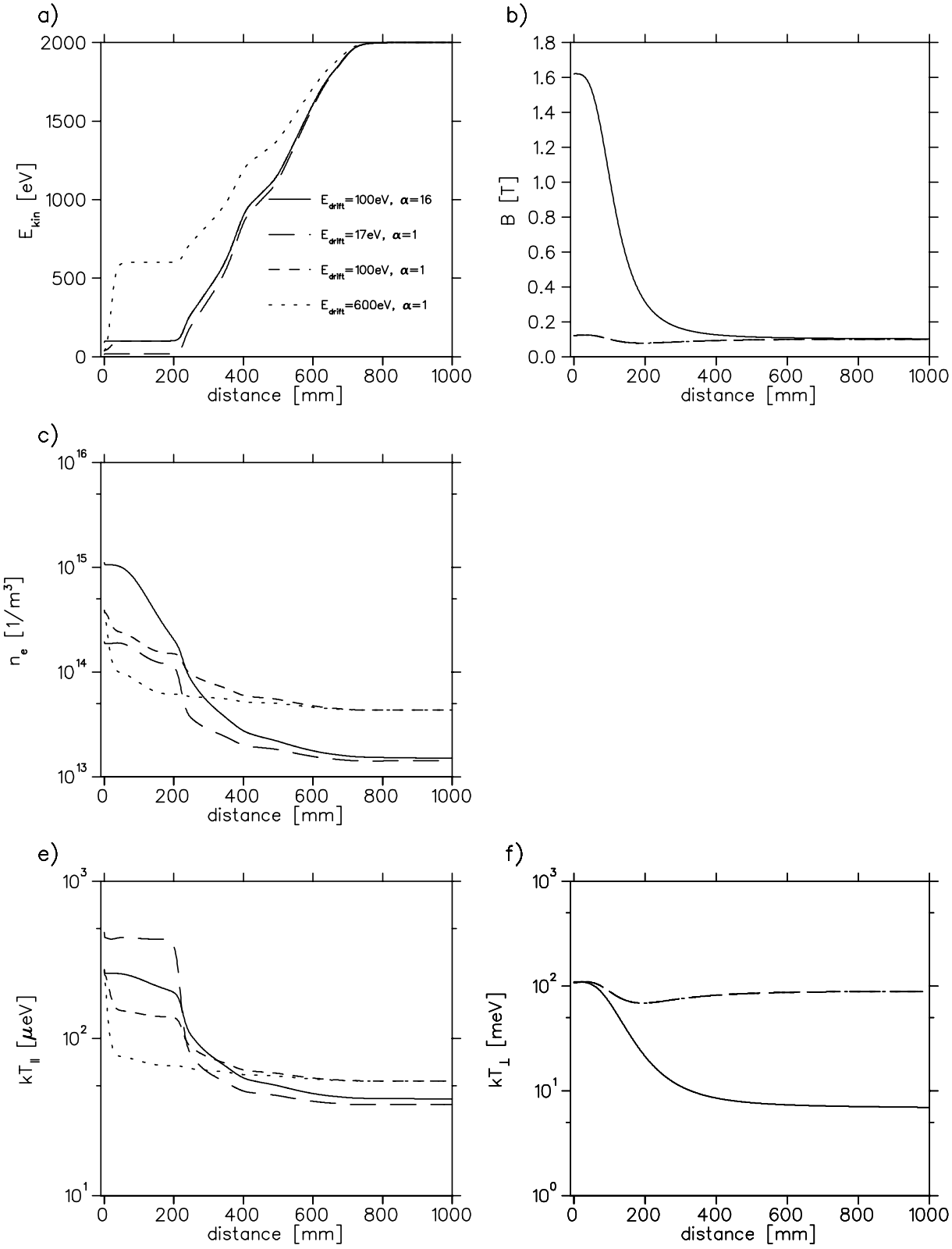

Figure 5.24: Several electron beam parameters as a function of the traveled distance along the beam axis. a) shows the kinetic energy for the acceleration structure from numerical calculations. b) magnetic field in the expansion region. c) electron density. e) longitudinal temperature and f) transverse temperature.

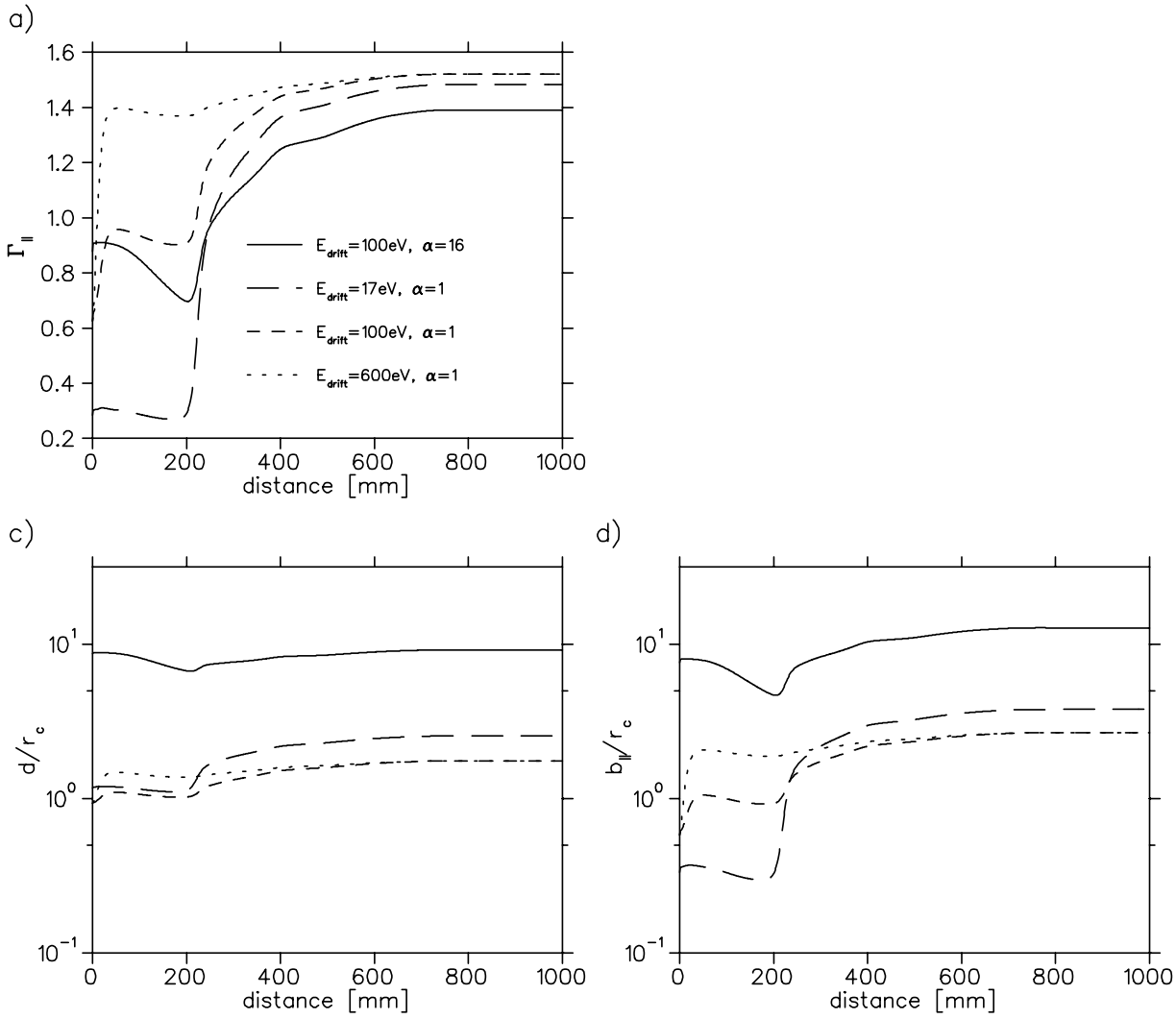

Figure 5.25: Estimation of the beam magnetization: a) longitudinal correlation factor. c) criterion for weak magnetization in a weakly correlated plasma. d) criterion for strong magnetization if the first criterion (c) is satisfied.

$kT_\parallel$ depends on the density n_e which is strongly reduced by the acceleration and the magnetic expansion. $kT_\perp$ depends only on α.
From this quantities we can estimate the degree of magnetization of the beam which is a measure how strong the TLR is suppressed by the magnetic field. In section 3.3.5 two criteria for the magnetization in the case of a weakly correlated plasma ($\Gamma_\parallel < 1$, kinetic energy larger than thermal energy) have been formulated: (i) Larmor radius much smaller than the mean particle distance ($r_c \ll d$) for weak magnetization and additionally (ii) thermal distance of closest approach much smaller than the Larmor radius ($r_c \ll b_\parallel$) for strong magnetization.
In Fig. 5.25 the calculated properties are shown as a function of the distance from the cathode: (a) correlation factor $\Gamma_\parallel$, (c) d/r_c and (d) $b_\parallel/r_c$. As one can see $\Gamma_\parallel$ reaches values

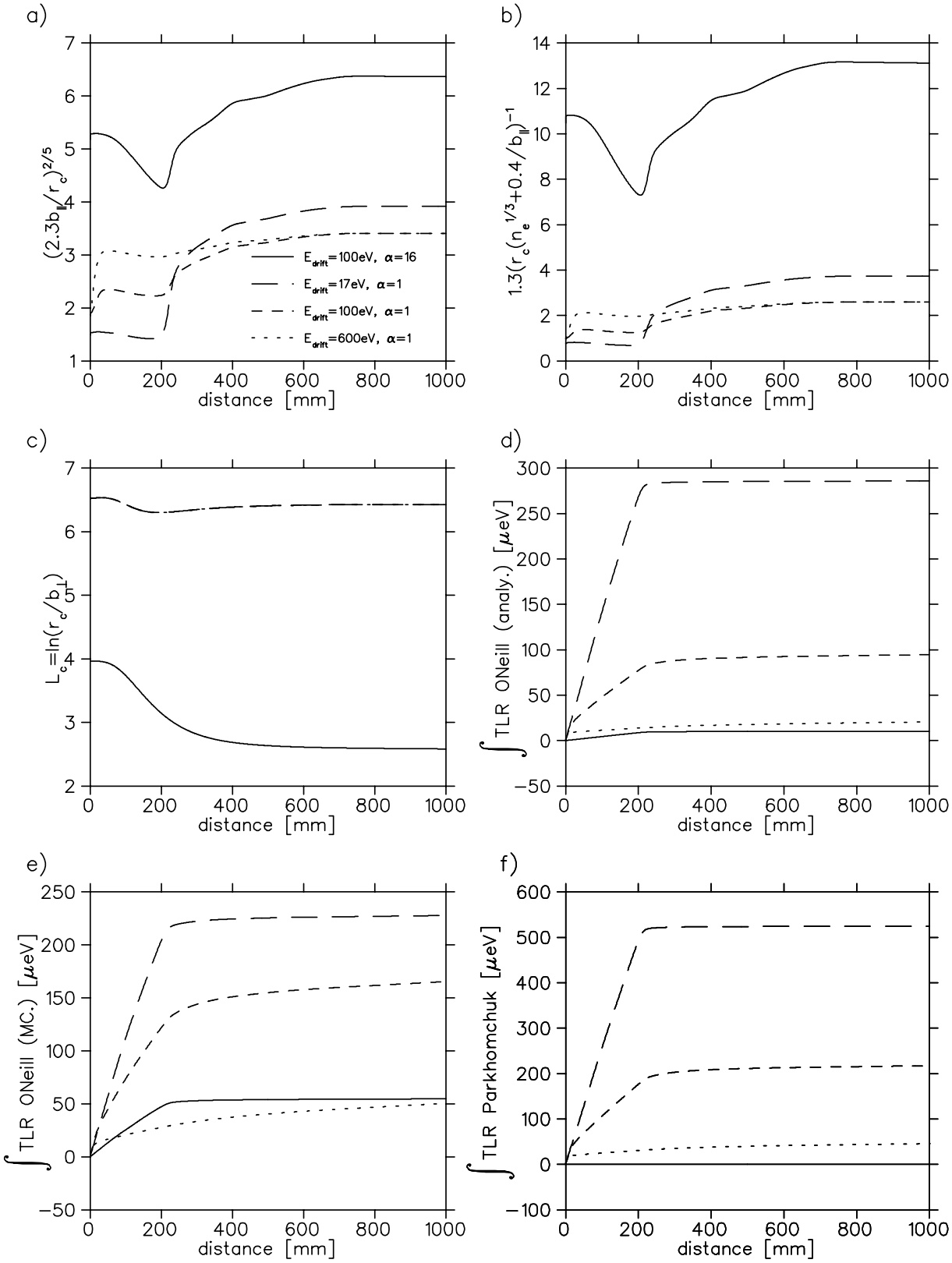

Figure 5.26: Calculation of TLR heating for different theoretical approaches (electron beam properties as indicated): a) shows the exponent from an analytical approach (O'Neill). b) shows the exponent from an empirical theory (Parkhomchuk). c) shows the Coulomb-logarithm from the O'Neill theory. In (d-f) the calculated TLR-integrals for the three different approaches are plotted: d) O'Neill analytical, e) Monte-Carlo and f) Parkhomchuk.

data set	α	E_{drift} [eV]	$kT_{\parallel}^{exp}$ [μeV]	O'Neill (analy.) $kT_{\parallel}^{calc}$ [μeV]	O'Neill (MC) $kT_{\parallel}^{calc}$ [μeV]	Parkhomchuk $kT_{\parallel}^{calc}$ [μeV]
1	16	100	35	51	96	42
2	1	17	55	324	266	562
3	1	100	82	148	219	271
4	1	600	67	74	104	99

Table 5.7: Calculated final temperatures using different theoretical formulas for TLR (see text).

up to ≈ 1.5. This is limited by the constant C from the LLR relaxation process for high kinetic energies to $\Gamma_{max} = (1/C)(4\pi/3)^{1/3} \approx 1.6$ (see section 3.2.1). We will consider this in the following as weakly correlated. The interesting part is always the expansion region where all beam parameters are strongly changing.
First we want to discuss the dependence on the expansion (data set 1 and 2). For $\alpha = 1$ and $E_{drift} = 17\,\mathrm{V}$ (long dashed line) the beam is not well magnetized in the expansion region because $d/r_c \approx 1$. For $z > 220\,\mathrm{mm}$, d/r_c is only slightly higher than 1 which could be considered as weakly magnetized. For $\alpha = 16$ (solid line), $d/r_c \gg 1$ and also $b_{\parallel}/r_c \gg 1$ over the complete distance. We can consider this as strongly magnetized. One thus expects a lower final electron temperature for $\alpha = 16$ which has been found in the experiment. This result is not really surprising because of the strong difference of the initial magnetic field.
More interesting is the observation for the kinetic energy given by E_{drift} in the expansion region (data sets 3 and 4). It has been seen that for $\alpha = 1$ the measured energy spread strongly depends on the drift energy. The calculations are shown in the figures with a short dashed line for $E_{drift} = 100\,\mathrm{eV}$ and with a dotted line for $E_{drift} = 600\,\mathrm{eV}$. For the higher energy the density is stronger reduced in the expansion region (see Fig. 5.24 (c)) which implies also a stronger reduction of the longitudinal temperature. The transverse temperature is the same in both cases. For $E_{drift} = 100\,\mathrm{eV}$, $d/r_c \approx 1$ in the expansion region and only slightly higher beyond. For $E_{drift} = 600\,\mathrm{eV}$, $d/r_c > 1$ in the expansion region and goes to the same value as for $E_{drift} = 100\,\mathrm{eV}$ at larger distances. Both beams are not well magnetized but one expects a lower temperature because of slightly higher magnetization for $E_{drift} = 600\,\mathrm{eV}$ what has been seen in the experiment.
After this qualitative approach where the experimental observations could be related to magnetization criteria we now try to calculate final temperatures with the different TLR theories presented in section 3.3.5. Two things are needed for that: the exponent for the exponential function and the prefactor where the Coulomb logarithm is the important value. In Fig. 5.26 we calculated the required quantities as a function of the traveled distance along the beam axis in the changing magnetic field and with the increasing potential energy as defined by the acceleration scheme (see above). Part (a) shows the exponent from eq. (3.70) (O'Neil analytical approach). (b) shows the exponent from eq. (3.57). There is no plot for the O'Neill Monte-Carlo results because the values for the integral are directly taken from Fig. 3.5. (c) shows the Coulomb-logarithm needed for eq. (3.70).

In (d-f) the calculated TLR-integrals for the three different approaches are plotted. We summarize the final temperatures calculated from the integrals in Tab. 5.7 together with the measured results.
In the O'Neill exponents (a) the curves for the four data sets are closer together than those from the Parkhomchuk formula (b) because of the exponent 2/5. The Parkhomchuk exponent gives a strong suppression for $\alpha = 16$ (solid line), but smaller values for $\alpha = 1$ than O'Neill. The values for $\alpha = 1$ are comparable. In (c) only two curves are visible because r_c and $b_\perp$ depend only on the magnetic field (three identical curves for $\alpha = 1$ and a different one for $\alpha = 16$). For $\alpha = 1$, L_C is almost constant ≈ 6.4 which agrees very well with the empirical factor of 6.43 from Parkhomchuk. For $\alpha = 16$, L_C decreases from 4 to ≈ 2.6. From the small values of L_C one already sees that the empirical formula does not well describe the expanded electron beam.
Looking now at the integrals we will start with part (d). For $\alpha = 16$ there is almost a complete TLR suppression and the integral is only slightly higher for $\alpha = 1$ and $E_{drift} = 600\,\text{eV}$ (dotted line). The highest values ($\approx 280\,\mu\text{eV}$) appear for $\alpha = 1$ and $E_{drift} = 17\,\text{eV}$ (long dashed line). As one can see almost all heating takes place in the expansion region where the transverse temperature is high.
The values calculated from the Monte-Carlo-theory show a different behavior. The smallest end value is calculated from $\alpha = 1$ and $E_{drift} = 600\,\text{eV}$ which shows a strong increase in the beginning (probably acceleration to the drift voltage) and then only a slow increase; the curve for $\alpha = 16$ is only slightly higher. All the heating happens in the expansion region. Again the values for $\alpha = 1$ and $E_{drift} = 17\,\text{eV}$ are the highest ($\approx 230\,\mu\text{eV}$) but they are smaller than in the analytical theory. The general trend of the empirical theory in (f) agrees with the analytical theory in (d) but the end values are almost a factor of 2 higher. For $\alpha = 16$ no heating is found, TLR is totally suppressed.
We can now compare the calculated final temperatures with the measured temperatures from the experiment (see table above). All theories produce the lowest value for $\alpha = 16$, which agrees with the experimental finding. But all calculated temperatures are too high. The calculated values for $\alpha = 1$ and $E_{drift} = 17$ and $100\,\text{eV}$ show a very big deviation from the measurement. The calculated values are a factor of 5–10 higher than measured for $E_{drift} = 17\,\text{eV}$ and slightly smaller for $E_{drift} = 100\,\text{eV}$ (factor 2–3). For $E_{drift} = 600\,\text{eV}$ the agreement with the experiment is better. Also the observation that the measured temperatures for $E_{drift} = 600\,\text{eV}$ are higher than for $E_{drift} = 100\,\text{eV}$ and $\alpha = 16$ is reproduced. Especially in the cases where stronger heating rates are expected (data sets 2 and 3) the theories are overestimating the heating processes.
We can conclude that none of the theories can reproduce the measured dependencies and the underlaying relaxation processes are not adequately implemented. The O'Neill theories are made for an isotropic strongly magnetized plasma which can not be assumed in our application. The Parkhomchuk theory is deduced from experimental results but under different conditions of the electron beam. Further measurements will be helpful to improve the understanding.

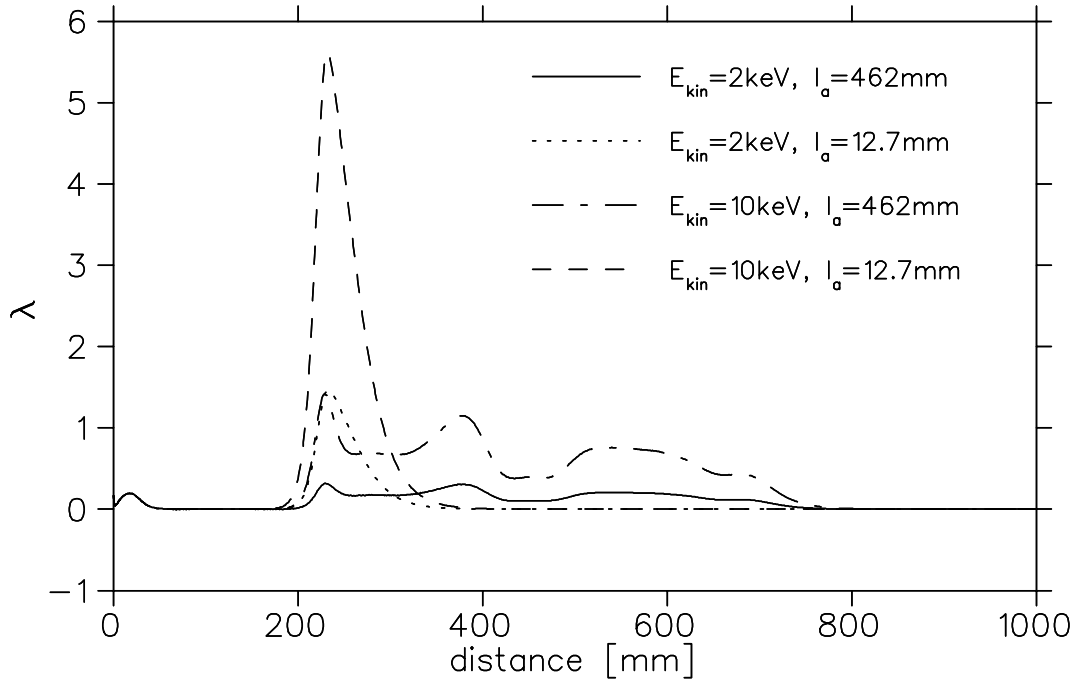

Figure 5.27: The calculated adiabaticity parameter of the acceleration along the beam axis is shown for two kinetic energies and two acceleration lengths (as indicated in the graph). The other beam parameters for the calculation are given by $E_{drift} = 200\,\text{eV}$, $\alpha = 8$ and $I_{tot} = 2\,\text{mA}$.

Adiabatic acceleration

The Coulomb interaction between the electrons leads to an increase of the final longitudinal temperature (LLR) which is described in the theory by the mean particle distance $n_e^{-1/3}$ and an empirical factor C that describes the acceleration (see section 3.3.4). By an adiabatic acceleration C can be decreased. The adiabaticity of the acceleration was defined in eq. (3.54) by $\lambda = \frac{v}{\omega_p(z)} \cdot \frac{1}{E_{kin}} \frac{dE_{kin}}{dz}$. The plasma frequency ω_p describes the time scale for the relaxation process and is proportional to $\sqrt{(n_e)}$. This implies that the relaxation towards equilibrium is faster for higher densities. We will now calculate λ for several acceleration schemes.
In Fig. 5.27 we compare two final kinetic energies $E_{kin} = 2\,\text{keV}$ and $10\,\text{keV}$ for two acceleration lengths $l_a = 12.7\,\text{mm}$ (1 electrode) and $462\,\text{mm}$ (30 electrodes, 11 voltage steps). The kinetic energy in the expansion region was $E_{drift} = 200\,\text{eV}$ for all cases. The shape of the acceleration potential is similar to the ones shown in Fig. 5.24 (a).
The highest λ value was calculated for $E_{kin} = 10\,\text{keV}$ and the short acceleration length (dashed line). By choosing the longer acceleration length, λ could be decreased about almost a factor of 4 at the maximum (dash-dotted line) and stays close to or below one over the whole acceleration structure. From that we expect a significant difference in the final longitudinal temperature in the experiment.
Looking at $E_{kin} = 2\,\text{keV}$ we see that for $l_a = 12.7\,\text{mm}$ (dotted line) the maximum has

about the same height as for $E_{kin} = 10\,\text{keV}$ and the long acceleration length. For the long acceleration length, λ stays always well below 1 (solid line). In the experiment there has been no heating seen at $E_{kin} = 2\,\text{keV}$ for both acceleration lengths (see Fig. 5.23) which is an indication that for $\lambda \approx 1$ the acceleration can be still called adiabatic.
The oscillations that appear in λ along the acceleration are produced by larger gaps between the acceleration electrodes where two acceleration tubes (see Fig. 4.13) are connected.

5.2.6 Conclusion

The measurements and calculations of the relaxation processes in the electron beam are only a first step towards a more detailed understanding. The beam properties are strongly changing during the transition from the cathode to the final energy in the magnetic expansion region. This could be clearly demonstrated by calculating the electron beam properties (density, temperatures) as a function of the kinetic energy and the magnetic guiding field. From these properties one can start to calculate the relaxation processes. Further measurements have to be performed to obtain a better model for the TLR process which is challenging because of the involved magnetic field. The magnetic fields are such that the electron plasma is often in an intermediate region between weak and strong magnetization. These are similar problems that occur also in the electron cooling theory. We also want to point out that the main goal of the first measurements was to implement the experimental procedures and to understand the basic processes especially in the expansion region. For a deeper understanding one has to try to separate the TLR and LLR processes by the experimental conditions which could not always be achieved. But the ETS is ideally suited for such measurements because of the great flexibility in the acceleration structure and the superconducting magnet that allows high expansion ratios.

6. First operation in the storage ring

Shortly after completion of the setup the new electron target section has been operated for the first time inside the TSR. In a first beamtime, a 73.3 MeV C^{6+} beam has been cooled with an ETS electron beam of 9 mm diameter and a density of $n_e = 10^{12}\,\mathrm{m}^{-3}$ without using the existing electron cooling device (EC) (see section 6.1). It could be shown that the storage ring can be operated with a horizontal cooler and the resulting vertical orbit perturbation due to the toroid magnets. With the gained experience and the detector system becoming operational meanwhile a second beamtime performing DR measurements with lithium-like F^{6+} at 46.4 MeV has been accomplished. F^{6+} is a well known system which allowed it to do benchmark tests and compare it with the existing data measured with the electron cooler (see section 6.2). In particular the low lying resonance at 11.4 meV was used to determine the longitudinal and the transverse temperatures to see effects of the magnetic expansion and the adiabatic acceleration. This was the first time that the transverse temperatures could be deduced at the ETS because the EDC measurements with the retarding field analyzer only deliver the longitudinal temperatures.

6.1 ETS in the TSR

6.1.1 Procedure

In the very first operation the ion beam has been stored and electron cooled with the ETS still switched off. We then started to turn on all magnetic fields in small steps adjusting the correction dipole magnets to keep the ion beam in the ring. Having found acceptable settings, we measured the ion beam position in the interaction section with the position pickup electrodes (see section 4.2.2). The electron target beam was now aligned as good as possible with the pickup electrodes to the ion beam. For that procedure the electron beam has to be modulated (typical amplitude 800 mV on the control signal for the extraction voltage, frequency $\approx$ 16 kHz) to see a signal on the pickup electrode. In Fig. 6.1 typical sum and difference signals on the Pickup electrode are shown. On the left side the ion beam signal is shown with the revolution frequency of the bunches of $\approx$ 3.1 MHz. On the right hand side the sinusoidal electron beam signal.
The electron beam in the ETS was then switched off and with the electron cooler currents in the range of 60 μA have been accumulated. Setting the electron energy and the density in the ETS to similar values like in the electron cooler we then tried to find an overlap where electron cooling should be visible. Switching now the electron beam in the ETS

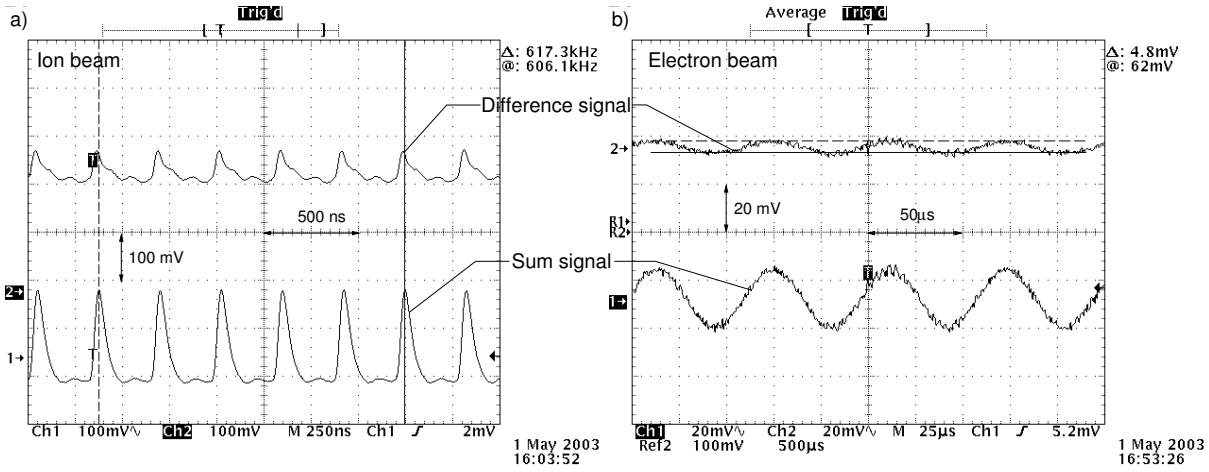

Figure 6.1: Signals measured with the position pickup electrodes: a) signal of the ion beam. b) signal of the modulated electron beam. The upper graphs show the difference signal and lower graphs the sum signal.

on, looking at the Schottky spectra and adjusting the parameters we could find settings where the electron target beam is shifting the ion beam to a different energy which is visible by a frequency shift in the Schottky spectrum. Once the electron energy was close to the ion beam energy, we moved the electron beam with the steering coils. With the toroid steering coils one can change the position of of the electron beam in the interaction section. The interaction steerers are changing the angle. Cooling can now be seen by observing the transverse ion beam profiles which become very narrow on the BPM while changing the position and the angle of the electron beam.
Once an overlap of the two beams is found, one has to align the center of the electron beam to the ion beam. This is again accomplished by observing the Schottky signal which moves to a lower frequency when the ion beam is coming to the electron beam center because of the space charge potential of the electron beam.

6.1.2 ETS as cooler

$^{12}C^{6+}$ at 73.3 MeV has been used in the first ETS beamtime because it is the standard species used at the TSR for studying electron cooling. C^{6+} can be stacked to high intensities (≈ 18 mA) and the lifetime inside the storage ring is long. In our measurements the lifetime of the electron cooled beam was in the order of 30 min because of an increased pressure in the storage ring related to the first installation of the ETS.

Transverse beam profiles

In Fig. 6.2 transverse beam profiles measured at the BPM are shown. Without using the TSR electron cooler, ion currents in the range of 30 μA have been stacked and cooled. The parameters and the widths of the profiles are summarized in Tab. 6.1. The lifetime of the beam cooled with the ETS was shorter than with the EC and was dependent

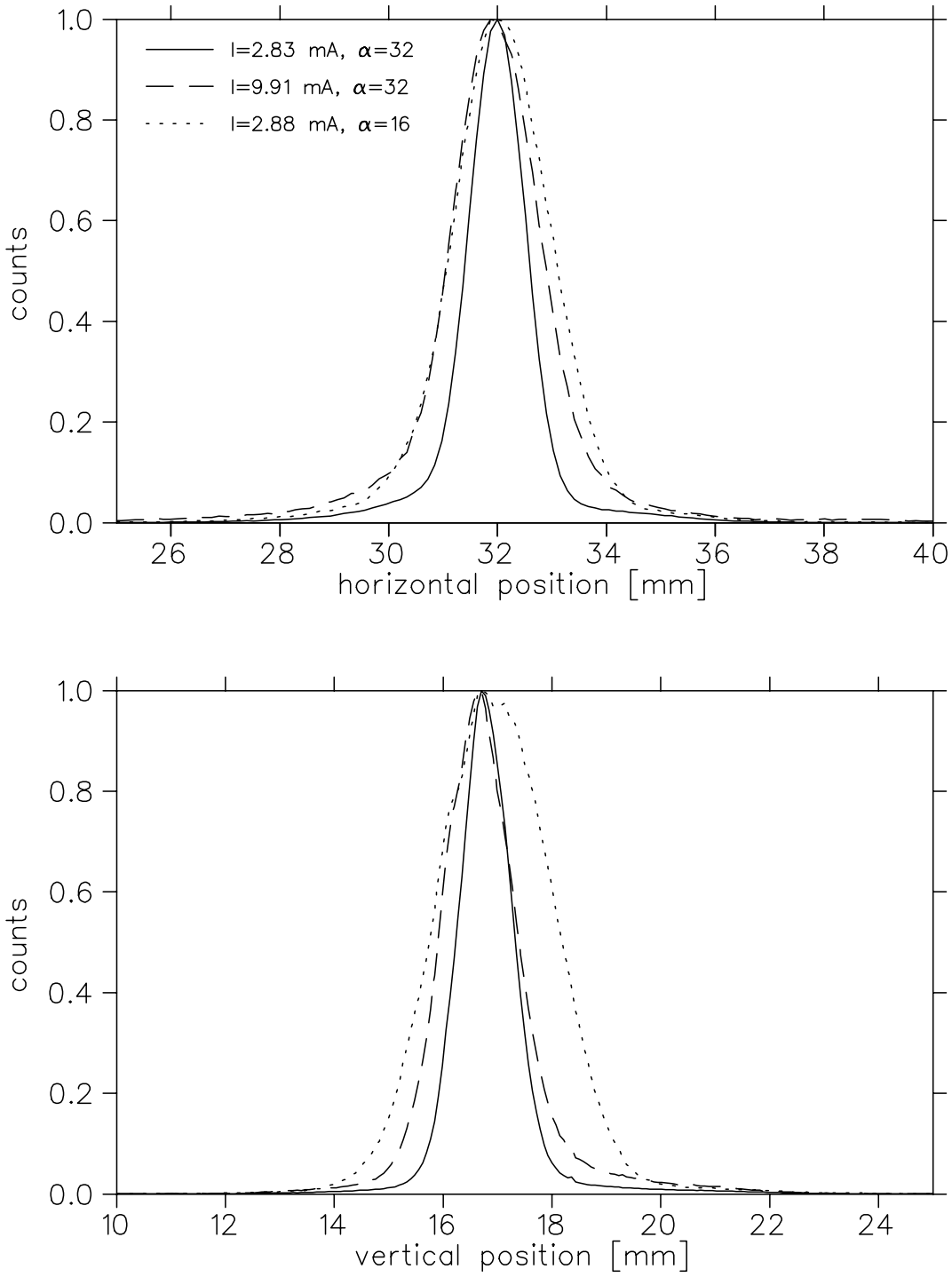

Figure 6.2: Transverse ion beam profiles from the ion beam cooled in the ETS. The BPM signals for three different electron currents and expansion ratios (as indicated in the graph) are shown.

electron beam		FWHM [mm]	
I_{tot} [mA]	α	horiz.	vert.
2.83	32	1.15	1.08
9.91	32	1.92	1.51
2.88	16	2.05	2.45

Table 6.1: Transverse widths of the ion beam measured with the beam profile monitor for several electron beam parameters (see Fig. 6.2).

of the electron current. At high electron currents (12 mA, corresponding to a density of $3.5 \cdot 10^{13}\,1/\mathrm{m}^3$ at expansion 32) the lifetime was very short (several minutes) and the beam could not be well cooled with the ETS. This is probably related to an unsatisfactory alignment between the ion beam and the electron beam in the ETS. The ion beam was not ideally centered in the ETS, which has been seen with the position pickup electrodes. The narrowest profiles have been obtained with the smallest electron current at an expansion of $\alpha = 32$ (electron beam diameter ≈ 9 mm). The profiles obtained with the electron cooler are not smaller. Increasing the electron current about a factor of 5 broadens the profiles significantly and the beam does not look optimally cooled anymore. With $I_e = 2.88$ mA and $\alpha = 16$ (electron beam diameter ≈ 6.4 mm) the same good result as with $\alpha = 32$ cannot be obtained. The electron density is a factor of 2 higher but probably the electron beam diameter is already too small for efficient cooling.

6.1.3 Two electron coolers - Drag effect

A situation that has never been studied in storage rings up to now is given by the operation of two electron coolers acting on the same ion beam. Having only one electron cooler, the electron cooler is exerting a certain cooling force on the ion beam and if the relative velocity between both beams is small the electron cooler is dragging the ion beam to the cooling velocity v_{EC} where the cooling force is zero. With two electron coolers at a certain detuning velocity the situation is a little more complicated because the ion beam will see the sum of two cooling forces. It will now depend on the magnitude of the cooling force and the detuning between them where the ion beam will be dragged to. We have been studying this operating the ETS and the EC together in the TSR doing Schottky analysis. The experiment was done with $^{19}\mathrm{F}^{6+}$ at 46.4 MeV.
In Fig. 6.3 and 6.4 Schottky spectra at the 8^{th} harmonic for different detuning velocities v_d between the electron cooler and the electron target v_d for electron currents in the ETS of $I_{ET} = 1$ and 5 mA are shown. The expansion ratio was set to $\alpha = 32$ which leads to electron densities of $n_e = 4.5 \cdot 10^{12}\,1/\mathrm{m}^3$ and $2.2 \cdot 10^{13}\,1/\mathrm{m}^3$, respectively. The electron current in the electron cooler was set to 59.3 mA at $\alpha = 9.3$ which leads to a density of $n_e = 2.6 \cdot 10^{13}\,1/\mathrm{m}^3$. The first graph in the upper left corner of both figures shows the Schottky signal with only the EC on and with the ETS beam switched off. The frequency of this electron cooling peak ν_{EC} is drawn in all following Schottky spectra as a vertical dotted line. The measurement was then done in the following way. The ETS was switched off and ion currents of typically 20 μA where accumulated and cooled in the storage ring. The detuning of the ETS was set to a certain value and then the ETS electron beam was switched on. The frequency position of the detuning velocity of the ETS electron beam

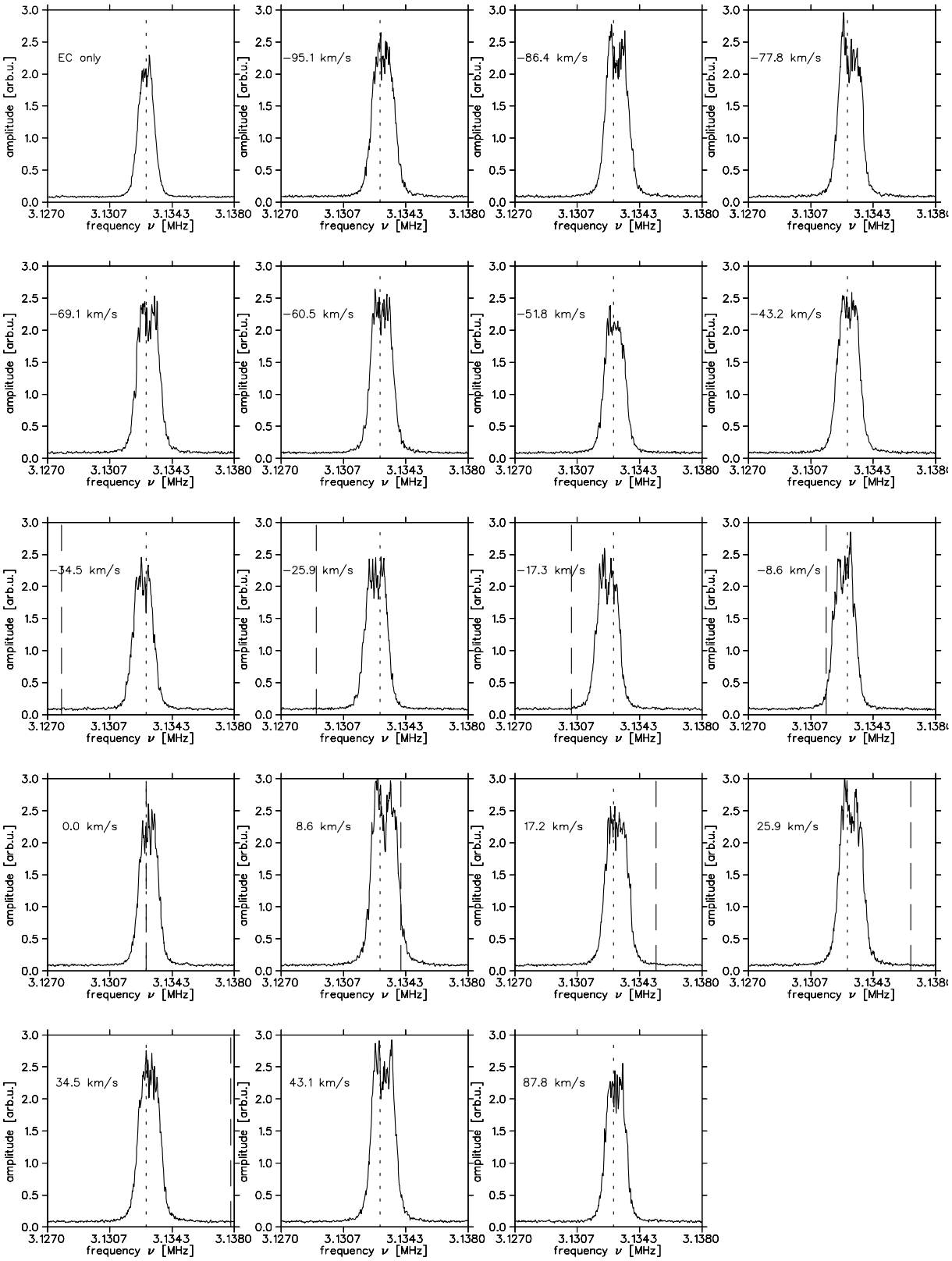

Figure 6.3: Series of Schottky spectra for different relative velocities between EC and ETS (values shown in each graph). The vertical lines indicate the frequency position of the EC (dotted line) and of the ETS (dashed line, value for the corresponding relative velocity is also given). In the upper left corner the Schottky spectrum of the EC without ETS is shown. The ETS electron current was $I_{ET} = 1\,\mathrm{mA}$.

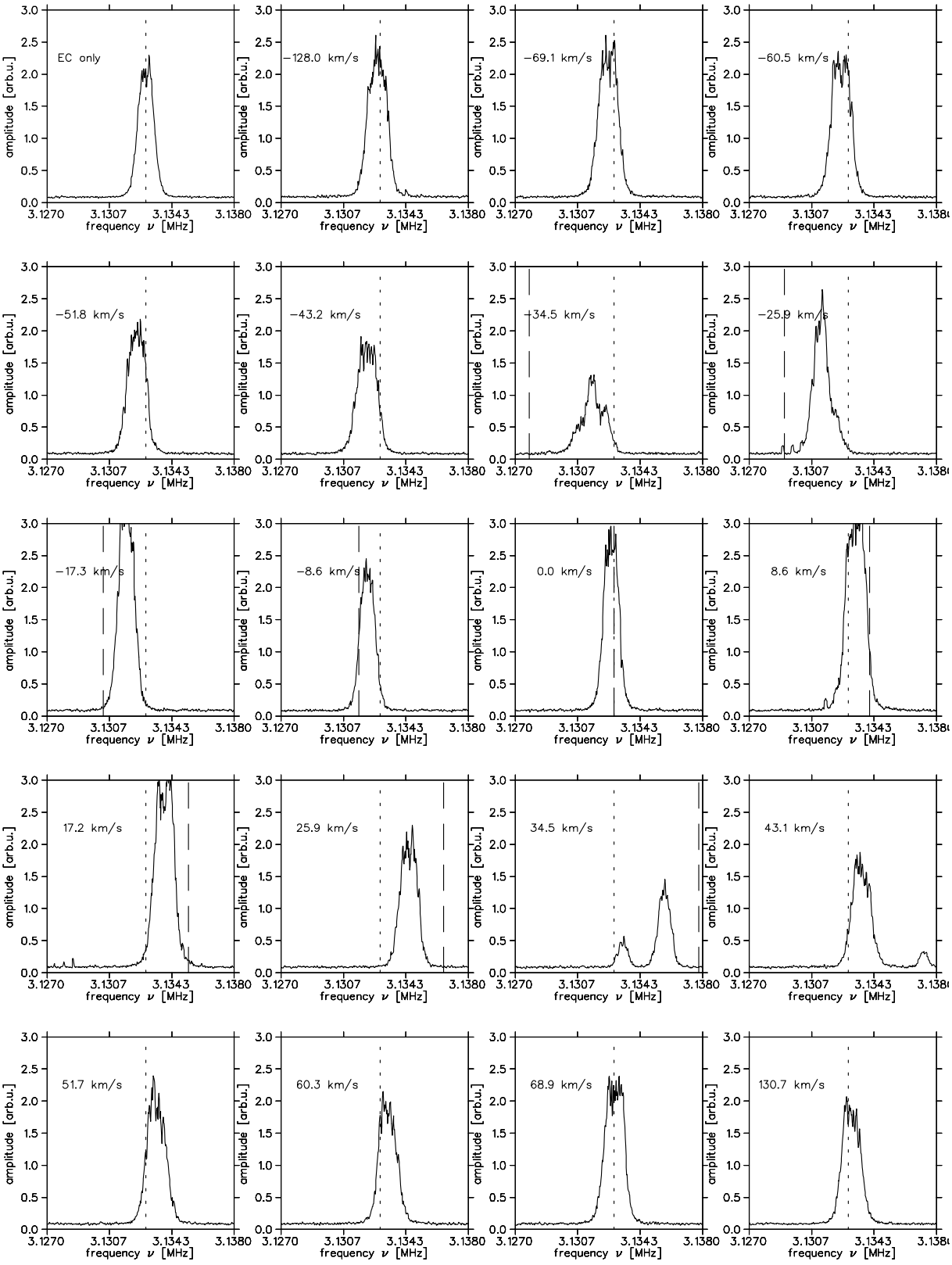

Figure 6.4: Series of Schottky spectra for different relative velocities between EC and ETS (values shown in each graph). The vertical lines indicate the frequency position of the EC (dotted line) and of the ETS (dashed line, value for the corresponding relative velocity is also given). In the upper left corner the Schottky spectrum of the EC without ETS is shown. The ETS electron current was $I_{ET} = 5\,\mathrm{mA}$.

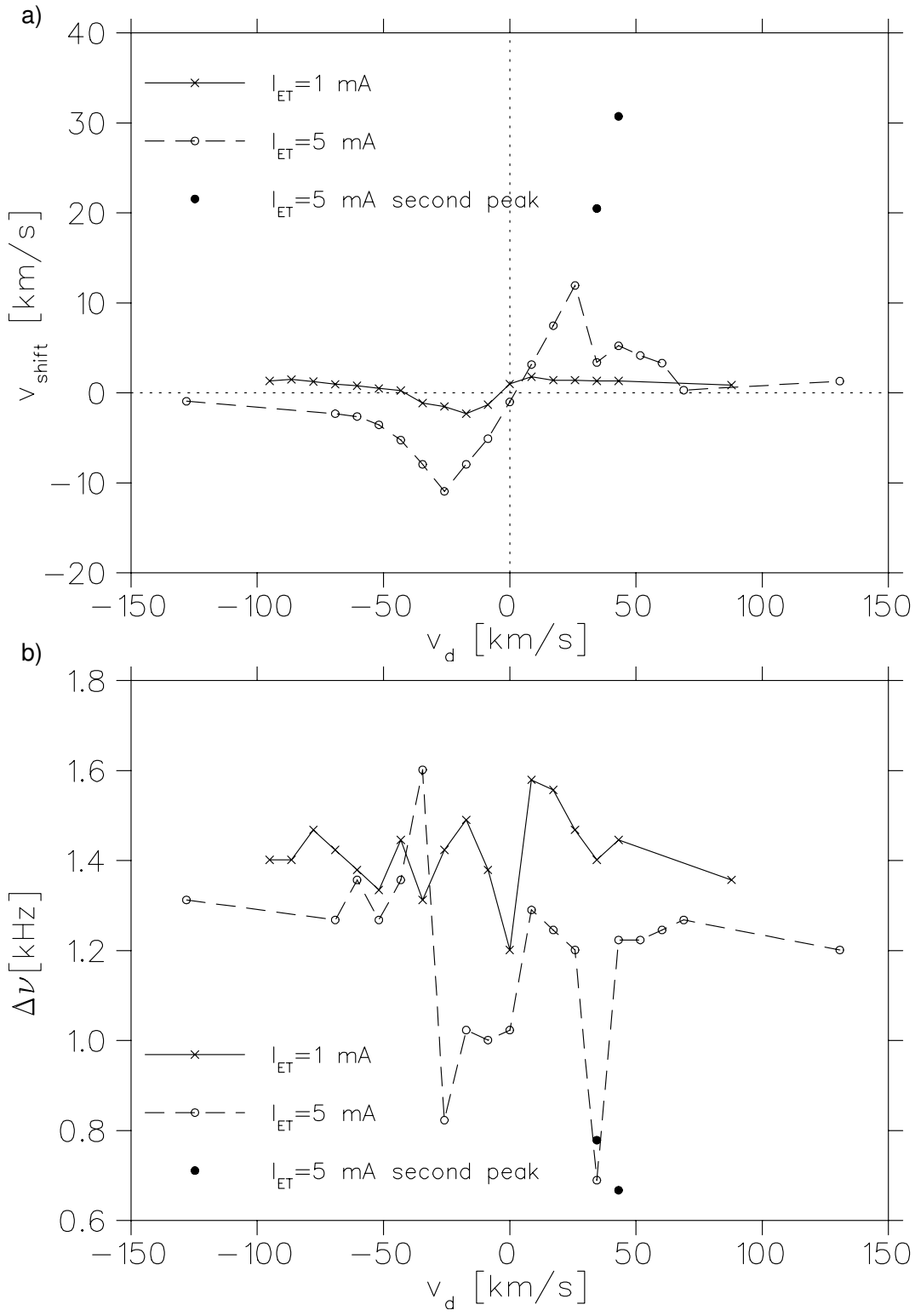

Figure 6.5: Velocity shift of the ion beam (upper graph a)) and width of the Schottky spectra (lower graph b)) as a function of the relative velocity between the electrons in the EC and in the ETS. Values derived from the Schottky spectra in Fig. 6.3 and 6.4 for two different currents in the ETS $I_{ET} = 1\,\text{mA}$ (solid line, crosses) and $I_{ET} = 5\,\text{mA}$ (dashed line circles). The solid circles indicate the shift for the second peak of the Schottky spectra where a double peak structure was observed.

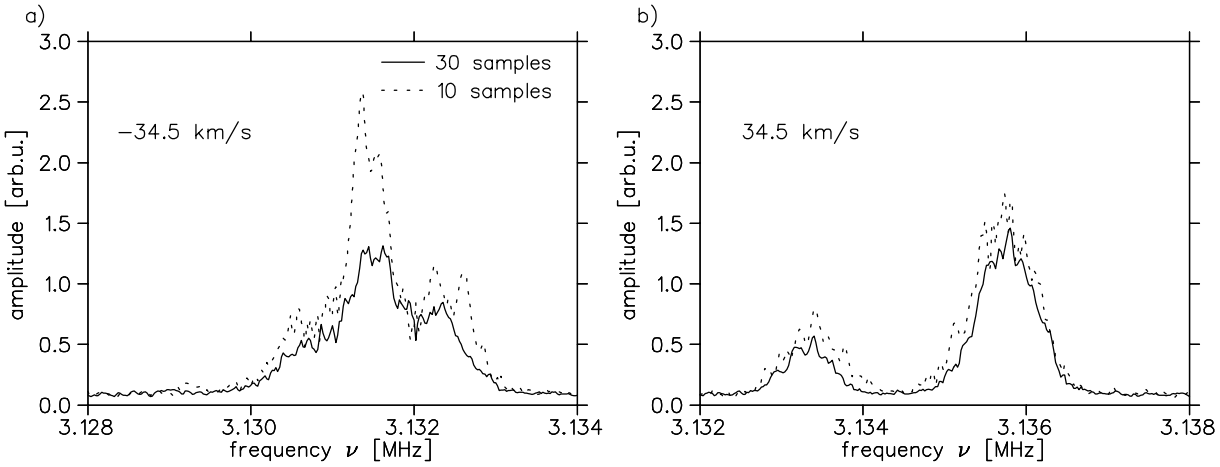

Figure 6.6: Time evolution of two Schottky spectra at the relative velocities (as indicated in the graph) where the Schottky shift was maximal. The solid line shows the result for a longer time interval of 30 samples of the spectra and the dashed line shows the result after only 110 samples.

is shown as a vertical dashed line (not visible in all graphs if the detuning is out of the shown range). As one can see in both figures the Schottky spectra are shifted away from ν_{EC}. The shift is only small for $I_{ET} = 1\,\mathrm{mA}$ but much stronger for $I_{ET} = 5\,\mathrm{mA}$ for several relative velocities. The most interesting is that there is a double peak structure appearing for $I_{ET} = 5\,\mathrm{mA}$ at $v_d = 34.5$ and $43.1\,\mathrm{km/s}$. For the lower detuning velocity the peak which is stronger shifted is the bigger one, while at the higher detuning velocity this is reversed. One could also suppose a double peak at $v_d = 8.6\,\mathrm{km/s}$ for $I_{ET} = 1\,\mathrm{mA}$ but this is not clearly resolved. To quantify this observations we deduced the position and widths of the peaks in the Schottky spectra and calculated the velocity shift v_{shift}. The result is shown in Fig. 6.5 as a function of the detuning velocity v_d between ETS and EC. The two peak positions of the second peaks of the double peak structures are shown as solid circles.

In Fig. 6.5 (a) one can see that the shift for the higher current (dashed line, circles) is much stronger than for the smaller current (solid line, crosses) from which one can suppose a stronger cooling force for $I_{ET} = 5\,\mathrm{mA}$. What can also be noticed is an asymmetry between $v_d < 0$ and $v_d > 0$. At the relative velocity where the first double peak appears ($v_d = 34.5\,\mathrm{km/s}$) the shift of the first peak is smaller than at $v_d = -34.5\,\mathrm{km/s}$. This can probably be explained by the experimental procedure. By switching on the ETS electron beam at a higher relative velocity ($v_d > 0$) the electron beam is moving over the slower ion beam while at $v_d < 0$ the ETS electron beam is always slower than the ion beam. We will analyze this in more detail below. For $I_{ET} = 1\,\mathrm{mA}$ there is a local minimum in the shift visible at $v_d \approx 20\,\mathrm{km/s}$ while the shift stays almost constant for lower or higher relative velocities.

Looking at Fig. 6.5 (b) the width $\Delta\nu$ of the Schottky peaks is shown as a function of the detuning velocity. For $I_{ET} = 1\,\mathrm{mA}$ the smallest peak was measured at $v_d = 0$. This is an indication that the cooling force is strongest for this conditions. For $I_{ET} = 5\,\mathrm{mA}$

$\Delta\nu$ is also smaller at $v_d = 0$ than for high detuning velocities $|v_d| > 50\,\mathrm{km/s}$. But it is still smaller at the detuning velocities close to where the velocity shift is maximal. The broadest spectrum on the other hand appears right at $v_d = -34.5$ where the velocity shift is the biggest. Looking at the Schottky spectrum for $v_d = -25.9$ in Fig. 6.4, one sees that the distribution looks asymmetric which could be a non resolved double peak. This is a clear hint that the ion beam is strongly influenced by both electron beams at $|v_d| \approx 30\,\mathrm{km/s}$.
We have been also looking for a change of the Schottky peaks for $I_{ET} = 5\,\mathrm{mA}$ with time at the interesting detuning velocities where the first double peak ($v_d = 34.5\,\mathrm{km/s}$) and where the broadest spectrum ($v_d = -34.5\,\mathrm{km/s}$) are appearing. The result is shown in Fig. 6.6. The Schottky spectra represent always the average of several samples, where one sample is obtained within 0.5 s. For $v_d = -34.5\,\mathrm{km/s}$ one sees a more pronounced difference between the short time (10 samples) and the longer time (30 samples). For longer times the shape is changing to one broad peak. At $v_d = 34.5\,\mathrm{km/s}$ the peak shape stays stable with time.

The cooling force of two electron beams

In order to understand the shifting of the Schottky frequency as a function of the detuning velocity v_d we will now calculate in a simple model the sum of two cooling forces at different velocities $v_{EC} = 0$ and v_d with different amplitudes. Using eq. (3.35) we get for the total cooling force

$$F_{cool}(v_{ion}, v_d) = F_0 \frac{v_{ion}}{|v_{ion}|^3 + 2\Delta_e^3} + a \cdot F_0 \frac{v_{ion} + v_d}{|v_{ion} + v_d|^3 + 2\Delta_e^3}. \tag{6.1}$$

The first term is representing the cooling force of the electron cooler, F_{EC}, and the second one the cooling force of the electron target, F_{ET}, with a factor a that determines the relative strength. Stable points for the ions appear at positions where $F_{cool} = 0$ and $F'_{cool} < 0$. We therefore calculated the zero points of eq. (6.1) as a function of the detuning velocity (in units of the ion velocity where the cooling force has its maximum (v_{max})) at the positions where the derivative is negative. The result is shown in Fig. 6.7 for three different cases in the large window: (i) $F_{EC} > F_{ET}$ (black, a=0.5), (ii) $F_{EC} = F_{ET}$ (red, a=1) and (iii) $F_{EC} < F_{ET}$ (green, a=1.5). The smaller windows show the cooling force as a function of the ion velocity at two different detuning velocities ($v_d/v_{max} = 2.1$ and -4, marked in the large window with arrows).
We can now compare the calculation with the observed shift (Fig. 6.5 (a)). The black curve where the cooling force of the electron cooler is stronger than the electron target force shows a similar behavior like the measurement for $I_{ET} = 1\,\mathrm{mA}$. The stable ion velocity is shifted a little bit to smaller velocities for $v_d < 0$ and to higher velocities for $v_d > 0$ in the calculation. In the measurement there was a small offset to higher ion velocities observed and only the shift to lower velocities for $v_d < 0$ was seen. But the shift is small and might be related to other effects. In the calculation there are more stable points found at higher detuning velocities ($|v_d/v_{max}| > 3$) for higher ion velocities. These points have not been observed in the measurement.
The red curve (cooling forces equal in electron cooler and electron target) looks quite

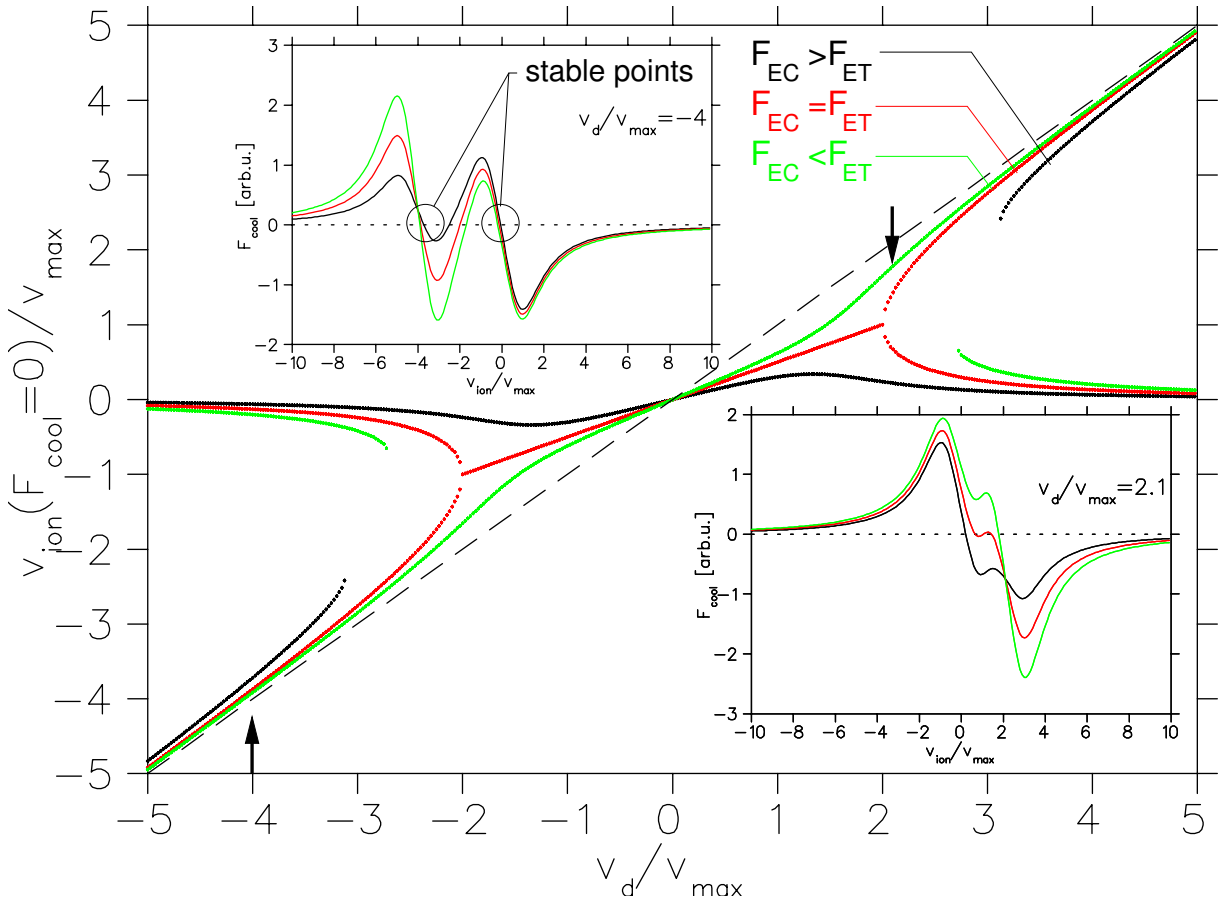

Figure 6.7: Model of two cooling electron beams (electron cooler EC and electron target ET) acting on the same ion beam. The total cooling force $F_{cool}(v_{ion}, v_d) = F_{EC}(v_{ion}, v_{EC} = 0) + a \cdot F_{ET}(v_{ion}, v_d)$ depends on the relative velocity v_{ion} between the ion beam and the electron beam and on the detuning velocity v_d between the two cooling electron beams. The position of the stable zero points ($F'_{cool} < 0$) of F_{cool} as a function of v_d/v_{max} is shown in the large window, where v_{max} is the ion velocity where the cooling force has its maximum. Three cases are distinguished: (i) $F_{EC} > F_{ET}$ (black, a=0.5), (ii) $F_{EC} = F_{ET}$ (red, a=1), (iii) $F_{EC} < F_{ET}$ (green, a=1.5). The dashed line indicates the limit $F_{ET} \gg F_{EC}$. In the smaller insets the cooling force is shown as a function of v_{ion}/v_{max} for two different detunings (values as indicated and marked with arrows, with the same color code) with the zero points visible.

similar to the measurement at the higher ETS current ($I_{ET} = 5\,\mathrm{mA}$). One would expect that the cooling forces are comparable because the electron densities in the electron cooler and in the ETS are almost equal for $I_{ET} = 5\,\mathrm{mA}$. For $|v_d/v_{max}| < 2$ the ion energy is shifted proportional to the detuning velocity because there is only one zero point in the cooling force which moves with the detuning. At $|v_d/v_{max}| = 2$ two stable zero points appear (see lower right small window in Fig. 6.7). This can be identified with the observed double peaks and the broad peak in the Schottky spectra ($v_d = \pm 34.5\,\mathrm{km/s}$). One can suppose that the broad peak has been measured directly at the position where the two new zero points appear. The double peak has been measured where the two zero points are already more pronounced separating the ion beam into two velocity classes.
The green curve, where the electron target is stronger cooling than the electron cooler, has not been observed experimentally. The qualitative agreement of this simple model with the observation is quite good. Future measurements will be helpful to study this behavior in more detail. For a more quantitative understanding cooling force measurements are needed.

6.2 First DR measurements

6.2.1 Procedure

Difference to EC measurements

With the ETS the procedure for DR measurements is modified in some important points. The standard procedure of DR measurements, if only the EC is used, is done in the following way. The EC is set to the cooling voltage U_0^{EC} (cooling energy E_0^{EC}), ions are injected into TSR for a certain time t^{inject} and they are precooled for same time t_0^{cool}. A second power supply which is installed on the HV-platform is now used to detune the electron velocity to $U_i^{meas} = U_0^{EC} + \Delta U_i$. Normally a voltage ramp is performed starting at energies below E_0^{EC} and then scanning towards smaller relative energies, above zero relative energy and then further to higher relative energies. At each point i of the ramp three steps have to be performed: (i) cooling of the ion beam for a time interval t_i^{cool} at U_0^{EC} to prevent the ion beam from blowing up because of IBS and defining the ion beam energy. (ii) Going to the measurement voltage U_i^{meas} for a time t_i^{meas} and measuring the recombination rate. (iii) Switching the EC voltage to a reference voltage U^{ref} for determination of the background rate which is dependent on the electron current which is not constant along the energy scan ($I_e = P \cdot (U_i^{meas})^{3/2}$). The varying electron current is changing the restgas pressure because of secondary ions created at the collector cup. The position of the reference energy is chosen in a way that there is no DR resonance in the spectrum at this location. This three step scheme is called "wobbling". After completion of the scan, ions are again injected and precooled and a new scan starts.
With the EC and the ETS together the situation is more simple. Because the EC is set to the cooling energy all the time and hence the ion beam is always well cooled. The ETS can be set to any relative velocity without going back to the cooling energy. Furthermore in the ETS the electron current does not depend on the measurement voltage, because the emission current is controlled only by the extraction voltage which is kept constant.

ETS measurements

The procedure for finding the overlap of the electron beam with the ion beam was the same as described in section 6.1.1. Additionally the ion beam has first been moved to the center of the vacuum chamber in the interaction section with the help of the position pickup electrodes.
Data acquisition was performed by using part of the existing TSR electronics [Lan02]. In Fig. 4.33 the electronic circuit with the power supply for the energy detuning (max. $\pm 1000\,\mathrm{V}$) for U_i^{meas} is shown. The power supply was controlled by a 12-bit CAMAC DAC that was controlled by a VME-bus computer ("*lynxonline*"). Also the detector readout was done by this VME-bus computer and the results were then transferred over the institute network to a second computer ("*pconline*"). All this procedure is driven by a dedicated software ("*CyrilNG*").
To increase the resolution of the energy scan, the output range of the detuning power supply, which is actually an HV-amplifier, was adjusted such that the full 12-bit range

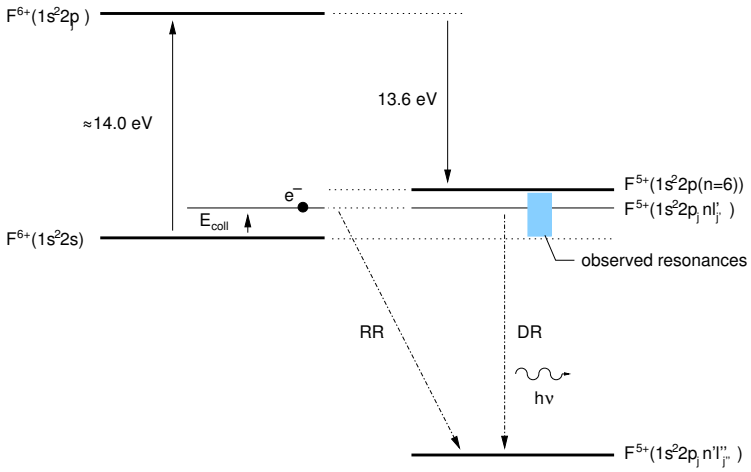

Figure 6.8: Dielectronic recombination in F^{6+}: A free electron at a certain collision energy is captured into a doubly excited bound state. A photon is emitted to stabilize the state.

corresponds to ±200 V output voltage. This is sufficient for the CM collision energy range of ±0.7 eV. For the ETS a new data acquisition system is in preparation which will replace some of the hardware modules by software programming [Les].
For the measurement procedure as described above the following timings where used $t_i^{cool} = 3\,\mathrm{s}$ after injection, $t_i^{meas} = 3\,\mathrm{ms}$ for collision energy and a waiting time of 1 ms between two data points. The injection timings where set such that an ion current of $\approx 20\,\mu\mathrm{A}$ was stored in the beginning of the scan. For one spectrum normally more than 120000 counts where recorded which is sufficient for a first temperature analysis trying to improve and understand the new ETS which was the goal of this beamtime. But this is not sufficient for high quality DR spectra that need a good statistics.
For all measurements the electron cooler was set to an electron current of 59.3 mA at $\alpha = 9.3$ which leads to a density of $n_e = 2.6 \cdot 10^{13}\,1/\mathrm{m}^3$.

6.2.2 F^{6+} DR spectra

As already mentioned in the theoretical part of this work (section 3.4) for the determination of the electron energies a system is needed with a low lying resonance close to the energy $\tilde{E}$ where the influence of both the $T_\parallel$ and $T_\perp$ can be seen. These requirements are fulfilled by F^{6+} where the $1s^2 2s(^2S) + e^- \rightarrow 1s^2 2p(^2P)6l$ resonances are well known from relativistic many-body perturbation theory calculations and experiments [Tok02]. The temperature is determined by fitting a theoretical curve to the measured resonances varying the electron temperatures.
Schematically the recombination process is shown in Fig. 6.8. In F^{6+} the $(1s^2 2s)$ level is separated by ≈ 14 eV from the $(1s^2 2p_j)$ level. The binding energy of the outer electron $(n = 6)$ in the excited F^{5+} is 13.6 eV which leaves about 400 meV where the accessible resonances are located. In detailed calculations and experiments resonances have been found between 7 and 520 meV.

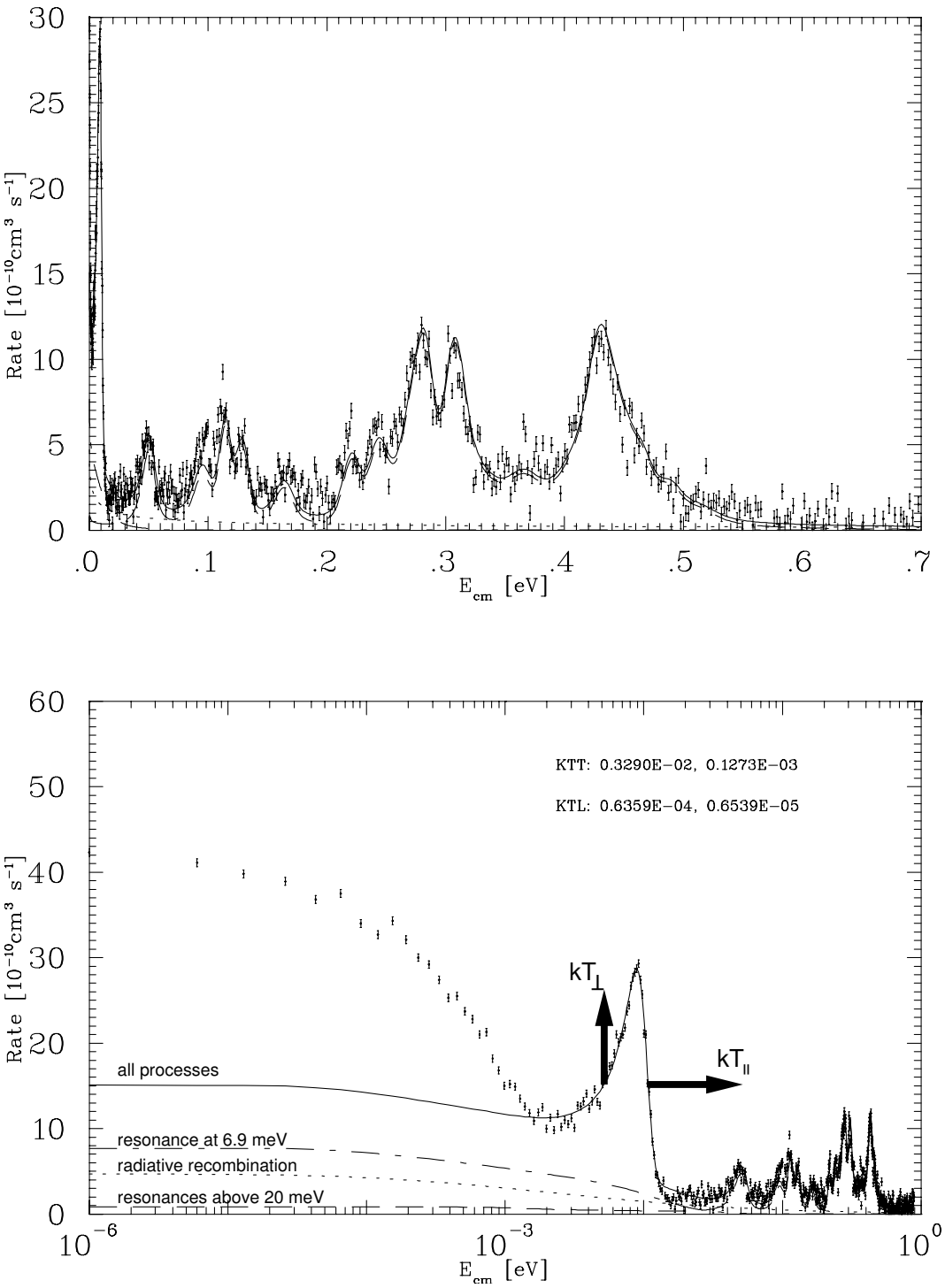

Figure 6.9: Recombination spectrum linear (upper graph) and logarithmic (lower) scale (left hand side of the spectra ($E_{ET} > E_{EC}$)).

A typical result of a background subtracted recombination spectrum together with the fitted theoretical spectrum is shown in Fig. 6.9. On the x-axis the collision energy has been calculated according to eq. (3.7) for the detuning voltage. The zero point energy is taken from the radiative recombination peak which has a maximum at collision energy zero. On the y-axis the recombination rate coefficient α calculated from the the detector count rate R by eq. (3.76) with $L = 1.5\,\mathrm{m}$ (estimated from the length of the interaction solenoid magnet) and $C = 55.4\,\mathrm{m}$ is drawn. In the measurements we were not interested in absolute rate coefficients the main goal was to compare the data to earlier results. Moreover, the background has not been measured during the experiment by a reference measurement. We therefore subtracted the background and scaled the rate coefficient in a pragmatic way such that the spectra can be compared to previous TSR data obtained with the EC (see section 6.2.2). The extracted temperatures are not influenced by the scaling. Besides, the toroid effect which can be treated by a deconvolution was not taken into account. From one energy scan two spectra are obtained belonging to ETS energies below the EC energy (low energy side, $E_{ET} < E_{EC}$) which we will refer to as the "left hand" side of the spectra and a "right hand" side with $E_{ET} > E_{EC}$. In the ideal case both spectra should be symmetric to the zero point energy. However, in our measurements a difference between the two sides has been found, which has not been further investigated experimentally, yet. A possible explanation could be a dragging effect which changes the collision energy (see section 6.1.3).
Taking a closer look at the spectrum, several contributions can be distinguished which can be produced by the fit and are plotted separately: the contribution from the radiative recombination (dotted line) which is proportional to $1/E_{coll}$, a broad DR resonance at 6.9 meV (dash-dotted line), all DR lines above 20 meV (dashed line) and all processes together (solid line). The rate enhancement of the recombination spectra, as observed in all storage rings, can be seen at low collision energies (area between the data points and the solid line). This effect depends on the longitudinal and the transverse electron temperature and strongly on the magnetic guiding field and is currently not completely understood [Gwi00].
For the application of temperature measurements the resonance at 11.4 meV (calculated) is the most interesting. In [Tok02] the configuration is given as a mixture of $(2p_{3/2}6p_{1/2})$ and $(2p_{3/2}6p_{3/2})$ with $J = 2$ in jj-configuration and a width of 0.1 meV. The resonance at 6.9 meV belongs to the configuration $(2p_{3/2}6p_{1/2})$ with $J = 1$ and a large width of 25.8 meV.
In the scope of this work we are not interested on further details of the DR process and we will focus in the following mainly on the low lying resonance at 11.4 meV. Moreover the double peak structure at 0.3 meV is qualitatively interesting because the separation and the resolution of the two peaks depend on the longitudinal temperature and give an rough estimate of the longitudinal temperature by "eye".

α	I_e [mA]	n_e [1/m^3]	U_0 [V]	E_{drift} [eV]
16	0.4	$3.56 \cdot 10^{12}$	1348.9	400
33	1.01	$4.36 \cdot 10^{12}$	1348.34	120
60	1.78	$4.22 \cdot 10^{12}$	1354.41	400

Table 6.2: ETS electron beam parameters for the DR measurements at different expansion ratios. E_{drift} is the electron energy in the expansion region of the ETS (see section 5.2).

Expansion

In this section longitudinal and transverse temperatures extracted from the measured DR spectra as a function of the expansion ratio α are presented. The parameters of the ETS electron beam used for the measurements are summarized in Tab. 6.2.
By changing the ETS electron current, the electron density has been kept almost constant. In the cathode potential U_0, one sees the effect of the space charge, which depends on the beam diameter. In Fig. 6.10 the results of the measurements are shown. In the upper graph the transverse temperature as a function of the expansion is shown. The expected temperature calculated from the cathode temperature and the expansion (dotted line) and a hypothetical curve for $kT_{cath} = 120\,\text{meV}$ (dashed line) are also plotted. The heating current for the cathode was $I_h = 1.25\,\text{A}$ which gives a cathode temperature calculated by (5.5) of 108.5 meV. In the lower graph the longitudinal temperature is drawn. The error bars represent the statistical error of the fit.
Looking at the transverse temperatures, one notices that almost all measured temperatures lie 1–2 meV above the expected theoretical values from the cathode temperature but follow the trend of the theoretical curve. This discrepancy cannot be explained by an error in the cathode temperature determination because even for an assumed cathode temperature of 120 meV all data points except one lie above the theoretical curve. The biggest deviation from the expected temperature is found for $\alpha = 60$ where the mean value of the measured temperature is a factor of 1.9 higher with large errors on the values on both sides. Measurements at the Stockholm CRYRING showed also higher transverse temperature than expected. For $\alpha = 100$ the measured temperature was a factor of 3 higher than the theoretical value [Gla99]. A more recent experiment with Pb^{53+} at CRYRING showed a tendency for a transverse temperature closer to the expected one [Lin01]. The reason for this effect is not yet understood. The alignment of the electron beam to the ion beam could be a reason for this observation.
For $\alpha = 16$ the left and right hand value differ about 4 meV from each other. At this relatively high transverse temperature the low energy part of the 11.4 meV resonance is broad and comes close to the radiative recombination peak. Because of the low statistics in our measurements this could then result in a higher temperature. However, this does not explain the big difference between both sides of the spectrum.
The error bars for the longitudinal temperatures are rather large and go up to $\approx 30\%$ for $\alpha = 60$. For $\alpha = 33$ the calculated longitudinal temperatures are the highest for both sides of the spectrum. This can be possibly explained by TLR which is not very well suppressed for the low energy $E_{drift} = 120\,\text{eV}$ in the drift section (see 5.2.5). For

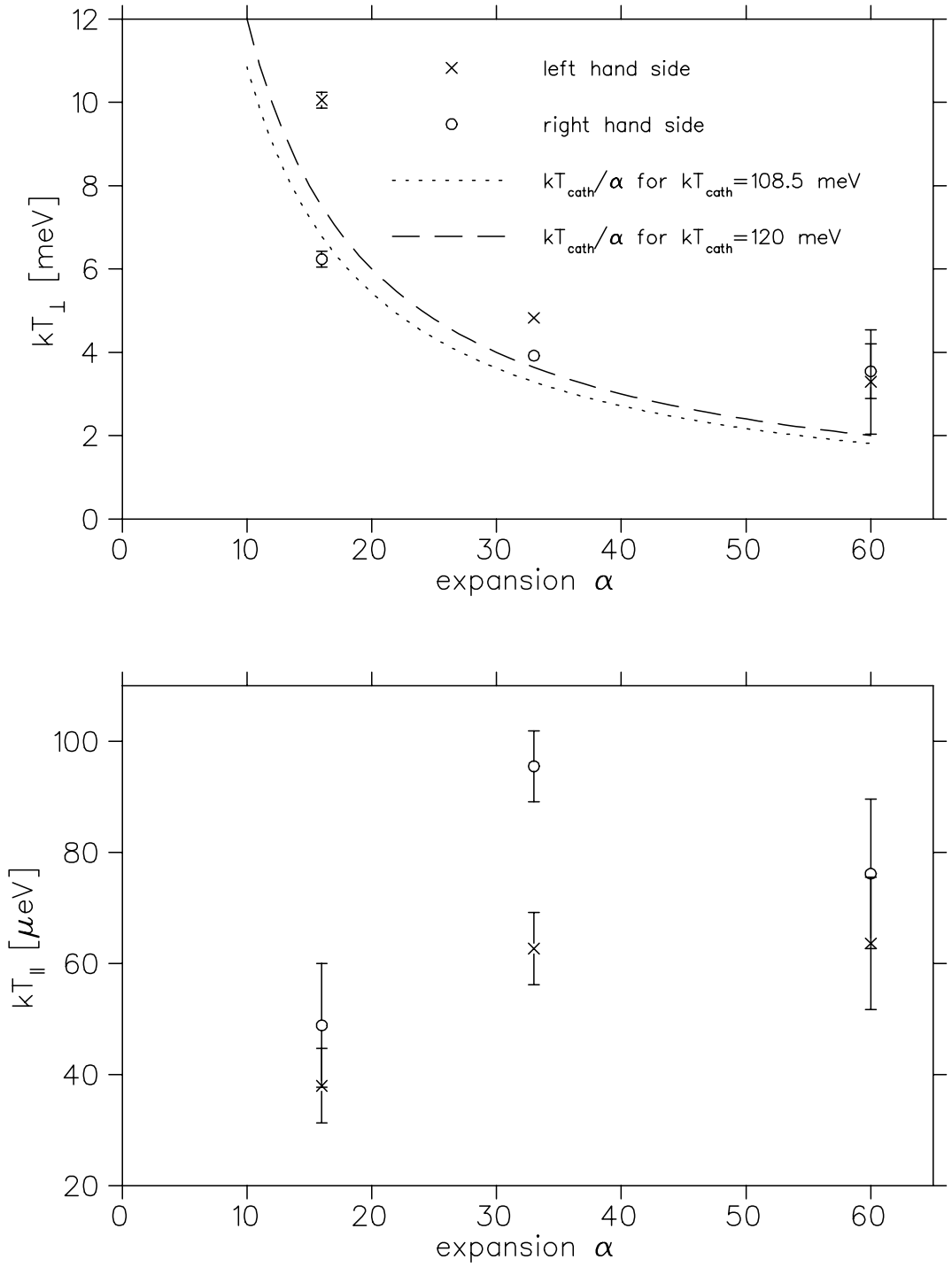

Figure 6.10: Dependence on the determined electron temperatures from the fitted spectra as a function of the expansion ratio. The dotted line shows the expected transverse temperature for a cathode temperature of 108.5 meV.

$\alpha = 60$, $kT_\parallel$ is higher than for $\alpha = 16$. According to theory there is no reason for that. The longitudinal temperature should not be influenced by the magnetic expansion. In the process of ATE energy is transferred from the transverse to the longitudinal degree of freedom but this happens at low kinetic energies and is therefore not strongly seen in the CM frame of the beam. There is a slight difference in the densities but LLR is only proportional to $n_e^{1/3}$ and should also be weak. From the EDC measurements a temperature in the range of 25–30 μeV is expected (see Fig. 5.22). However, for an accurate temperature determination the longitudinal temperature has to be extrapolated to zero ion current [Gwi03]. The dependence on the ion current will be discussed in the next paragraph.

Ion current

In Fig. 6.11 two spectra measured at different ion currents are shown. The normal ion current of $I_i \approx 20\,\mu$A has been reduced by reducing the injection time and by reducing the current from the accelerator to $I_i \approx 6\,\mu$A. The expansion ratio for both runs was $\alpha = 60$ and the ETS electron current $I_e = 1.84\,$mA. For $I_i \approx 6\,\mu$A the energy scan range has been reduced to shorten the measurement time because the recombination rate is reduced at the lower current and more time is needed for the same statistics. In the logarithmic plot of the spectrum the data points for the smaller current on the low energy side of the 11.4 meV resonance lie below of that for the higher ion current. From that we expect already a lower transverse temperature. As one can see a statement for the longitudinal temperature is hard to make without fitting a theoretical spectrum.
The results from the fits are shown in Fig. 6.12. Again the expected transverse temperature is plotted as a dashed line. The error in the ion current is estimated to be at least $1\,\mu$A. In fact, the lower transverse temperature for the lower current is produced by the fit with both side lying close together. Compared to the higher current the deviation from the expected temperature is decreased to a factor of ≈ 1.5.
On the other hand the situation for the longitudinal temperature is inverse. The low current results in a higher longitudinal temperature but again the results from both sides are close together even within the error bars. For the higher current the error bars are very large, making a clear statement difficult. Altogether the lower ion current seems to improve the temperature determination as one would expect.

Comparison with EC data

It is now interesting to compare the data obtained with the ETS to the data from earlier experiments at the TSR. In Fig. 6.13 two spectra are compared. Both spectra have been measured under comparable conditions. In the case of the EC spectrum the electron density was $n_e \sim 10^{13}\,1/\mathrm{m}^3$ at $\alpha = 25.6$ with a magnetic guiding field of $\sim 0.04\,$T and an ion current of 10–20 μA (data published in [Tok02]). The ETS data was obtained at $\alpha = 60$ and have already been discussed in the previous paragraph (see Fig. 6.10). On the first glance one sees already that the statistics of the EC spectrum is much better than for the ETS. The energetic positions of the resonances agree very well.
In the logarithmic plot one sees a great difference on the low energy side of the low lying resonance. Because of the higher expansion ratio in the ETS the transverse temperature

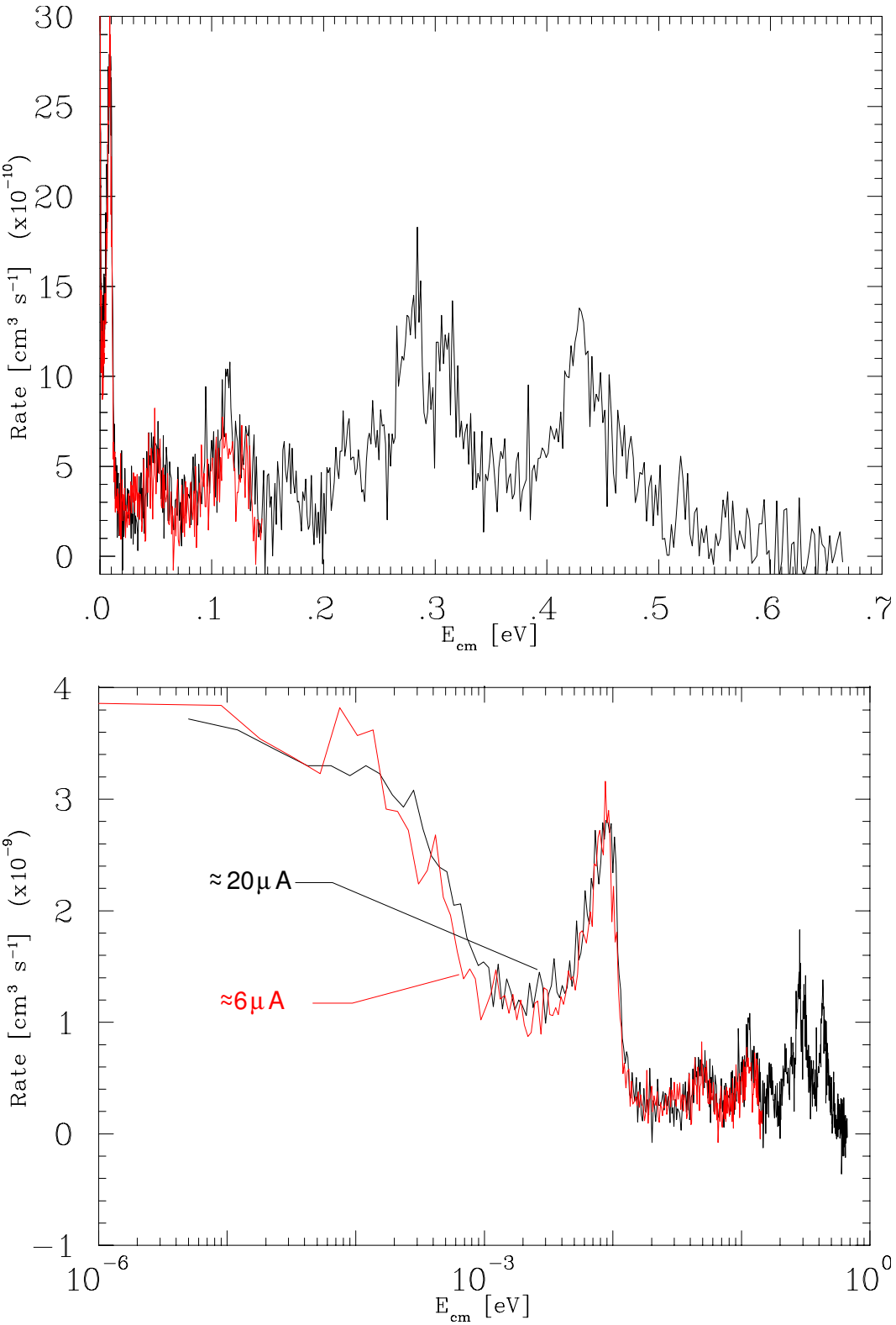

Figure 6.11: Comparison of two spectra measured at different ion currents $I_i \approx 6$ (red) and 20 μA (black). The upper graph shows the rate coefficient on a linear scale, on the lower on a logarithmic one.

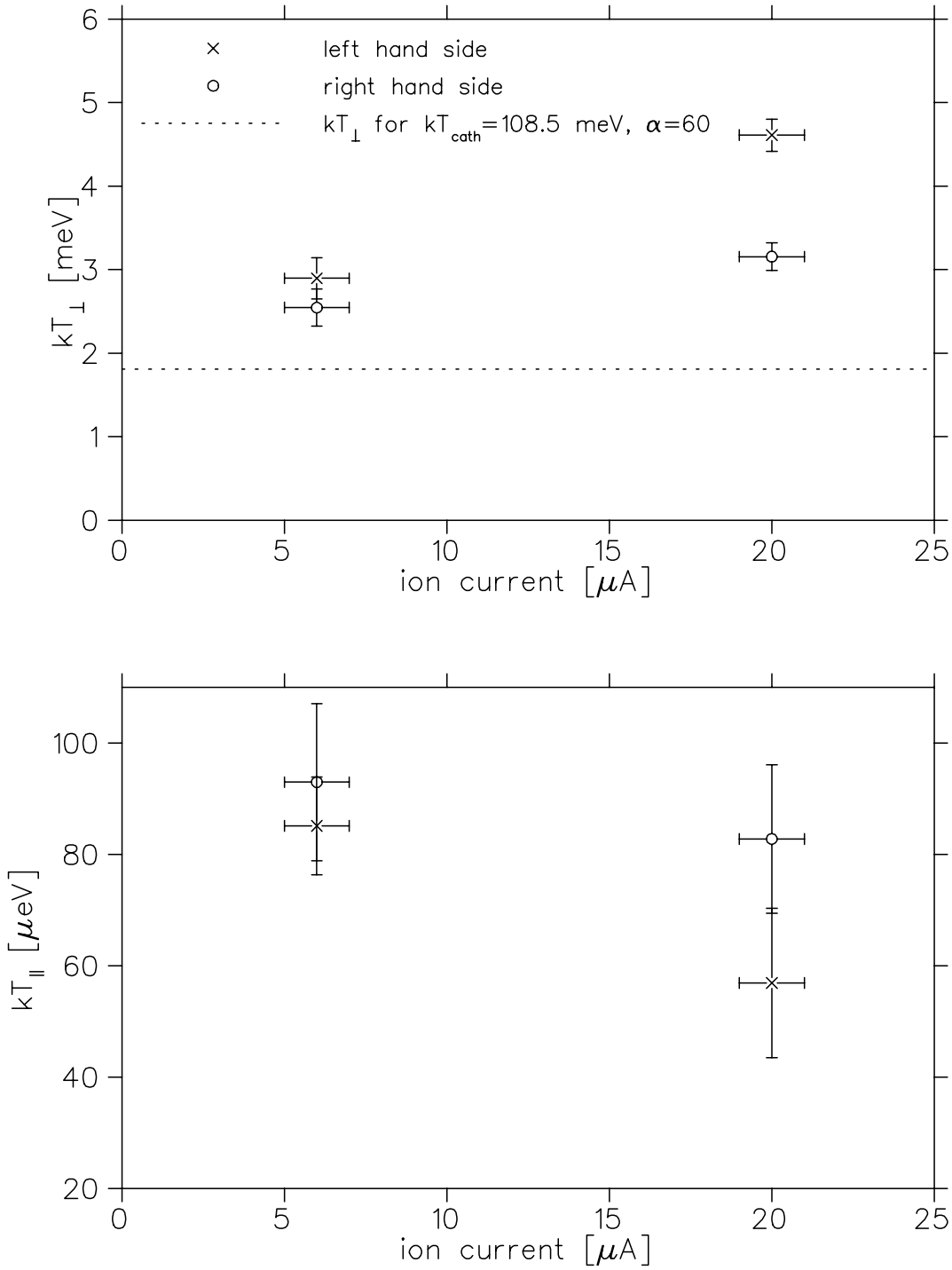

Figure 6.12: Dependence on the determined electron temperatures from the fitted spectra as a function of the ion current. The dotted line shows the expected transverse temperature for a cathode temperature of 108.5 meV. The error in the ion current is estimated to at least $1\,\mu$A.

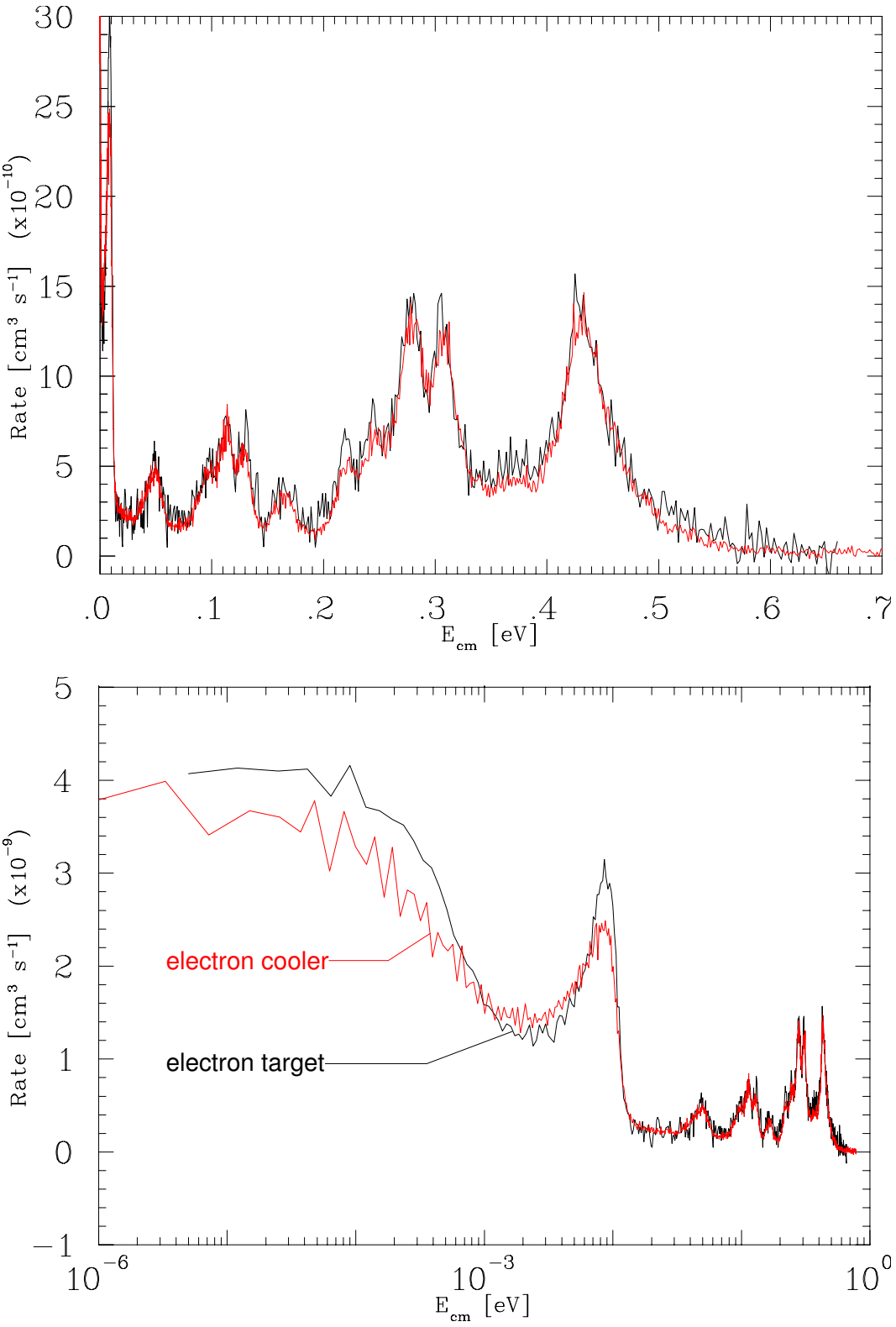

Figure 6.13: Comparison of recombination spectra measured with the ETS to earlier results obtained with the EC. The upper graph shows the rate coefficient on a linear scale, on the lower on a logarithmic one. The EC data has been measured at $\alpha = 25.6$, ETS data at $\alpha = 60$.

is clearly reduced. The calculated transverse temperatures are $kT_\perp = 3.5\,\mathrm{meV}$ for the ETS and $kT_\perp = 5\,\mathrm{meV}$ for the EC. Also the longitudinal temperature was found to be reduced in the ETS spectrum from $\approx 90\,\mu\mathrm{eV}$ in the EC to 65–75 μeV (mean values from both sides of the spectrum without error) in the ETS.
In the linear plot of the spectrum several observations can be made. There are two peaks visible at 0.22 and 0.24 eV which are more pronounced in the ETS spectrum. The second peak of the double peak structure at 0.3 eV seems also better resolved in the ETS than in the EC spectrum which is a hint on the smaller longitudinal temperature. For more quantitative data spectra with better statistics will have to be measured.

6.2.3 Conclusion

Summarizing, it has been found that under comparable experimental conditions to the existing electron cooler device the energy resolution has been clearly improved using the new ETS. The transverse temperature has been reduced about a factor of 1.4 and the longitudinal one about a factor of 1.2–1.4. However, the expected low transverse and longitudinal temperatures could not be observed which will be studied in more detail in the future.
We want to point out that these results were obtained under new experimental conditions that are not completely understood and optimized which lets space for further improvements. We will mention some problematic aspects in the following.
For several expansion ratios we were not able to measure recombination spectra even if the ETS electron beam was aligned such that the ion beam was cooled by the electron target. This problem is probably related to the alignment of the ion beam with the ETS electron beam. The EC and the ETS cathode potential was produced by two different power supplies. This makes energy shifts due to voltage drifts or ripples possible. This will be improved in the future by using one single main power supply. In the measurements the background was not monitored and the spectra were background corrected in a simple procedure. Moreover the toroid effect has not been included into the data evaluation and the statistics of the measurements was relatively low.

7. Summary and Outlook

In this work the requirements for the production of cold electron beams for collision experiments and the experimental implementation of the new TSR electron target section have been discussed. The availability of a dedicated electron target that separates the electron cooling process from the target operation is preferable because of several reasons. The electron beam in the target can be used continuously for the experiment without loosing ion beam quality because the electron cooler is operated in parallel. The event rates in the experiment are higher and the experimental situation is more stable. The properties of the electron beam in the target can be optimized for the target operation, in particular by a smaller beam size which reduces the total electron current.
The main design considerations for the ETS were the following. The beam formation in the electron gun and the electron acceleration to the final energy were separated. This opens up several possibilities for reducing relaxation processes in the beam that lead to a beam heating. A long acceleration section allows the slow (adiabatic) acceleration of the beam which reduces the potential energy relaxation (LLR) that leads to an increase of the longitudinal temperature. A high initial magnetic field compared to the guiding field of the electrons allows the strong reduction of the transverse temperature by adiabatic transverse expansion (ATE).
The length of the interaction section inside the storage ring was made as long as possible for a maximum interaction time between the electrons and the ions. This could be achieved by very compact toroid regions with a short bending radius and a high bending angle. This geometry also reduces relative velocities between ions and electrons in the toroid region. The solenoid magnet in the interaction region was designed and manufactured to achieve high precision in the magnetic field homogeneity. On the other hand the magnet is split in the center, allowing it to create a gap for the installation of photon detectors.
In the electron collector, diagnostic tools are installed for measuring the longitudinal electron temperature and two-dimensional current density distributions. This is done by an retarding field energy analyzer that can be displaced in two transverse directions. In the ETS the collector section can be exchanged with the acceleration section, which leads to an electron beam opposite to the ion beam in the interaction section. This makes very high collision energies accessible.

Preparatory measurements for the operation in the storage ring have been performed. With current density distribution measurements it could be shown that the density distribution in the beam can be manipulated by changing the potential between the Pierce electrode of the electron gun and the cathode. It was seen that the deformation of the

electron beam from the ideal round shape is small (also for higher expansion ratios).
Using the retarding field energy analyzer longitudinal energy distribution curves (EDC) have been measured. This allowed us to study the influence of operational parameters on the longitudinal temperature and to look for relaxation processes. For the experiments electrons with energies up to 2 keV, densities up to $5 \cdot 10^{13}\,1/\mathrm{m}^3$ and expansion ratios up to $\alpha = 60$ have been used. From the technical point of view it could be shown that a collector cup potential $U_{cup} \approx -1000$ reduced the measured energy spreads about 10%. Between a pulsed and a DC electron beam only a small deviation was seen.
Regarding the relaxation processes, it could be observed that the magnetic guiding field suppresses transverse-longitudinal relaxation (TLR) as expected. At low expansion ratios the measured energy spreads could be reduced by a preacceleration directly after the electron extraction from the gun. This could be qualitatively explained, using calculations of the local beam properties during the acceleration, by a different beam magnetization. The qualitative comparison showed that the available models were sometimes overestimating the heating effect by TLR, in particular if they predict strong heating effects.
The dependence of the final electron energy spread on the kinetic energy was found to agree with the theoretical expectations. For low kinetic energy the temperature is limited by TLR and for high kinetic energy by potential energy relaxation in the beam. At high densities ($3 \cdot 10^{13}\,1/\mathrm{m}^3$) a longitudinal temperature of 25–30 μeV has been found, while at small densities ($1 \cdot 10^{10}\,1/\mathrm{m}^3$) the temperature was below 10 μeV for a kinetic energy of 2 keV.
An increase of the acceleration length did not lead to a further improvement of the final longitudinal temperature at kinetic energies of 2 keV and a density of $2.2 \cdot 10^{13}\,1/\mathrm{m}^3$. By a calculation of the adiabaticity of the acceleration it could be shown that even for a short acceleration length of 12.7 mm the acceleration is still slow enough.

The ETS has been implemented into the storage ring and first measurements have been performed. The ETS electron beam could be aligned to the stored ion beam and used for electron cooling without the electron cooler (EC) device. By operating the ETS together with the EC the drag forces of the ETS on the stored beam could be observed. In the Schottky spectra of the ion beam in same cases a double peak structure was observed as a result of the two electron beams acting on the same ion beam. Using a simple model describing the sum cooling force of both electron beams the observations could be qualitatively explained with the stable points of the total cooling force.
In a first dielectronic recombination beamtime, $^{19}\mathrm{F}^{6+}$ has been used to determine the transverse and longitudinal electron temperatures. The observed transverse temperatures were close to the values expected from the magnetic expansion factor α, but generally larger by $\approx$1–2 meV. This causes a substantial deviation by a factor of 1.7–1.9 at maximum expansion $\alpha = 60$. The reason for the increase compared to the expectation is still unclear. The longitudinal temperatures from the dielectronic recombination measurements were found to be higher than the values obtained by EDC measurements, typically 40–80 μeV. The measured spectra could be compared to earlier measurements performed with the EC. An improvement in the energy resolution was clearly seen in the spectra.

After the completion and the first successful operation that has been discussed in this work, the ETS is ready for further beamtimes. Recombination measurements will be carried out. Of special interest are $\Delta N = 1$ transitions in highly charged ions. From the experimentally point of view the understanding of the influence of the alignment on the measured temperatures and the interaction of the ETS and electron cooler will be important.
Soon the photocathode will be installed into the ETS. The preparations for this are already taking place. This will lead to an ultracold electron beam with temperatures down to $kT_{\parallel} \gtrsim 3\,\mu$eV and $kT_{\perp} \gtrsim 100\,\mu$eV. The very low transverse temperature is necessary, e.g. to resolve very low lying vibrational resonances of H_2^+ which are predicted by theory [Sch03].
For experiments with molecular ions the molecular fragments detector will be installed in addition to the periscope detector into the detector chamber. Work on this detector is currently carried out in the workshops. Experiments with molecular ions can even be performed without the ETS molecular detector by using the ETS for beam cooling and the existing EC as target. The assembly of the beamline for the neutral molecular fragments is currently done.
The physics of magnetized electron beams and the related suppression of TLR and the adiabatic acceleration will be studied further. This can be done outside of the storage ring using the retarding field energy analyzer or with dielectronic recombination.

Bibliography

[Alb93] Albrecht F., *Entwicklung eines Strahllagemeßsystems für den Heidelberger Testspeicherring TSR*, Master's thesis, Universität Heidelberg, 1993.

[Ale90] Aleksandrov A.V., *Electron Spread from GaAs Photoemitter*, unpublished, 1990.

[Ash76] Ashcroft N.W., *Solid state physics*, Saunders College Publishing, 1976.

[Böm01] Bömmels J. Leber E., Gopalan A., Weber J.M., Barsotti S., Ruf M.W., Hotop H., *Energy broadening due to photo ion space charge in a high resolution laser photoelectron source*, Rev. Scien. Instr. **72** (2001), no. 11, 4098–4105.

[Beu00] Beutelspacher M., *Systematische Untersuchungen zur Elektronenkühlung am Heidelberger Schwerionenspeichering TSR*, Ph.D. thesis, Universität Heidelberg, 2000.

[Blu87] Blum M., *Der Prototyp Kühlsolenoid des TSR - Messungen der Magnetfeldhomogenität und des Mikrowellenspektrums an der Teststrecke*, Master's thesis, Universität Heidelberg, 1987.

[Bud78] Budker G.I., Skrinsky A.N., , Sov. Phys.-Usp. **277** (1978), no. 21.

[Cro79] Cronin J.L., *Technical Aspects of Modern Dispenser Cathodes*, Microwave Journal (1979).

[Dan94] Danared H., Andler G., Bagge L., Herrlander C.J., Hilke J., Jeansson J., Källberg A., Nilsson A., Paál A., Rensfelt K.G., Rosengård U., Starker J., af Ugglas M., *Electron cooling with an ultracold electron beam*, Phys. Rev. Lett. **72** (1994), no. 24, 3775–8.

[Dan00] Danared H., Källberg A., Andler G., Bagge L., Österdahl F., Paál A., Rensfelt K.G., Simonsson A., Skeppstedt Ö., af Ugglas M., *Studies of electron cooling with a highly expanded electron beam*, Nucl. Instr. and Meth. A **441** (2000), no. 1-2, 123–33.

[Dik88] Dikansky N.S., Kudelainen V.I., Lebedev V.A., Meshkov I.N., Parkhomchuk V.V., Sery A.A., Skrinsky A.N., Sukhina B.N., *Ultimate possibilities of electron cooling*, Preprint 88-61 (Institute of Nuclear Physics, Novosibirsk), 1988.

[Eis00] Eisenbarth U., Mudrich M., Grieser M., Grimm R., Luger V., Schatz T., Schramm U., Schwalm D., Weidemüller M., *Anomalous behaviour of laser-cooled fast ion beams*, Hyperfine Inter. **127** (2000), no. 1-4, 223–35.

[Ger99] Gerthsen C., *Gerthsen Physik*, Springer, Heidelberg, 1999.

[Gla99] Glans P., Lindroth E., Eklöw N., Zong W., Gwinner G., Saghiri A.A., Pajek M., Danared H., Schuch R., *Dielectronic recombination of Li-like fluorine ions*, Nucl. Instrum. Methods Phys. Res. B **154** (1999), no. 1-4, 97–101.

[Gli92] Glinsky M.E., O'Neil T.M., Rosenbluth, M.N., *Collisional equipartion rate for a magnetized pure electron plasma*, Phys. Fluids B **5** (1992), no. 4, 1156–1166.

[GSI03] *Conceptual Design Report: An International Accelerator Facility for Beams of Ions and Antiprotons*, available at www.gsi.de, 2003.

[Gwi00] Gwinner G., et al., *Influence of Magnetic Fields on Electron-Ion recombination at Very Low Energies*, Phys. Rev. Lett. **84** (2000), no. 21, 4822–25.

[Gwi03] Gwinner G., 2003, private communication.

[Hab88] Habs D., Kramp J., Krause P., Matl K., Neumann R., Schwalm D., *Ultracold Ordered Electron Beam*, Physica Scipta **T22** (1988), 269–276.

[Hab89] Habs D. et al., *First Experiments with the Heidelberg Test Storage Ring TSR*, Nucl. Instr. and Meth. B **43** (1989), 390–410.

[Hop01] Hoppe M., *Differential energy analysis of electron beams: A study of photoemission from NEA-GaAs*, Ph.D. thesis, Universität Heidelberg, 2001.

[Ich70] Ichimaru S., Rosenbluth M.N., *Relaxation processes in plasmas with magnetic field. Temperature relaxations*, Phys. Fluids **13** (1970), no. 11, 2778–89.

[Ich82] Ichimaru S., *Strongly coupled plasmas: high-density classical plasmas and degenerate electron liquids*, Rev. Mod. Phys. **54** (1982), no. 4, 1017.

[Jan90] Jansen G.H., *Coulomb interactions in particle beams*, Adv. in electronics and electron physics, supplement **21** (1990).

[Ken95] Kenntner J., *Messungen zur Elektronenstoß-Ionisation und dielektronischer Rekombination hochgeladener lithiumartiger Ionen*, Ph.D. thesis, Universität Heidelberg, 1995.

[Kie03] Kieslich S., Schippers S., Shi W., Müller A., Gwinner G., Schnell M., Wolf A., Lindroth E., Tokman M., *High resolution spectroscopy of doubly excited states in berylliumllike scandium utilizing dielectronic recombination*, to be published, 2003.

[Kil90] Kilgus G., *Hochauflösende Messungen zur dielektronischen Rekombination*, Ph.D. thesis, Universität Heidelberg, 1990.

[Kil92] Kilgus G., Habs D., Schwalm D., Wolf A., Badnell N.R., Müller A., *High resoultion measurement of dielectronic recombination of lithiumlike Cu^{26+}*, Phys. Rev. A **46** (1992), no. 9, 5730–5740.

[Kir67] Kirstein P., Kino G., Waters W., *Space-charge Flow*, Mc Graw-Hill, New York, 1967.

[Kra92] Krause P., *Temperaturrelaxation in magnetisierten Elektronenstrahlen*, Ph.D. thesis, Universität Heidelberg, 1992.

[Kro00] Krohn S., Amitay Z., Baer A., Zajfman D., Lange M., Knoll L., Levin J., Schwalm D., Wester R., Wolf A., *Electron-induced vibrational deexcitation of H_2^+*, Phys. Rev. A **62** (2000), no. 3, 032713/1–8.

[Kro02] Krohn S., *Inelastic collisions and recombination between electrons and molecular ions*, Ph.D. thesis, Universität Heidelberg, 2002.

[Kud82] Kudelaĭnen V.I, Lebedev V.A., Meshkov I.N., Parkhomchuk V.V., Sukhina B.N., *Temperature relaxation in a magnetized electron beam*, Sov. Phys. JETP **56** (1982), no. 6, 1191–96.

[Kur98] Kurz C., Gilbert S.J., Greaves R.G., Surko C.M., *New source of ultra-cold positron and electron beams*, Nucl. Instrum. Methods Phys. Res. A **143** (1998), 188–194.

[Lan01] Lange B., *Optimierung des Elektronenstrahls des ultrakalten Elektronentargets für den Speicherring TSR*, Master's thesis, Universität Heidelberg, 2001.

[Lan02] Lange M., *Competition between reaction channels in electron collisions of the hydrogen molecular ion HD^+*, Ph.D. thesis, Universität Heidelberg, 2002.

[Les] Lestinsky M., Ph.D. thesis in preparation.

[Lin01] Lindroth E., Danared H., Glans P., Pešić Z., Tokman M., Vikor G, Schuch R., *QED effects in Cu-like Pb recombination resonances near threshold*, Phys. Rev. Lett. **86** (2001), no. 22, 5027–30.

[Möh93] Möhl D., *Advances of Accelerator Physics and Technologies*, ch. Cooling of particle beams, World Scientific, Singapore, 1993.

[Mül97] Müller A., Wolf A., *Production of antihydrogen by recombination of p with e^+: what can we learn from electron-ion collision studies?*, Hyperfine Interactions **109** (1997), 233–267.

[O'N83] O'Neil T.M., *Collision operator for a strongly magnetized pure electron plasma*, Phys. Fluids **26** (1983), no. 8, 2128–2135.

[O'N85] O'Neil T.M., Hjorth P.G., *Collisional dynamics of a strongly magnetized pure electron plasma*, Phys. Fluids **28** (1985), no. 11, 3241–3252.

[Orl01] Orlov D.A., Hoppe M., Weigel U., Schwalm D., Terekhov A.S., Wolf A., *Energy distributions of electrons emitted from GaAs(Cs, O)*, Appl. Phys. Lett. **78** (2001), no. 18, 2721–3.

[Orl02] Orlov D.A., 2002, private communication.

[Pas96] Pastuszka S., Schramm U., Broude C., Grimm R., Habs D., Kenntner J., Miesner H.J., Schüßler T., Schwalm D., Wolf A., *Electron cooling and recombination experiments with an adiabatically expanded electron beam*, Nucl. Instrum. Methods Phys. Res. A **369** (1996), no. 1, 11–22.

[Pas97a] Pastuszka S., *Erzeugung kalter Elektronenstrahlen durch Photoemission aus GaAs*, Ph.D. thesis, Universität Heidelberg, 1997.

[Pas97b] Pastuszka S., Kratzmann D., Schwalm D., Wolf A., Terekhov A.S., *Transverse energy spread of photoelectrons emitted from GaAs photocathodes with negative electron affinity*, Appl. Phys. Lett. **71** (1997), no. 20, 2967–9.

[Pas00] Pastuszka S., Hoppe M., Kratzmann D., Schwalm D., Wolf A., Jaroshevich A.S., Kosolobov S.N., Orlov D.A., Terekhov A.S., *Preparation and performance of transmission-mode GaAs photocathodes as sources for cold dc electron beams.*, J. Appl. Phys. **88** (2000), no. 11, 6788–800.

[Pie40] Pierce J.R., *Rectilinear flow in electron beams*, Appl. Phys. Lett. **11** (1940), 548.

[Pie54] ———, *Theory and design of electron beams*, Van Nostrand, New York, 1954.

[Pot90] Poth H., *Electron cooling: theory, experiment, application*, Phys. Rep. **196** (1990), 135–297.

[ROO] ROOT, see root.cern.ch.

[Rub77] Rubbia C., *On the Formation of Intense Electron Beams with Small Transverse velocities for (Anti-)Proton Cooling*, CERN EP Internal Report **77-2** (1977).

[Sav02] Savin D.W., Kahn S.M., Linkemann J., Saghiri A.A., Schmitt M., Grieser M., Repnow R., Schwalm D., Wolf A., Bartsch T., Müller A., Schippers S., Chen M.H., Bradnell N.R., Gorczyca T.W., Zatsarinny O., *Dielectronic recombination of Fe XIX forming Fe XVIII: Laboratory measurements and theoretical calculations*, Astrophys. J. **576** (2002), 1098–1107.

[Sch73] Schnell G., *Magnete*, Thiemig, München, 1973.

[Sch97] Schmitt M., 1997, private communication.

[Sch99] Schippers S., *Recombination of HCI with electron-fundamental atomic physics and applications.*, Physica Scripta **T80** (1999), 158–62.

[Sch00a] Schmitt M., *Erzeugung energiescharfer Elektronenstrahlen*, Ph.D. thesis, Universität Heidelberg, 2000.

[Sch00b] Schmöller T., Zwicknagel G., Toepffer C., *Numerical simulations of the adiabatic acceleration of electron beams*, Nucl. Instrum. Methods Phys. Res. A **441** (2000), 50–53.

[Sch02] Schramm U., Schatz T., Habs D., *Three-dimensional crystalline ion beams*, Phys. Rev. E **66** (2002), no. 3, 36501–1–9.

[Sch03] Schneider I.F., private communication, 2003.

[Sig02] Sigmaphi S.A, Vannes, France, 2002, private communication.

[Sik99] Sikler G., *Lagemessung von Elektronen- und Ionenstrahl für das TSR-Elektronentarget*, Master's thesis, Universität Heidelberg, 1999.

[Sør87] Sørenson, A.H., *Introduction to intrabeam scattering*, CERN Accelerator School (87-10), 1987.

[Spe02] Spectramat, 2002, private communication.

[Spi62] Spitzer jr L., *Physics of fully Ionized Gases*, Wiley and Sons, New York, 1962.

[Spr00] Sprenger F., *Testaufbau für das ultrakalte Elektronentarget am Speicherring TSR*, Master's thesis, Universität Heidelberg, 2000.

[Ste01] Steck M., Beckert K., Beller P., Franzke B., Nolden F., *Extremely cooled ion beams in the ESR with evidence of ordering*, 1IEEE **1** (2001), 137–41.

[Str00] Strasser D., Pedersen H.B., Altstein N., Heber O., Wester R., Bhushan K.G., Zaifman D., *An innovative approach to multiparticle three-dimensional imaging*, Rev. Scien. Instr. **71** (2000), no. 8, 3092–8.

[Tho01] Thong J.T.L., Oon C.H., Eng W.K., Zhang W.D., Gan L.M., *High-current field emission from a vertically aligned carbon nanotube field emitter array*, Appl. Phys. Lett. **79** (2001), no. 17, 2811–13.

[Tok02] Tokman M., Eklöw N., Glans P., Lindroth E., Schuch R., Gwinner G., Schwalm D., Wolf A., Hoffknecht A., Müller A., Schippers S., *Dielectronic recombination resonances in F^{6+}*, Phys. Rev. A **66** (2002), no. 1, 012703/1–13.

[Wei03] Weigel U., *Cold intense electron beams from Gallium Arsenide photocathodes*, Ph.D. thesis, Universität Heidelberg, 2003.

[Wil92] Wille K., *Physik der Teilchenbeschleuniger und Synchrotronstrahlungsquellen*, Teubner, Stuttgart, 1992.

[Wis03] Wissler G., *Ein Detektorsystem für Fragmentations- und Umladungsexperimente mit gespeicherten Ionen*, Ph.D. thesis, Universität Heidelberg, 2003.

[Zwi91] Zwickler S., Habs D., Krause P., Neumann R., Schwalm D., Wolf A., *Photocathode studies for an ultracold electron beam device*, Electron Cooling and New Cooling Techniques (World Scientific, Singapore) (Techhio L. Calabrese L., ed.), 1991.

[Zwi93] Zwickler S., *Energieverteilungen intensiver Elektronenstrahlen aus InGaAsP-Photokathoden*, Ph.D. thesis, Universität Heidelberg, 1993.

Ich möchte mich ganz herzlich bei allen bedanken, die zum Entstehen dieser Arbeit und zur Realisierung des Elektronentargets beigetragen haben. Mein besonderer Dank gilt Prof. Andreas Wolf für die hervorragende Betreuung der Arbeit und die unermüdliche Hilfe bei allen kleinen und großen Problemen. Weiterhin danke ich Prof. Dirk Schwalm für die Möglichkeit in der TSR-Truppe mitzuwirken.
Meinen Kollegen danke ich für die tatkräftige Mithilfe beim Aufbau und bei den Experimenten: Dimitri Orlov für vielfältige Diskussionen und vor allem für die Hilfe bei den Energieverteilungsmessungen. Peter Witte für die Mithilfe beim Zusammenbauen der Vakuumkammern als "Not am Mann" war. Michael Schnell und Michael Lestinsky für die ausdauernde Unterstützung bei den ersten Strahlzeiten, vor allem auch mit dem Detektor und der Datenaufnahme. Frederik Spiegelhalder für seine treuen Hiwi-Dienste. Markus Schmitt für die prima Vorarbeit und die Vererbung des Elektronentargets. Birgit Lange für die Mithilfe beim Umzug an den Speicherring.
Ohne die Arbeit der Konstruktionsabteilung hätten die Ideen nicht in die Realität umgesetzt werden können. Herzlichen Dank an H. Weber, H. Gahn und Fr. Burwitz, auch für die schönen 3D-Modelle der verschiedenen Komponenten.
Ein Großteil der mechanischen Komponenten entstand in der Hauptwerkstatt unter der Leitung von H. Mallinger. Bei ihm möchte ich mich ganz herzlich bedanken für seine stete Hilfsbereitschaft auch bei schwierigen Unterfangen. Der Wechselwirkungsmagnet entstand in den Händen von H. Heldner, der hierfür sehr viel Energie investiert hat. Vielen Dank auch an H. Bender für die Hilfe bei der Reinigung der UHV-Komponenten.
Die Arbeit vor Ort wurde natürlich von den Männern aus der Hahn-Werkstatt durchgeführt. Alles was nicht paßte wurde passend gemacht und alles was noch fehlte wurde hergestellt. Vielen Dank an H. Hahn und H. Fleckenstein und besonders an Christian Kaiser, ohne die der endgültige Zusammenbau nicht möglich gewesen wäre.
Vielen Dank an Manfred Grieser und Kurt Horn für die Hilfe bei der Integration in den Speicherring und für die Unterstützung bei den ersten Strahlzeiten.
Ein besonderer Dank gilt auch Oliver Koschorrek für alles was mit dem Ausheizen zu tun hatte und für die unkomplizierte Lösung von Elektronikproblemen.
Beim Aufbau des Kontrollsystems konnte ich immer auf die Unterstützung von Holger Schneider, Rolf Epking und H. Schreiner zurückgreifen. Die Anlaufschwierigkeiten mit dem EUNet konnten dadurch schnell behoben werden.
Nicht zu vergessen die zentralen Einrichtungen des MPI, die für die Versorgung der Apparatur mit Strom und Wasser gesorgt haben und allen anderen Mitarbeitern die zum gelingen der Arbeit beigetragen haben.
Vielen Dank an Helga Krieger für ihren steten Einsatz für die Arbeitsgruppe und an Doris Cerny für die Hilfe bei organisatorischen Angelegenheiten.
Ein herzliches Dankeschön an Julie für den Versuch mein Englisch etwas aufzubessern und die schlimmsten Fehler auszubügeln.
Schließlich ein ganz besonderer Dank an Carolin, die mich ermutigt hat diese Arbeit zu schultern und mich immer bei allem unterstützt hat.

Vielen Dank!